Title	Carbonization of polyimide using CO2 laser and femtosecond laser for sensor applications
Author(s)	Biswas, Ratul Kumar
Publication Date	2023-10-05
Publisher	NUI Galway
Item record	http://hdl.handle.net/10379/17938

Carbonization of Polyimide using CO_2 laser and Femtosecond laser for Sensor Applications

by

Ratul Kumar Biswas

A thesis submitted in partial fulfilment

of the requirements for the degree of

Doctor of Philosophy

Academic supervisor: Dr. Patricia J. Scully

Academic co-supervisor: Dr. Gerard M. O'Connor

National Centre for Laser Applications, Physics

School of Natural Sciences

College of Science and Engineering

University of Galway

August 2023

Dedicated to my parents, family, and friends.

Table of Contents

List of Figures…………………………………………………………….……….…………viii

List of Tables……………………………………………………………….………………xviii

Abbreviations………………………………………………………......……...……xix

List of Variables………………………………………………...….…………………..xx

Abstract………………………………………………………...……………..…....xxii

Declaration……………………………………………………....……….…......xxiii

Acknowledgements………………………………………………………...….……..xxiv

Chapter 1: Introduction…………………………………………………...…………..1

1.1. Research Questions…………………………………………………...……………3

1.2. Aims and Objectives………………………………………………...………...3

1.3. Organization of Thesis………………………………………………...…………4

Bibliography…………………………………………………………………………...6

Chapter 2: Laser-Materials Interaction…………………………………………….....…..8

2.1. Laser Fundamentals…………………………………………………………....……8

2.2. Interaction of a laser pulse with material……………………………………....……8

2.2.1. Photothermal Process…………………………………………………......……..9

2.2.2. Photochemical Process…………………………………………………......……11

2.2.3. Photomechanical Process…………………………………………….....……..12

2.3. Laser Polyimide Interaction…………………………………………......…………13

2.3.1. Laser Carbonization of Polyimide………………………………….…………13

2.3.1.1. Molecular Dynamics of Laser Carbonization………………………..…………15

2.3.1.2. Femtosecond laser carbonization of Polyimide…………………………..………17

2.3.2. Laser Ablation of Polyimide………………………………………..…....…17

2.3.2.1. Femtosecond Laser Ablation of Polyimide……………………………...………...19

2.4. Summary…………………………………………………………………...………20

Bibliography...…………………………………………………………………………..21

Chapter 3: Laser Induced Graphene……………………………………….……….…...23

3.1. 3D Mesoporous Carbon……………………………..………………...…23

3.1.1. Percolation Theory…………………………………………………...……...…25

3.2. Laser carbonization compared with conventional graphene manufacturing

Methods……………………………………………………………………………...…..25
3.3. Laser Graphitization……………………………………………………...…..28
3.4. Modes of Graphene Growth……………………………………………..………29
3.5. Raman Spectroscopy of Graphene……………………………..………………..32
3.6. Electronic structure under strain- Graphene as strain sensor……………………...…..34
3.6.1. Intraflake……………………………………………………………………….....34
3.6.2. Interflake……………………………………………………………………….....36
3.7. Applications of Laser Induced Graphene (LIG)…………………………………………37
3.8. Summary…………………………………………………………………………...….39
Bibliogrphy…………………………...…………………………………………………40

Chapter 4: Materials and Methods……………………………………………...…….44
4.1. Numerical Simulation……………………………………………………...…….46
4.1.1. Modelling of thermal interaction of CO_2 laser beam……………………..………..46
4.1.2. Modelling of Thermal Interaction of femtosecond Laser Beam…………..………..51
4.2. CO_2 Laser………………………………………………………………..………53
4.2.1. Active Medium…………………………………………………...………53
4.2.2. Beam Delivery System……………………………………………...………53
4.3. Yb:KYW Femtosecond laser…………………………………………………………55
4.4. Cold Plasma Tool……………………………………………………………………...56
4.5. Polyimide…………………………………………………………………..……..57
4.5.1. Background………………………………………………………………..……57
4.5.2. Types………………………………………………………………………………..58
4.5.3. Synthesis…………………………………………………………………..……58
4.5.4. Properties……………………………………………………………………………59
4.6. Sensor demonstration study………………………………………………………..60
4.6.1. Kirigami design……………………………………………………………………..51
4.6.2. Structural mechanics of the Kirigami sensor……………………………………..63
4.6.3. Sensor Data Acquisition (DAQ)………………………………………………....65
4.7. Characterization Methods…………………………………………………………..66
4.7.1. Raman Spectroscopy……………………………………….……………………..66
4.7.2. Scanning Electron Microscopy (SEM)………………………….………………..68
4.7.3. Profilometer………………………………………………………………………70
4.8. Summary……………………………………………………………………………70

Bibliography……………………………………………………………………………….71

Chapter 5: Laser carbonization and graphitization………………………………………....74
5.1. Introduction………………………………………..……………………………………75
5.2. Experimental and Simulation Method………………………………………………….77
5.2.1. Experimental parameters for Direct Laser Writing using CO_2 Laser………………..…77
5.2.2. Modelling of carbonization and graphitization of PI by CO_2 Laser……………………78
5.2.3. Structural and Electrical Characterization of the carbonized and graphitized tracks…..80
5.3. Results and Discussion………………………………………………………………...81
5.3.1. Calculation of Incubation coefficient, spot-size radius, and Single Pulse Threshold Power of Carbonization ………………………………………………………………….82
5.3.2. Calculation of Threshold Power of Graphitization……………………………………..82
5.3.3. Estimation of Temperature for Single-Pulse Threshold Power, Temperature due to Pulse Overlap factor for Carbonization and Temperature at threshold power for Graphitization……………………………………………………………………………83
5.3.4. Structural Characterization of the Carbonized tracks…………………………………86
5.3.5. Electrical Characterization of the carbonized tracks……………………….………..89
5.4. Conclusion………………………………………………………………………………92
5.5. Study with integrated area under the peaks in Raman spectroscopy…………….……93
5.6. Summary…………………………………………………………………………………96

Chapter 6: Graphene growth kinetics in laser carbonization……………………………..…100
6.1. Graphene Growth Kinetics for CO_2 Laser Carbonization of Polyimide……….….…101
6.1.1. Introduction……………………………………………………………………..…101
6.1.2. Experimental Method…………………………………………………………..…….102
6.1.3. Structural Characterization of carbonized tracks…………………………….….…102
6.1.4. Modelling of laser irradiation temperature…………………………………..….…103
6.1.5. Results and Discussion……………………………………………………….………103
6.1.5.1. Calculation of spot-size, threshold laser fluence, and irradiation temperature…....103
6.1.5.2. Surface morphology of LIG……………………………………………….……….104
6.1.5.3. Calculation of Arrhenius kinetic parameters from crystallite size at different laser fluence and scan-speed………………………………………………….……105
6.1.5.4. Optical microscopy and Electrical characterization of LIG at different laser fluence and scan-speed……………………………………………………….…….109

6.1.6. Conclusion…………………………….……………………………………………...113
6.2. Plasma Enhanced Planar Crystal Growth of Laser Induced Graphene…………….……..114
6.2.1. Introduction…………………………………………………………..…………114
6.2.2. Experimental Method……………………………………………..…………115
6.2.3. Results and discussion…………………………………………………..…116
6.2.4. Test of uniformity of conductivity and crystallite size of LIG………………………...123
6.2.5. Conclusion……………………………………………………………………128
6.3. Summary…………………………………………………………………………..129
Bibliography…………………..…………………………………………………………130

Chapter 7: Femtosecond laser carbonization and ablation of Polyimide……………………132
7.1. Introduction…………………………..……………………………………………..133
7.2. Experimental Methods……………………………………………………………136
7.2.1. Laser System………………………………………………………………………136
7.2.2. Laser Carbonization and Ablation of Polyimide……………………………………...136
7.2.3. Laser Scan Feature Measurements and Characterizations……………………………137
7.2.4. Laser printing of Kirigami Inspired Sensor…………………………………………..137
7.2.5. Electromechanical Characterization of the Sensor……………………………………137
7.3. Results and Discussion……………………………………………………………138
7.3.1. Calculation of spot-size and ablation threshold………………………………………138
7.3.2. Laser Carbonization of PI…………………………………………………………141
7.3.3. Modelling of Heat Accumulation…………………………………………………..146
7.3.4. Laser Ablation of Polyimide………………………………………………………150
7.3.5. Kirigami Designed Sensor Characterization…………………………………………152
7.3.5.1. Repeatability and reproducibility test of the Kirigami sensor……………………...155
7.3.5.2. Comparative Analysis of the Kirigami sensor vs Planar sensor……………………157
7.3.5.3. Plastic regime of the sensor………………………………………………………158
7.4. Conclusion…………………………………………………………………………...159
7.5. Comparative study of femtosecond laser carbonization and CO_2 laser Carbonization…………………………………………………………………...160
7.6. Summary……………………………………………………………………………161
Bibliography……………………………………………………………………………...162

Chapter8: Summary………………………………………………………………………165

8.1. Review of papers……………………………………………………………………..165
8.2. Conclusions…………………………………………………………………………167
8.3. Future Work…………………………………………………………………………168
Publications and Conferences………………………………………………………….169
Appendix………………………………………………………………………………170
Bibliography…………………………………………………………………………...181

List of Figures

1.1. Laser carbonization of Polyimide and its applications in motion, voice, gesture and temperature sensors.

2.1. Three leading processes during laser-materials interaction, E_{bond}= Bond energy, λ_{abs}= absorption wavelength, τ_{Th}= time for thermal expansion=d/c_{ac}, where d= film thickness, c_{ac}= acoustic velocity and is in the order of 10 ps.

2.2. A simple two-level scheme of single photon absorption.

2.3. 1 photon and 2 photon excitations in hydrogel.

2.4. (a-c) Laser carbonization by Multiphoton absorption at the bulk of Polyimide using fs laser, and (d) Thermal modelling of Ti-Sapphire femtosecond laser-PI interaction.

2.5. (a) Chemical structure of Polyimide, (b) Stages in laser carbonization.

2.6. Reported reaction mechanisms of PI. (a) Thermal decomposition process. (b) Carbonization process.

2.7. Bond scissions obtaining graphitic structure from PI.

2.8. (a) Temperature profiles used in MD simulation, (b) Pressure achieved in the NVT simulation at T_P= 2400 K, 2700 K, and 3000 K, (c,d,e) Snapshots of final clusters at T_P= 2400 K, 2700 K, and 3000 K, (f,g) Enlarged views of the clusters in fig 5e.

2.9. Norrish type bond scissions in PMMA.

2.10. (a) Photochemical ablation pathways for PMMA, (b) PI under 308 nm UV laser.

2.11. Schematic diagrams of the photoionization excited by femtosecond laser. (A) Tunnelling ionization, (B) mixture of tunnelling and multiphoton ionization, (C) multiphoton ionization, and (D, E) avalanche ionization.

3.1. Synthesis and applications of mesoporous carbon.

3.2. Conduction mechanism in graphene containing composites.

3.3. (a, b) High resolution TEM (HRTEM) image of LIG edge with scale-bar 10 nm and 5 nm respectively, (c) STEM image of LIG edge, (d) TEM image showing 5-7 membered rings.

3.4. Varying LIG morphology with varying focal length (*z*), Process window showing the transitions of LIG morphology from porous to woolly in CO_2 laser carbonization process.

3.5. Laser graphitization of CVD deposited DLC film.

3.6. (a-c) Modes of thin-film growth, (d) Equilibrium angle of contact with surface (s), fluid (f) and vapour (v)**.**

3.7. Contact angle measurement on (a) HDP-SiO_2 with wetting angle = 31^0, (b) Thermal SiO_2 with wetting angle =45^0, and (c) PE-Si_3N_4 with wetting angle = 38^0. Optical microscopy images of graphene on (d) HDP-SiO_2, (e) Thermal SiO_2, and (f) PE-$Si_3N_{4.}$

3.8. (a) Vibration absorption process, (b) Raman shifts in vibrational spectra.

3.9. Resonance mechanisms for D, G and 2D band, Phonon excitations in 2-layer graphene.

3.10.Vibrational modes in graphene (b) Phonon dispersion in graphene, (c) Raman spectra of single layer graphene and multiplayer graphene, (d) Band-fitting of D and G peaks, (e) Full Raman spectrum of graphene showing the TA and LA modes.

3.11. (a) Graphene unit cell, (b) reciprocal lattice, (c) Reciprocal lattice vectors, (d) TEM of 1-4 LG, (e) 3D band dispersion curve of graphene.

3.12. E-***k*** diagram of single layer graphene upon (a) zero strain, (b) uniaxial strain, (c) Shear strain.

3.13. (a) *GF* vs λ simulated using Eq 2.35 for filler fraction V_c=0.2-0.4, , (b) *R* vs λ simulated using Eq 2.35 for filler fraction V_c=0.2-0.4, (c) *R* vs force measured from 0-0.5 N for LIG, (d) *R* vs deflection measured from 0-7 mm for LIG.

3.14. Applications of LIG.

4.1. (a) *k* vs *T*, (b) *n* vs *T* , (c) *K* vs *T* , (d) C_P vs *T* of Polyimide plotted in COMSOL.

4.2. (a) Geometry for thermal simulation in COMSOL, (b) Cut point and (c) cut line for temperature analysis, and (d) Physics controlled mesh in COMSOL.

4.3. Temperature evolution at 0.15 W and 0.21 W for carbonization and graphitization respectively.

4.4. Temperature evolution by laser power 0.2 W and 0.3 W at scan speed 3 mm/s and 2 mm/s respectively.

4.5. Band diagram of the active medium in CO_2 laser.

4.6. Schematic diagram of sealed-tube CO_2 laser.

4.7. Schematic of beam path arrangement of CO_2 laser.

4.8. Beam Path of Yb:KYW femtosecond laser.

4.9. (A) Plasma jet kINPen09 (Neoplas GmbH, Greifswald, Germany), (B) schematic diagram of kINPen09.

4.10. Imide group formation.

4.11. Classification of Polyimides.

4.12. Synthesis mechanism of aromatic polyimide.

4.13. Inverse problem for generation of Kirigami design.

4.14. (a) LIG sensor pattern inscribed inside (b) Kirigami pattern designed in AUTOCAD.

4.15. Overall design of the Kirigami-inspired sensor designed in AUTOCAD.

4.16. (a) Kirigami-inspired strain sensor, (b) Kirigami sensor connected to Wheatstone Bridge and PhidgetBridge DAQ, R_2, R_3 and R_4 used in this application are of 1 MΩ each and potentiometer was used in series with R_2 to balance the bridge.

4.17. Geometry of Kirigami design in COMSOL.

4.18. Meshing of the geometry.

4.19. (a) Equations for solid mechanics, (b) fixed constraints, (c) material properties of Polyimide.

4.20. Wheatstone Bridge setup for strain sensor.

4.21. Wheatstone Bridge connected with Op-amp.

4.22. Schematic diagram of Raman spectrophotometer.

4.23. (a) Raman imaging of I_D/I_G of graphene on Si(100) grown at temperature ranging from 600-1000^{0}C, (b) Raman imaging of I_D/I_G of graphene on SiO_2 grown at temperature ranging from 600-1000^{0}C, (c) I_D/I_G vs temperature of graphene on Si(100), (d) I_D/I_G vs temperature of graphene on SiO_2.

4.24. Configuration of Scanning Electron Microscope.

4.25. Interaction of e-beam with sample.

4.26. Working principle of optical profilometer.

5.1: Laser Beam Delivery system used for Step 1- carbonization of PI, followed by Step 2- graphitization of the track.

5.2. (a) D^2 vs ln(P) plot for 3-7 pulses, (b) ln(N.$F_{N,Th}$) vs ln(N) plot.

5.3. D^2 vs *ln(P)* for CO_2 laser scanning at 120 m/min and repetition rate 0.1 kHz.

5.4. (a) Raman spectra of tracks graphitized at 0.21, 0.32, 0.41, 0.5 and 0.65 W, (b) Variation of G-peak position of the Graphitized tracks with increasing power.

5.5. Simulation results at (a) single pulse threshold power $P_{1,Th}$= 0.324 W, (b) laser with power 0.15, 0.21, 0.32, 0.41, 0.5 and 0.65 W at scan speed 120 mm/min and repetition rate 0.1 kHz. for carbonization (c) laser with power 0.21, 0.32, 0.41, 0.5 and 0.65 W at scan speed 120 mm/min and repetition rate 0.1 kHz. for graphitization, and (d) Variation of peak temperature with laser power both for carbonization and graphitization as obtained from simulation.

5.6. (a) Temperature contour of PI, and (b) Temperature along the cut line 0.5 W.

5.7. (a) Temperature contour of ta-C, and (b) Temperature along the cut line 0.5 W.

5.8. Cross-sectional SEM image of (a) graphitized track at 0.5 W on a 0.21 W pre-carbonized track, (b) Varying width of the carbonized and graphitized tracks with power, (c) Varying depth of the carbonized and graphitized tracks with power, (d) Raman spectra of tracks carbonized at 0.15, 0.21, 0.32, 0.41, 0.5 and 0.65 W.

5.9. (a) Varying I_D/I_G ratio of carbonized and graphitized tracks with laser power, (b) Varying average crystallite domain size as a function of laser power, (c) Raman mapping of carbonized track at 0.21 W, (d) Raman mapping of graphitized track at 0.5 W on a 0.21 W pre-carbonized track.

5.10. Measurement of cross-sectional area of LIG track.

5.11. Microscopic images of Carbonized vias.

5.12. Microscopic images of Graphitized vias on pre-carbonized vias at 0.21 W.

5.13. (a) I-V plot for carbonized tracks under laser irradiation of power 0.21, 0.32, 0.41, 0.50 and 0.65 W, (b) I-V plot for carbonized tracks under laser irradiation of power 0.21, 0.32, 0.41, 0.5 and 0.65 W on 0.21 pre-carbonized track, (c) Variation of electrical conductivity of the carbonized and graphitized tracks.

5.14. Lorrentzian fitted D, G, D' and 2D peaks in carbonized tracks with laser drawn at (a) 0.15 W, (b) 0.21 W, (c) 0.32 W, (d) 0.41 W, (e) 0.5 W, amd (f) 0.65 W.

5.15. Lorrentzian fitted D, G, D' and 2D peaks in carbonized tracks with laser drawn at (a) 0.21 W, (b) 0.32 W, (c) 0.41 W, (d) 0.5 W, (e) 0.65 W and (f) G-peak position vs power.

5.16. (a) A_D/A_G vs power, (b) L_a vs power, (c) $A_D/A_{D'}$ vs power and (d) A_{2D}/A_G vs power for carbonized and graphtitized tracks.

5.17. FWHM of (a) G, (b) D and (c) 2D peaks of carbonized and graphitized tracks.

6.1. (a-f) Carbonized spots on PI with single pulse CO_2 laser for power 0.55-1.12 W, (g) D^2 vs ln(P) of LIG. (h) Temporal evolution of temperature at laser fluence of $6.07x10^3$-$1.23x10^4$ mJ/cm^2.

6.2. Cross-sectional SEM images of carbonized tracks at P=0.55W, 0.651W, 0.775W, 0.892 W, 0.995 W, and 1.115 W at scan speeds 350-750 mm/min.

6.3. Raman spectroscopy of LIG written at scan-speed 350-750 mm/min at laser fluence (a) $6.07x10^3$ mJ/cm^2, (b) $7.19x10^3$ mJ/cm^2, (c) $8.56x10^3$ mJ/cm^2, (d) $9.85x10^3$ mJ/cm^2, (e) $1.09x10^4$ mJ/cm^2, and (f) $1.23x10^4$ mJ/cm^2.

6.4. (a) I_D/I_G vs laser scan-speed, (b) Crystallite size vs irradiation time at individual fluence $6.07x10^3$-$1.23x10^4$ mJ/cm^2, (c) Nuclei size vs laser fluence, and (d) *ln(k)* vs *1/T*.

6.5. Raman mapping of LIG across (a) length, and (b) width of the track, (c) LIG track written at 0.892 W, 650 mm/min, (d) Raman spectra taken at 5 points along Y-axis with inset of I_D/I_G values at 5 points.

6.6. Optical microscopy images of carbonized tracks at P=0.55W, 0.651W, 0.775W, 0.892 W, 0.995 W, and 1.115 W at scan speeds 350-750 mm/min.

6.7. IV measurement of LIG written at scan-speed 350-750 mm/min at laser power (a) 0.55 W, (b) 0.651 W, (c) 0.775 W, (d) 0.892 W, (e) 0.995 W, and (f) 1.115 W.

6.8. (a) Carbonized width vs scan speed, (b) carbonized depth vs scan speed, (c) Resistance vs scan speed, and (d) Conductivity vs scan speed of LIG at P= 0.55 W, 0.651 w, 0.775 W, 0.892W, 0.995 W, 1.115 W.

6.9. Graphical abstract of laser carbonization of plasma-activated Polyimide.

6.10. (a, b) Contact angle measurement of water droplets on untreated PI and plasma treated PI at scan-speed 200 mm/min), (c, d) Contact angle measurement of EG on untreated PI and plasma treated PI at scan-speed 200 mm/min, (e) Contact angle vs Plasma scan-speed, (f) Surface roughness measurement of untreated PI, (g) of plasma treated PI at 200 mm/min.

6.11. IV measurements of LIG drawn at 0.65-1.12 W on untreated PI and plasma treated PI at scan speed 200-1000 mm/min.

6.12. (a) Resistance vs laser power of LIG drawn at 0.65-1.12 W on untreated PI and plasma treated PI at scan speed 200-1000 mm/min.

6.13. Cross-sectional SEM images of LIG drawn at 0.65-1.12 W at 450 mm/min, f=100 Hz on (a-e) untreated PI, and on (f-j) plasma treated PI at plasma scan speed 200 mm/min.

6.14. (a) Raman spectra of LIG on untreated PI, and (b) on plasma treated PI at scan speed 200 mm/min, (c) L_a vs plasma scan-speed, and (d) Conductivity vs plasma scan-speed on untreated PI and plasma treated PI at 200-1000 mm/min, (e) I_{2D}/I_G vs laser power, and (f) width and depth of LIG on untreated and plasma-treated PI at 200 mm/min.

6.15. Conductive ink-based contacts at distances 10 mm, 20 mm and 30 mm on LIG drawn at 9a) 0.65 W, (b) 0.77 W, (c, d, e) IV-measurement probes placed at the contacts for resistance measurement.

6.16. IV of LIG drawn at 0.65 W on (a) untreated PI, and (b) plasma treated PI, (c) Resistance vs length of LIG track drawn at 0.65 W, (d) Conductivity measured at 3 points 10 mm, 20 mm, 30 mm drawn at 0.65 W; IV of LIG drawn at (e) 0.77 W on untreated PI, and (f) plasma treated PI, (g) Resistance vs length of LIG track drawn at 0.65 W, (h) Conductivity measured at 3 points 10 mm, 20 mm, 30 mm drawn at 0.65 W, the conductivity was found to be consistent throughout the track.

6.17 Raman mapping of LIG at laser power 0.65 W, 0.77 W on untreated PI.

6.18 Raman mapping of LIG at laser power 0.65 W, 0.77 W on plasma-treated PI at scan speed 200 mm/min.

6.19. Raman spectra of LIG on plasma treated PI at scan speed (a) 400 mm/min, (b) 600 mm/min, (c) 800 mm/min, (d) 1000 mm/min.

6.20. Contact angle measurement of (a-f) deionized water and (g-l) Ethylene Glycol on untreated and plasma-treated PI at scan speed 400-1000 mm/min.

7.1. (a) Process conditions of femtosecond laser printing, (b) Kirigami sensor connected to Wheatstone Bridge and PhidgetBridge DAQ, R_2, R_3 and R_4 used in this application are of 1 MΩ each and potentiometer was used in series with R_2 to balance the bridge.

7.2. Spot-size measurement from ablated spots on PI.

7.3. SEM images of laser ablated spots on PI.

7.4. Ablated depth by single laser pulses of power 0.8-3 W measured by Zygo profilometer. Detailed results in the Appendix B.

7.5. Single pulse ablation threshold power measured from ablated spots on PI.

7.6. Optical microscope images of LIG drawn at laser power 0.242-0.281 W at 2-3 mm/s at 200 kHz.

7.7. (a-e) Raman Spectra of LIG drawn at laser power 0.242-0.281 W at 2-3 mm/s at 200 kHz, (f) Defect ratio (I_D/I_G) of the LIG.

7.8. (a-e) IV measurement of LIG drawn at laser power 0.242-0.281 W at 2-3 mm/s at 200 kHz.

7.9. (a) L_a of LIG vs *v*, (b) electrical conductivity vs v for laser power 0.242-0.281 W.

7.10. (a) D^2 vs ln *F*, (b) Calculation of incubation coefficient in the photothermal regime from ln($N.\ F_{N,Th}$) vs ln(N), (c) *T* vs *t* from heat accumulation model at threshold fluences for scan speed 2-3 mm/s, (d) Raman spectra of LIG drawn at 0.242 W at 2-3 mm/s.

7.11. (a-e) Cross-sectional SEM images of femtosecond LIG at 0.242W, 0.251 W, 0.264 W, 0.272 W and 0.281 W respectively at 2-3 mm/s at 200 kHz, (f) d vs ln F.

7.12. Parameter Space of 1030 nm fs laser microfabrication on Polyimide.

7.13. Optical microscope images of fs laser drawn patterns on PI at power 0.31 W at *v*=2-3 mm/s and 1.1-2.1 W at *v*= 2-150 mm/s at *f*=200 kHz. The patterns show that spallation of LIG occurs at power above ablation threshold (0.29 W) at low scan speed and carbonization occurs along with the ablation at high power-low scan speed.

7.14. Optical microscope images of ablated track drawn at laser power 1.726-2.512 W at 200-300 mm/s at 200 kHz.

7.15. (a) D^2 vs ln *F*, (b) Calculation of incubation coefficient in the photochemical regime from ln($N.\ F_{N,Th}$) vs ln(N).

7.16. (a-e) Cross-sectional SEM images of ablated tracks at 1.726W, 1.921W, 2.125W, 2.316W,2.512W-2.512 W at 200-300 mm/s at 200 kHz, (b) *d* vs ln *F*.

7.17. The saturation effect is observed from the effective absorption coefficient (α_{eff}) measured from slopes in Figure. 3f.

7.18. (a) Kirigami designed Sensor, (b) ASTM D638 Dog-Bone Structure of PI for *GF* measurement, (c) Tensile Stress measurement of Polyimide by UTM, (d) $\Delta R/R$ vs Strain for Gauge Factor measurement of 30 mm LIG track made by femtosecond laser (0.242 W, 2 mm/s, 200 kHz).

7.19. (a) Sensor designed on Fusion 360, (b) Edge probe at the notches, (c,d) Edge probe at the boundaries, (e) von Mises Stress distribution under 500 mg load, (f) von Mises Stress at edge probe 1, 2, 3 for a parametric scan of load 0-700 mg.

7.20. I-V measurement of the Kirigami sensor.

7.21. (a) Displacement measurement setup upon loading of weight bars (Inset: Deformation of the Kirigami Sensor upon loading of 500 mg, (b) Change in PhidgetBridge voltage upon loading of 100-700 mg, (c) *GF* measurement from $\Delta V/V$ vs strain, (d) Stress Distribution in the Kirigami sensor under a load of 500 mg modelled in COMSOL (Inset: Stress Accumulation around the notches), (e) Out-of-plane displacement vs load mass from simulation and experiment, (f) Femtosecond laser printed Kirigami inspired strain sensor used under knee-cap along with gyroscope (Inset: Conformal fitting of the sensor on knee-joint under Knee-Cap), (g) Relative change in output voltage from PhidgetBridge DAQ system upon bending along X-Z plane, and (h) twisting of the knee along X-Y plane for 16 times.

7.22. (a-c) Voltage output from Phidget Sensor DAQ system at amplification 128x using 3 sensors fabricated using the same laser parameters (Carbonization at P=0.242 W at v=2mm/s, f=200 kHz, Ablation at P=2.524 W at v=300mm/s, f=200 kHz), (d-f) Calculation of *GF* from $\Delta V/V$ vs strain for the three sensors respectively, (g-i) Percentage change in $\Delta V/V$ vs time for bending of knee-joint for 16 cycles.

7.23. Stress distribution upon 500 mg placed at centre of (a) Kirigami sensor and (b) Planar sensor, (c) Top-view of 500 mg placed at centre of planar sensor, (d) Side-view shows no change in displacement upon loading of 500 mg at the centre of the planar sensor and no change in Phidget signal was observed, and (e) Relative change in voltage of 3.0 %±0.7 % from the planar sensor upon bending of knee, (f) Top-view of 500 mg placed at centre of Kirigami sensor, (g) Side-view shows change in displacement upon loading of 500 mg at the centre of the Kirigami sensor and no change in Phidget signal was observed, and (h) Relative change in voltage of 10.7 %±1.4 % from the Kirigami sensor upon bending of knee.

7.24. (a) Stress vs Strain curve of ASTM D638 Dog-Bone Structured PI measured by UTM, (b) Measured and simulated displacement vs mass on the Kirigami sensor, (c) Phidget voltage output for varying load-mass, (d) Relative change in voltage vs strain shows that the dV/V is non-linear at 800 mg.

7.25. Gauge Factor measurement of LIG using CO_2 laser at 0.65 W, 2 mm/s, 100 Hz.

List of Tables

3.1. Methods of graphene synthesis.
3.2. Summary of LIG as strain sensor.
4.1. Summary of Materials and methods.
4.2. Laser parameters in COMSOL.
4.3. Laser variables in COMSOL.
4.4. Polyimide properties in COMSOL used for carbonization study.
4.5. ta-C properties in COMSOL used for graphitization study.
4.6. Summary of parameters for the Heat Accumulation Model.
4.7. Properties of Dupont Kapton HN of thickness 125 µm at 23^0C.
5.1. Properties of both PI and ta-C.
5.2. Summary of threshold power and fluence for a varying number of pulses (N).
5.3. Summary of temperatures obtained from simulation for carbonization and graphitization with varying levels of laser power.
5.4. Calculation of conductivity of carbonized and graphitized vias.
6.1. Summary of optical and thermal properties of Polyimide.
6.2. Calculation of uncertainty in conductivity
6.3. Calculation of uncertainty in crystallite-size
6.4. Calculations of uncertainty in conductivity.
6.5. Table for uncertainty calculation of crystallite-size.
6.6. Slope and R-Square values of regression plots of conductivity along the LIG track.
6.7. Slope and R-Square values of regression plots of I_D/I_G ratio along the LIG track.
7.1. Calculation of uncertainties in threshold fluences.
7.2. Calculation of uncertainties in conductivity.
7.3. Summary of Laser carbonization and ablation.
7.4. Summary of sensor reproducibility test.

Abbreviations

CO_2	Carbon dioxide
LASER	Light Amplified Stimulated Emission of Radiation
LIG	Laser Induced Graphene
MC	Mesoporous carbon
PI	Polyimide
IR	Infra-Red
UV	Ultraviolet
3D	Three dimensional
2D	Two dimensional
DAQ	Data Acquisition
CVD	Chemical Vapour Deposition
ta-C	Tetrahedral Amorphous Carbon
DLC	Diamond like Carbon
Yb:YKW	Ytterbium doped Yttrium Potassium Tungsten
Nd:YAG	Neodymium doped Yttrium Aluminium Garnet
CW	Continuous Wave
TPA	Two Photon Absorption
SEM	Scanning Electron Microscopy
HOMO	Highest Occupied Molecular Orbital
LUMO	Lowest Unoccupied Molecular Orbital
IV	Current- Voltage

List of Variables

P	Laser power
f	Repetition rate
F	Laser fluence
E	Laser energy
ω_0	Laser beam spot diameter
v	Scan speed
ρ	Density
C_P	Specific heat
D_T	Thermal diffusivity
Eg	Band-gap
ω	Laser frequency
τ_p	Laser pulse duration
λ	Laser wavelength
γ	Keldish parameter
K, Γ	Symmetry points in the Brillouin zone.
$\boldsymbol{k}$	Wave-vector
κ	Extinction coefficient
k	Reaction rate constant
K	Thermal conductivity
k_0	Arrhenius pre-exponential growth constant

E_A	Activation energy
T_A	Activation temperature
I_D/I_G	Defect ratio of graphene
L_a	Graphene crystallite size
L_o	Nuclei size
R_e	Reflectivity
α	Absorption coefficient
γ_{sv}, γ_{fs}, γ_{fv}	Equilibrium contact angles between surface-vapour, film-surface and film-vapour respectively
ΔG	Free energy of thin film growth
D	Laser carbonization/ablation width
d	Laser carbonization/ablation depth
R	Resistance
σ	Electrical conductivity
ε	Strain
GF	Gauge Factor

Abstract

Laser carbonization is the process of photothermal conversion of polymers rich in aromatic carbons such as Polyimide (PI) into graphene, via a process called Laser Induced Graphene (LIG) using a laser as the source of heat and pressure. This process allows the printing of conductive graphene-circuits on flexible polymeric substrates without chemicals in liquid or gaseous state and transfer printing process used in other graphene deposition methods. The Carbon-di-oxide (CO_2) laser is most commonly for this process due to the strong absorption of PI at 10.6 µm. Femtosecond lasers reduce the interaction with the material and include multiphoton absorption process in dielectrics and polymers allowing both carbonization and ablation using a single IR laser source.

In this project, the interaction of both CO_2 laser and femtosecond laser radiation with PI is studied and techniques such as laser graphitization and plasma treatment of PI surface were applied to improve the electrical conductivity of LIG by ~2.6 times and ~51% respectively. Photothermal models were solved using Finite Element Method to estimate the irradiation temperatures (400-900 K) of PI and were experimentally validated from threshold conditions. The temperature estimated was used to study the thin film growth kinetics of LIG using the Arrhenius model and the activation temperature and energy of formation of LIG from PI were calculated as $2.35 \pm 0.30 \times 10^3$ K and 0.20 ± 0.03 eV respectively. Finally, the carbonization of PI using femtosecond laser radiation was modelled using heat accumulation model and the multiphoton absorption of laser radiation by PI was used to create ablation which enables precise cutting without any thermal damage. This technique was used to print a Kirigami-inspired strain sensor using a single laser source. Kirigami patterning of PI was used to improve the sensitivity of strain sensors. Kirigami cuts showed ~3 times better sensitivity to body-motions when compared to planar sensors, and femtosecond laser processed LIG showed that the Gauge Factor was improved by ~4 times than that obtained using CO_2 laser due to different morphology of LIG.

Declaration

The work in this thesis is based on the research carried out at the National Centre for Laser Applications (NCLA), School of Physics, University of Galway. I, Ratul Kumar Biswas, hereby certify that this thesis has been written by me, that it is the record of work carried out by me and that it has not been submitted in any previous application for a degree or qualification.

Ratul Kumar Biswas

Galway, April 2023

Acknowledgements

I would like to extend my eternal gratitude to all those who have helped in the project at the National Center for Laser Applications (NCLA), University of Galway (UoG). The work could not have been completed without the guidance and support of my project supervisor Professor Patricia J. Scully and co-supervisor Professor Gerard M. O'Connor. Thanks also to Dr. Nazar Farid and all my other colleagues at the Department of Physics of whom there are too numerous to mention here.

I am grateful to my parents for their continuous support, encouragement and enthusiasm in pursuing higher education which has made possible for me to seek the Doctorate degree. Also, I want to extend my sincere thanks to my family and friends whose support has always been an essential ingredient and is gratefully acknowledged.

I want to extend my thanks and recognition to the College of Science and Engineering Research Scholarship, and Science Foundation Ireland (SFI) through Grant numbers 16/RC/3872 and 20/FFP-P/8627 for the project funding.

I want to thank Professor Dipti Gupta and Bharat Bhushan Bhatt at PEEL lab, IIT Bombay for their support with the electromechanical characterization of the sensor.

Finally, the acknowledgements would be incomplete without giving special thanks to Cormac O'Brien, James Nallen, Connor McBrierty, Stuart Harries and Eoin O'Connor for all of their technical guidance, support and insights.

1. Chapter 1: Introduction

Humankind has evolved through different ages based on technological revolutions such as the stone age, bronze age, iron age and the next revolution is claimed to be the Graphene age[1] since theoretically graphene is the thinnest, lightest, strongest, most electrically and thermally conductive material with highest carrier mobility [2] and has elastic properties which allows graphene to be printed into flexible circuits. The first theoretical understanding of the band-dispersion of graphene was elucidated by P. R. Wallace in 1947 [3] where the linear E-***k*** band with zero bandgap was shown for a single layer graphene which finally got separated from bulk graphite using a scotch-tape by Andre Geim and Konstantin Novoselov in the year 2004 [4]. Such research opened the doors for flexible electronics and other 2D materials but also carries a lot of hype for applications such as paper electronics, electronic skin, smart tattoos (Fig. 1.1) which has already been discussed by Terrance Barker et al [2]. In reality, most of the work on graphene has led to "technology push" rather than "market pull" because of the lack of research in scalable manufacturing of large-area graphene crystallites, no standard grade of graphene and control of band-gap in graphene for semiconductor applications [2].

Reduced Graphene-oxide (RGO) has been synthesized on a bulk scale by different methods such as Hummer's method [5], shear, and electrochemical exfoliation method [6], but all these processes produce sheets of graphene with uneven crystallite size-distribution which need to be separated in the post-process stage to obtain a graphene emulsion with maximum crystallite size [7]. Later this ink is printed on a flexible substrates such as Polyimide (PI), Polydimethylsiloxane (PDMS), Polyethylene terephthalate (PET) and sintered to create a patterned layer of RGO [8]. Roll-to-roll single layer graphene has been synthesized on copper/nickel catalytic substrates by Chemical Vapour Deposition method but the graphene needs to be etched out from the substrate for transfer printing [9]. Such chemical transfer creates defects which reduces the overall conductivity. Hence, the underlying trade-off is between scalability and crystallinity.

Laser carbonization process can overcome limitations such as usage of toxic chemicals, transfer methods, post-processes prevalent in the existing processes. In this process, a focussed laser beam is scanned over carbon-rich polymeric substrate such as Polyimide (PI) to create a photothermal reaction to convert the polymer to Laser Induced Graphene (LIG) [5, 10-15]. This process eliminates the need for transfer printing on PI. PI transforms itself to graphitic structures upon laser irradiation because of its unique molecular structure containing aromatic rings as shown in the molecular dynamics studies [16]. Laser-based processes enable the digital control of the process and does not involve any wet chemicals which provides a wide adaptability in the scalable manufacturing of graphene.

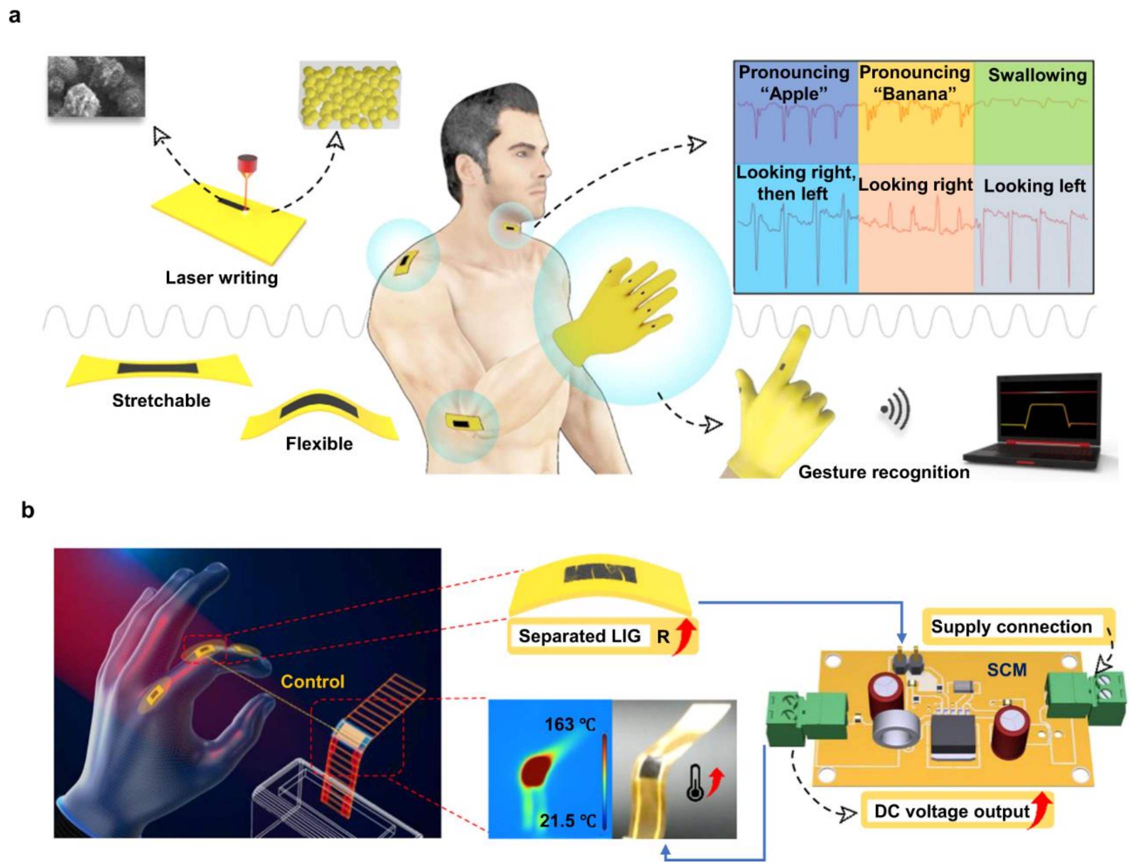

Fig. 1.1. Laser carbonization of Polyimide and its applications in motion, voice, gesture and temperature sensors [17].

The carbonaceous structures obtained from this process have porous microcrystalline structure with many defects and impurities [18]. Hence, if the crystallite size of LIG can be increased and defects reduced, the trade-off between scalability and conductivity can be broken leading to roll-to-roll printing of high-quality graphene on flexible polymeric substrates. For such a goal, the fundamentals of interaction of laser with Polyimide and thin film growth kinetics of graphene need to be studied in detail.

LIG shows excellent piezoresistive behaviour because of the tunnelling of electrons in between the crystallites which makes it viable for application as strain sensors [10, 14]. However, the stiffness of PI hinders its application on uneven surfaces [19]. Kirigami designs allow the transformation of 2D non-conformal substrates to 3D conformal surfaces which allows the sensors to fit conformally on uneven body parts such as shoulder-joints, knee-joints [20-24].

Hence, a laser is required which can be used for both carbonization and ablation, in which the carbonization process will be used for creating piezoresistive LIG and ablation will be used for creating the Kirigami cut patterns. The femtosecond laser can be used for both carbonization and ablation and can be utilized to prepare Kirigami-inspired strain sensors [25]. Femtosecond laser has been used for carbonization of PI [26, 27] for supercapacitor applications, however theoretical modelling of the carbonization process has not yet been done and comparative studies of the physical characteristics of LIG generated by both CO_2 laser and femtosecond laser are non-existent. Filling these gaps will provide a pathway for scalable manufacturing of highly conductive LIG and its applications in sensors.

1.1. Research Questions

In this thesis the following research questions are defined:

a) How do the CO_2 laser and femtosecond laser interact with Polyimide?
b) What is the growth kinetics of graphene in the laser carbonization process?
c) How can the crystallinity of the LIG be improved?
d) What is the difference in LIG generated by CO_2 laser and femtosecond laser in terms of morphology and sensor performance?
e) How does the sensor perform using LIG prepared using the femtosecond laser?

1.2. Aim and Objectives

The overall aim of this project is to understand the interaction of CO_2 laser radiation and femtosecond pulsed IR laser with Polyimide (PI) and to study the underlying process of transformation of PI to graphene. This work intends to study the growth kinetics of thin film growth of graphene on PI and methods to improve the conductivity of LIG. Finally, the incorporation of laser carbonization process into scalable microfabrication of sensors will be demonstrated in this work. The main objectives of this work are listed below based on the research questions above:

a) Investigation of the transformation of Polyimide to sp^2 hybridized carbon controlled by the CO_2 laser-Polyimide interaction.
b) Study of the kinetics of thin-film growth of graphene on PI in the laser carbonization process.
c) Improvement of the crystallite size to optimize the electrical conductivity of LIG.

d) Contrast and comparison of the CO_2 laser-PI interaction and fs IR laser-PI interaction by analysis of the morphology of the laser-induced graphene (LIG) from the two processes.
e) Demonstration of a sensor utilizing the process conditions of femtosecond laser for carbonization and ablation for wearable electronics applications.

1.3. Organization of thesis

In Chapter 1, the introduction to the research covered by this thesis is presented and the aims and objectives of the thesis are discussed. In this chapter, the concept of laser carbonization of polyimide and the research questions, and aims and objectives are introduced.

In Chapter 2, the literature survey on laser-materials interaction and laser-polyimide interactions for both broad pulsed CO_2 laser and femtosecond laser is presented. A clear comparison between the photothermal, photochemical and photomechanical processes during laser-polymer interaction is elucidated in this chapter. The chemical reaction pathways and molecular dynamics for laser carbonization are discussed.

After discussing laser-Polyimide interaction in Chapter 2, the literature survey of the laser induced graphene on PI is provided in Chapter 3, and a comparative analysis of laser carbonization versus other graphene manufacturing methods is discussed. In this chapter, methods of improving of the crystallite-size and conductivity of LIG are discussed and their effects on the Gauge Factor is elucidated.

In Chapter 4, the materials and methods used in this project thesis are introduced. In this chapter, the numerical methods to estimate the laser beam parameters for the CO_2 laser and femtosecond laser are explained, and the thermal, mechanical, and optical properties of Polyimide are elucidated. The techniques and instruments used for characterization including Raman spectroscopy, profilometer, Scanning Electron Microscope are discussed in detail.

Using the materials and instruments discussed in Chapter 4, the methodology for improvement of electrical conductivity and crystallinity of CO_2 laser-induced graphene using laser graphitization are presented in Chapter 5. The concept of laser graphitization is discussed, and the laser-PI interaction and laser-ta-C interaction are modelled using COMSOL software. The chapter contents are published in the Journal of Materials Chemistry C [28].

Based on the photothermal model discussed in Chapter 5, the kinetics of the carbonization process and the effect of PI surface wettability on crystal growth are described comprising two published journal papers in Chapter 6. In the first paper, the growth kinetics of graphene in the laser carbonization process using CO_2 laser is presented [29]. The irradiation temperature of PI is calculated using the same model from Chapter 5 for varying irradiation time and the activation energy of graphene formation in this process is calculated. This work is published in Materials Letters [29]. In this second paper, the effect of PI surface wettability on the crystallite size and conductivity of LIG is studied. The wettability of PI was increased using the argon cold plasma treatment followed by laser carbonization using CO_2 laser. This work is published in Materials Letters [30].

After explaining the CO_2 laser-Polyimide interaction in Chapters 5 and 6, the femtosecond infra-red laser-Polyimide interaction is discussed in Chapter 7 and a detailed study is performed on two process-conditions of the laser, low power-low scan speed and high power-high scan speed. The carbonization process at low power-low scan speed is modelled using the heat accumulation model using Python software and this process is used to print LIG on PI. Ablation occurs at the high power-high scan-speed and is used for cutting applications and is used to print a Kirigami-inspired strain sensor for knee-movement monitoring. This work is published in the Journal of Physics D: Applied Physics [25].

In Chapter 8, the outputs from all the four papers are summarized. The conclusion from this research, how they meet the research objectives and how they answer the research questions are discussed. The future work and impact of this thesis are explained.

Bibliography

1. Flynn, G.W., *Perspective: The dawning of the age of graphene.* The Journal of Chemical Physics, 2011. **135**(5): p. 050901.
2. Barkan, T., *Graphene: the hype versus commercial reality.* Nature Nanotechnology, 2019. **14**(10): p. 904-906.
3. Wallace, P.R., *The Band Theory of Graphite.* Physical Review, 1947. **71**(9): p. 622-634.
4. Novoselov, K.S., et al., *Electric Field Effect in Atomically Thin Carbon Films.* Science, 2004. **306**(5696): p. 666-669.
5. Marcano, D.C., et al., *Improved Synthesis of Graphene Oxide.* ACS Nano, 2010. **4**(8): p. 4806-4814.
6. Shinde, D.B., et al., *Shear Assisted Electrochemical Exfoliation of Graphite to Graphene.* Langmuir, 2016. **32**(14): p. 3552-3559.
7. Nemala, S.S., et al., *Liquid phase high shear exfoliated graphene nanoplatelets as counter electrode material for dye-sensitized solar cells.* Journal of Colloid and Interface Science, 2017. **499**: p. 9-16.
8. Torrisi, F., et al., *Inkjet-Printed Graphene Electronics.* ACS Nano, 2012. **6**(4): p. 2992-3006.
9. Yoshihara, N. and M. Noda, *Chemical etching of copper foils for single-layer graphene growth by chemical vapor deposition.* Chemical Physics Letters, 2017. **685**: p. 40-46.
10. Chyan, Y., et al., *Laser-Induced Graphene by Multiple Lasing: Toward Electronics on Cloth, Paper, and Food.* ACS Nano, 2018. **12**(3): p. 2176-2183.
11. Duy, L.X., et al., *Laser-induced graphene fibers.* Carbon, 2018. **126**: p. 472-479.
12. Lin, J., et al., *Laser-induced porous graphene films from commercial polymers.* Nature Communications, 2014. **5**(1): p. 5714.
13. Stanford, M.G., et al., *High-Resolution Laser-Induced Graphene. Flexible Electronics beyond the Visible Limit.* ACS Applied Materials & Interfaces, 2020. **12**(9): p. 10902-10907.
14. Ye, R., D.K. James, and J.M. Tour, *Laser-Induced Graphene.* Accounts of Chemical Research, 2018. **51**(7): p. 1609-1620.
15. Zhang, J., et al., *Efficient Water-Splitting Electrodes Based on Laser-Induced Graphene.* ACS Applied Materials & Interfaces, 2017. **9**(32): p. 26840-26847.
16. Kato, T., et al., *Carbonization mechanisms of polyimide: Methodology to analyze carbon materials with nitrogen, oxygen, pentagons, and heptagons.* Carbon, 2021. **178**: p. 58-80.
17. Wang, H., et al., *A soft and stretchable electronics using laser-induced graphene on polyimide/PDMS composite substrate.* npj Flexible Electronics, 2022. **6**(1): p. 26.
18. Liu, M., J. Wu, and H. Cheng, *Effects of laser processing parameters on properties of laser-induced graphene by irradiating CO2 laser on polyimide.* Science China Technological Sciences, 2022. **65**(1): p. 41-52.
19. Yong, K., et al., *Kirigami-inspired strain-insensitive sensors based on atomically-thin materials.* Materials Today, 2020. **34**: p. 58-65.
20. Evke, E.E., D. Meli, and M. Shtein, *Developable Rotationally Symmetric Kirigami-Based Structures as Sensor Platforms.* Advanced Materials Technologies, 2019. **4**(12): p. 1900563.
21. Brooks, A.K., et al., *Kirigami-Inspired Biodesign for Applications in Healthcare.* Advanced Materials, 2022. **34**(18): p. 2109550.

22. Evke, E.E., et al., *Kirigami-Based Compliant Mechanism for Multiaxis Optical Tracking and Energy-Harvesting Applications.* Advanced Engineering Materials, 2021. **23**(4): p. 2001079.
23. Shyu, T.C., et al., *A kirigami approach to engineering elasticity in nanocomposites through patterned defects.* Nature Materials, 2015. **14**(8): p. 785-789.
24. Zhang, H. and J. Paik, *Kirigami Design and Modeling for Strong, Lightweight Metamaterials.* Advanced Functional Materials, 2022. **32**(21): p. 2107401.
25. Biswas, R.K., et al., *Femtosecond infra-red laser carbonization and ablation of polyimide for fabrication of Kirigami inspired strain sensor.* Journal of Physics D: Applied Physics, 2023. **56**(8): p. 085101.
26. Yuan, Y., et al., *Bottom-up scalable temporally-shaped femtosecond laser deposition of hierarchical porous carbon for ultrahigh-rate micro-supercapacitor.* Science China Materials, 2022. **65**(9): p. 2412-2420.
27. Zhang, W., et al., *3D Laser Scribed Graphene Derived from Carbon Nanospheres: An Ultrahigh-Power Electrode for Supercapacitors.* Small Methods, 2019. **3**(5): p. 1900005.
28. Biswas, R.K., et al., *Improved conductivity of carbonized polyimide by CO2 laser graphitization.* Journal of Materials Chemistry C, 2020. **8**(13): p. 4493-4501.
29. Kumar Biswas, R., et al., *Graphene growth kinetics for CO2 laser carbonization of polyimide.* Materials Letters, 2022. **307**: p. 131097.
30. Kumar Biswas, R., et al., *Plasma enhanced planar crystal growth of laser induced graphene.* Materials Letters, 2023. **343**: p. 134362.

2. Chapter 2: Laser-Materials Interaction

In this chapter, a literature review on laser-material interaction is explained to answer the research question about how a laser pulse interacts with Polyimide is answered. To answer this question, we first need to understand how a single laser pulse interacts with polymers. The interaction occurs via three processes such as photothermal, photochemical and photomechanical, depending on the type of laser and polymer. Then, the mechanism of how this interaction leads to carbonization and ablation is discussed for both the CO_2 laser and the femtosecond laser. This chapter is written 100% by the author Ratul Kumar Biswas.

2.1. Laser Fundamentals

Laser is an acronym of Light Amplified Stimulated Emission of Radiation. Laser is a beam of monochromatic, collimated, and coherent photons produced by stimulation of atoms or molecules in a crystal. The concept of laser was first theorized by Albert Einstein in 1917 [1]. Lasers can have different wavelengths such as Ultraviolet (UV), visible, and Infra-Red (IR) and can come in various pulsed conditions such as Continuous Wave (CW), short-pulsed (microsecond, nanosecond), and ultrashort-pulsed (picosecond, femtosecond). The repetition rate of laser pulses may vary from Hertz to Mega-Hertz.

Ultra-fast lasers (t_p< 1 ps) have opened many possibilities in the field of multiphoton microfabrication, 3D stereolithography and spectroscopy [2]. The first pulsed laser, Ruby laser was invented in 1960 by Dr. Theodore H. Maiman which had a pulse duration in milliseconds [3]. With time, further lasers with lower pulsed duration have been developed such as Dye lasers, Nd:YAG, Yb:glass lasers for growing number of scientific and industrial applications. In this work, CO_2 laser and Yb:KYW fs laser are used to study their interaction with PI. Hence these lasers will be further discussed in detail in Chapter 4.

2.2. Interaction of a laser pulse with material

When a laser is incident on a metal, interaction of optical electrical field with conduction band electrons in the metal occurs, the motion of which is restricted by the collisions with vibrational states of the lattice, which in turn thermalizes the lattice. In the case of semiconductors, both electrons and holes are responsible for thermalization, and in dielectrics, the thermalization is induced by the relaxation of the polarized molecule coupled to the lattice, induced by the optical field [4].

The temperature of the substrate for short-duration laser pulses (up to nanosecond) is obtained from the Analytical solution or Finite Element Method solution of the Fourier equation 2.1:

$$[\rho C_p(T)\left(\frac{\partial T}{\partial t}\right)] - \nabla[K(T)\nabla T] = Q(x,y) \tag{2.1}$$

where $C_P(T)$ is the specific heat, ρ is the density, $K(T)$ is the thermal conductivity, and $Q(x,y)$ is the time variant Gaussian laser heat source density per unit volume:

$$Q(x,y,t) = 2\, F_{eff} \cdot \left[\frac{\alpha(\lambda)}{\sqrt{(\pi/ln\,2)\tau_p}}\right].(1-R).\,[exp\left\{-2\left(\frac{x}{\omega_0}\right)^2 - 4\,ln\,2\left(\frac{t-t_c}{t_P}\right)^2\right\}]\,exp(\alpha(\lambda)y) \tag{2.2}$$

Fluence, $$F = \frac{2P}{f\pi\omega_0^2} \tag{2.3}$$

Effective fluence, $F_{eff} = F(1+\gamma)$, where the overlapping factor, $\gamma = \left[1-\left(\frac{v}{2f\omega_0}\right)\right]$ (2.4)

Absorption coefficient, $\alpha(\lambda) = \frac{4\pi\kappa}{\lambda}$ and Reflectivity, $R_e = \left[\frac{(1-n)^2+\kappa^2}{(1+n)^2+\kappa^2}\right]$ (2.5)

Where, κ is the extinction coefficient, and n is the refractive index of the material.

Carslaw and Yaeger solved the heat equation for a semi-infinite solid for time of diffusion, t at depth x as [5]:

$$T_x = T_s erfc\left(\frac{x}{2\sqrt{Dt}}\right) \tag{2.6}$$

Where, the surface temperature, T_s at x=0 is:

$$T_s = \frac{2F}{K}\sqrt{\frac{Dt}{\pi}} \tag{2.7}$$

and, thermal diffusivity, $D_T = \frac{K(T)}{\rho C_p(T)}$ (2.8)

When a laser pulse interacts with non-metallic materials, three major processes occur as shown in Fig. 2.1 [6]:

2.2.1.Photothermal Process

The photothermal process occurs due to purely thermal excitation of the phonon system in the material by linear absorption of IR laser wavelength which leads to heating of the material causing melting, vaporization, and carbonization. This occurs when the photon energy of the laser is less than the bond-dissociation energy of the material. The difference between the Photothermal and photochemical processes can be described by a two-level energy diagram (Fig. 2.2) [6]. Molecule A has two energy states: Ground state A and Excited state A^*. τ_T is the electron relaxation-time. The dissociation of molecule A to products B and C can happen in two routes: 1. A ⟶ B+C; and 2. A^* ⟶ B+C. τ_A and τ_A^* are the relaxation times for routes 1 and 2 respectively as shown in Fig 2.2. Photothermal process dominates when τ_T , τ_A<< τ_A^*; while photochemical process dominates when τ_A^*<< τ_T, τ_A. Combined Photothermal and photochemical processes can also occur when τ_A^*<< τ_T, τ_A, and τ_A^*<τ_A. The pulse duration plays a major role in the selection of governing process because the thermalization after photoexcitation depends on the pulse-duration [7]. Photothermal process becomes dominant when the pulse-duration is more than the timescale of electron-phonon coupling as the electrons thermalize within its pulse-duration. Also, with increasing the pulse-duration, the absorption mechanism changes from multiphoton absorption to the linear absorption because initially there are a few photoexcited electrons which later get abundant to undergo linear absorption causing thermal effects [7].

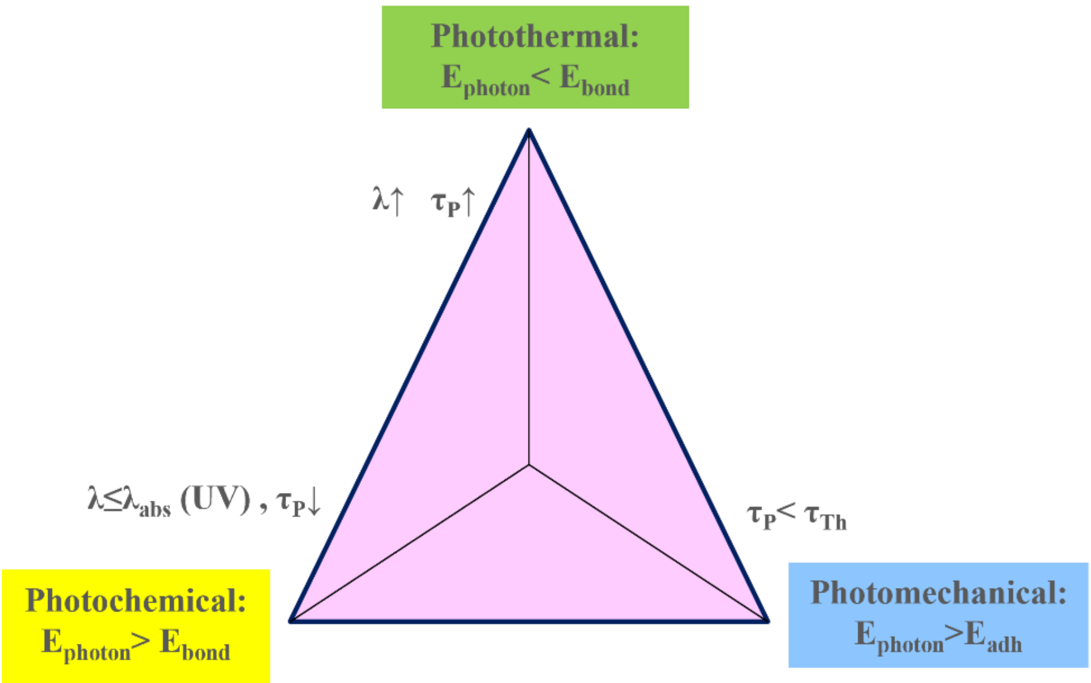

Fig. 2.1. Three leading processes during laser-materials interaction, E_{bond}= Bond energy, λ_{abs}= absorption wavelength, τ_{Th}= time for thermal expansion=d/c_{ac}, where d= film thickness, c_{ac}= acoustic velocity and is in the order of 10 ps [8-10].

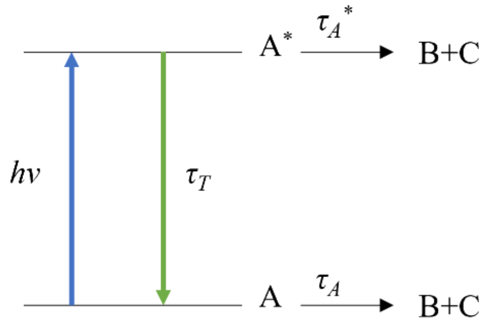

Fig. 2.2. A simple two-level scheme of single photon absorption [6].

2.2.2. Photochemical Process

The photochemical process occurs when the photon energy of the laser is more than the bond-dissociation energy of the material which leads to electronic excitation from Higher Occupied Molecular Orbital (HOMO) to Lower Unoccupied Molecular Orbital (LUMO) [11] resulting in direct bond-breaking of the material. Such process creates ablation without any debris.

a. Single Photon Process

The Photochemical process may occur by a single photon of the laser when the energy of the photon is more than the HOMO-LUMO bandgap, i.e., $E_g \geq \hbar\omega$, where E_g= material bandgap, ω= laser frequency. This is mostly the case when UV laser irradiates on polymers since UV lasers have higher photon energy than the bandgap in polymers and linear absorption of energy occurs following Beer-Lamberts' Law. Such process is useful for surface ablation of polymers.

b. Multiphoton Process

Multiphoton absorption occurs when the bandgap of the material is less than the cumulative energy of one photon, i.e., $E_g \leq \hbar\omega$. Non-linear absorption of the photon energy by the material occurs and Beer- Lambert's Law is not maintained. Such processes occur at higher laser intensity which has higher photon flux and lower pulse duration. Such a process can be used for polymers which are transparent to the wavelength of the laser, but absorbing at higher intensity. Hence, the laser can be focussed inside the bulk of the polymer (Fig. 2.3b) and direct laser writing of LIG has been performed by the P. Scully research group under the surface of PI for preparation of conducting interconnects (Fig. 2.4) [12].

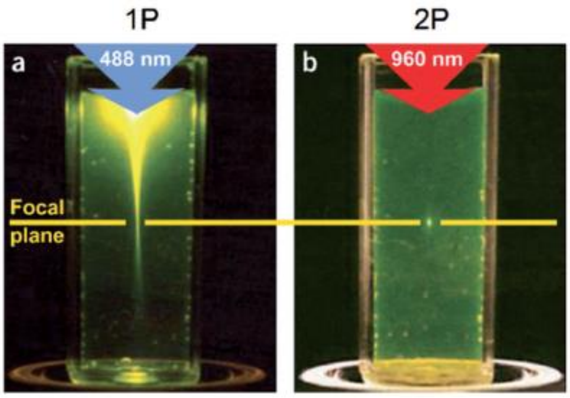

Fig. 2.3. 1 photon and 2 photon excitations in hydrogel [11].

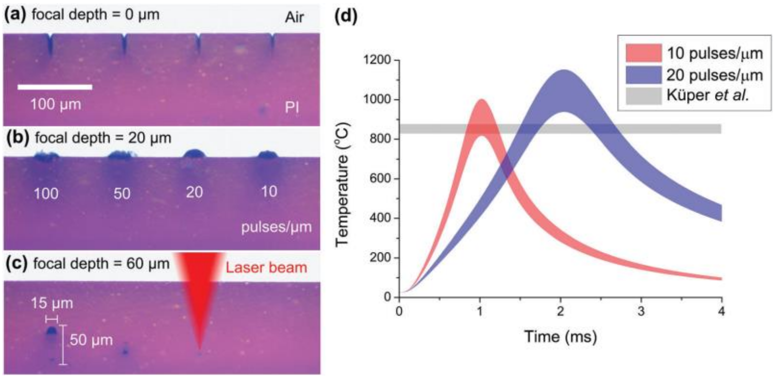

Fig. 2.4. (a-c) Laser carbonization by Multiphoton absorption at the bulk of Polyimide using fs laser, and (d) Thermal modelling of Ti-Sapphire femtosecond laser-PI interaction [12].

2.2.3.Photomechanical Process

Here, both thermal and non-thermal processes play a role. This process is most adequate for fs and ps lasers. The photochemical process occurs in two ways:

a. Shock-assisted ablation occurs when $\tau_P < \tau_{Th}$, $E<E_{adh}$. Such ablation occurs when the laser pulse heats up the material faster than the speed of thermal expansion.
b. Stress-assisted ablation occurs when $\tau_P > \tau_{Th}$, $E>E_{adh}$. Such ablation occurs due to stress accumulation on the laser-heated zone as compared to the surroundings which opposes the radial thermal expansion, leading to ablation of the laser-heated zone [13].

Where E_{adh} is the adhesion energy of the ablated material with the substrate.

2.3. Laser Polyimide Interaction

2.3.1. Laser Carbonization of Polyimide

Laser carbonization is the photothermal process assisted conversion of PI to tetrahedral amorphous carbon (ta-C) as shown in Fig. 2.5.b, also known as Diamond like Carbon (DLC) which is a mixture of sp3 and sp2 hybridized carbon using an CO_2 IR laser. The study on the laser carbonization and graphitization started in 1980's and focused research on laser induced graphene started in the mid-2010's [14]. Polyimide shows strong absorption in the IR spectrum at wavelengths 9.2 μm and 10.6 μm with absorption coefficients 2340 cm^{-1} and 270 cm^{-1} respectively [15]. Hence, when PI is irradiated with IR lasers at such wavelengths, photothermal decomposition of PI occurs under rapid heating. The chemical structure of PI is shown in Fig. 2.5.a. The thermal decomposition of polymers occurs by four chemical pathways (Fig. 2.7) [16]:

a. **Random Chain Scission-** In this reaction, scission of chemical chains occurs at random locations in the polymer motif.
b. **End-Chain Scission-** In this case, scission of chemical bonds occurs at the chain-end of the monomer units, known as unzipping.
c. **Chain-stripping-** Here, side groups or atoms of the polymer backbone are cleaved.
d. **Cross-linking-** Here, bonds are created in between polymer chains creating new compounds. Elimination reaction of the side groups occur, and cyclization reactions occur between adjacent groups producing cyclic structures. Such reaction leads to formation of chars.

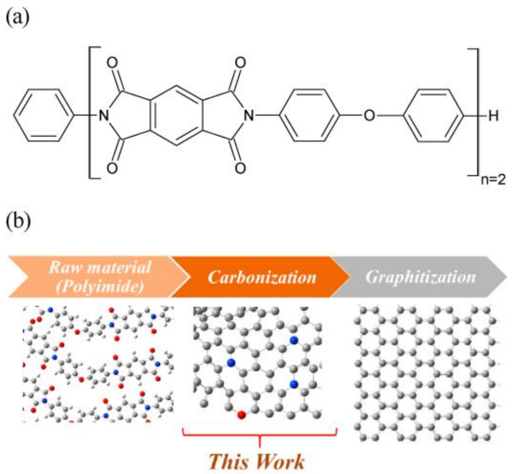

Fig. 2.5. (a) Chemical structure of Polyimide, (b) Stages in laser carbonization [17].

Thermal degradation of PI occurs in 5 routes [17]:

Route A- Cleavage of C-N and C-C bond in the imide group.

Route B- Dibenzofuran ring formation.

Route C- Benzonitrile formation.

Route D- Cleavage of C-N, C-C, and C-O bond.

Route E- Ether C-O bond cleavage.

Although thermal decomposition of PI starts at 673 K, formation of a mixture of sp^2 and sp^3 hybridized carbon atoms starts at 900 K by a process called carbonization. Transformation of sp^3 hybridized carbon to sp^2 hybridized carbon occurs at a temperature range of 773-1273 K [17] by a process called graphitization.

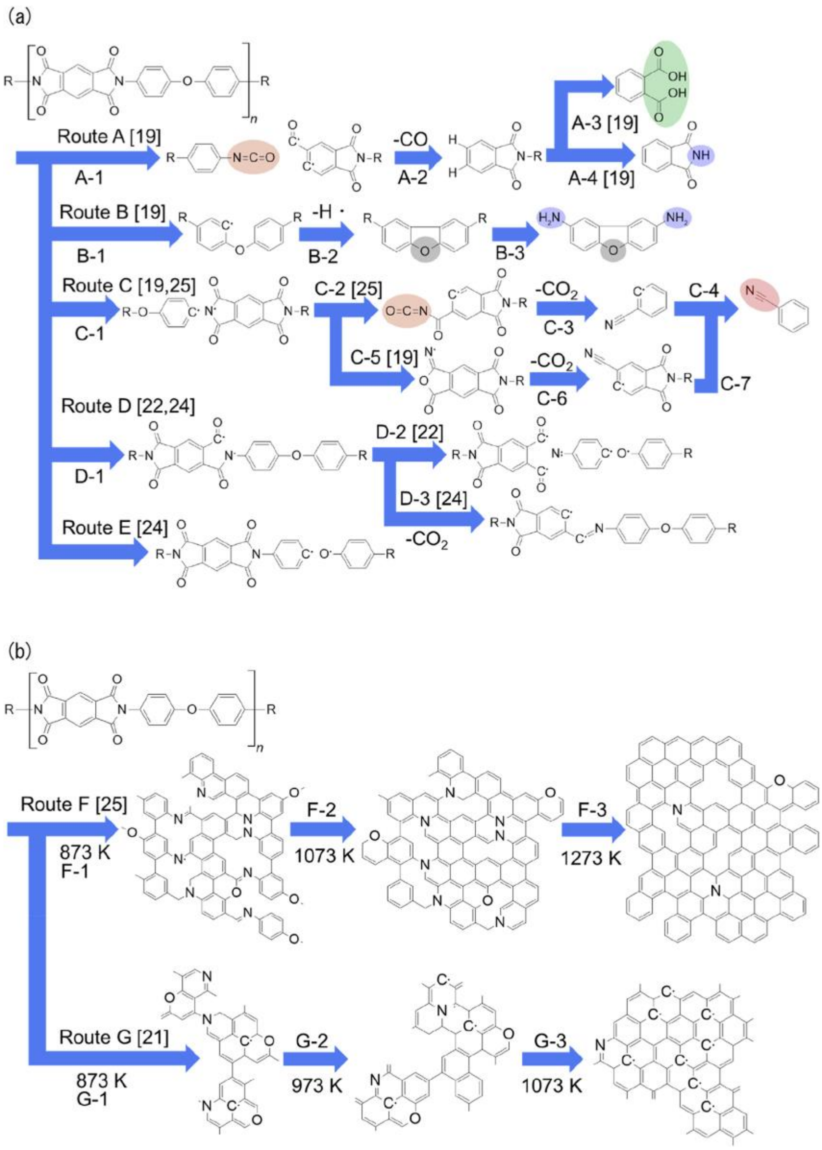

Fig. 2.6. Reported reaction mechanisms of PI. (a) Thermal decomposition process. (b) Carbonization process [17].

Thermal decomposition at 1273 K occurs by two reaction pathways (Fig. 2.6.b) [17]:

i. Route F- Cyclic hexagonal carbon rings containing pyridinic N, N-N bonding, cyclic ether and point defects.
ii. Route G- Cyclic hexagonal carbon rings containing radicals.

Zhang et al showed a simple pathway for chemical bond scission occurring during carbonization of PI as explained in Fig. 2.7 [18].

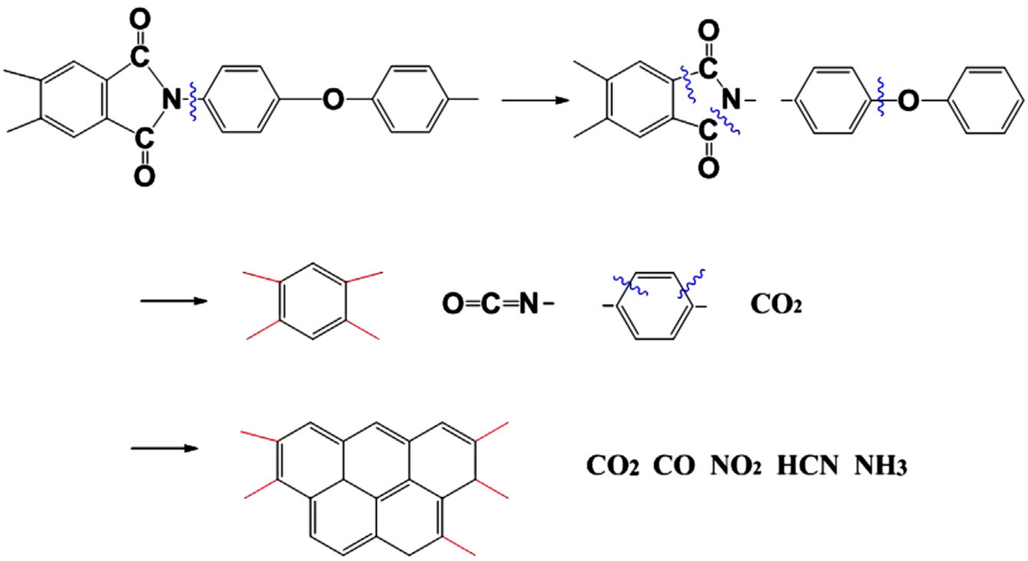

Fig. 2.7. Bond scissions obtaining graphitic structure from PI [18].

2.3.1.1. Molecular Dynamics of Laser Carbonization

Molecular Dynamics (MD) study helps us to study the process-structure relationship for laser carbonization of Polyimide. While the temporal evolution of temperature is studied based on the surface and bulk Photothermal models, the microstructural evolution of the carbon-structures in response to the temperature is studied using MD [19, 20]. It also answers the question why certain polymers form layered carbonaceous structures while others do not. MD simulation with Reactive Force Fields (ReaxFF) helps to study the effect of monomer molecular structures on the carbonaceous structure obtained after carbonization. The PI monomers ($C_{22}H_{12}N_2O_5$) were constructed using VAMP package to obtain the equilibrium bond length and angles of the monomers. Then 32 monomer molecules were assigned in an FCC cubic cell and compressed to achieve a density of 1.308 gm/cm^3. The ring-shaped structures of the carbon clusters were found to be prominent with increasing peak temperature T_P and at T_P=3000 K, double-layered graphene-like structures. It also showed that the hexagonpentagon defects called Stone-Thrower-Wales (STW) defects is present in the carbonized structures and the 2D-connected hexagonal rings is present in maximum of 95.6% when T_P=3000 K. Also, the cluster-size reaches maximum for T_P=3000 K (Fig. 2.8.c-g).

The defects were self-healed while the temperature was cooled to 300 K. The effect of heat preservation time is also studied, and the size of the graphene flakes was found to increase with increasing heat-preservation time. The heating rate and the cooling rate have very little effect on the process of carbonization. Then the system was kept at an equilibrium temperature of 300 K for 40 ps.

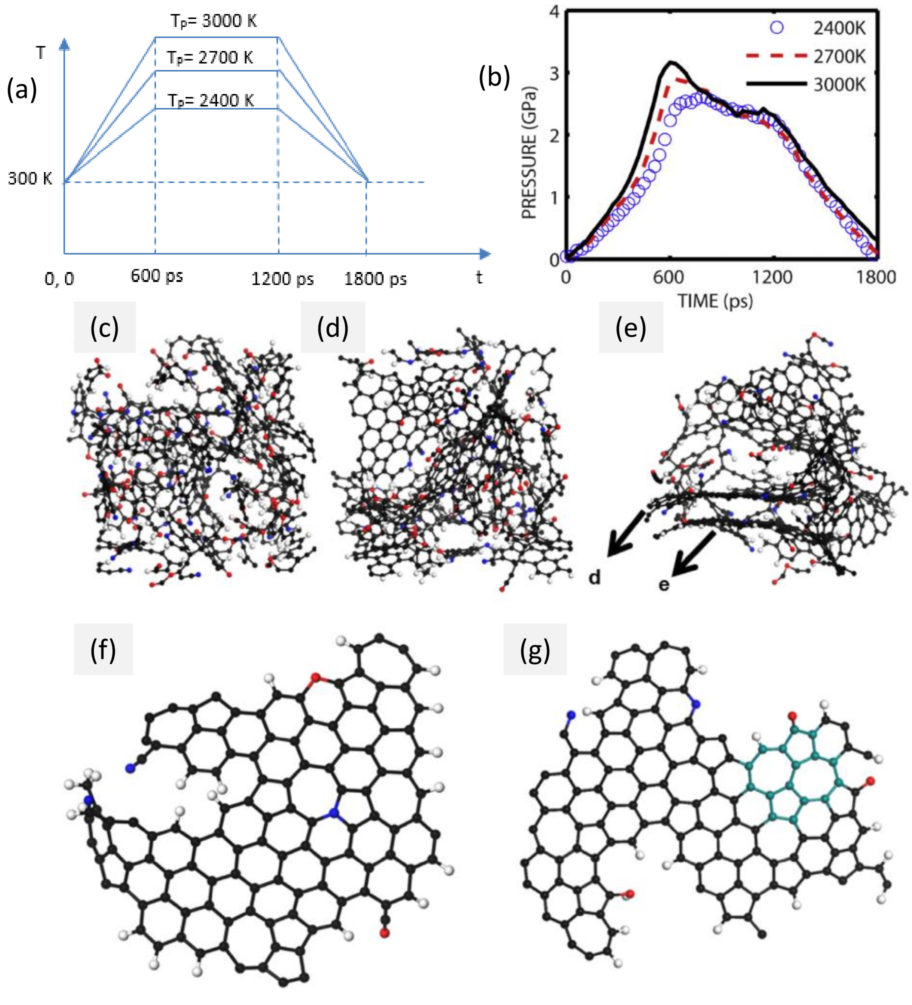

Fig. 2.8. (a) Temperature profiles used in MD simulation, (b) Pressure achieved in the NVT simulation at T_P= 2400 K, 2700 K, and 3000 K, (c,d,e) Snapshots of final clusters at T_P= 2400 K, 2700 K, and 3000 K, (f,g) Enlarged views of the clusters in fig. e [19].

The temperature was controlled by Nosé-Hoover Thermostat. A time-step of 0.25 fs was used for the study. Thereafter, the system was heated to peak temperature (T_P= 2400 K, 2700 K, and

3000 K) in 600 ps and kept for 600 ps which is the heat preservation time and finally cooled to 300 K in 600 ps reaching a pressure of 2.6, 2.9 and 3.2 GPa respectively (Fig. 2.8.a, b). The thermal models explained in this thesis will help to obtain the temporal evolution of temperature under various laser parameters which can be used by MD simulation in later works to study the growth of graphene in this process. Such study will enable optimization of the laser parameters to reduce the defects in LIG.

2.3.1.2. Femtosecond laser carbonization of Polyimide:

Femtosecond laser radiation has been used for carbonization of PI for various applications such as supercapacitors[21, 22], chemical sensors[23] applications. Since the pulse duration in femtosecond scale is shorter than the thermalization duration of PI (~34 ps) and possesses high pulse intensity (~10^{14} W/cm^2) [11] , such lasers can be focussed inside the bulk of polymers and can be used to print conducting structures inside the PI which has been done by B. Dorin et al using Ti: Sapphire 800 nm laser [12] . But the process behind the carbonization process and the comparative study with broad-pulsed lasers has not studied until now. Mostly, interaction of femtosecond laser with metals or dielectric occurs according to two-temperature model where the photon interacts with the free electrons at first which later thermalizes the lattice by electron-lattice coupling. Such process occurs only when there is any free electron in the outer molecular orbitals. But PI is a non-conducting polymer with no free electrons. Hence, such interaction would be different as compared to metals or dielectrics. B. Dorin et al developed a photothermal model [12] which solved the 3D heat diffusion equation using the Green's function in MATLAB and took the pulse duration into account which increased the computational time. In this thesis, we have developed a 1D heat accumulation model in Python which estimates the temperature evolution for a given number of pulses for a particular scan speed and repetition rate irrespective of any pulse duration, in 2 seconds and allows to model the interaction with lasers having repetition rate upto 80 MHz. Such a study has been performed in the Chapter 7.

2.3.2. Laser Ablation of Polyimide

Laser ablation is the photochemical assisted process of removal of polymeric materials from the substrate. When the photon energy is greater than the bandgap in polymers, bond-scission occurs creating photochemical ablation. Mostly UV lasers have such higher photon energy causing ablation of polymers [11]. Femtosecond IR lasers ablates the polymers by multiphoton ionization. In this thesis, laser parameters for ablation of PI by femtosecond IR laser radiation is discussed in details in Chapter 7, but the chemical reactions occurring during the ablation need to be discussed to understand the ablation process. Polymers such as PMMA get depolymerized into monomers upon ablation, while polymers such as PI decompose into new fragments.

Photochemical degradation occurs through two reaction pathways (Fig. 2.9):

a. **Norrish Type I:** This reaction involves cleavage of side chains mostly ester side chain (C-CO bond) [24].
b. **Norrish Type II:** This reaction involves the cleavage of bond in the main chain (CH_2-C bond) leading to formation of monomers [25].

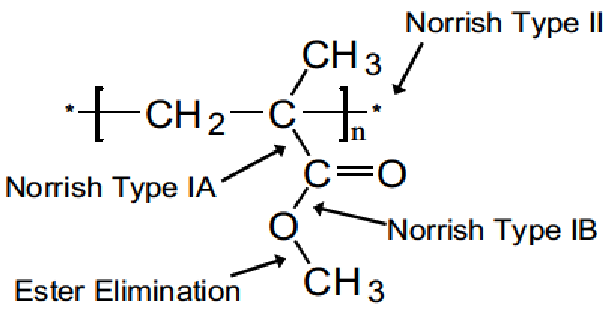

Fig. 2.9. Norrish type bond scissions in PMMA [25].

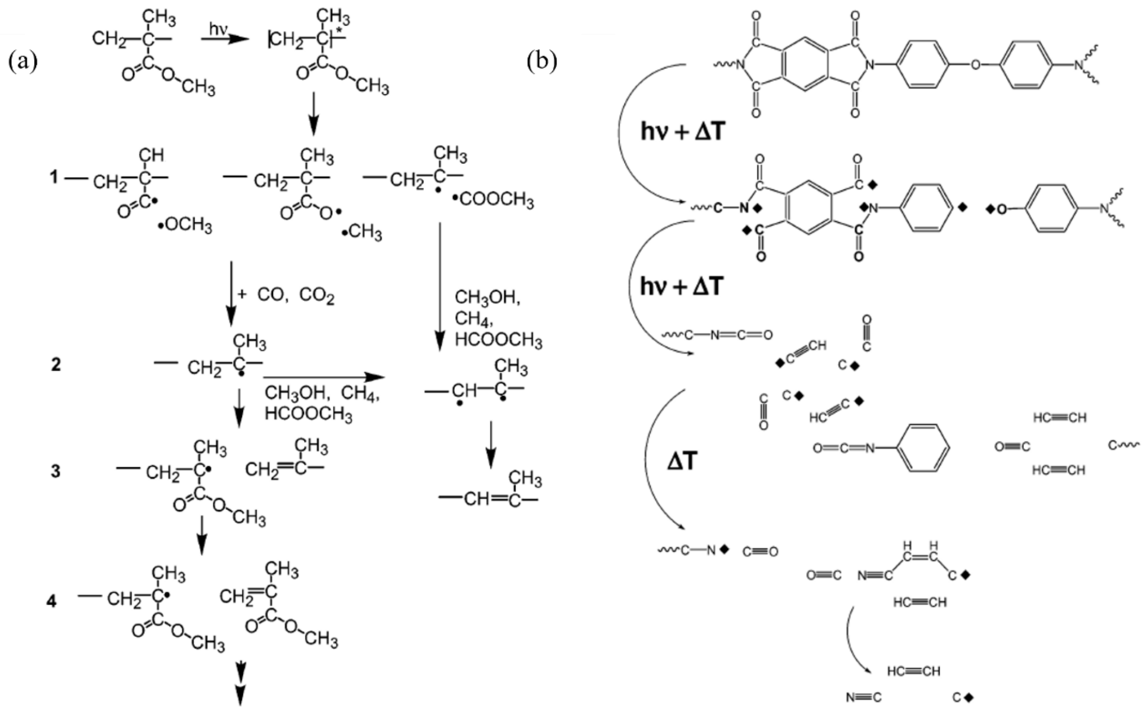

Fig. 2.10. (a) Photochemical ablation pathways for PMMA, (b) PI under 308 nm UV laser [26].

UV laser wavelength at 308 nm initiates decomposition in PI at two reaction sites (Fig. 2.10 a,b): Phenyl-O and the N-C bond leading to scission of the polymer backbone creating ablation[26].

2.3.2.1. Femtosecond Laser ablation of Polyimide

Photochemical degradation by femtosecond laser occurs only when the free electrons are generated at the focal volume of the laser. Such electron generation occurs due to HOMO-LUMO excitation by the Ionization process. Ionization by femtosecond laser can happen through two processes or their combination as mentioned in Fig. 2.11.A-E [11]:

a. **Multiphoton Ionization (MPI):** This mechanism occurs at high pulse intensity (I), high laser frequency (ω).

b. **Tunnelling Ionization:** This mechanism occurs at high pulse intensity, low laser frequency.

Femtosecond and picosecond laser have a high pulse intensity (~10^{13} W/m^2) which at high laser frequency (~80 MHz) causes the electrons constantly get excited from HOMO to LUMO causing MPI. At lower laser frequencies (~8 MHz), the electrons can relax between the pulses and the MPI is inhibited.

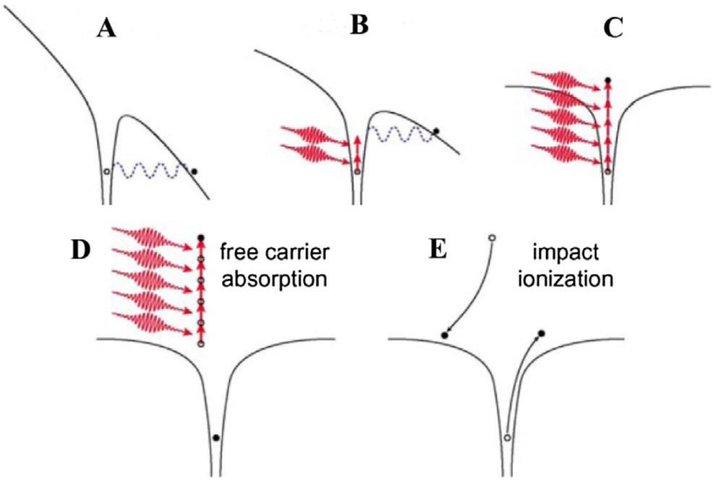

Fig. 2.11. Schematic diagrams of the photoionization excited by femtosecond laser. (A) Tunnelling ionization, (B) mixture of tunnelling and multiphoton ionization, (C) multiphoton ionization, and (D, E) avalanche ionization [27].

However, the higher pulse intensity may suppress the atomic potential barrier, causing tunnelling of the bound electrons through the barrier causing Tunnelling ionization. The transition from tunnelling to MPI is governed by the Keldysh parameter (γ):

$$\gamma = \frac{\omega}{e}\sqrt{\frac{mcn\varepsilon_0 E_g}{I}} \tag{2.10}$$

Where, c= velocity of light, n= refractive index of the material, ε_0= Permittivity of free space, and E_g= bandgap of the material.

Tunnelling Ionization occurs when $\gamma<1.5$, and MPI occurs when $\gamma>1.5$. MPI can occur by two possible pathways, Photoionization and avalanche ionization[27].

PI has a band-gap of 3.1 eV [28]. Hence for IR lasers with wavelength 800-1040 nm, multiphoton absorption is necessary to ensure that sufficient photons required for photochemical ablation. Baudach et al [29] studied the ablation effect of PI by Ti:sapphire laser (800 nm) and found highly oriented ripple structures by the laser pulses. The single pulse absorption coefficient (α) at 800 nm is 23 cm^{-1} [29] but α calculated from ablation experiments was found to be 17500 cm^{-1} which is closer to the values for UV laser ($\alpha_{193\ nm}$= 10000-26000 cm^{-1}) which shows that the ablation process is a multiphoton absorption process [30]. Hence, a femtosecond laser is capable of switching between two modes of operation: carbonization and clean ablation, which when combined can give rise to various applications such as fabrication of conformal sensors which is later discussed in Chapter 7 in this thesis.

2.4. Summary

In this chapter, the interaction of laser pulses with materials and Polyimide were elucidated and the three main interactions such as photothermal, photochemical and photochemical interactions were classified. The chemistry of laser carbonization and laser ablation was discussed. Laser carbonization was explained to be a linear absorption process causing excitation of the phonon energy level in PI which thermalizes the lattice causing photothermal reaction creating LIG and occurs predominantly by laser with wavelength in the IR range (760 nm-1 mm) [31]. Laser ablation was explained to be a linear absorption process by UV laser and non-linear absorption of femtosecond laser.causing excitation of electronic energy level in PI causing photochemical scission of chemical bond in PI. Femtosecond laser was found to be capable of both carbonization and ablation depending on the pulse duration, laser energy and scan speed, but no comparative study has been done yet which is a research gap. Hence, such study is necessary and will be presented in Chapter 7.

Bibliography

[1] S.K. Verma, S. Maheshwari, R.K. Singh, P.K. Chaudhari, Laser in dentistry: An innovative tool in modern dental practice, Natl J Maxillofac Surg 3(2) (2012) 124-32.
[2] M.E. Jason, L. Mingwei, R. Ian, M. Stefan, F. Philippe, B. Rich, K. Jim, Future trends and applications of ultrafast laser technology, Proc.SPIE, 2006, p. 61000H.
[3] J.L. Bromberg, The Birth of the Laser, Physics Today 41(10) (1988) 26-33.
[4] A.A. Voevodin, M.S. Donley, Preparation of amorphous diamond-like carbon by pulsed laser deposition: a critical review, Surface and Coatings Technology 82(3) (1996) 199-213.
[5] F.P. Gagliano, R.M. Lumley, L.S. Watkins, Lasers in industry, Proceedings of the IEEE 57(2) (1969) 114-147.
[6] D. Bäuerle, Thermal, Photophysical, and Photochemical Processes, in: D. Bäuerle (Ed.), Laser Processing and Chemistry, Springer Berlin Heidelberg, Berlin, Heidelberg, 2000, pp. 13-37.
[7] J. Hrabovsky, C. Liberatore, I. Mirza, J. Sladek, J. Beranek, A. Bulgakov, N.M. Bulgakova, SURFACE STRUCTURING OF KAPTON POLYIMIDE WITH FEMTOSECOND AND PICOSECOND IR LASER PULSES, 7(2) (2019) 113-121.
[8] I. Itzkan, D. Albagli, M.L. Dark, L.T. Perelman, C. von Rosenberg, M.S. Feld, The thermoelastic basis of short pulsed laser ablation of biological tissue, Proceedings of the National Academy of Sciences 92(6) (1995) 1960-1964.
[9] C.L.B.a.M.M. Hirschler, Thermal decomposition of polymers, SFPE Handbook of Fire Protection Engineering, 3rd edition ed.2001.
[10] S.L. Malhotra, J. Hesse, L.-P. Blanchard, Thermal decomposition of polystyrene, Polymer 16(2) (1975) 81-93.
[11] S. Pradhan, K.A. Keller, J.L. Sperduto, J.H. Slater, Fundamentals of Laser-Based Hydrogel Degradation and Applications in Cell and Tissue Engineering, Advanced Healthcare Materials 6(24) (2017) 1700681.
[12] B. Dorin, P. Parkinson, P. Scully, Direct laser write process for 3D conductive carbon circuits in polyimide, Journal of Materials Chemistry C 5(20) (2017) 4923-4930.
[13] S.G. Koulikov, D.D. Dlott, Ultrafast microscopy of laser ablation of refractory materials: ultra low threshold stress-induced ablation, Journal of Photochemistry and Photobiology A: Chemistry 145(3) (2001) 183-194.
[14] M. Terakawa, Laser-Induced Carbonization and Graphitization, in: K. Sugioka (Ed.), Handbook of Laser Micro- and Nano-Engineering, Springer International Publishing, Cham, 2021, pp. 857-878.
[15] J.H. Brannon, J.R. Lankard, Pulsed CO2 laser etching of polyimide, Applied Physics Letters 48(18) (1986) 1226-1228.
[16] C.L. Beyler, M.M. Hirschler, Thermal decomposition of polymers, SFPE handbook of fire protection engineering 2(7) (2002).
[17] T. Kato, Y. Yamada, Y. Nishikawa, H. Ishikawa, S. Sato, Carbonization mechanisms of polyimide: Methodology to analyze carbon materials with nitrogen, oxygen, pentagons, and heptagons, Carbon 178 (2021) 58-80.
[18] M.Y. Zhang, H.Q. Niu, S.L. Qi, G.F. Tian, X.D. Wang, D.Z. Wu, Structure evolutions involved in the carbonization of polyimide fibers with different chemical constitution, Materials Today Communications 1(1) (2014) 1-8.
[19] Y. Dong, S.C. Rismiller, J. Lin, Molecular dynamic simulation of layered graphene clusters formation from polyimides under extreme conditions, Carbon 104 (2016) 47-55.

[20] A. Vashisth, M. Kowalik, J.C. Gerringer, C. Ashraf, A.C.T. van Duin, M.J. Green, ReaxFF Simulations of Laser-Induced Graphene (LIG) Formation for Multifunctional Polymer Nanocomposites, ACS Applied Nano Materials 3(2) (2020) 1881-1890.
[21] S. Wang, Y. Yu, R. Li, G. Feng, Z. Wu, G. Compagnini, A. Gulino, Z. Feng, A. Hu, High-performance stacked in-plane supercapacitors and supercapacitor array fabricated by femtosecond laser 3D direct writing on polyimide sheets, Electrochimica Acta 241 (2017) 153-161.
[22] Y. Yuan, Z. Zhang, X. Li, L. Jiang, X. Zhang, P. Zuo, C. Xu, L. Ma, S. Wang, Y. Zhao, L. Qu, Bottom-up scalable temporally-shaped femtosecond laser deposition of hierarchical porous carbon for ultrahigh-rate micro-supercapacitor, Science China Materials 65(9) (2022) 2412-2420.
[23] C. Cheng, S. Wang, J. Wu, Y. Yu, R. Li, S. Eda, J. Chen, G. Feng, B. Lawrie, A. Hu, Bisphenol A Sensors on Polyimide Fabricated by Laser Direct Writing for Onsite River Water Monitoring at Attomolar Concentration, ACS Applied Materials & Interfaces 8(28) (2016) 17784-17792.
[24] T. Lippert, Interaction of Photons with Polymers: From Surface Modification to Ablation, Plasma Processes and Polymers 2(7) (2005) 525-546.
[25] P.F. Conforti, Y.G. Yingling, B.J. Garrison, Computational studies of ultraviolet ablation of poly(methyl methacrylate), Journal of Physics: Conference Series 59 (2007) 322-327.
[26] T. Lippert, J.T. Dickinson, Chemical and Spectroscopic Aspects of Polymer Ablation: Special Features and Novel Directions, Chemical Reviews 103(2) (2003) 453-486.
[27] D. Tan, K.N. Sharafudeen, Y. Yue, J. Qiu, Femtosecond laser induced phenomena in transparent solid materials: Fundamentals and applications, Progress in Materials Science 76 (2016) 154-228.
[28] M.-S. Jung, T.-W. Lee, J. Hyeon-Lee, B. Hee Sohn, I.-S. Jung, Synthesis and characterizations of a polyimide containing a triphenylamine derivative as an interlayer in polymer light-emitting diode, Polymer 47(8) (2006) 2670-2676.
[29] S. Baudach, J. Bonse, W. Kautek, Ablation experiments on polyimide with femtosecond laser pulses, Applied Physics A 69(1) (1999) S395-S398.
[30] M. Forster, W. Kautek, N. Faure, E. Audouard, R. Stoian, Periodic nanoscale structures on polyimide surfaces generated by temporally tailored femtosecond laser pulses, Physical Chemistry Chemical Physics 13(9) (2011) 4155-4158.
[31] S.R. Tsai, M.R. Hamblin, Biological effects and medical applications of infrared radiation, J Photochem Photobiol B 170 (2017) 197-207.

3. Chapter 3: Laser Induced Graphene

After discussing laser-polyimide interaction in Chapter 2, the mechanism of how this interaction leads to carbonization creating Laser Induced Graphene (LIG) is explained through a literature review on LIG in this chapter and a study on thin fim growth methods is performed to improve the conductivity of LIG. LIG is a mesoporous carbon (MC)-based material produced by carbonization of Polyimide using laser and is advantageous over other methods of preparation of mesoporous graphene because the laser carbonization is a single-step, low-cost process and does not require any clean-room conditions [1]. In this chapter, the research question about whether the porosity and surface properties of LIG can be controlled to make it a useful functional material will be explored.

Graphene is a 2D material consisting of single layer sp^2 hybridized carbon and it was isolated by Andre Geim and Konstantin Novoselov using the “Scotch-Tape Method” in 2004 making them the recipient of the Nobel prize [2]. So far, CVD has been the best method for preparing a single layer graphene over larger dimensions [3], but other methods such as shear exfoliation and Hummer’s method has also found to be useful in preparing graphene-based suspensions in bulk which is used for ink-jet printing on flexible substrates [4, 5]. Most of these processes involves copious chemicals and transfer processes which acts as bottlenecks in scalability.

Laser carbonization process will eliminate such bottlenecks and pave a pathway for scalable printing of graphene on flexible substrates. This chapter is written 100% by the author Ratul Kumar Biswas.

3.1. 3D Mesoporous carbon

Mesoporous carbon (MC) is a class of highly ordered porous carbon materials having high specific surface area and excellent chemical, mechanical and thermal stability and used in energy storage, catalysis and sensing applications. MC allows functionalization with organic, inorganic and biomaterials which go inside the porous channels making it useful for targeted applications such as catalysis and drug delivery [6]. MC is prepared by templating methods which is of two types (Fig. 3.1):

A. **Hard templating:** In this method, hard inorganic templates such as silica and zeolites are impregnated with carbon-rich polymers such as Furfuryl alcohol (FA), phenol at elevated temperature of 900 ^{0}C [7] where polymers get carbonized into the template. The template is later removed by highly toxic acid such as hydrofluoric acid (HF) [8]. The porosity of the MC is controlled by the porosity of the template and can be used for applications such as electrochemical energy storage, CO_2 gas capture [7].

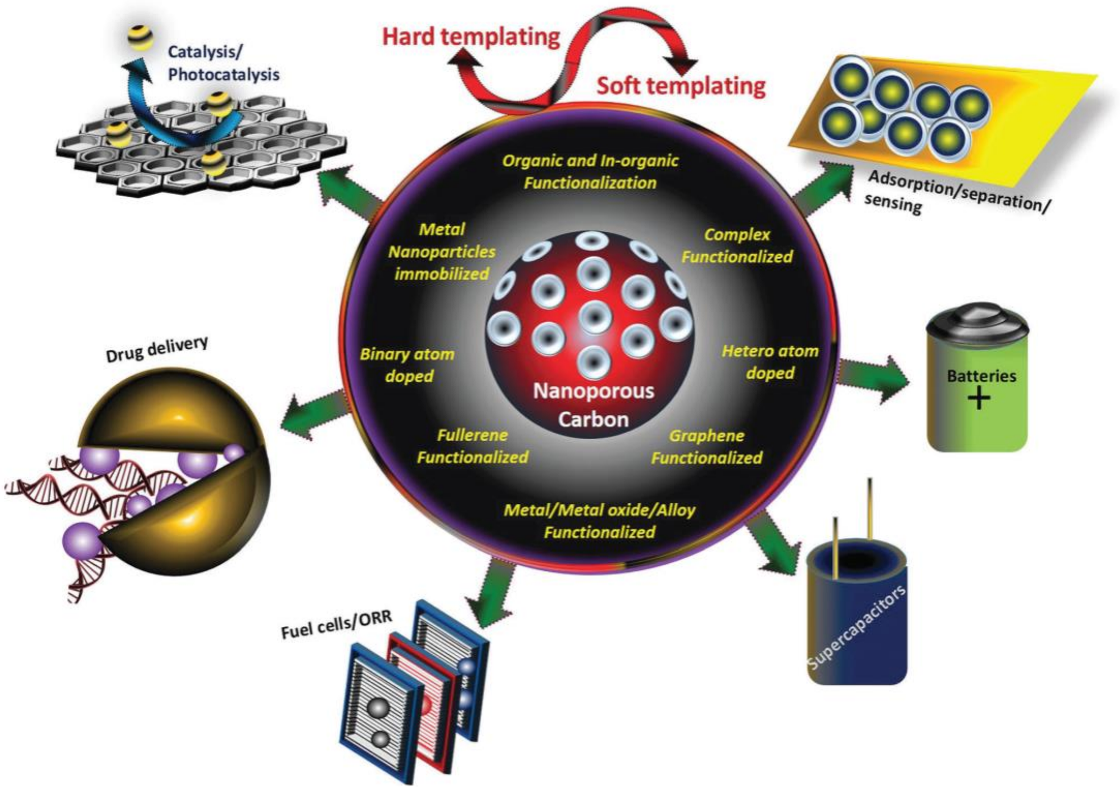

Fig. 3.1. Synthesis and applications of mesoporous carbon [7].

B. Soft templating: In this method, MC is formed by the self-assembly of carbon-rich precursors such as resorcinol, formaldehyde in surfactant solution such as Pluronic F127 followed by carbonization at 350^0C. The porosity is controlled by the intermolecular interaction of the carbon-rich precursor with the surfactant and polymerization kinetics [9]. In this method, better control over porosity and order is achieved at lower temperatures [7].

The templating methods involve the use of harsh and toxic chemicals producing graphene in bulk amount, but the reaction site cannot be controlled spatially. Spatially produced graphene will help in scalable manufacturing of biosensors, energy devices, for which the template methods will bring additional costs due to post-processing such as substrate transfer, graphene-ink processing.

3.1.1.Percolation theory:

The electrical conductivity of MC depends on the interconnectivity of carbon atoms which in turn depends on the porosity of the MC. For a randomly distributed conductive filler in an insulating medium, the electrical conductivity remains low for a low volume fraction of the filler (p) and increases with increasing p (Fig. 3.2.). The conductivity rises suddenly after a threshold value of p which is called the percolation threshold (p_c) and is given by the equation 3.1 based on the Fermi-Dirac distribution [10]:

$$log(\sigma_c) = log(\sigma_{gr}) + \frac{log(\sigma_m)-log(\sigma_{gr})}{1+exp\,[b(p-p_c)]} \tag{3.1}$$

where σ_{gr}, σ_c, and σ_m are the conductivities of graphene, composite and matrix, and b is an empirical constant. The flow of electrons within the conducting network occurs due to tunnelling conduction and is dependent on the spacing between the fillers. The spacing decreases with increasing aspect ratio of the filler and graphene having higher aspect ratio demonstrates this property. Hence, if the crystallite size of LIG is increased, the tunnelling conduction will be improved and the overall electrical conductivity will be improved.

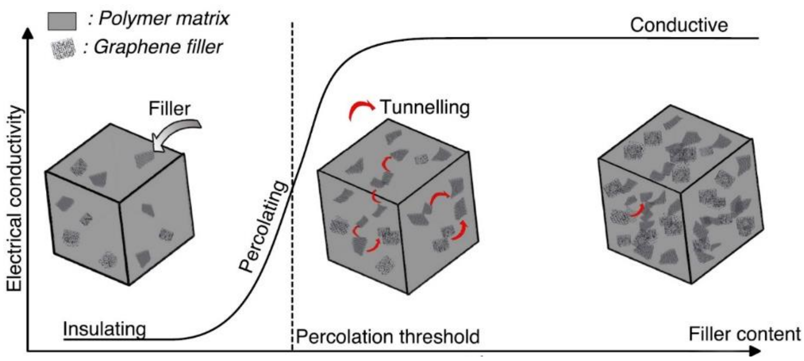

Fig. 3.2. Conduction mechanism in graphene containing composites [10].

3.2. Laser carbonization compared with conventional graphene manufacturing methods:

James Tour from Rice University pioneered the process of laser carbonization of carbon-rich polymers such as PI and lignin in 2014 [11] and used in various applications such as supercapacitors, strain and chemical sensors [11-18]. The conductivity of LIG ranges from 500-2340 S/m which is far lower compared to the single-layer graphene obtained from CVD which is 10^6 S/m [19]. Tour's group studied the fibrous growth of LIG on PI and the height of the fibers was found to increase with laser fluence [13]. Due to the short laser-PI interaction time, defects are generated in the 2D lattice structure forming 5, 6, 7 membered rings (Fig. 3.3) and crystallite size ranged from 20 to 40 nm measured from Raman spectroscopy [11]. The structural evolution of graphene from PI in the laser carbonization process was studied by Moataz et al (Fig. 3.4) [20], who performed a fluence dependent study. Fluence was varied by raster scanning the CO_2 laser at a fixed power of 18.4 W on a PI surface which allowed the beam cross-section to change upon varying spot-size due to the tilt. Porous carbon was observed at lower fluence, and fibrous growth was observed at higher fluence. The transition occurred changing from porous morphology to cellular network morphology (*T1*) and from cellular network to woolly fibers (*T2*) (Fig. 3.4) [20]. Hence, research on improving the conductivity and kinetics of growth of graphene prepared by this process is necessary. The properties such as morphology and conductivity of graphene obtained from various processes are tabulated in Table 3.1 which elucidates the advantages and disadvantages of the laser carbonization process over other processes.

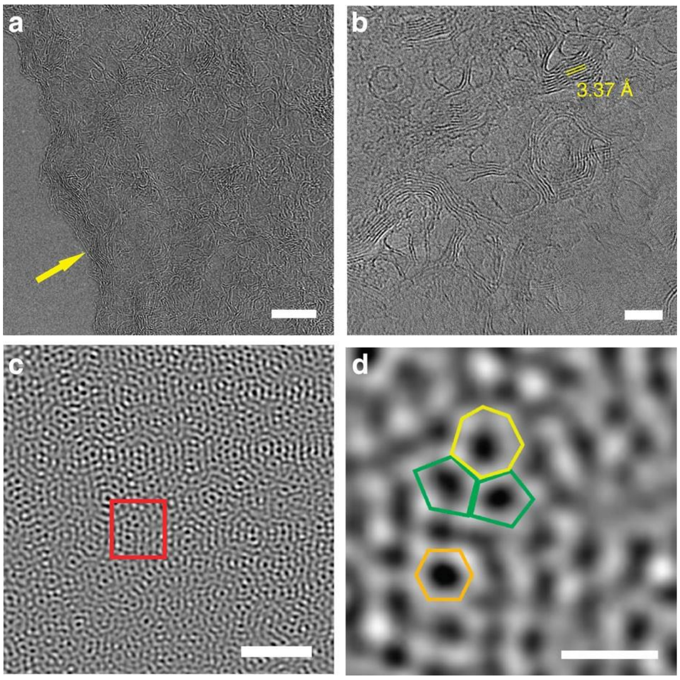

Fig. 3.3. (a, b) High resolution TEM (HRTEM) image of LIG edge with scale-bar 10 nm and 5 nm respectively, (c) STEM image of LIG edge, (d) TEM image showing 5-7 membered rings [11].

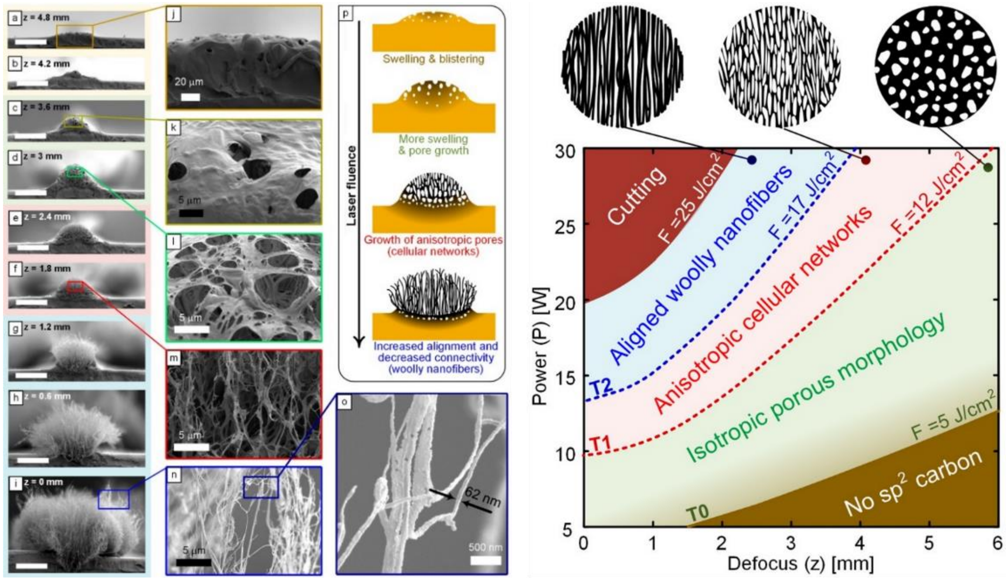

Fig. 3.4. Varying LIG morphology with varying focal length (*z*), Process window showing the transitions of LIG morphology from porous to woolly in CO_2 laser carbonization process [20].

Table 3.1. Methods of graphene synthesis.

Method	**Type of graphene**	**Electrical Conductivity/sheet resistance**	**Advantages**	**Disadvantages**
Laser carbonization	3D mesoporous and fibrous carbon [20]	500-2340 S/m [11, 21, 22]	Digital control, precise, scalable, no clean-room condition.	Non-planar graphene flakes with defects, low electrical conductivity.
CVD	Large area single layer graphene (~0.5 mm) [23]	10^6 S/m, $10^3 \Omega$/sq [19]	Uniform film with less defects.	Highly expensive instruments and toxic gaseous side-products [24].
Epitaxial growth	Large area single layer graphene	(5-6.4) x 10^6 S/m [25]	No substrate transfer required.	High cost of SiC [26].

Chemical Exfoliation	Graphene based nanosheets	2 x 10^2 S/m [27]	Bulk production of graphene possible.	Contains plenty of oxygen defects [28].
Liquid Phase Exfoliation	GNP, GNS	2.2 x 10^5 S/m [29] 3 x 10^3 S/m [30]	Bulk production of graphene in stable dispersion [31].	Low yield of monolayer graphene, time consuming [32].
Electrochemical Exfoliation	GNS with 1-3 layers [32]	6 x 10^4 S/m [33]	High yield (85%), cost effective.	Slight oxidation, inhomogeneous flake thickness [32].

Table 3.1 shows that the laser carbonization process provides precise control and repeatable results for microstructural properties and can be printed on the substrate itself but the graphene obtained from this process does not form a planar structure but porous foam-like structures instead which brings down the conductivity. Graphene obtained from other methods comes as large planar crystallites and has higher conductivity, but they need to be stored as ink-emulsions and transferred on substrates for printing purposes. Hence, a control of crystallite size of graphene is the laser carbonization process is necessary.

3.3. Laser Graphitization

Laser graphitization is the method of conversion of ta-C or DLC to graphitic sp^2 hybridized carbon using a laser radiation and such conversion occurs at around 773 K [34, 35]. Armeyev et al. studied the laser graphitization of Diamond like Carbon (DLC) film which is a hard amorphous hydrogenated carbon (a-C:H) using an Argon laser and found increasing sp^2 carbon content after laser irradiation [36]. Boubiche et al. studied the kinetics of graphitization of DLC film deposited by pulsed laser deposition on quartz substrate with a thin Nickel metal layer as catalyst using annealing method and found the complete growth of graphitized clusters to occur at 773 K [37] with an improvement of conductivity from $8x10^2$ S/cm to $7x10^3$ S/cm. Liu et al [38] used femtosecond laser for laser graphitization of CVD deposited DLC (Fig. 3.5) and found a 20% improvement in conductivity. Such transition from DLC to graphitized phase can be observed from the formation of G-peaks in the Raman spectra of the graphitized phase and a blue shift in the G-peak position and shows improved electrical conductivity of ~2.6 times [35, 38]. Hence, laser graphitization can be a possible method for improvement of conductivity of LIG.

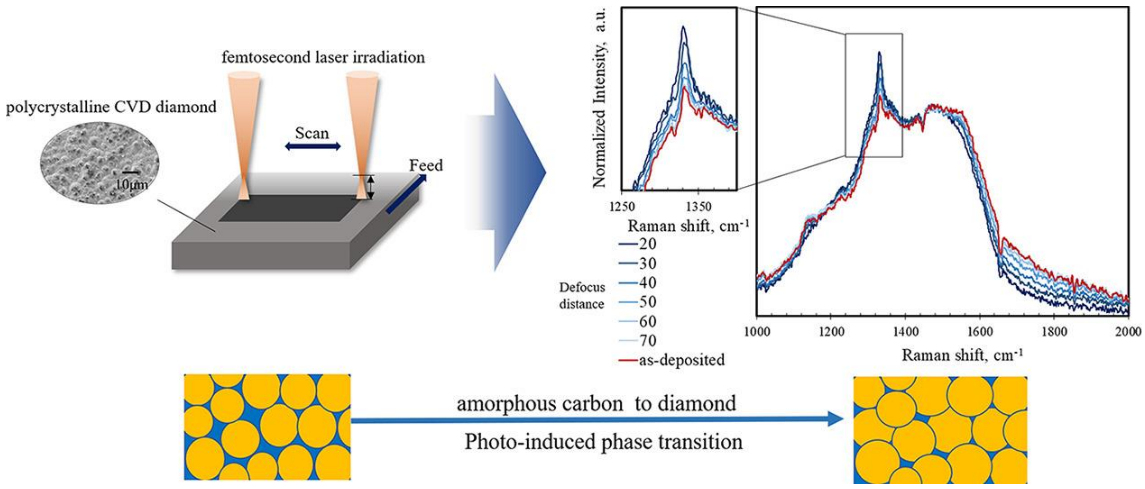

Fig. 3.5. Laser graphitization of CVD deposited DLC film [38].

3.4. Modes of Graphene Growth

After discussing the porous nature of LIG, it is important to understand the control of its morphology in the laser carbonization process. The growth of graphene on any substrate is controlled by the interdynamics of interfacial surface energies and free energy. The free energy for thin-film growth on a substrate is given as [39, 40]:

$$\Delta G = a_1 r^2 \gamma_{fv} + a_2 r^2 \gamma_{fs} - a_2 r^2 \gamma_{sv} + a_3 r^3 \Delta G_v \tag{2.30}$$

where γ_{sv}, γ_{fs}, and γ_{fv} are the interfacial surface energy between substrate and vapour, film and substrate, and film and vapour respectively. ΔG_v is the volumetric free energy of thin film, a_1, a_2 and a_3 are constants, and r is the radius of curvature of the film.

The equilibrium contact angle (θ) of a liquid on solid-gas interface (Fig. 3.6.d) is given by Young's equation:

$$\gamma_{sv} = \gamma_{fs} + \gamma_{fv} cos\theta \tag{2.31}$$

Based on the energetics, the mode of thin-film growth is classified into three main categories (Fig. 3.6.a-c) [41, 42]:

a) **Volmer-Weber Growth (Island-Growth):** $\theta > 0, \gamma_{sv} < \gamma_{fs} + \gamma_{fv}$ (2.32)

In this case, the binding force between the thin film atoms is stronger than that between the film atoms and substrate and three-dimensional growth of films directly on the substrate is favoured.

b) Frank-van-Der-Merwe Mode (Layer by Layer (LBL) Mode): $\theta \approx 0, \gamma_{sv} \geq \gamma_{fs} + \gamma_{fv}$ (2.33)

In this case, the binding force between the thin film atoms and substrate is stronger than that between the film atoms and two-dimensional growth of films directly on the substrate is favoured.

c) Stranski-Krastanov Mode (LBL + Island Mode): $Initial: \gamma_{sv} > \gamma_{fs} + \gamma_{fv}$,

$$Final: \gamma_{sv} < \gamma_{ff}, \gamma_{fv} = 0 \qquad (2.34)$$

This is an intermediate case between the Volmer-eber mode and the LBL mode. Here, the three-dimensional growth of thin films occurs after formational of a certain number of two-dimensional layers of thin films.

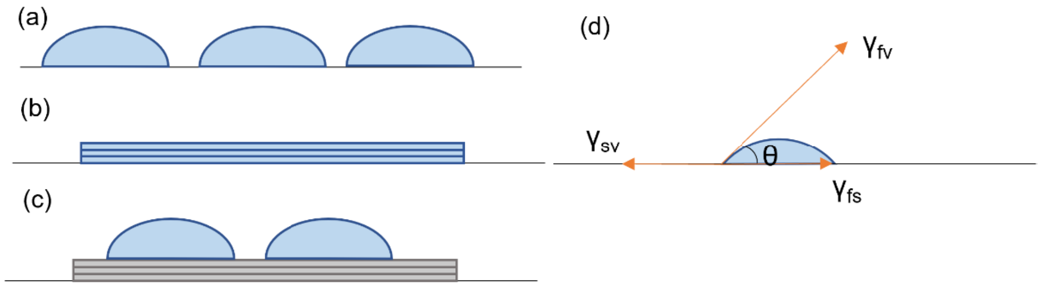

Fig. 3.6. (a-c) Modes of thin-film growth, (d) Equilibrium angle of contact with surface (s), fluid (f) and vapour (v).

Hence, by proper control of interfacial surface energies, γ_{sv}, γ_{fs}, and γ_{fv}, the mode of growth of graphene on a substrate can be controlled [43].

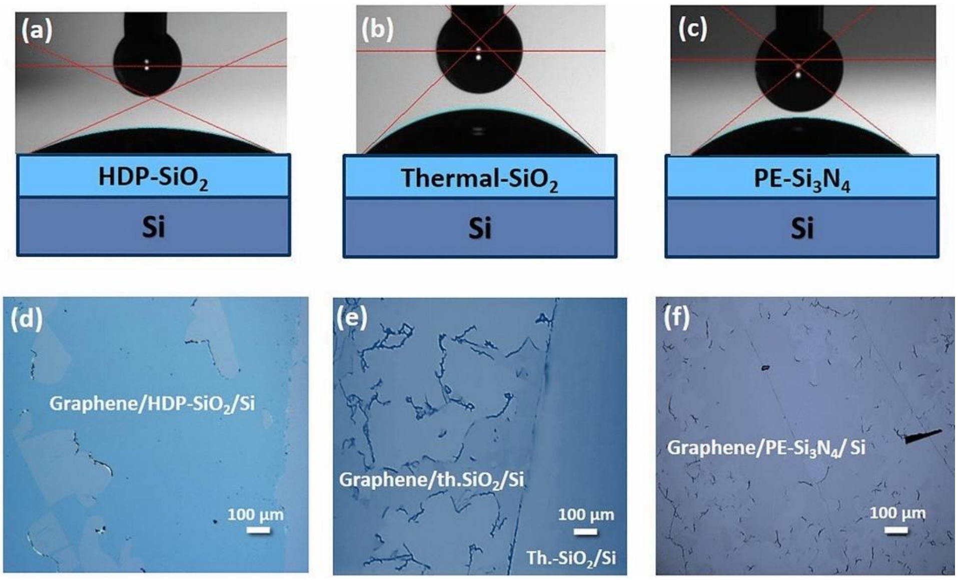

Fig. 3.7. Contact angle measurement on (a) HDP-SiO_2 with wetting angle = 31^0, (b) Thermal SiO_2 with wetting angle =45^0, and (c) PE-Si_3N_4 with wetting angle = 38^0. Optical microscopy images of graphene on (d) HDP-SiO_2, (e) Thermal SiO_2, and (f) PE-Si_3N_4 [44].

From Equation 2.30, it is understood that the surface energy of the substrate plays a crucial role in determining the mode of crystal growth on the substrate. Increasing the interfacial energy (γ_{fs}) increases the tendency of the Frank-der-Merwe mode (LBL) of growth. Further reduction in γ_{fs} leads to Stranski-Krastanov growth and minimum γ_{fs} leads to Volmer-Weber mode of growth which leads to island-based thin films. The interfacial energy can be increased using plasma treatment which can be reflected by the increasing wettability of the substrate.

R. Lukose et al [44] studied the effect of hydrophilicity of Si-substrate on the transfer process of graphene from 200 mm Ge/Si donor wafer. The hydrophilicity was varied by growing SiO_2 on Si wafer by two methods such as High Density Plasma (HDP) deposition using silane (SiH_4) precursor , thermal treatment at 1000^0C,of Silane and and by growing Si_3N_4 on Si wafer by Plasma Enhanced (PE) CVD of Silane and NH_3/N_2 gases. The contact angle measured from the three substrates were found to be 31^0, 45^0 and 38^0 respectively (Fig. 3.7 a-c) and the graphene film coverage was found to be maximum for HDP-SiO_2, followed by PE-Si_3N_4 and Thermal SiO_2, which shows that the growth is favoured with decreasing contact angle. Further plasma treatment on HDP-SiO_2 substrate decreased the contact angle upto 2.4^0 and large-area graphene deposition with better adhesion was achieved. Hence, the morphological growth of graphene on PI can be improved by activation of the PI surface using plasma to improve the conductivity and such a study will be presented in Chapter 6.

3.5. Raman Spectroscopy of Graphene

Raman Spectroscopy is a method to measure the vibrational modes of molecules in a material. The vibrational energy of a molecule is quantized into phonons which is distributed into quantized energy levels obeys Bose-Einstein statistics, and the energy in a vibrational mode ***k*** at v_{th} level is given as: $E_{vk}^{k} = \hbar \nu_{\boldsymbol{k}}(v + \frac{1}{2})$, where ν_k is the frequency of the $\boldsymbol{k_{th}}$ mode. Light with frequency (ν_0) gets scattered upon falling on molecule because of polarization, which leads to excitation of phonons to higher vibrational energy states. Such scattering can happen in two ways, elastic scattering when the phonon returns to the exact initial energy state releasing photon of the same frequency (ν_0) as the incident light, known as Rayleigh scattering; and inelastic scattering when the phonons return to a higher energy state than the initial, causing a positive shift ($+\nu_m$) in the frequency of the releasing photon, called Stokes shift, and when the phonons return to a lower energy state than the initial, causing a negative shift ($-\nu_m$) in the frequency of the releasing photon, called anti-Stokes shift. The process is explained in Fig. 3.8. a,b. Both Stokes and anti-Stokes scattering are together called Raman scattering. Stokes scattering is mostly measured because of its higher probability owing to the Maxwell-Boltzmann distribution law.

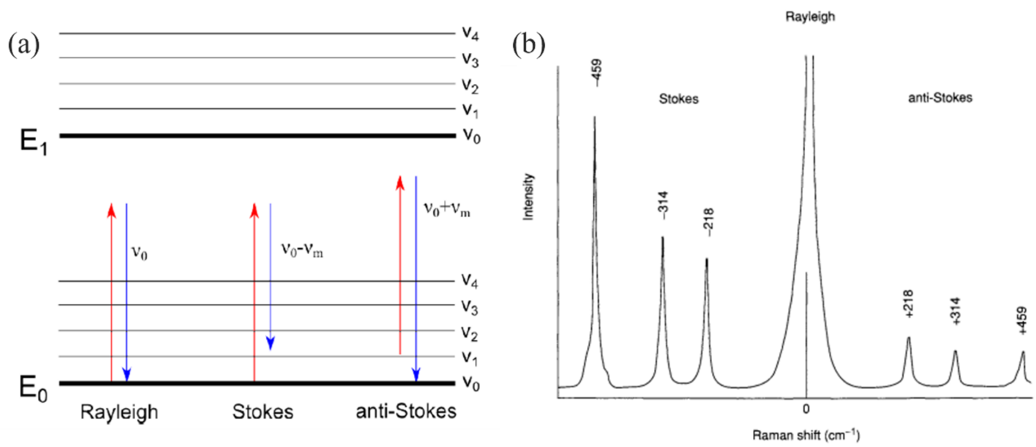

Fig. 3.8. (a) Vibration absorption process, (b) Raman shifts in vibrational spectra [45].

The shift of frequency in the Raman scattering is used as a chemical signature of molecules and thus as characterization tool for determining the presence of sp^2 hybridized carbon and defects in graphene.

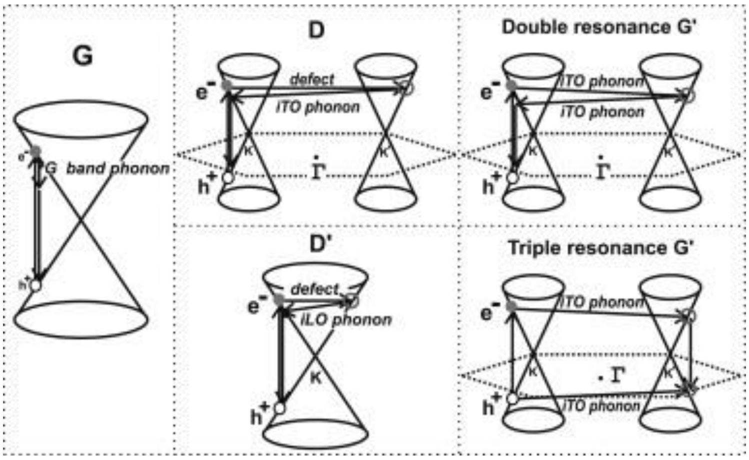

Fig. 3.9. Resonance mechanisms for D, G and 2D band, Phonon excitations in 2-layer graphene [46].

The Raman spectra of graphene and graphite is dominated by three major peaks (Fig. 3.5, Fig. 3.10.c) [47] at wavenumbers ~1350 cm^{-1}, ~1580 cm^{-1} and ~2700 cm^{-1} which are termed as D band, G band and 2D band respectively. D band is a disorder-induced band where the excitation of Transverse Optical (TO) phonon is assisted by the disorder around the **K** point by a double resonance mechanism (Fig. 3.9). The electron around **K** point with wavevector ***k*** gets scattered inelastically by a phonon and elastically by a defect of wavevector **q** and energy E_{phonon}, to **K'** point with wavevector ***k+q*** [46]**.** A phonon is emitted after the electron scatters back to ***k*** state after recombining with a hole at ***k*** state. G band is a first order Raman band and arises from E_{2g} in-plane vibration modes at the ***Γ*** point where the TO and Longitudinal Optical (LO) branches touch each other. 2D band is a higher order process which is a result of double resonance enhanced two-TO phonon process around the **K** point (Fig. 3.10.b). The process is like D-band, only in this case the double resonance occurs by inelastic scattering by two phonons. Hence, the D, G and 2D peaks provide a fingerprint of the graphene and can be used to study the defects in LIG.

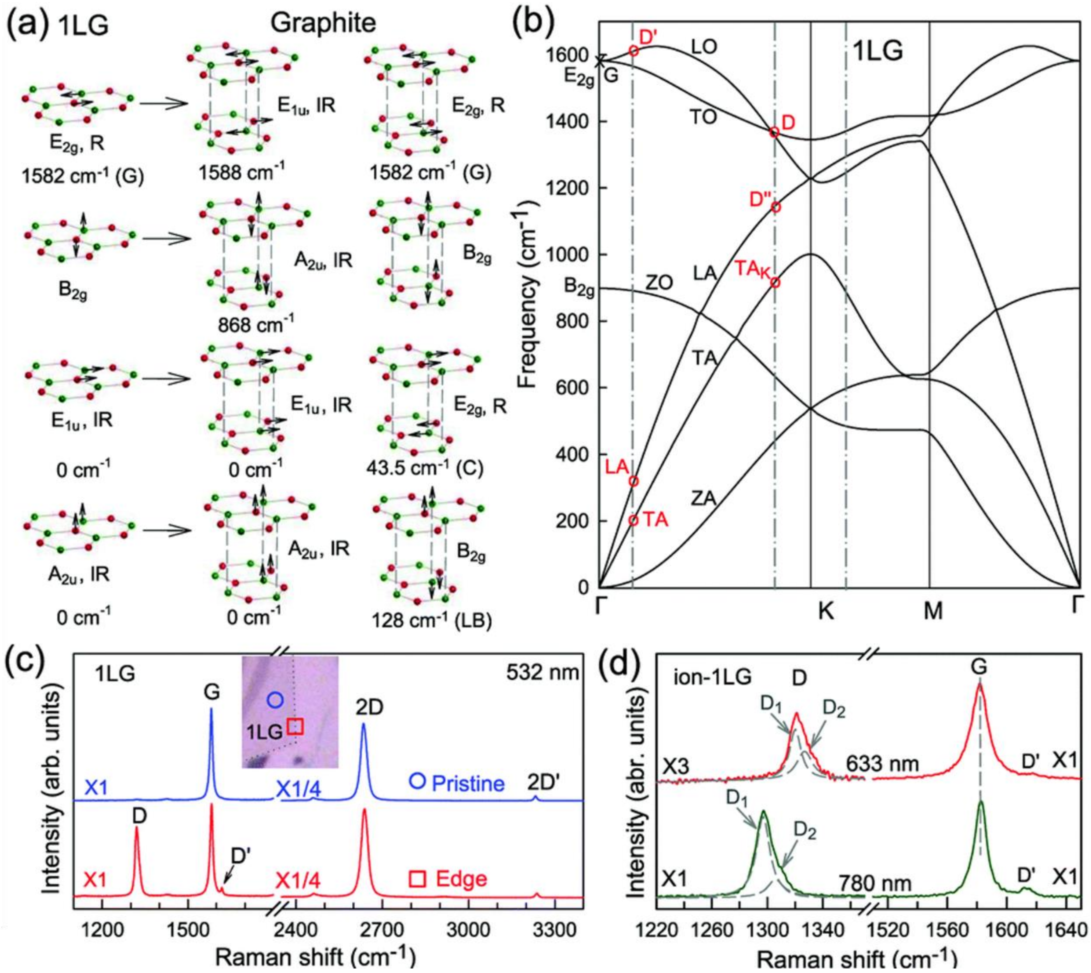

Fig. 3.10. Vibrational modes in graphene (b) Phonon dispersion in graphene, (c) Raman spectra of single layer graphene and multiplayer graphene, (d) Band-fitting of D and G peaks, (e) Full Raman spectrum of graphene showing the TA and LA modes [48].

3.6. Electronic structure under strain- Graphene as strain sensor

The sensitivity to strain in the graphene comes from two effects: (1) intraflake where the single crystal is strained upon an external stimuli causing change in conductivity, and (2) interflake where the separation between the individual crystals changes upon external stimuli changing the conductivity. This is further discussed below.

3.6.1. Intraflake

The sensing nature of graphene depends on its morphology and crystallite size. Hence, controlling the morphology will also help to control the sensitivity of graphene. To understand the sensing mechanism of graphene, it is important to understand what happens to the electronic structure of a single flake of the graphene. Graphene unit cell comprises a triangular lattice with two atoms (A and B) as basis per unit cell. The lattice vectors are given as: a_1=AA'=a/2(3,√3) and a_2=AA"=a/2(3,- √3), where a=C-C bond length=1.42A. The first Brillouin Zone (BZ) is a hexagon with vectors b_1=2π/√3a(1, √3) and b_2=2π/√3a(1, -√3) [49] as shown in Fig. 3.11. As per Cauchy-Born rule, the lattice vectors (a_1, a_2) and the reciprocal vectors (b_1, b_2) of graphene are affected when strained [50]. The BZ of graphene has hexagonal D_{6h} (6/mmm) symmetry under zero-strain (Fig.3.12.a).

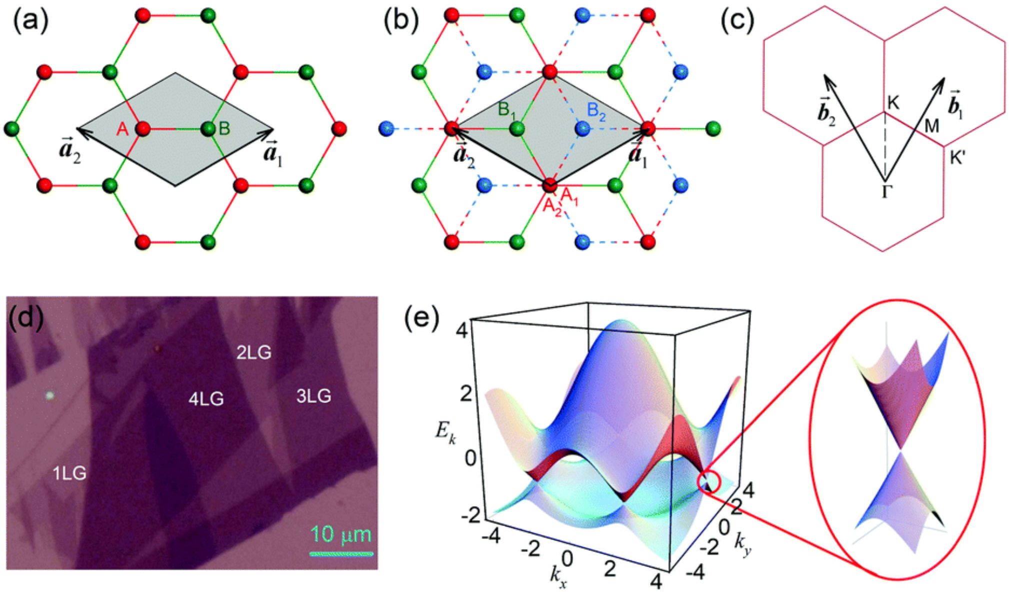

Fig. 3.11. (a) Graphene unit cell, (b) reciprocal lattice, (c) Reciprocal lattice vectors, (d) TEM of 1-4 LG, (e) 3D band dispersion curve of graphene [48].

Under an uniaxial strain, the six-fold and three-fold symmetries are lost and the BZ makes a transition to rhombic D_{2h} (mmm) symmetry, opening a pseudo-gap at **K** and **K'** (Fig.3.12.b) [50]. Under shear strain, the BZ makes a transition to 2/m monoclinic symmetry (Fig.3.12.c), which leads to a bandgap of 0.72 eV for strain $\varepsilon \approx 20\%$. A combination of uniaxial strain and shear leads to bandgap of ~0.6 eV for $\varepsilon \approx 15\%$ in uniaxial arm-chair graphene, while no gap-opening occurs for uniaxial zigzag graphene. Hence, graphene is an excellent piezoresistive material since under strain, a bandgap forms which leads to decreasing electrical conductivity.

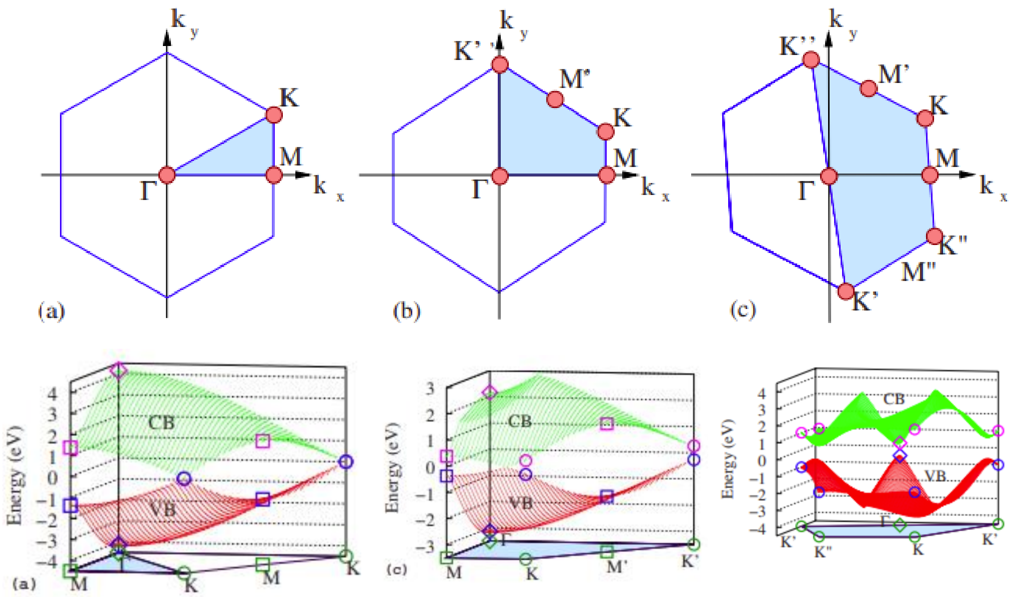

Fig. 3.12. E-***k*** diagram of single layer graphene upon (a) zero strain, (b) uniaxial strain, (c) Shear strain [50].

3.6.2. Interflake

For randomly oriented graphene flakes in an assembly, transport of electrons in between the flakes occurs by a tunnelling mechanism. The electrons need to overcome the tunnelling barrier for electrical conduction. Closer the flakes will create a lower energy-barrier and decrease the tunnelling resistivity, and vice-versa. Tunnelling resistivity is given by the Simmons equation [51]:

$$\rho_{Tunnelling} = \frac{h^2}{e^2\sqrt{2m\lambda}} \exp\left(\frac{4\pi d}{h}\sqrt{2m\lambda}\right) \quad (2.35)$$

Where, d= tunnelling distance between two adjacent graphene flakes, λ= tunnelling barrier, m=electron mass, e=electron charge, and h= Planck's constant.

The piezoresistive effect is quantified by Gauge Factor (GF) given as:

$$GF = \frac{1}{\epsilon}\frac{\Delta R}{R} = \frac{1}{\epsilon}\frac{\Delta\rho}{\rho} \quad (2.36)$$

Where, ε = strain, R = initial resistance, ΔR = change in resistance, ρ = resistivity, and $\Delta\rho$ = change in resistivity. GF and R increase with increasing λ (Fig. 3.13.a,b) [51]. Under tension, the spacing between the graphene flakes increases which increases the resistance and vice-versa [52]. Tests have shown linear responses to bending (Fig. 3.13.c,d), and demonstrated that graphene is an excellent material for strain measurements.

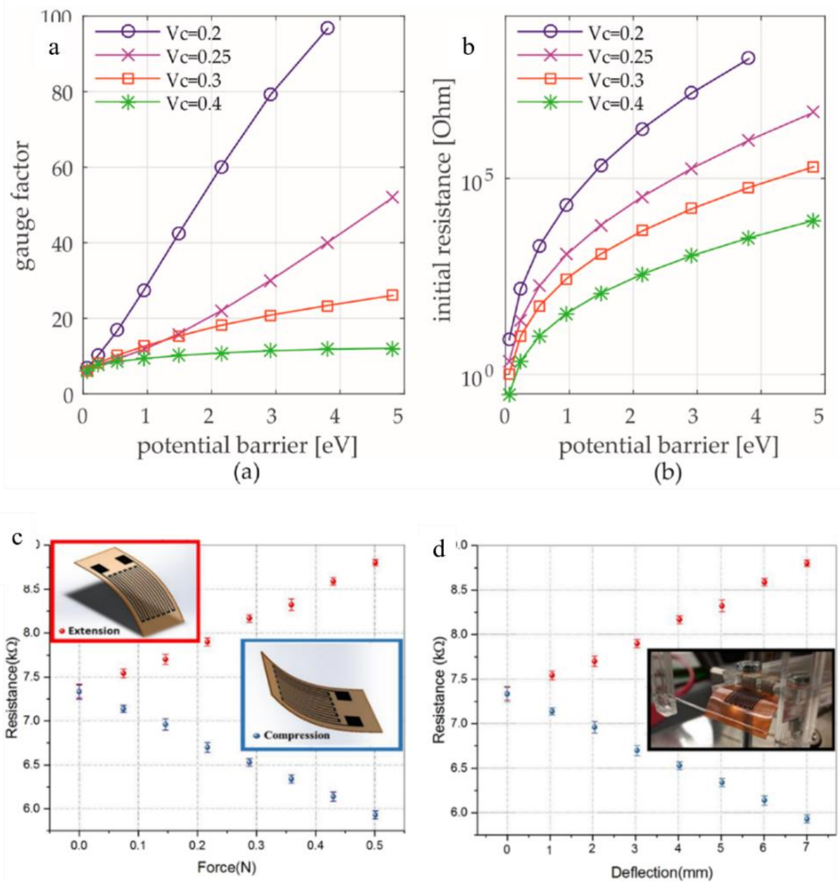

Fig. 3.13. (a) *GF* vs *λ* simulated using Eq 2.35 for filler fraction V_c=0.2-0.4, [51], (b) *R* vs *λ* simulated using Eq 2.35 for filler fraction V_c=0.2-0.4, [51], (c) *R* vs force measured from 0-0.5 N for LIG [52], (d) *R* vs deflection measured from 0-7 mm for LIG [52].

3.7. Applications of Laser Induced Graphene (LIG)

Laser carbonization of Polyimide has found applications in various fields such as biosensors, energy storage, electrocatalysts, transducers, etc. because of the versatility of graphene applications (Fig. 3.14). The combination of digital control of laser and the chemical nature of Polyimide enables the printing graphene of user-defined designs and dimensions with excellent precision. Although single-crystalline monolayer graphene has not been printed yet with this process, the 3D porous and multilayer graphene still finds applications in diverse fields. The porous nature of LIG enables absorption of chemicals in the edges of the graphene crystallites, which act as reaction sites for electrochemical reactions and can be used for electrochemical sensors and electrocatalytic applications [53]. 3D mesoporous graphene is prepared by template methods which involves the use of toxic chemicals and used widely in catalysis, drug-delivery applications. Laser carbonization is a one-step process without use of liquid chemicals and has better control over microporosity when compared to template based methods.

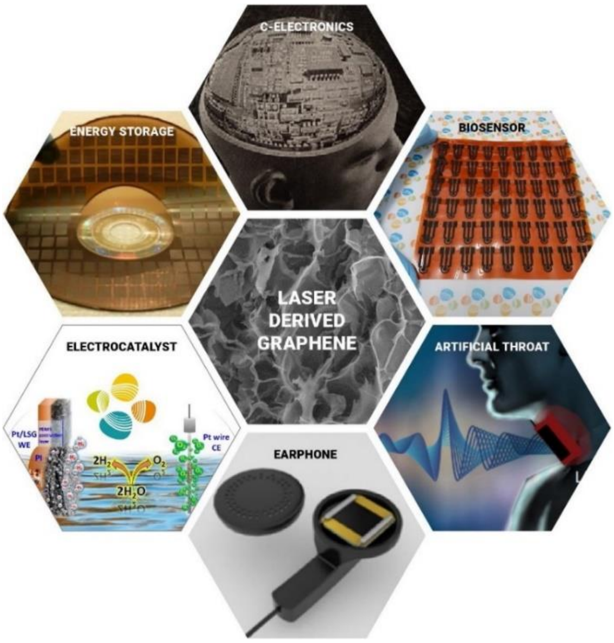

Fig. 3.14. Applications of LIG [53].

The presence of graphene crystallites with spacings in between them allows the tunnelling of electrons to change the spacing due to stretching and bending of PI which enables the LIG to be useful for strain sensors with high sensitivity (*GF*=400-700) [54, 55]. Such high strain sensitivity allows LIG to be used for tactile sensing, heartbeat sensing, voice recognition. *GF* of LIG obtained still so far is tabulated in table 3.2.

Table 3.2. Summary of LIG as strain sensor.

Laser	Parameters	GF	Applications	Date
CO_2, 10.6 μm	1.5W-7.5 W, 25.4-88.9 mm/s	4.9-112	Tactile sensing, Heartbeat sensing [21]	2016
UV, 355 nm, Nd:YVO_4	3 W, f= 150 kHz, 60 mm/s,	20	Pulse wave monitoring [56]	2018
CO_2, 10.6 μm	7 W, 70 m/min	0.47	Joint movement monitoring [57]	2019
CO_2, 10.6 μm	800 mW, 30 mm/s	42	Mechanical sensor [58]	2021

3.8. Summary

In this chapter, the synthesis of laser-induced graphene was discussed and comparative analysis with other conventional graphene manufacturing methods was tabulated. Laser graphitization was discussed as a possible method of improving the conductivity of LIG and will be explained in the Chapter 5. The underlying physics of thin film growth was discussed and was linked with the laser carbonization process which will enable the study on LIG growth kinetics in the Chapter 6. Plasma activation of substrate was discussed as a possible technique to improve crystal growth of graphene. The sensing performance of graphene was discussed and the Gauge Factor of LIG was tabulated. The morphology and crystal growth in LIG controls the spacing between the graphene flakes which changes the tunnelling distance and hence the conductivity and the Gauge Factor of LIG. Hence, by proper control of crystal growth and morphology, the *GF* can be controlled.

Bibliography

[1] A. Velasco, Y.K. Ryu, A. Hamada, A. de Andrés, F. Calle, J. Martinez, Laser-Induced Graphene Microsupercapacitors: Structure, Quality, and Performance, Nanomaterials, 2023.
[2] K.S. Novoselov, A.K. Geim, S.V. Morozov, D. Jiang, Y. Zhang, S.V. Dubonos, I.V. Grigorieva, A.A. Firsov, Electric Field Effect in Atomically Thin Carbon Films, Science 306(5696) (2004) 666-669.
[3] H.C. Lee, W.-W. Liu, S.-P. Chai, A.R. Mohamed, C.W. Lai, C.-S. Khe, C.H. Voon, U. Hashim, N.M.S. Hidayah, Synthesis of Single-layer Graphene: A Review of Recent Development, Procedia Chemistry 19 (2016) 916-921.
[4] J.K. Lynch-Branzoi, A. Ashraf, A. Tewatia, M. Taghon, J. Wooding, J. Hendrix, B.H. Kear, T.J. Nosker, Shear exfoliation of graphite into graphene nanoflakes directly within polyetheretherketone and a spectroscopic study of this high modulus, lightweight nanocomposite, Composites Part B: Engineering 188 (2020) 107842.
[5] P. Li, C.-A. Tao, B. Wang, J. Huang, T. Li, J. Wang, Preparation of Graphene Oxide-Based Ink for Inkjet Printing, Journal of Nanoscience and Nanotechnology 18(1) (2018) 713-718.
[6] M. Mamai, D. Giasafaki, E.A. Salvanou, G. Charalambopoulou, T. Steriotis, P. Bouziotis, Biodistribution of Mesoporous Carbon Nanoparticles via Technetium-99m Radiolabelling after Oral Administration to Mice, Nanomaterials (Basel) 11(12) (2021).
[7] M.R. Benzigar, S.N. Talapaneni, S. Joseph, K. Ramadass, G. Singh, J. Scaranto, U. Ravon, K. Al-Bahily, A. Vinu, Recent advances in functionalized micro and mesoporous carbon materials: synthesis and applications, Chemical Society Reviews 47(8) (2018) 2680-2721.
[8] K. Kim, Y. Kwon, T. Lee, S.J. Cho, R. Ryoo, Facile large-scale synthesis of three-dimensional graphene-like ordered microporous carbon via ethylene carbonization in CaX zeolite template, Carbon 118 (2017) 517-523.
[9] D. Liu, J.-H. Lei, L.-P. Guo, D. Qu, Y. Li, B.-L. Su, One-pot aqueous route to synthesize highly ordered cubic and hexagonal mesoporous carbons from resorcinol and hexamine, Carbon 50(2) (2012) 476-487.
[10] A.J. Marsden, D.G. Papageorgiou, C. Vallés, A. Liscio, V. Palermo, M.A. Bissett, R.J. Young, I.A. Kinloch, Electrical percolation in graphene–polymer composites, 2D Materials 5(3) (2018) 032003.
[11] J. Lin, Z. Peng, Y. Liu, F. Ruiz-Zepeda, R. Ye, E.L.G. Samuel, M.J. Yacaman, B.I. Yakobson, J.M. Tour, Laser-induced porous graphene films from commercial polymers, Nature Communications 5(1) (2014) 5714.
[12] Y. Chyan, R. Ye, Y. Li, S.P. Singh, C.J. Arnusch, J.M. Tour, Laser-Induced Graphene by Multiple Lasing: Toward Electronics on Cloth, Paper, and Food, ACS Nano 12(3) (2018) 2176-2183.
[13] L.X. Duy, Z. Peng, Y. Li, J. Zhang, Y. Ji, J.M. Tour, Laser-induced graphene fibers, Carbon **126** (2018) 472-479.
[14] D.X. Luong, K. Yang, J. Yoon, S.P. Singh, T. Wang, C.J. Arnusch, J.M. Tour, Laser-Induced Graphene Composites as Multifunctional Surfaces, ACS Nano 13(2) (2019) 2579-2586.
[15] D.C. Marcano, D.V. Kosynkin, J.M. Berlin, A. Sinitskii, Z. Sun, A. Slesarev, L.B. Alemany, W. Lu, J.M. Tour, Improved Synthesis of Graphene Oxide, ACS Nano 4(8) (2010) 4806-4814.
[16] M.G. Stanford, C. Zhang, J.D. Fowlkes, A. Hoffman, I.N. Ivanov, P.D. Rack, J.M. Tour, High-Resolution Laser-Induced Graphene. Flexible Electronics beyond the Visible Limit, ACS Applied Materials & Interfaces 12(9) (2020) 10902-10907.

[17] R. Ye, D.K. James, J.M. Tour, Laser-Induced Graphene, Accounts of Chemical Research 51(7) (2018) 1609-1620.
[18] J. Zhang, C. Zhang, J. Sha, H. Fei, Y. Li, J.M. Tour, Efficient Water-Splitting Electrodes Based on Laser-Induced Graphene, ACS Applied Materials & Interfaces 9(32) (2017) 26840-26847.
[19] Y. Wu, Y. Wu, K. Kang, Y. Chen, Y. Li, T. Chen, Y. Xu, Characterization of CVD graphene permittivity and conductivity in micro-/millimeter wave frequency range, AIP Advances 6(9) (2016) 095014.
[20] M. Abdulhafez, G.N. Tomaraei, M. Bedewy, Fluence-Dependent Morphological Transitions in Laser-Induced Graphene Electrodes on Polyimide Substrates for Flexible Devices, ACS Applied Nano Materials 4(3) (2021) 2973-2986.
[21] S. Luo, P.T. Hoang, T. Liu, Direct laser writing for creating porous graphitic structures and their use for flexible and highly sensitive sensor and sensor arrays, Carbon 96 (2016) 522-531.
[22] J.B. In, B. Hsia, J.-H. Yoo, S. Hyun, C. Carraro, R. Maboudian, C.P. Grigoropoulos, Facile fabrication of flexible all solid-state micro-supercapacitor by direct laser writing of porous carbon in polyimide, Carbon 83 (2015) 144-151.
[23] X. Li, C.W. Magnuson, A. Venugopal, R.M. Tromp, J.B. Hannon, E.M. Vogel, L. Colombo, R.S. Ruoff, Large-Area Graphene Single Crystals Grown by Low-Pressure Chemical Vapor Deposition of Methane on Copper, Journal of the American Chemical Society 133(9) (2011) 2816-2819.
[24] P. Karfa, K. Chandra Majhi, R. Madhuri, Chapter 2 - Synthesis of two-dimensional nanomaterials, in: R. Khan, S. Barua (Eds.), Two-Dimensional Nanostructures for Biomedical Technology, Elsevier2020, pp. 35-71.
[25] J. Krupka, W. Strupinski, Measurements of the sheet resistance and conductivity of thin epitaxial graphene and SiC films, Applied Physics Letters 96(8) (2010) 082101.
[26] A.A. Lebedev, S.Y. Davydov, I.A. Eliseyev, A.D. Roenkov, O. Avdeev, S.P. Lebedev, Y. Makarov, M. Puzyk, S. Klotchenko, A.S. Usikov, Graphene on SiC Substrate as Biosensor: Theoretical Background, Preparation, and Characterization, Materials (Basel) 14(3) (2021).
[27] S. Stankovich, D.A. Dikin, R.D. Piner, K.A. Kohlhaas, A. Kleinhammes, Y. Jia, Y. Wu, S.T. Nguyen, R.S. Ruoff, Synthesis of graphene-based nanosheets via chemical reduction of exfoliated graphite oxide, Carbon 45(7) (2007) 1558-1565.
[28] A.A. Moosa, M.S. Abed, Graphene preparation and graphite exfoliation, Turk J Chem 45(3) (2021) 493-519.
[29] H. Wu, L.T. Drzal, Graphene nanoplatelet paper as a light-weight composite with excellent electrical and thermal conductivity and good gas barrier properties, Carbon 50(3) (2012) 1135-1145.
[30] D.J. Finn, M. Lotya, G. Cunningham, R.J. Smith, D. McCloskey, J.F. Donegan, J.N. Coleman, Inkjet deposition of liquid-exfoliated graphene and MoS2 nanosheets for printed device applications, Journal of Materials Chemistry C 2(5) (2014) 925-932.
[31] L. Li, M. Zhou, L. Jin, L. Liu, Y. Mo, X. Li, Z. Mo, Z. Liu, S. You, H. Zhu, Research Progress of the Liquid-Phase Exfoliation and Stable Dispersion Mechanism and Method of Graphene, Frontiers in Materials 6 (2019).
[32] A. Amiri, M. Naraghi, G. Ahmadi, M. Soleymaniha, M. Shanbedi, A review on liquid-phase exfoliation for scalable production of pure graphene, wrinkled, crumpled and functionalized graphene and challenges, FlatChem **8** (2018) 40-71.
[33] S.A. Mirkhani, A. Iqbal, T. Kwon, A. Chae, D. Kim, H. Kim, S.J. Kim, M.-K. Kim, C.M. Koo, Reduction of Electrochemically Exfoliated Graphene Films for High-Performance Electromagnetic Interference Shielding, ACS Applied Materials & Interfaces 13(13) (2021) 15827-15836.

[34] T.V. Kononenko, S.M. Pimenov, V.V. Kononenko, E.V. Zavedeev, V.I. Konov, G. Dumitru, V. Romano, Laser-induced spallation in diamond-like carbon films, Applied Physics A 79(3) (2004) 543-549.
[35] R.K. Biswas, N. Farid, G. O'Connor, P. Scully, Improved conductivity of carbonized polyimide by CO2 laser graphitization, Journal of Materials Chemistry C 8(13) (2020) 4493-4501.
[36] V.Y. Armeyev, A.H. Arslanbekov, N.I. Chapliev, V.I. Konov, V.G. Ralchenko, V.E. Strelnitsky, Laser Induced Graphitization of Diamond-Like Carbon Films: Applications to Optical Storage, in: Y. Tzeng, M. Yoshikawa, M. Murakawa, A. Feldman (Eds.), Materials Science Monographs, Elsevier1991, pp. 799-803.
[37] N. Boubiche, J.E. Hamouchi, J. Hulík, M. Abdesslam, C. Speisser, F. Djeffal, F.L. Normand, Kinetics of graphitization of thin diamond-like carbon (DLC) films catalyzed by transition metal, Diamond and Related Materials (2019).
[38] X. Liu, K. Natsume, S. Maegawa, F. Itoigawa, Improvement of crystallization in CVD diamond coating induced by femtosecond laser irradiation, Diamond and Related Materials 107 (2020) 107883.
[39] C.L. Andrea, K. Miroslav, Theory and simulation of crystal growth, Journal of Physics: Condensed Matter **9**(2) (1997) 299.
[40] I.V. Markov, Crystal Growth for Beginners, WORLD SCIENTIFIC2003.
[41] H.Q. Ta, D.J. Perello, D.L. Duong, G.H. Han, S. Gorantla, V.L. Nguyen, A. Bachmatiuk, S.V. Rotkin, Y.H. Lee, M.H. Rümmeli, Stranski–Krastanov and Volmer–Weber CVD Growth Regimes To Control the Stacking Order in Bilayer Graphene, Nano Letters 16(10) (2016) 6403-6410.
[42] K. Oura, M. Katayama, A.V. Zotov, V.G. Lifshits, A.A. Saranin, Growth of Thin Films, in: K. Oura, M. Katayama, A.V. Zotov, V.G. Lifshits, A.A. Saranin (Eds.), Surface Science: An Introduction, Springer Berlin Heidelberg, Berlin, Heidelberg, 2003, pp. 357-387.
[43] H. Wang, Z. Yao, G.S. Jung, Q. Song, M. Hempel, T. Palacios, G. Chen, M.J. Buehler, A. Aspuru-Guzik, J. Kong, Frank-van der Merwe growth in bilayer graphene, Matter 4(10) (2021) 3339-3353.
[44] R. Lukose, M. Lisker, F. Akhtar, M. Fraschke, T. Grabolla, A. Mai, M. Lukosius, Influence of plasma treatment on SiO2/Si and Si3N4/Si substrates for large-scale transfer of graphene, Scientific Reports 11(1) (2021) 13111.
[45] J.R. Ferraro, K. Nakamoto, C.W. Brown, Chapter 1 - Basic Theory, in: J.R. Ferraro, K. Nakamoto, C.W. Brown (Eds.), Introductory Raman Spectroscopy (Second Edition), Academic Press, San Diego, 2003, pp. 1-94.
[46] L.M. Malard, M.A. Pimenta, G. Dresselhaus, M.S. Dresselhaus, Raman spectroscopy in graphene, Physics Reports 473(5) (2009) 51-87.
[47] V. Zólyomi, J. Koltai, J. Kürti, Resonance Raman spectroscopy of graphite and graphene, physica status solidi (b) 248(11) (2011) 2435-2444.
[48] J.-B. Wu, M.-L. Lin, X. Cong, H.-N. Liu, P.-H. Tan, Raman spectroscopy of graphene-based materials and its applications in related devices, Chemical Society Reviews 47(5) (2018) 1822-1873.
[49] A.H. Castro Neto, F. Guinea, N.M.R. Peres, K.S. Novoselov, A.K. Geim, The electronic properties of graphene, Reviews of Modern Physics 81(1) (2009) 109-162.
[50] G. Cocco, E. Cadelano, L. Colombo, Gap opening in graphene by shear strain, Physical Review B 81(24) (2010) 241412.
[51] V. Yokaribas, S. Wagner, D.S. Schneider, P. Friebertshäuser, M.C. Lemme, C.-P. Fritzen, Strain Gauges Based on CVD Graphene Layers and Exfoliated Graphene Nanoplatelets with Enhanced Reproducibility and Scalability for Large Quantities, Sensors 17(12) (2017).

[52] A. Kaidarova, M.A. Khan, M. Marengo, L. Swanepoel, A. Przybysz, C. Muller, A. Fahlman, U. Buttner, N.R. Geraldi, R.P. Wilson, C.M. Duarte, J. Kosel, Wearable multifunctional printed graphene sensors, npj Flexible Electronics 3(1) (2019) 15.
[53] N. Kurra, Q. Jiang, P. Nayak, H.N. Alshareef, Laser-derived graphene: A three-dimensional printed graphene electrode and its emerging applications, Nano Today 24 (2019) 81-102.
[54] Y. Qiao, Y. Wang, H. Tian, M. Li, J. Jian, Y. Wei, Y. Tian, D.-Y. Wang, Y. Pang, X. Geng, X. Wang, Y. Zhao, H. Wang, N. Deng, M. Jian, Y. Zhang, R. Liang, Y. Yang, T.-L. Ren, Multilayer Graphene Epidermal Electronic Skin, ACS Nano 12(9) (2018) 8839-8846.
[55] L.-Q. Tao, D.-Y. Wang, H. Tian, Z.-Y. Ju, Y. Liu, Y. Pang, Y.-Q. Chen, Y. Yang, T.-L. Ren, Self-adapted and tunable graphene strain sensors for detecting both subtle and large human motions, Nanoscale 9(24) (2017) 8266-8273.
[56] A.F. Carvalho, A.J.S. Fernandes, C. Leitão, J. Deuermeier, A.C. Marques, R. Martins, E. Fortunato, F.M. Costa, Laser-Induced Graphene Strain Sensors Produced by Ultraviolet Irradiation of Polyimide, Advanced Functional Materials 28(52) (2018) 1805271.
[57] T. Han, A. Nag, R.B.V.B. Simorangkir, N. Afsarimanesh, H. Liu, S.C. Mukhopadhyay, Y. Xu, M. Zhadobov, R. Sauleau, Multifunctional Flexible Sensor Based on Laser-Induced Graphene, Sensors, 2019.
[58] B. Kulyk, B.F.R. Silva, A.F. Carvalho, S. Silvestre, A.J.S. Fernandes, R. Martins, E. Fortunato, F.M. Costa, Laser-Induced Graphene from Paper for Mechanical Sensing, ACS Applied Materials & Interfaces 13(8) (2021) 10210-10221.

4. Chapter 4: Materials and Methods

After discussing the laser carbonization process and LIG, possible methods to answer the research questions around improving the conductivity and sensitivity of LIG, will be discussed in this chapter. The laser instruments and plasma tool used for such methods will be described and instruments used for characterization of LIG are elucidated. Numerical modelling is done using COMSOL for CO_2 laser carbonization and graphitization, and the heat accumulation model for femtosecond laser carbonization is modelled in Python to estimate the laser parameters required to perform the experiments. The threshold powers of carbonization and graphitization using CO_2 laser are calculated experimentally and the irradiation temperatures are estimated for the calculated powers using the heat solver model in COMSOL. The model is validated by finding the estimated temperatures close to the values of threshold temperatures of carbonization and graphitization.

The CO_2 laser source is used for long-pulsed laser carbonization and the Yb:KYW laser source is used for femtosecond laser carbonization and ablation. The carbonized graphene crystallite size will be calculated by measuring the defect ratio (I_D/I_G) using Raman Spectroscopy, the carbonization and ablation depths in PI are measured using cross-sectional Scanning Electron Microscopy (SEM), and surface roughness is measured using the optical profilometer. Measurement of graphene crystallite size will be used to study the graphene growth kinetics for CO_2 laser carbonization using Arrhenius model. Argon cold plasma pre-treatment of PI is performed on PI before CO_2 laser carbonization to study the effects of surface wettability on the conductivity of carbonized tracks. The fs laser carbonization and ablation process parameter space will be defined, and the carbonization will be related to heat accumulation. Ablation and carbonization will be used to prepare Kirigami inspired strain sensor where a 2D printed sensor is folded conformally into 3D shapes and the structural mechanics of such sensor will be studied using COMSOL. Sensor DAQ was performed using Phidget Wheatstone Bridge interface which consists of in-build op-amp circuit for sensor signal amplification. The materials and methods used in this thesis project are summarized in Table 4.1. This chapter is written 100% by the author Ratul Kumar Biswas.

Table 4.1. Summary of Materials and methods.

Papers	**Materials**	**Method**	**Parameters**	**Thesis Objective**	**Outcome**

Paper 1 [1]	Polyimide	CO_2 laser. Characterization: Raman, SEM, IV	*f*= 0.1 kHz, *P*= 0.15-0.65 W, *v*= 120 mm/min.	Improving conductivity by laser graphitization.	Improved conductivity by ~2.6 times.
Paper 2 [2]	Polyimide	CO_2 laser. Characterization: Raman, SEM, IV	*f*= 0.1 kHz, *P*= 0.55-1.12 W, *v*= 350-750 mm/min.	Studying Arrhenius kinetics of laser carbonization.	Estimated activation energy of laser carbonization to be 0.2 eV.
Paper 3 [3]	Polyimide	CO_2 laser, Argon Plasma-pen. Characterization: Raman, SEM, Profilometer, IV	*f*= 0.1 kHz, *P*= 0.55-1.12 W, *v*= 450 mm/min, plasma scan speed= 200-1000 mm/min.	Improving conductivity by plasma activation of PI surface.	Improved conductivity by ~51%.
Paper 4 [4]	Polyimide	Yb: KYW femtosecond laser, 1030 nm. Characterization: Raman, SEM, IV	Process Condition 1 (For carbonization): 0.242-0.281 W, *v*= 2-3 mm/s, *f*= 200 kHz. Process Condition 2	Comparative study of laser carbonization and ablation and application in strain sensor.	Calculated threshold and incubation coefficient values and patterned a Kirigami-inspired strain sensor to demonstrate ~3 times better

			(For Ablation): 1.726-2.512 W, *v*= 200-300 mm/s, *f*= 200 kHz.		sensitivity than planar sensor.

4.1. Numerical Simulation

Numerical simulation is done for estimation of laser parameters required for laser carbonization. COMSOL Multiphysics ® software is used for numerical simulation of CO_2 laser-materials interaction by Finite Element Method (FEM). The thermal response of Polyimide and ta-C to a Gaussian CO_2 laser pulse was modelled in two-dimension (2D). Python is used to solve numerically the temporal evolution of temperature for femtosecond laser irradiation at threshold powers at scan speeds ranging from 2 to 3 mm/s.

4.1.1. Modelling of thermal interaction of CO_2 laser beam

The COMSOL module named "Heat Transfer in Solids" was used to model the thermal response to a Gaussian laser pulse. The laser parameters were fed into the COMSOL software. A sample size of 10 mm x 127 µm was used as the 2D geometry. The heat equation was solved using a time dependent solver from 0-5 ms with an interval of 20 µs. The temperature independent properties were taken from the in-build materials library. The laser parameters, variables, PI properties and ta-C properties used in COMSOL are tabulated in Tables 4.2, 4.3, 4.4 and 4.5 respectively.

Table 4.2. Laser parameters in COMSOL.

Name	Expression	Value	Description
ϖ_0	201 µm	2.01 E-4 m	Spot diameter

alpha	4 x 3.14 x k/*lambda*	35547 1/m	Absorption coefficient
t_p	100 µs	1E-4 s	Pulse width
t_c	2**tp*	2E-4 s	Reference time
Lambda	10.6 um	1.06E-5 m	Wavelength
P	0.15 W	0.15 W	Laser power
F	0.1 kHz	100 Hz	Frequency
R_e	$[(1-n)^2+\kappa^2]/[(1+n)^2+\kappa^2]$	0.07499	Reflectivity
N	1.75	1.75	Refractive index
κ	0.03	0.03	Extinction coefficient
v	120 mm/min	0.002 m/s	Scan speed
OF	$1-(v/(2 \times f \times \omega_0))$	0.095022	Overlapping Factor
P_{eff}	$P \times (1+OF)$	0.29253 W	Effective power

Table 4.3. Laser variables in COMSOL.

Name	Expression	Unit	Description
I	$Q(x,y) = 2\,F_{eff} \cdot \left[\frac{\alpha(\lambda)}{\sqrt{(\pi/\ln 2)\tau_p}}\right].(1 - R).\left[exp\left\{-2\left(\frac{x}{\omega_0}\right)^2 - 4\ln 2\left(\frac{t-t_c}{t_P}\right)^2\right\}\right] exp(\alpha(\lambda)y)$	W/m^2	Gaussian Laser pulse equation
F_{eff}	$F_{eff} = \frac{2P_{eff}}{f\pi\omega_0^2}$	J/m^2	Effective fluence

Table 4.4. Polyimide properties in COMSOL used for carbonization study.

Properties	Variable	Value	Unit
Thermal conductivity	*K*	$0.213 + 3.416 \times 10^{-5}T \quad \forall\, 200K < T < 729K$ $-1.314 + 2.13 \times 10^{-3}T \quad \forall\, 729K < T < 1500K$ [5]	W/m. K

Heat capacity	C_p	$1000[\,0.96 + 1.39\left(\frac{T-300}{400}\right) - 0.43\left(\frac{T-300}{400}\right)^2\,]$ $\forall 200K < T < 1500K$ [5]	J/kg.K
Density	ρ	*1300*	kg/m^3

Table 4.5. ta-C properties in COMSOL used for graphitization study.

Properties	Variable	Value	Unit
Thermal conductivity	*K*	0.69 W/mK [6]	W/m.K
Heat capacity	C_p	790 J/kg-K [7]	J/kg.K
Density	ρ	2335 [8]	kg/m^3

Temperature dependent *n*, *k* and *K* values were defined using the Piecewise function in COMSOL (Fig. 4.1 a, b, c). Temperature dependent C_p value was defined using the Analytic function in COMSOL (Fig. 4.1 d). Thermal simulation was studied using the Heat transfer in solids in 2 dimensions. Geometry of width 10000 µm and height 127 µm was defined (Fig. 4.2 a) and the point of study and line of study (Fig. 4.2.b,c) were defined using Cut point and cut line (Fig. 4.2 d). Meshes were selected as finer meshes from Physics controlled mesh to solve the heat equation and obtain the temperature distribution in Polyimide. The tables 4.2-4.5 are explained in Chapter 5 and used for solving the equation 2.1 to measure the temperature of PI due to CO_2 laser irradiation.

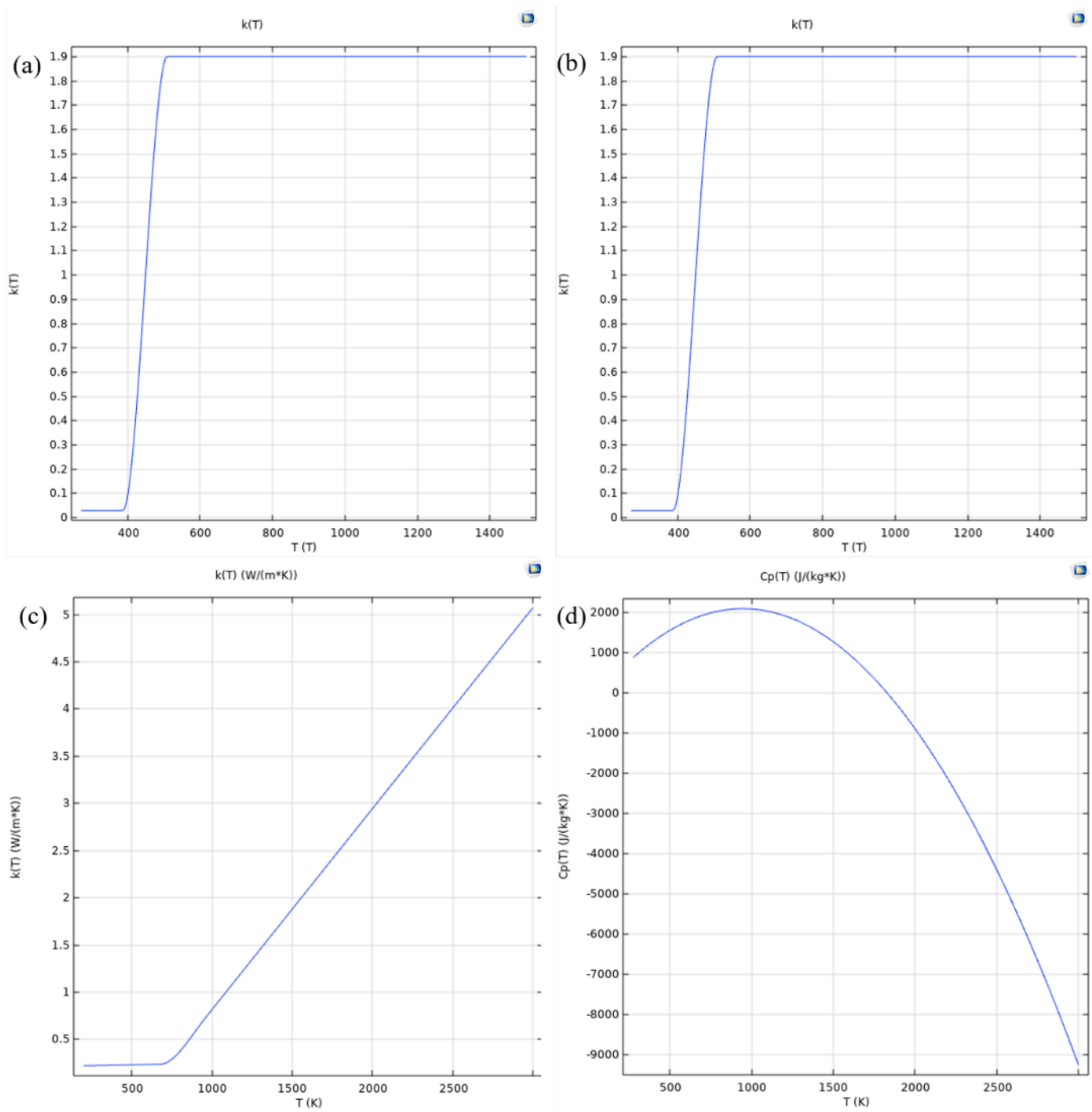

Fig. 4.1. (a) *k* vs *T*, (b) *n* vs *T* , (c) *K* vs *T* , (d) C_P vs *T* of Polyimide plotted in COMSOL.

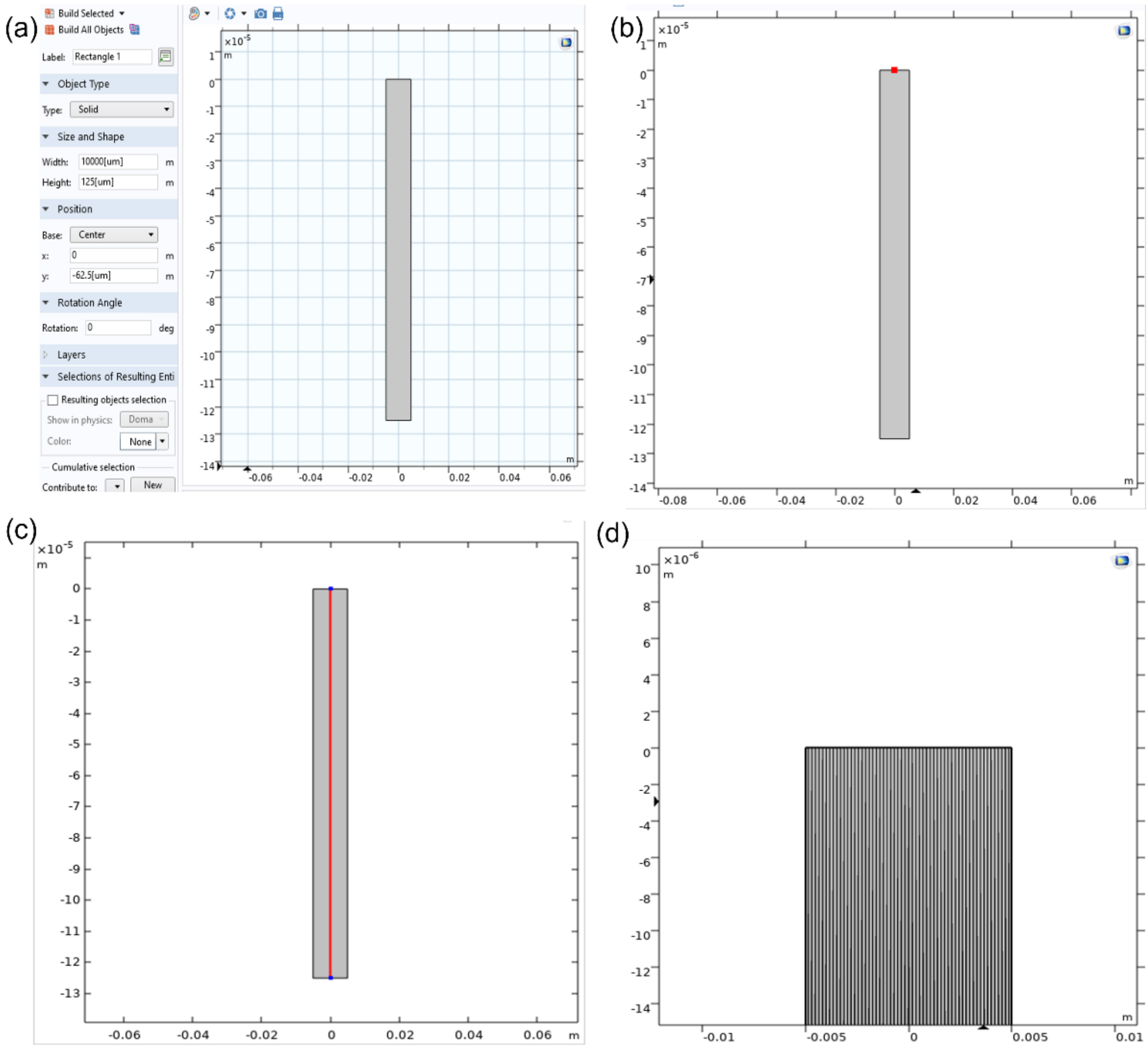

Fig. 4.2. (a) Geometry for thermal simulation in COMSOL, (b) Cut point and (c) cut line for temperature analysis, and (d) Physics controlled mesh in COMSOL.

The study was performed within a time range of 0 to 500 x 10^{-5} seconds at an interval of 2 x 10^{-5} seconds.

From the COMSOL study, it was found that at scan speed of 120 mm/min, the threshold laser power for thermal degradation and graphitization are 0.15 W and 0.21 W respectively at repetition rate of 0.1 kHz (Fig. 4.3) to reach the thermal degradation temperature at 673 K and graphitization temperature at 773K.

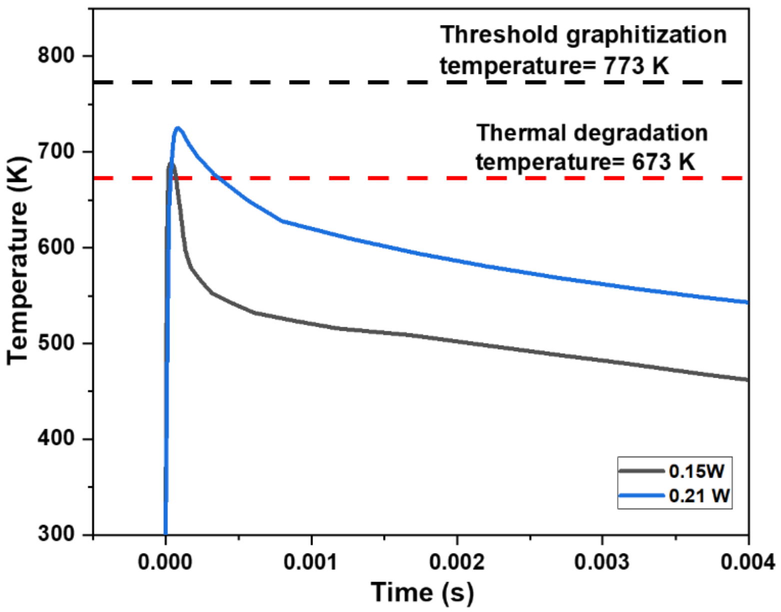

Fig. 4.3. Temperature evolution at 0.15 W and 0.21 W for carbonization and graphitization respectively.

4.1.2. Modelling of Thermal Interaction of femtosecond Laser Beam

The carbonization of PI by femtosecond laser is theorized to occur by heat accumulation methods where the fraction of heat from each laser pulse accumulates over the number of pulses per laser spot to generate sufficient heat required for carbonization [4]. Such carbonization is different process from the CO_2 laser since in this case, each femtosecond laser pulse is unable to create any carbonization. Hence, a different mathematical approach is needed to model this process. The heat accumulation process is modelled using the equation [4]:

$$\Delta T = \frac{8\,\eta_{abs}\,\eta_{Heat}(v)E_p\sqrt{f}}{\pi d_s^2}.\frac{1}{\rho C_p\sqrt{4\pi D_T}}.(2\sqrt{ft}\ \text{-}1.46) \qquad 4.1$$

Where the parameters are explained in Table 4.6. Equation 4.1. was solved using Pyhton programme using the syntax code in Appendix A. From the modelling it was found that the laser powers of 0.2-0.3 W at scan speed of 2-3 mm/s and repetition rate of 200 kHz should produce sufficient temperature required for carbonization (900 K) as shown in Fig. 4.4. Beam parameters will be further discussed in section 4.3.

Table 4.6. Summary of parameters for the Heat Accumulation Model.

Parameters	Equations	Values
α (Absorption coefficient)	$\alpha = 4\pi\kappa/\lambda$	
η_{abs}(Absorption Quota)	$\eta_{abs} = 1 - exp(-\alpha.d_m)$	
d_m (PI film thickness)		125 µm
κ (extinction coefficient)		10^{-4} [9]
λ (Laser wavelength)		1030 nm
ω_0 (spot radius)		22 µm
ρ (PI density)		1420 $kg.m^{-3}$
C_p (specific heat)		1.09 $kJ.kg^{-1}.K^{-1}$
Υ(overlapping factor)	$\Upsilon = 1 - v/2\omega_0 f$	
f (repetition rate)		200 kHz
K (thermal conductivity)		0.12 $W.m^{-1}.K^{-1}$
D_T (thermal diffusivity)	$D_T = K/\rho Cp$	
σ	Geometry dependent factor (1D -heat flow)[10]	2
C_1	Geometry dependent factor (1D- heat flow)[10]	-1.46

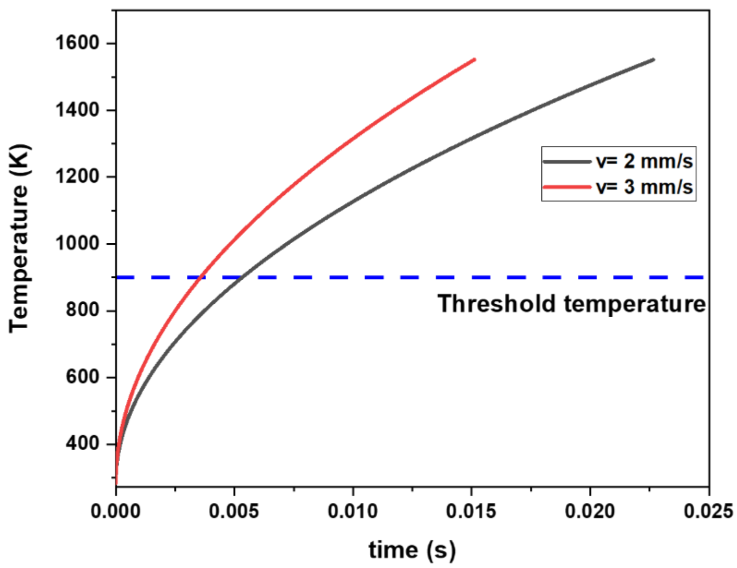

Fig. 4.4. Temperature evolution by laser power 0.2 W and 0.3 W at scan speed 3 mm/s and 2 mm/s respectively.

4.2. CO_2 Laser

4.2.1.Active Medium

CO_2 laser was invented in the year 1964 by Kumar Patel in the Bell Labs, USA. The active medium in CO_2 laser consists of a mixture of 3 gases [11], CO_2, N_2, and He in the molecular ratio CO_2:N_2:He = 1:22:5 [12]. When the active medium is energized using arc discharge, the N_2 molecule is excited to a higher vibrational energy level. Elastic collision occurs between N_2 and CO_2 molecules causing the exchange of energy between them which results into two types of transitions between vibrational levels (Fig. 4.5): 1. Asymmetric stretch (001) to symmetric stretch (100) causing laser at wavelength 10.6 μm, and 2. Asymmetric stretch (001) to Bending (020) causing laser at wavelength 9.6 μm. To maintain the population inversion, the ground level (000) of CO_2 molecule must be depopulated, which is done by removing the energy from CO_2 molecule by collision with the He molecule.

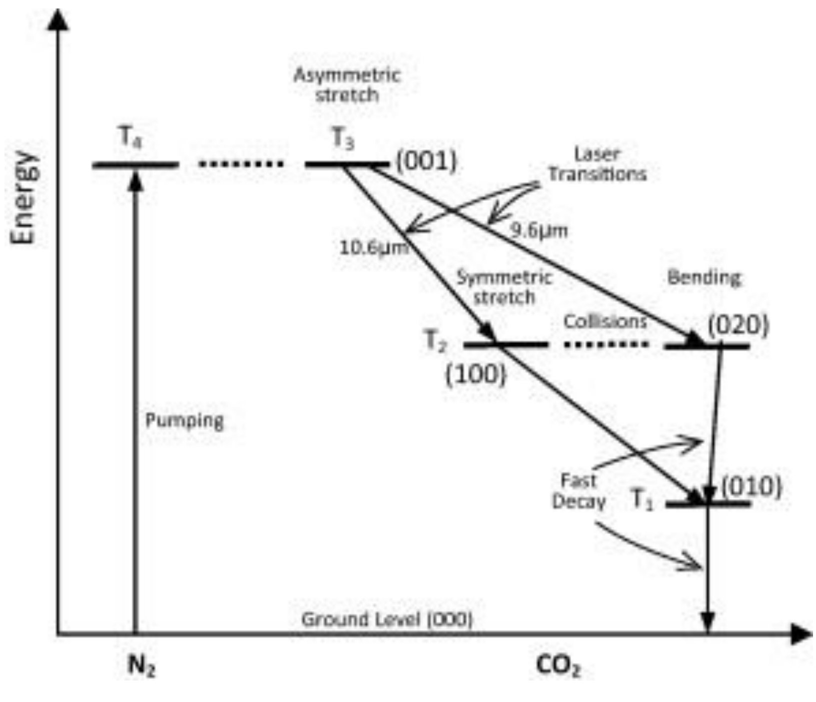

Fig. 4.5. Band diagram of the active medium in CO_2 laser [12].

4.2.2.Beam Delivery System

A GEM 6O Coherent DEOS CO_2 Laser system equipped with DEI PDG-2510 Digital Pulse Generator was used for CO_2 laser system. The CO_2 laser resonator consists of two mirrors, one perfectly reflective and one partially reflective which is the output coupler (OC) in a sealed chamber with gas inlets and outlets (Fig. 4.6). An AC/DC power supply is used for arc discharge of the gas. The active medium is enclosed between the mirrors, the light generated within the gain medium, reflects to and fro creating further excitations until population inversion is achieved and the laser ejects out of the OC. The continuous wave (CW) CO_2 laser is then passed through a filter which blocks any backscattered beam from reaching the source. The light then passes through a polarizer to convert the linearly polarized beam to circular polarized beam which is then reflected by a mirror to a focussing lens of focal length 100 mm. The CW wave is modulated using the pulse modulator (Fig. 4.7). The laser spot-size is 200.90 um and beam quality M^2=1.3. The laser is scanned at laser power 0.15-0.65 W and scan speed 120 mm/min for carbonization and graphitization study with parameters informed by the COMSOL model estimation in Chapter 5 and at laser power 0.65-1.12 W for growth kinetics study in Chapter 6, both at repetition rate 0.1 kHz.

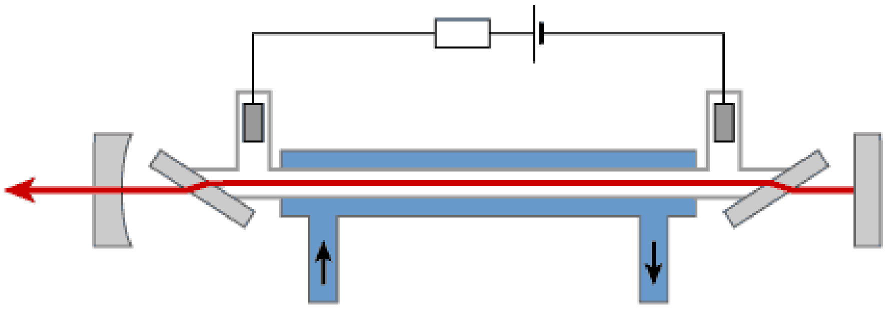

Fig. 4.6. Schematic diagram of sealed-tube CO_2 laser [13].

PI film (Dupont Kapton ® HN) of thickness 127 μm and dimension 15 mm x 10 mm cleaned with ethanol and deionized (DI) water was placed at 100 mm from the focussing lens and Advanced Laser Software and Unidex 500 program were used to write LIG patterns on PI.

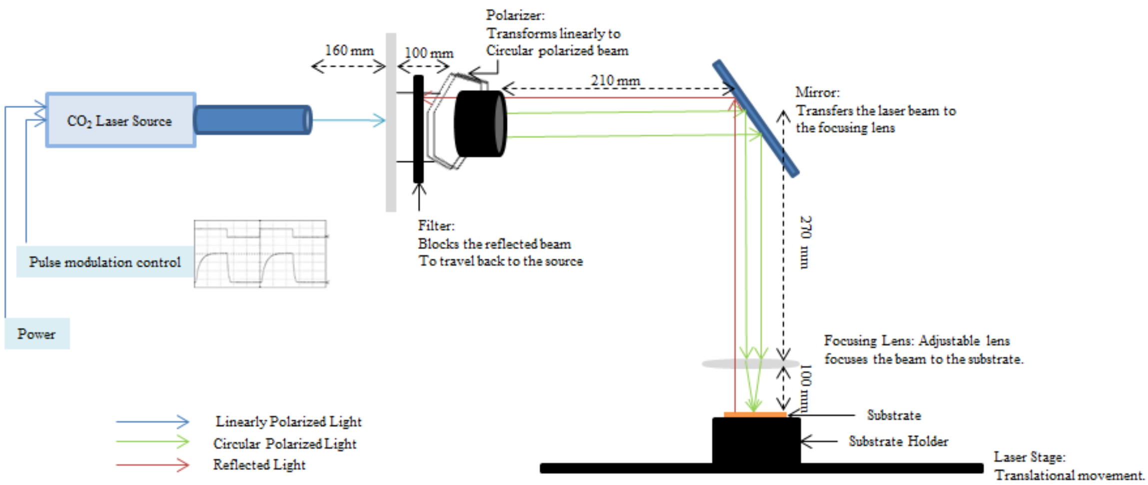

Fig. 4.7. Schematic of beam path arrangement of CO_2 laser.

4.3. Yb:KYW Femtosecond laser

An Amplitude Systems SPulse HP laser system was used in the experiments. The laser head consists of a pumping medium and a mode-locked oscillator, followed by optics for pulse stretching, then pulse amplification, pulse compression and finally pulse modulation by a pulse picker. The active medium is ytterbium doped crystalline material (Yb:KYW crystal). Irradiation of the active medium by a diode laser takes place inside a Fabry–Perot cavity. The mode locked laser oscillator head emits a weakly powered pulse (≈ 20 nJ), 250 femtosecond pulses, with a repetition rate of 30 MHz, at a wavelength of 1030 nm. Chirped pulse amplification technique is used or amplification of mode locked ultra-short pulses by using a pair of reflective diffraction gratings. At first, the femtosecond laser pulse was stretched temporally reducing the laser pulse intensity and peak power. An electro-optic shutter which is a Pockel cell in our case is used for pulse-amplification in the resonator and once the amplified energy reaches a maximum value, it was extracted through the resonator using a Faraday rotator. This modulator is an acousto-optic device that controls frequency of a laser by generating an acousto-optic effect in the Amplitude systems. It consists of a transparent crystal attached with a piezoelectric transducer ($LiNbO_3$). The stretched, high-intensity laser pulse is then compressed, using a pair of diffractive gratings, using the reverse process to the pulse stretching gratings.

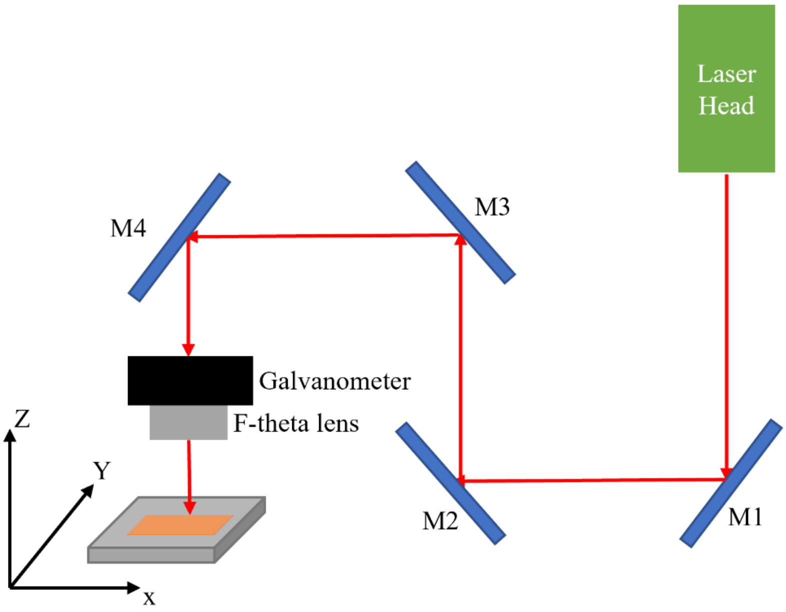

Fig. 4.8. Beam Path of Yb:KYW femtosecond laser.

Fig. 4.8. shows the beam path in this work, where the laser source having wavelength 1030 nm is sent to the PI substrate on an XYZ stage using 4 mirrors M1, M2, M3 and M4 and a Galvoscanner with F-theta lens is used to scan the laser beam across the substrate.

The final pulse duration of the compressed and amplified pulse is ~500 fs and repetition rate 0.001 to 300 kHz. The output laser from the laser head is then directed onto four mirrors M1, M2, M3 and M4 and then transmitted through a Galvanometer having an F-theta lens to scan the laser beam onto the substrate placed at 100 mm below the galvo-lens (Fig. 4.8). The F-theta lens has a numerical aperature (NA) of 0.014, creating the beam with spot-size 22.6 μm. The laser is used for purposes such as thin film crystallization, ablation, and microfabrication of polymers at the NCLA [14-16]. The operational parameters are average power, scan speed and repetition rate. In this study, the femtosecond laser centered at 1030 nm wavelength is used for modification of PI and is performed at two process conditions (PC's): PC1 at low power ranging from 0.24 W to 0.28 W and scan speed 2-3 mm/s and PC2 at high power ranging from 1.73 W to 2.51 W and scan speed 200-300 mm/s, both at repetition rate of 200 kHz. PC1 was used for carbonization with parameters as estimated from the numerical modelling in Python and PC2 was used for ablation. The 1030 nm wavelength was used since 1030 nm is an IR wavelength, we can achieve carbonization at low laser intensity by linear absorption and ablation at high laser intensity by multiphoton absorption. The sensor designs are then printed using the Direct Machine Control (DMC) software. The process condition is further discussed in Chapter 7.

4.4. Cold Plasma Tool

After discussing the plasma treatment of substrate as a possible method of improving the conductivity of LIG in Chapter 3, the tool used for the plasma treatment will be further discussed. Cold plasma pen is a tool used for surface activation of samples without heating it. Cold plasma is a partially ionised gas consisting of ions, electrons and neutral particles which operates at lower temperature. It is produced by ionizing a flowing noble gas at higher alternating voltage at high frequency as 1 kHz and input power of 20 W [17]. The advantage of this plasma is that it is available in pen and can be used as a tool-head to pre-process the substrate while printing. The cold plasma does not alter the roughness and optical properties of the substrate and hence is non-invasive. Cold plasma was first discovered by John R. Hollahan's group in the year 1969 where plasma containing amino group (-NH_2) was produced using nitrogen and hydrogen gas and was used for surface treatment of polymers to make them bio-compatible. In the cold plasma, the temperature of the ionized species is close to the room temperature (25-100 ^{0}C) while the electronic temperature is much higher (5000-1000 ^{0}C) and is generated using direct current, radio frequency, microwave or pulsed discharge systems (Fig. 4.9) [18]. Such plasma treatment of surfaces is used to enhance the hydrophilicity of the surfaces, in-situ treatment of skin, teeth and chronic wounds. In this thesis, the neoplas kINPen MED plasma tool was used for the cold plasma scan at Ar gas flow rate of 5 slm with an effective diameter of 1 mm on PI film (Dupont Kapton HN) with dimensions of 20 mm x 20 mm at varying scan speeds between 200-1000 mm/min with a hatch spacing of 0.25 mm placed at 2 mm below the tip of the plasma tool. The work is further discussed in Chapter 6.

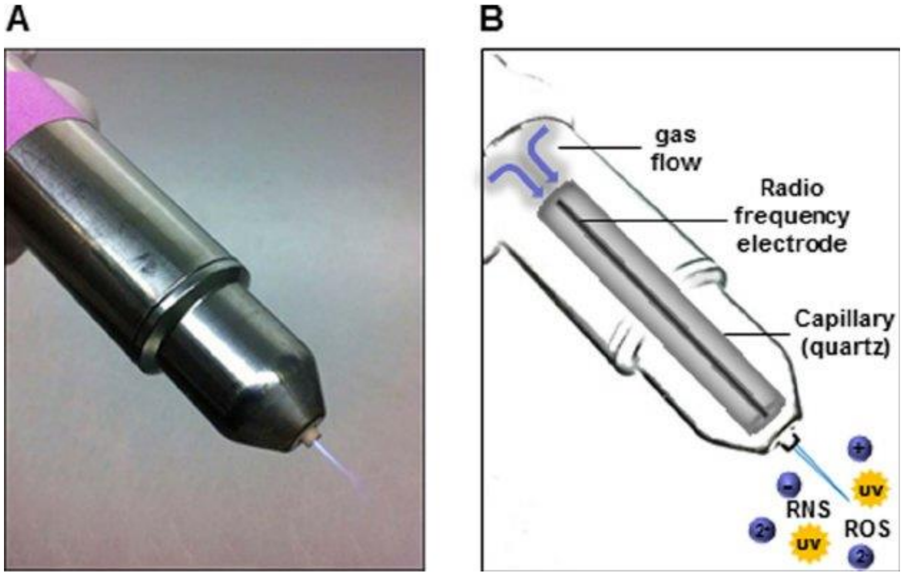

Fig 4.9. (A) Plasma jet kINPen09 (Neoplas GmbH, Greifswald, Germany), (B) schematic diagram of kINPen09 [19].

4.5. Polyimide

4.5.1.Background

In this project, Kapton HN supplied by Dupont of thickness 125 um was used for carbonization and ablation study whose properties are tabulated in table 4.7. Kapton HN was chosen due to its exceptional thermal and chemical stability upto 673 K, insulating properties and its applications in microelectronics, medical and aerospace. P. Scully research group used the same material for the laser carbonization study [20] and this thesis will provide further evidences for the laser carbonization process. Aromatic polyimide was first synthesized in 1908 by Marston Bogert and since 1960s, high molecular weight PI's were synthesized commercially by Dupont[21, 22]. The polymer backbone consists of the imide group (R_1-C=O-NR_2-C=O-R_1) formed due to the polycondensation reaction between diamines (NH_2-R_2-NH_2) and dianhydrides (OOC-R_1-COO) (Fig. 4.10).

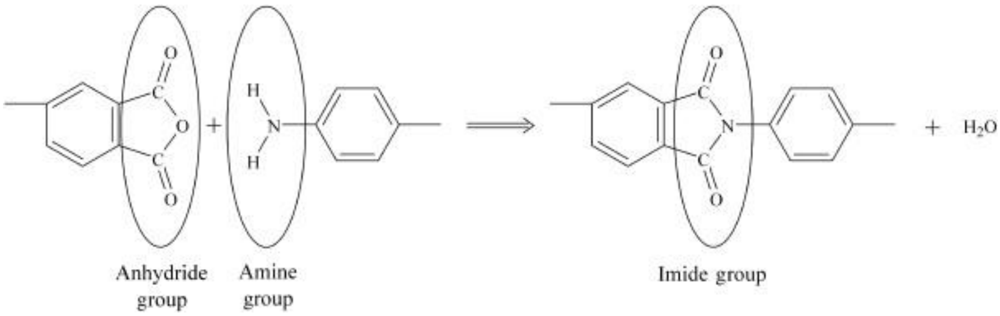

Fig. 4.10. Imide group formation [23].

4.5.2.Types of PI:

Based on the monomeric units, PI's can be classified into three categories (Fig. 4.11):

a. **Aromatic PI's:** These are derived from aromatic diamine and aromatic dianhydride. Fully aromatic PI's have strong interchain interactions causing poor solubility and non-melting properties [23]. Kapton HN is an example of aromatic PI.
b. **Semi-aromatic PI's:** These are derived when one of the monomer units are non-aromatic, i.e., anyone of the diamine or dianhydride is aromatic and the other is aliphatic [24].
c. **Aliphatic PI's:** These are derived when both monomer units are aliphatic.

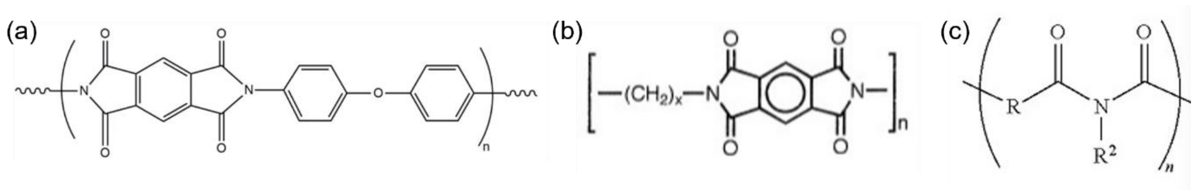

Fig. 4.11. Classification of Polyimides.

4.5.3.Synthesis of PI:

PI's are made by polycondensation reaction which involves two steps (Fig. 4.12):

a. Polycondensation of diamine and dianhydride.
b. Cyclodehydration of poly(amic acid) to form Polyimide.

However, this process lacks the processability due to high softening temperature and low solubility nature of the monomers. Hence, a soluble poly(amic acid) is used as a precursor to make PI by casting films and thermal dehydration [21].

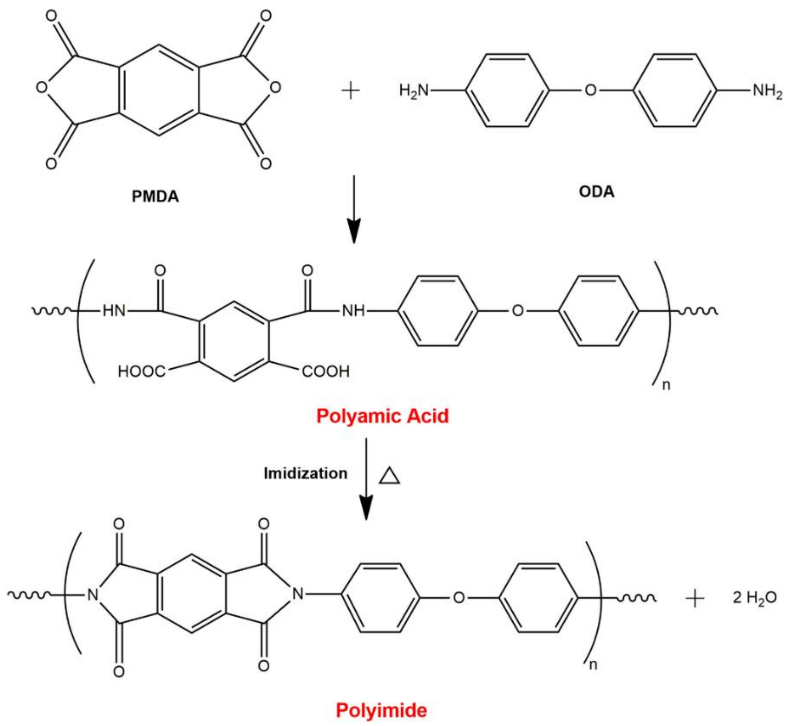

Fig. 4.12. Synthesis mechanism of aromatic polyimide [25].

4.5.4.Properties

The high temperature stability, resistant to solvents and high mechanical strength of aromatic PI's arise from the rigid chains and interchain interactions in the polymer backbone. The strong electron acceptor nature of imides and the electron donor nature of amines lead to strong interchain and intrachain charge transfer complex (CTC) formation and electronic polarization which creates close stacking of the aromatic segments and lower mobility of the polymer backbone making the polymer stiffer. Such CTC formation leads to brownish nature of the colour of the aromatic PI. The properties of Kapton HN are discussed in Table 4.7.

Table 4.7. Properties of Dupont Kapton HN of thickness 125 µm at 23^{0}C [26].

Property	**Value**	**Unit**
Elastic Modulus	2.76	GPa
Density	1.42	g/cc
Poisson's Ratio	0.34	
Refractive Index	1.70	

Coefficient of Thermal Conductivity	0.12	W/m.K
Specific Heat	1.09	J/g.K
Dielectric constant	3.5	
Volume resistivity	1.0×10^{17}	Ω.cm
Glass Transition Temperature[21]	315-340	^{0}C

4.6. Sensor Demonstration Study

4.6.1. Kirigami design

Since one of the research aims is to improve the sensitivity of LIG, substrate restructuring using Kirigami design is a unique method to do this which can be done by utilizing the carbonization and ablation properties of the femtosecond laser. Kirigami is a Japanese art to transform a two-dimensional paper into three dimensional structures by proper choice of cut dimensions and angles. Such designs have unusual properties such as negative Poisson's ratio as found in auxetic materials and morph into open structures and have been used in many applications such as design of airbags, soft-robotic grippers, reprogrammable materials [27, 28]. Any 3D shape can be reprogrammed into 2D tessellated structures using the inverse problem (Fig. 4.13) [28]. Such inverse problem was solved by Gary et al using MATLAB and can be used to create Kirigami planar cut pattern for any 3D deformable shape. Kirigami designs provide excellent design strategy for wearable sensor and soft-robotic applications given its conformal nature [29].

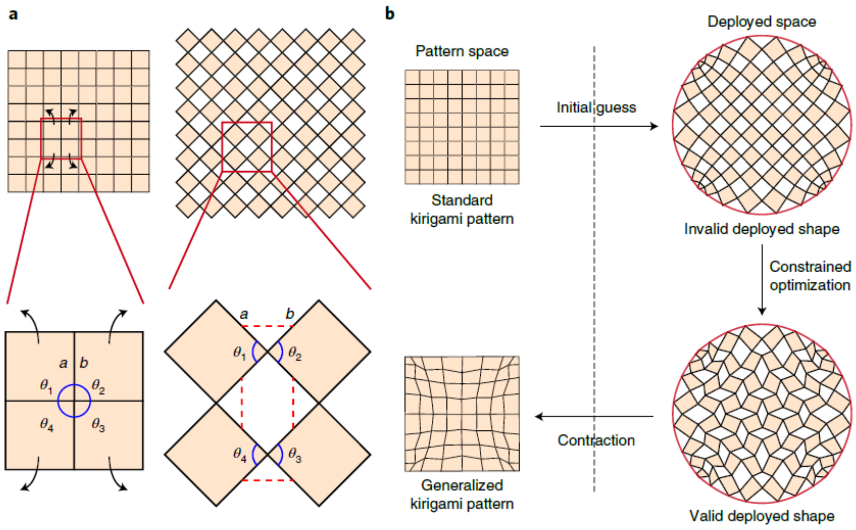

Fig. 4.13. Inverse problem for generation of Kirigami design [28].

In this work, a concentric circular Kirigami-inspired sensor was designed in AUTOCAD. The design was prepared in two steps. At first, the LIG pattern was designed (Fig. 4.14a) with an outermost radius of 24.75 mm and inner-spacing of 1.5 mm. Then, the cut-pattern was designed (Fig. 4.14b) with an outermost radius of 51 mm and inner-spacing of 1.5 mm. After that, both of the deigns were uploaded in the Direct Machine Control (DMC) software to prepare the Kirigami sensor using two different laser parameters and fitted together as shown in Fig. 4.15.

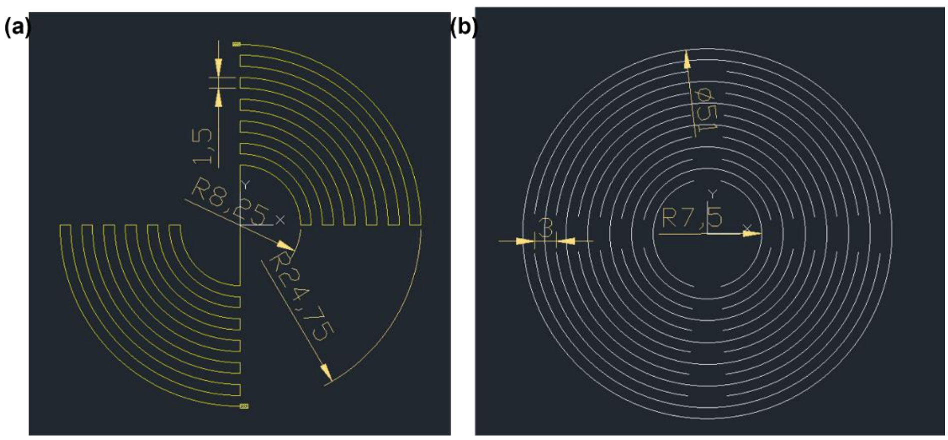

Fig. 4.14. (a) LIG sensor pattern inscribed inside (b) Kirigami pattern designed in AUTOCAD.

The sensor was prepared using two process conditions of femtosecond laser. The piezoresistive LIG was fabricated using laser carbonization at laser power 0.242±0.001 W, scan speed 2 mm/s, repetition rate 200 kHz, single pass, and the Kirigami patterns were cut using laser ablation at power 2.524 W, scan speed 300 mm/s, repetition rate 200 kHz and 100 passes. The

LIG was encapsulated with a scotch tape to prevent any spallation to occur and silver contacts encapsulated with epoxy resin were used to create connection of the sensor to the Wheatstone Bridge and Phidget Wheatstone Bridge sensor interface for DAQ (Fig. 4.16 b). The resistance of the sensor was measured using the source meter unit (Keysight B2900A). A planar sensor was also prepared without any Kirirgami cuts to compare the sensor performance with the Kirirgami sensor. Structutral mechanical study of the sensor in COMSOL showed that upon loading on the sensor with weights (0-700 mg), stresses get accumulated around the Kirigami cuts (shown in the section 4.6.2) which causes strain in the LIG and the LIG being piezoresistive shows changes in the voltage output from the DAQ device. The *GF* was calculated by measuring the voltage change versus strain measured from COMSOL for each loading weights placed at the centre. Kirigami cuts showed better response to loads as compared to the planar sensor since the stresses formed in the Kirigami sensor was in the order of ~10^7 N/m^2 as compared to ~10^5 N/m^2 in the planar sensor. The *GF* of a single LIG track of length 30 mm drawn using the femtosecond laser at power 0.242 W, scan speed 2 mm/s, repetition rate 200 kHz, printed on ASTM D638 Dog-Bone PI, was measured by a stress-strain curve measurement using a motorized force tester system (MARK-10 ESM303) and resistance measurement using the source meter unit (Keysight B2900A) at the same sampling rate. The *GF* was found to be 96.97±3.17 which is close to the *GF* calculated from the COMSOL study of the Kirigami sensor. Similar experiment was performed for LIG drawn using CO_2 laser at power 0.65 W, scan speed 2 mm/s, repetition rate 0.10 kHz. The *GF* was found to be 21.67±0.05. The sensor performance is further explained in the Chapter 7.

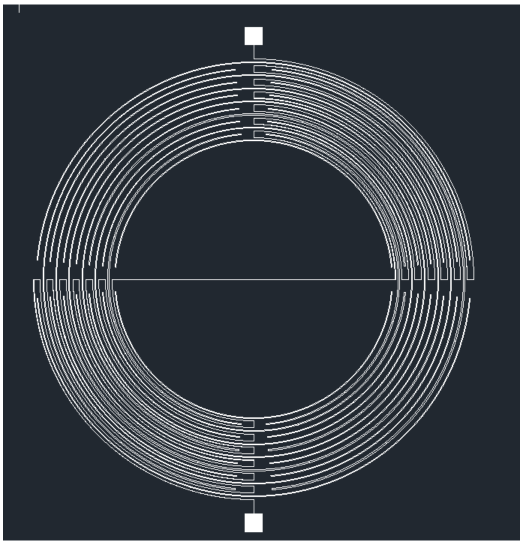

Fig. 4.15. Overall design of the Kirigami-inspired sensor designed in AUTOCAD.

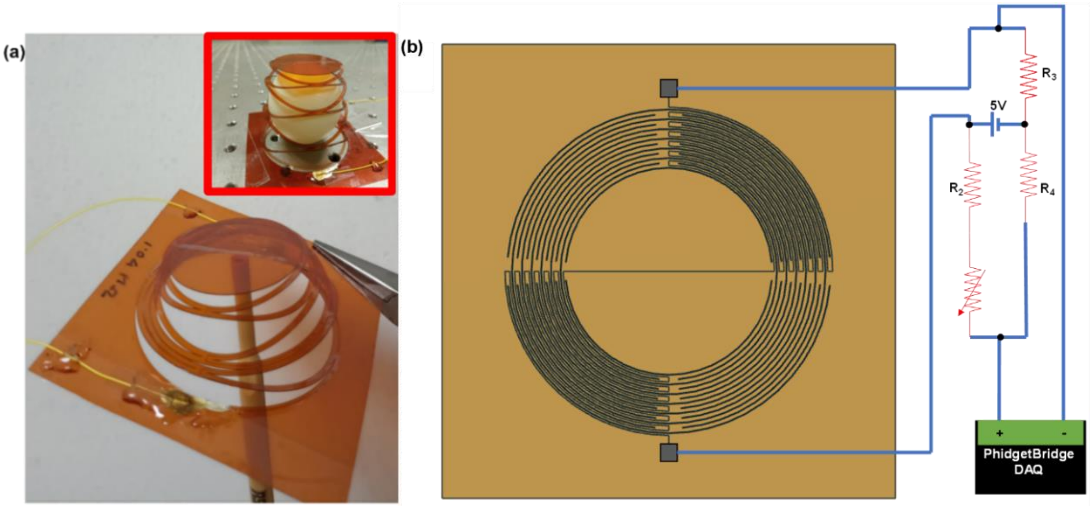

Fig. 4.16. (a) Kirigami-inspired strain sensor, (b) Kirigami sensor connected to Wheatstone Bridge and PhidgetBridge DAQ, R_2, R_3 and R_4 used in this application are of 1 MΩ each and potentiometer was used in series with R_2 to balance the bridge.

4.6.2.Structural mechanics of the Kirigami sensor

The structural simulation of the Kirigami-inspired Polyimide sensor was performed using COMSOL software using the Solid Mechanics module. The geometry was prepared on AUTOCAD which is later imported into COMSOL geometry (Fig. 4.17) and meshed (Fig. 4.18) for solving the stress distribution and vertical displacement for a given load at the centre of the design. The centre of the design was selected as the cut point for the simulation. A stationary study was performed using the module (Fig. 4.19 a). Elastic modulus was taken from the experimentally calculated of the LIG-PI composite for the elastic region. The rest of the materials properties were chosen from the materials library (Fig. 4.19 c). Such estimation of stress and strain values from COMSOL will enable estimation of the sensor response upon loading.

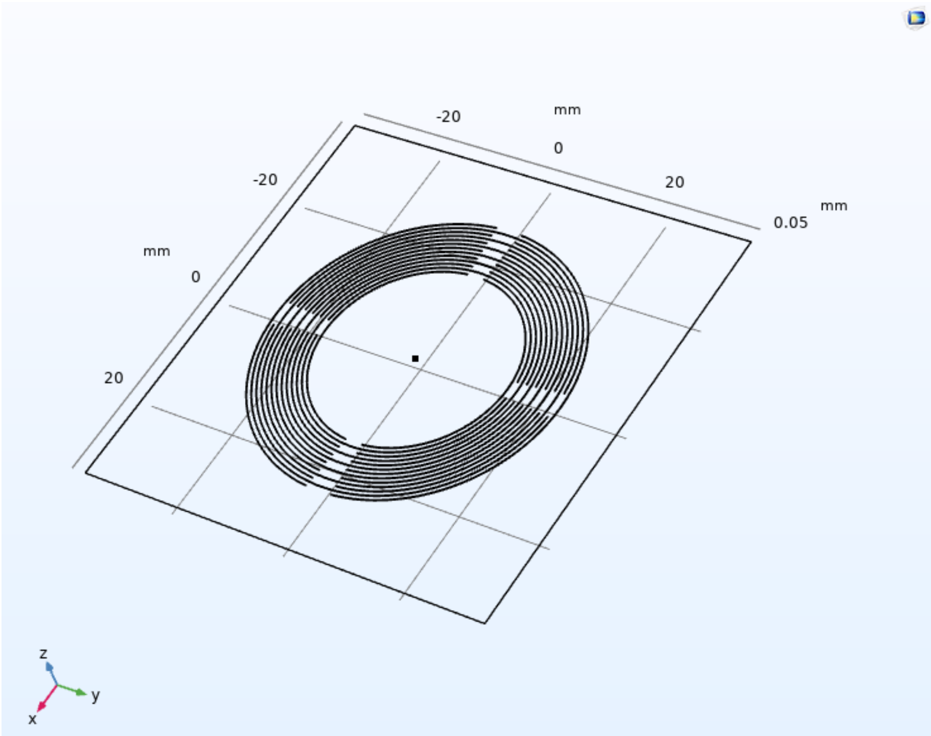

Fig. 4.17. Geometry of Kirigami design in COMSOL.

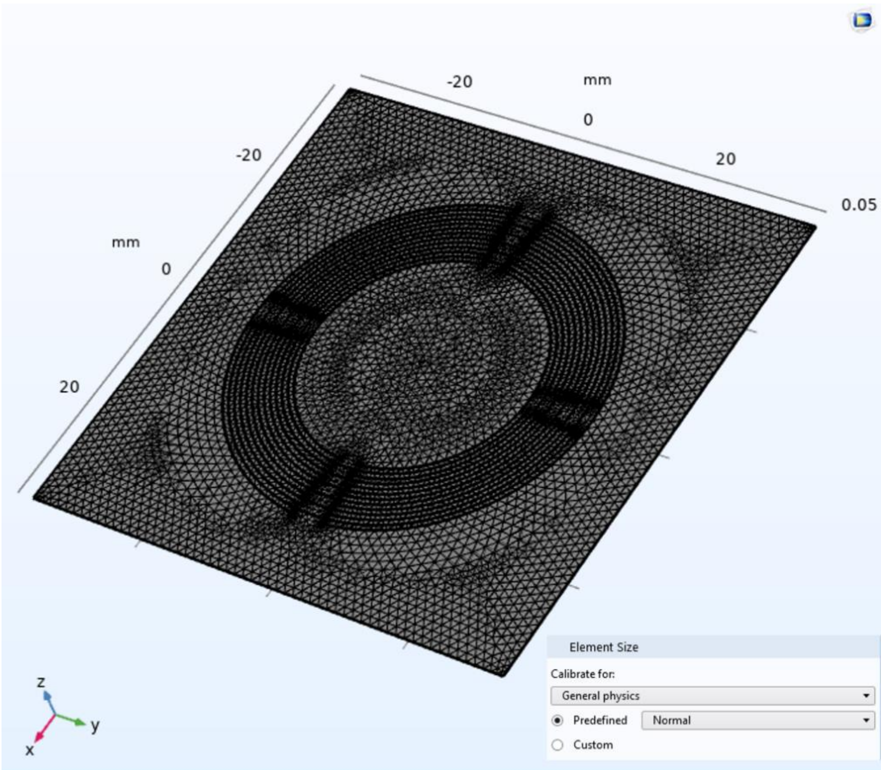

Fig. 4.18. Meshing of the geometry.

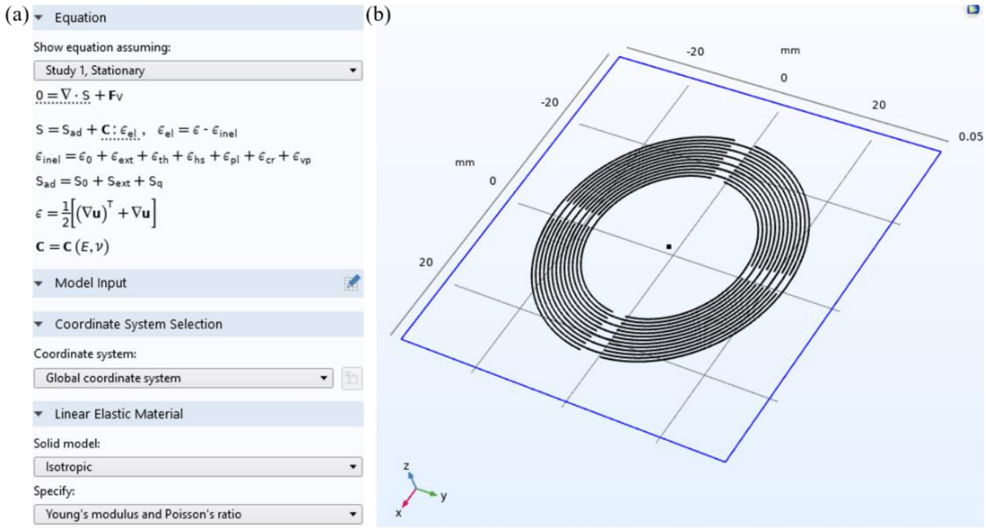

(c) Material Contents

	Property	Variable	Value	Unit	Property group
☑	Density	rho	1420[kg/m^3]	kg/m³	Basic
☑	Young's modulus	E	7.154e9[Pa]	Pa	Young's modulus and Poisson's ratio
☑	Poisson's ratio	nu	0.34	1	Young's modulus and Poisson's ratio
	Heat capacity at constant pressure	Cp	1100[J/(kg*K)]	J/(kg·K)	Basic
	Thermal conductivity	k_iso ; kii...	0.15[W/(m*...	W/(m·K)	Basic

Fig. 4.19. (a) Equations for solid mechanics, (b) fixed constraints, (c) material properties of Polyimide.

4.6.3. Sensor Data Acquisition (DAQ)

For application of LIG obtained using laser carbonization, it needs to be integrated with sensor Data Acquisition (DAQ) systems for which it is connected with a Wheatstone Bridge and operational amplifier (OpAmp).

The Wheatstone bridge arrangement is the most widely used circuit for strain gauge measurements. Wheatstone Bridge is a diamond-shaped configuration consisting of 4 resistive elements connected with an external voltage source (Fig. 4.20). Under balanced condition, the output voltage from the circuit is zero.

The balanced condition is [30]:

$$\frac{R_1}{R_3} = \frac{R_S}{R_2} \tag{4.1}$$

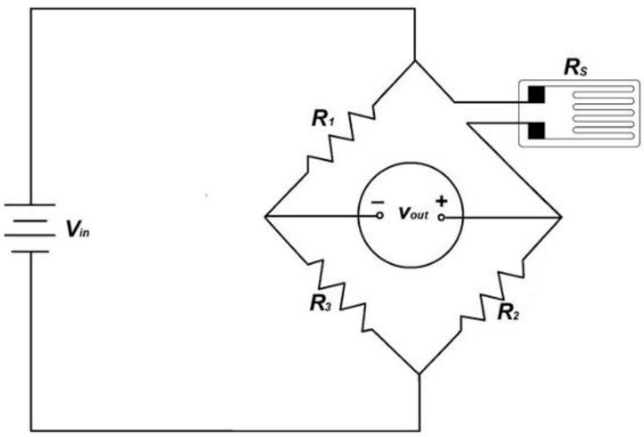

Fig. 4.20. Wheatstone Bridge setup for strain sensor [30].

The overall output voltage from the bridge is given by the equation [30]:

$$V_{out} = V_{in}[\frac{R_S R_3 - R_1 R_2}{(R_2+R_S).(R_1+R_3)}] \quad (4.2)$$

Where V_{in} is the voltage source, R_1, R_2, *and* R_3 are the resistor arms of the bridge and R_s is the resistance of the strain gauge.

Strain gauge is used as one of the resistive arms of the bridge which under strain becomes unbalanced producing voltage depending on the change in resistance upon strain.
The output voltage from the Wheatstone Bridge (V_{Ref}) is amplified using an op-amp as shown in Fig. 4.21 and the amplified output voltage (V_0) is given by the Eq 4.5 [31]:

$$V_0 = V_{out}\left(\frac{\delta}{2}\right)\frac{R_f}{R}, \delta \ll 1, R_f \gg R \quad (4.5)$$

Where R_f= resistance of the feedback resistor, R= resistance of the Wheatstone bridge arms, and δ= chanhe in resistance in one of the arms.

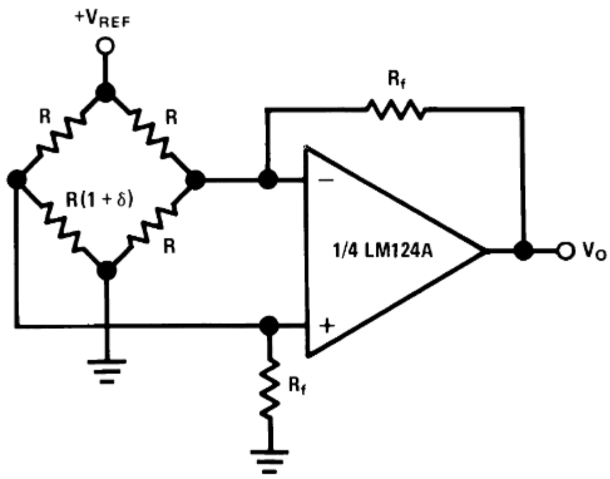

Fig. 4.21. Wheatstone Bridge connected with Op-amp [31].

From Eq 2.36 and Eq 4.5, $$GF = \frac{1}{\in}\frac{\Delta R}{R} = \frac{1}{\in}\frac{\Delta V}{V_0} \quad (4.6)$$

Where, ΔV is the change in op-amp voltage due to change in resistance [32].

Hence, LIG needs to be used as one of the four arms of Wheatstone Bridge under balanced condition (Fig. 4.17b). Putting strain on the LIG will unbalance the bridge which will create a differential voltage across the two points and the signal can be amplified by integrating OpAmps with the bridge (Fig. 4.23b). In this work Phidget Wheatstone Bridge amplifiers are used which has the bridge and the amplifier built into the device and the sensing application is described in the Chapter 7.

4.7. Characterization Methods

4.7.1. Raman Spectroscopy

Raman spectroscopy is used to measure the vibrational spectra of a sample which is unique to the chemical bonds present in it and is used as a fingerprint of the chemical structure of the sample. The vibrational peak Full Width Half Maxima (FWHM), peak ratio can also be used to image the sample on a surface.

Raman spectrophotometer consists of 4 basic components (Fig. 4.22) [33]:

a. A laser source for excitation of target materials. In our study, a 532 nm green laser source has been used.
b. A notch filter to filter the Raman scattered light and filters out the Rayleigh and Anti Stokes light.

c. A diffraction grating to bend the Raman shifted light according to wavelength.

d. A detector to record the signal and post-processing of signal using computer.

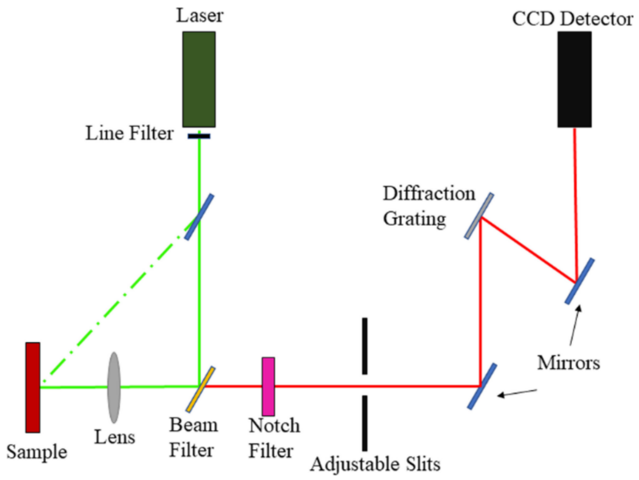

Fig. 4.22. Schematic diagram of Raman spectrophotometer [33].

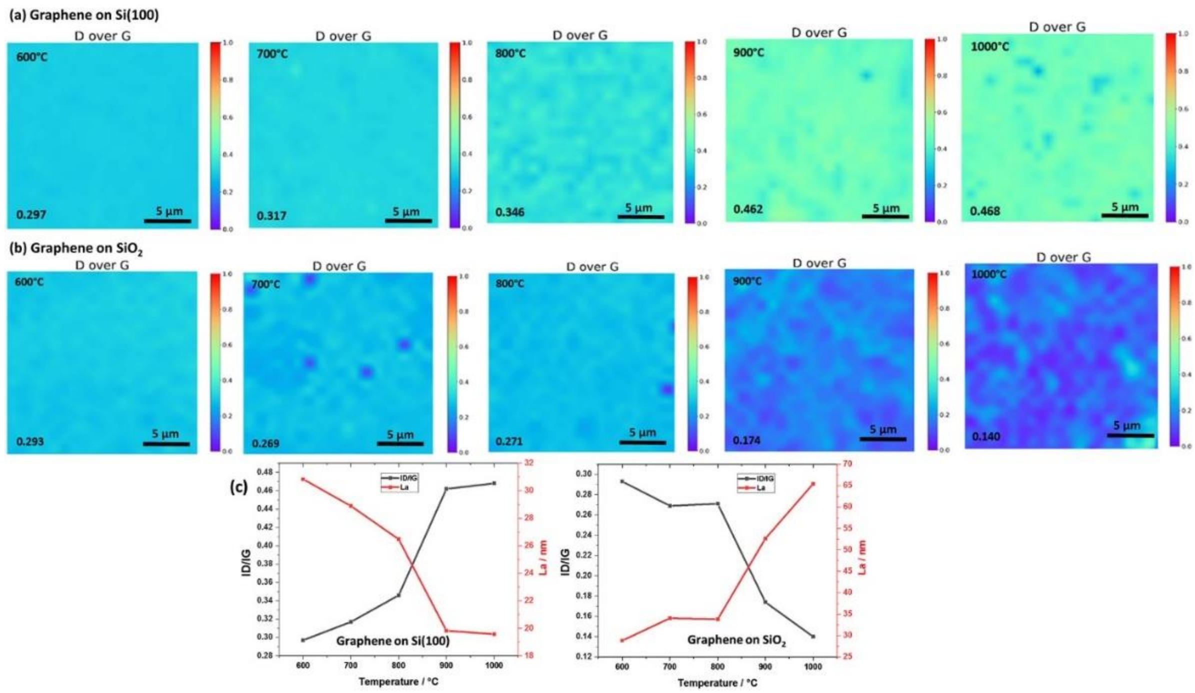

Fig. 4.23. (a) Raman imaging of I_D/I_G of graphene on Si(100) grown at temperature ranging from 600-1000^{0}C, (b) Raman imaging of I_D/I_G of graphene on SiO_2 grown at temperature ranging from 600-1000^{0}C, (c) I_D/I_G vs temperature of graphene on Si(100), (d) I_D/I_G vs temperature of graphene on SiO_2 [34].

The spectral intensity of the Raman shifts can be stored in terms of pixel intensity and then be used for imaging applications. Such imaging is useful to detect defects in graphene or other 2D materials. The ratio of D peak and G peak (I_D/I_G) shows a distribution of detects (Fig. 4.23) of graphene in a two-dimensional image.

In this thesis, Raman spectroscopy of LIG is performed using a 532 nm excitation laser with the RENISHAW inTrack Raman Microscope to measure the defect levels of the carbonized tracks and uniformity of defect levels in LIG in Chapters 5, 6 and 7.

4.7.2. Scanning Electron Microscopy (SEM)

SEM is used to study the surface morphology of a sample by image the surface using high energy electron beam and is used in imaging of various samples such as nanoparticles, circuit boards, biological with a resolution of ~2nm [35].

A SEM consists of four main parts (Fig. 4.24):

a. **Electron gun:** The electron gun is made of metallic filament usually tungsten, which is used as cathode in the SEM setup and emits electron beam (e-beam) under high voltage.

b. **Focussing lenses:** The emitted electrons then pass through a vacuum medium and focussed on the sample holder using condenser lens and objective lens. Each lens contains copper wire coils within an iron pole piece which create a magnetic field which causes the electron beam to spiral through lens while focussing on the sample. The e-beam is then scanned on the sample using scanning coils by deflecting the beam in a zigzag pattern.

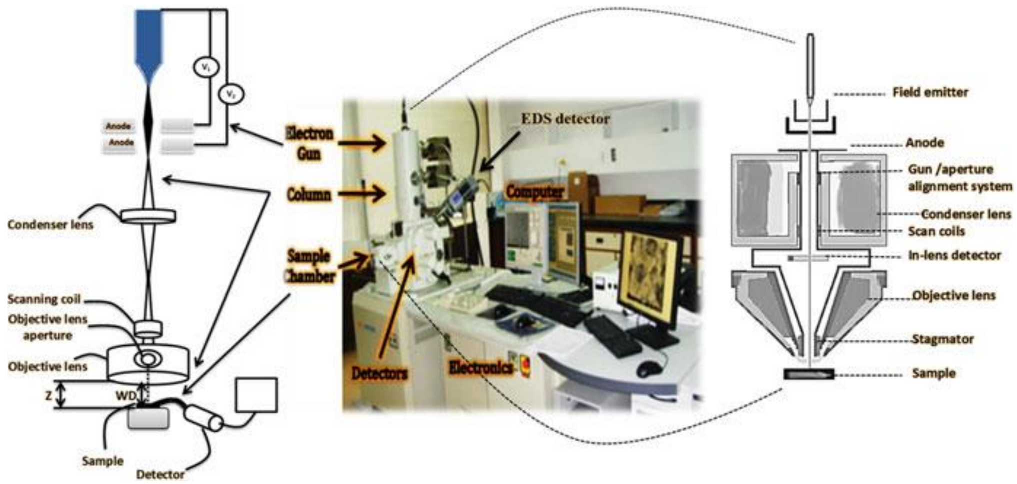

Fig. 4.24. Configuration of Scanning Electron Microscope [36].

c. **Sample Holder:** The focused e-beam then passes through the aperture to the specimen chamber where the sample holder is fixed with a stub using carbon tape, silver paste, copper tape etc. to avoid overcharging for electrically conductive samples. If the sample is nonconductive, then charge accumulation can occur creating extreme brightness and poor images. Hence, the non-conducting samples are sputter coated with thin metallic layer to conduct away the surface charge. The primary e-beam coming from the electron gun interacts with the sample and elastic-inelastic collision occurs between the primary electrons and the electrons in the outer orbitals in the sample which altogether causes emission of variety of signals such as secondary electrons (SEs), backscattered electrons (BSEs), photons (Energy Dispersive X-Ray Spectroscopy (EDX)), Auger electrons and cathodoluminescence. The most used signals are SEs and BSEs where SEs are used to study the surface morphology and BSEs are used to contrast the multiple phases in the sample. EDS is used for elemental analysis in the sample [36]. The interaction of e-beam with a sample is explained in Fig. 4.25.

d. **Detector:** The signals are then detected by the detectors and processed into signals for imaging of the sample surface.

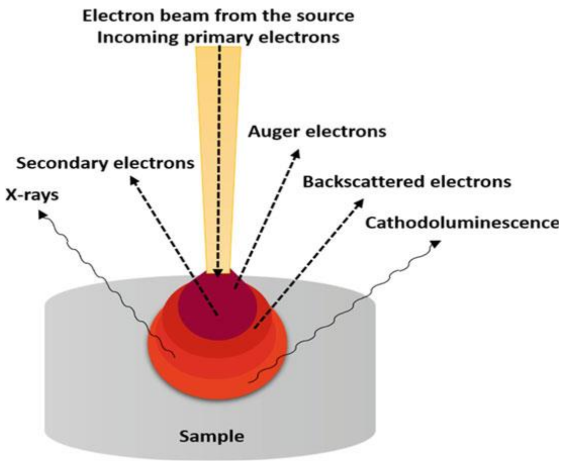

Fig. 4.25. Interaction of e-beam with sample.

The depth of the tracks and morphology of LIG at different powers and scan speed were studied from cross-sectional SEM using the PHENOM FEI Scanning Electron Microscope (SEM) and Hitachi S-2600 SEM and will be discussed in Chapters 5-7.

4.7.3. Profilometer

An optical profilometer was used to measure the roughness and ablation depth on PI. This is a non-contact and non-invasive technique to study the topology of the surface of the sample. It works on the principle of optical interference. The light from the profiler light source is split into two parts, one in the direction of the sample and the other in the direction of the reference mirror. Both of these reflected light is then captured by an array of detectors and based on the optical interference of the light from these two paths, a surface topology of the sample is captured. The working principle is explained in Fig. 4.26.

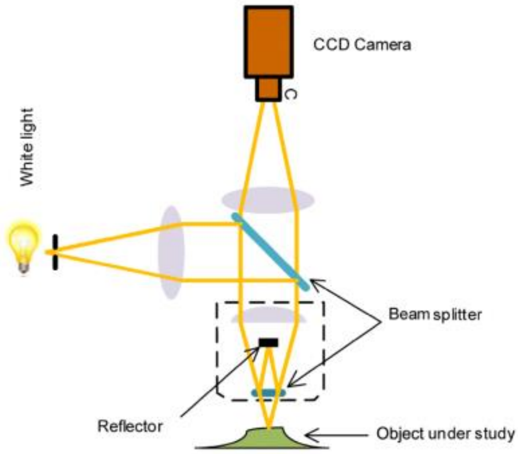

Fig. 4.26. Working principle of optical profilometer [37].

In this thesis, the surface roughness of the untreated and plasma-treated PI was measured using the Zygo OMP-0360C profilometer and is explained in Chapter 6.

4.8. Summary

In this chapter, an in-depth summary of materials, equipment used, and characterization methods to improve the conductivity and *GF* of LIG are explained. The beam path delivery and band diagrams of both CO_2 laser and Yb:YKW femtosecond laser are shown. Numerical methods for modelling the response of Polyimide and ta-C to a Gaussian CO_2 laser pulse and mechanical response of the Kirigami-inspired strain sensor in COMSOL are shown and the application of Wheatstone Bridge and Operational amplifier for sensor data acquisition (DAQ) are explained. The methods for characterizing graphene using Raman spectrophotometer, Scanning Electron Microscope and surface texture measurements using profilometer are summarized.

Bibliography

[1] R.K. Biswas, N. Farid, G. O'Connor, P. Scully, Improved conductivity of carbonized polyimide by CO2 laser graphitization, Journal of Materials Chemistry C 8(13) (2020) 4493-4501.

[2] R. Kumar Biswas, R.K. Vijayaraghavan, P. McNally, G.M. O'Connor, P. Scully, Graphene growth kinetics for CO2 laser carbonization of polyimide, Materials Letters 307 (2022) 131097.
[3] R. Kumar Biswas, P. McGlynn, G.M. O'Connor, P. Scully, Plasma enhanced planar crystal growth of laser induced graphene, Materials Letters 343 (2023) 134362.
[4] N.F. Ratul Kumar Biswas, Bharat Bhushan Bhatt, Dipti Gupta, Gerard O'Connor and Patricia Scully, Femtosecond Infra-Red Laser Carbonization and Ablation of Polyimide for Fabrication of Kirigami Inspired Strain Sensor, Journal of Physics D: Applied Physics (2023).
[5] X. Ruan, R. Wang, J. Luo, Y. Yao, T. Liu, Experimental and modeling study of CO2 laser writing induced polyimide carbonization process, Materials & Design 160 (2018) 1168-1177.
[6] M. Shamsa, W.L. Liu, A.A. Balandin, C. Casiraghi, W.I. Milne, A.C. Ferrari, Thermal conductivity of diamond-like carbon films, Applied Physics Letters 89(16) (2006) 161921.
[7] M. Hakovirta, J.E. Vuorinen, X.M. He, M. Nastasi, R.B. Schwarz, Heat capacity of hydrogenated diamond-like carbon films, Applied Physics Letters 77(15) (2000) 2340-2342.
[8] N. Ohtake, M. Hiratsuka, K. Kanda, H. Akasaka, M. Tsujioka, K. Hirakuri, A. Hirata, T. Ohana, H. Inaba, M. Kano, H. Saitoh, Properties and Classification of Diamond-Like Carbon Films, Materials (Basel) 14(2) (2021).
[9] Y. Wang, Y. Abe, Y. Matsuura, M. Miyagi, H. Uyama, Refractive indices and extinction coefficients of polymers for the mid-infrared region, Appl. Opt. 37(30) (1998) 7091-7095.
[10] R. Weber, T. Graf, C. Freitag, A. Feuer, T. Kononenko, V.I. Konov, Processing constraints resulting from heat accumulation during pulsed and repetitive laser materials processing, Opt. Express 25(4) (2017) 3966-3979.
[11] S. Jelvani, A.M. Koushki, Optimization of gas pressures ratio in a fast-axial-flow CO2 laser with genetic algorithm, Optik 123(16) (2012) 1421-1424.
[12] V.V. Nevdakh, M. Gandzhali, Optimization of the CO2:N2:He Ratio in the Active Media of Continuous-Wave Electric-Discharge CO2 Lasers, Journal of Applied Spectroscopy 71(4) (2004) 532-538.
[13] D.R. Paschotta, CO2 Lasers. https://www.rp-photonics.com/co2_lasers.html.
[14] N. Farid, A. Brunton, P. Rumsby, S. Monaghan, R. Duffy, P. Hurley, M. Wang, K.-L. Choy, G.M. O'Connor, Femtosecond Laser-Induced Crystallization of Amorphous Silicon Thin Films under a Thin Molybdenum Layer, ACS Applied Materials & Interfaces 13(31) (2021) 37797-37808.
[15] A. Sharif, N. Farid, P. McGlynn, G.M. O'Connor, Ultrashort laser sintering of printed Ag and Au nanoparticle thin tracks on heat sensitive substrates, 2022 Conference on Lasers and Electro-Optics (CLEO), 2022, pp. 1-2.
[16] A. Sharif, N. Farid, P. McGlynn, M. Wang, R.K. Vijayaraghavan, A. Jilani, G. Leen, P.J. McNally, G.M. O'Connor, Ultrashort laser sintering of printed silver nanoparticles on thin, flexible, and porous substrates, Journal of Physics D: Applied Physics 56(7) (2023) 075102.
[17] S. Reuter, T. von Woedtke, K.-D. Weltmann, The kINPen—a review on physics and chemistry of the atmospheric pressure plasma jet and its applications, Journal of Physics D: Applied Physics 51(23) (2018) 233001.
[18] F.L. Tabares, I. Junkar, Cold Plasma Systems and their Application in Surface Treatments for Medicine, Molecules 26(7) (2021).
[19] M. Weiss, D. Gümbel, E.-M. Hanschmann, R. Mandelkow, N. Gelbrich, U. Zimmermann, R. Walther, A. Ekkernkamp, A. Sckell, A. Kramer, M. Burchardt, C.H. Lillig, M.B. Stope, Cold Atmospheric Plasma Treatment Induces Anti-Proliferative Effects in Prostate Cancer Cells by Redox and Apoptotic Signaling Pathways, PLOS ONE 10(7) (2015) e0130350.
[20] B. Dorin, P. Parkinson, P. Scully, Direct laser write process for 3D conductive carbon circuits in polyimide, Journal of Materials Chemistry C 5(20) (2017) 4923-4930.

[21] D.-J. Liaw, K.-L. Wang, Y.-C. Huang, K.-R. Lee, J.-Y. Lai, C.-S. Ha, Advanced polyimide materials: Syntheses, physical properties and applications, Progress in Polymer Science 37(7) (2012) 907-974.
[22] L. Baxter, K. Herrman, R. Panthi, K. Mishra, R. Singh, S. Thibeault, E. Benton, R. Vaidyanathan, Chapter 3 - Thermoplastic micro- and nanocomposites for neutron shielding, in: S.T. Abdulrahman, S. Thomas, Z. Ahmad (Eds.), Micro and Nanostructured Composite Materials for Neutron Shielding Applications, Woodhead Publishing2020, pp. 53-82.
[23] L.W. McKeen, 6 - Polyimides, in: L.W. McKeen (Ed.), The Effect of Long Term Thermal Exposure on Plastics and Elastomers, William Andrew Publishing, Oxford, 2014, pp. 117-137.
[24] Y. Kumagai, K. Itoya, M.-A. Kakimoto, Y. Imai, High-pressure synthesis of aliphatic polypyromellitimides via nylon-salt-type monomers composed of aliphatic diamines and pyromellitic acid diesters, Journal of Polymer Science Part A: Polymer Chemistry 38(8) (2000) 1391-1395.
[25] A. Sezer Hicyilmaz, A. Celik Bedeloglu, Applications of polyimide coatings: a review, SN Applied Sciences 3(3) (2021) 363.
[26] D.K. HN, Polyimide Film Datasheet.
[27] A. Lamoureux, K. Lee, M. Shlian, S.R. Forrest, M. Shtein, Dynamic kirigami structures for integrated solar tracking, Nature Communications 6(1) (2015) 8092.
[28] G.P.T. Choi, L.H. Dudte, L. Mahadevan, Programming shape using kirigami tessellations, Nature Materials 18(9) (2019) 999-1004.
[29] A.K. Brooks, S. Chakravarty, M. Ali, V.K. Yadavalli, Kirigami-Inspired Biodesign for Applications in Healthcare, Advanced Materials 34(18) (2022) 2109550.
[30] S. Tayebi, A. Gutierrez, I. Mohout, E. Smets, R. Wise, J. Stiens, M.L.N.G. Malbrain, A concise overview of non-invasive intra-abdominal pressure measurement techniques: from bench to bedside, Journal of Clinical Monitoring and Computing 35(1) (2021) 51-70.
[31] LMx24-N, LM2902-N Low-Power, Quad-Operational Amplifiers Datasheet, Texas Instruments, 2015.
[32] A.D. Smith, F. Niklaus, A. Paussa, S. Vaziri, A.C. Fischer, M. Sterner, F. Forsberg, A. Delin, D. Esseni, P. Palestri, M. Östling, M.C. Lemme, Electromechanical Piezoresistive Sensing in Suspended Graphene Membranes, Nano Letters 13(7) (2013) 3237-3242.
[33] M. Kanmalar, S.F. Abdul Sani, N.I.N.B. Kamri, N.A.B.M. Said, A.H.B.A. Jamil, S. Kuppusamy, K.S. Mun, D.A. Bradley, Raman spectroscopy biochemical characterisation of bladder cancer cisplatin resistance regulated by FDFT1: a review, Cellular & Molecular Biology Letters 27(1) (2022) 9.
[34] Y. Bleu, F. Bourquard, A.-S. Loir, V. Barnier, F. Garrelie, C. Donnet, Raman study of the substrate influence on graphene synthesis using a solid carbon source via rapid thermal annealing, Journal of Raman Spectroscopy 50(11) (2019) 1630-1641.
[35] P.P. Pednekar, S.C. Godiyal, K.R. Jadhav, V.J. Kadam, Chapter 23 - Mesoporous silica nanoparticles: a promising multifunctional drug delivery system, in: A. Ficai, A.M. Grumezescu (Eds.), Nanostructures for Cancer Therapy, Elsevier2017, pp. 593-621.
[36] K. Akhtar, S.A. Khan, S.B. Khan, A.M. Asiri, Scanning Electron Microscopy: Principle and Applications in Nanomaterials Characterization, in: S.K. Sharma (Ed.), Handbook of Materials Characterization, Springer International Publishing, Cham, 2018, pp. 113-145.
[37] A. Bakhtazad, S. Chowdhury, An evaluation of optical profilometry techniques for CMUT characterization, Microsystem Technologies **25**(9) (2019) 3627-3642.

5. Chapter 5: Laser carbonization and graphitization

In this chapter, the first attempt has been made to meet the objective of improving the crystallite size and electrical conductivity by the laser graphitization method using a CO_2 laser, where the laser was scanned on a pre-printed tetrahedral carbon (ta-C) carbonized track prepared by the same laser. The interaction of CO_2 laser with PI and ta-C was modelled in COMSOL and was validated using the threshold conditions. In the scope of the thesis, it explains the theoretical understanding of the CO_2 laser-PI and CO_2 laser-ta-C interaction and how such a study can be useful to improve the conductivity of LIG. The work has been published in the Journal of Materials Chemistry C, Royal Society of Science. Nazar Farid assisted this chapter with the COMSOL simulation. The contribution of Ratul Kumar Biswas in this chapter is 70%, and Nazar Farid is 30%. Gerard O'Connor and Patricia Scully supervised and helped in the overall conceptualization of the project and Gerard O'Connor co-supervised and provided access to the lasers and characterization tools at the NCLA.

The complete work has been performed in NCLA, University of Galway. Ratul Biswas performed all the experiments, characterizations, analysis of the data, and wrote the paper. Nazar Farid aided with the simulation in COMSOL. The supplementary information of the paper is included in this chapter within the context.

Improved conductivity of carbonized polyimide by CO_2 laser graphitization

Ratul Kumar Biswas[1], Nazar Farid[1], Gerard O'Connor[1], Patricia Scully[1]

[1]*NCLA, National University of Ireland, Galway, Ireland.*

J. Mater. Chem. C, 2020, **8**, 4493-4501

Abstract: Direct laser writing (DLW) is a fast and cost-effective technique for printing conductive structures on flexible substrates such as polyimide (PI) by the conversion of insulative PI to conductive carbon. However, the conductivity (~10^3 S.m^{-1}) obtained by this method needs to be improved to compete with ink-jet printing of carbon-based materials. The reason behind the low conductivity achieved by the DLW process is due to the crystallinity and hybridization of bonding in carbonaceous structures. In this work, the DLW process has been implemented in two steps: the first step called carbonization was performed by writing pulsed CO_2 laser on PI to form tracks which consist of amorphous tetrahedral carbon (a mixture of sp^2 and sp^3 hybridized carbon) having intrinsically low conductivity. The second step called graphitization is overwriting of the laser on the pre-carbonized tracks to convert sp^3 hybridized bonds to sp^2 hybridized bonds by the process called laser graphitization. The conductivity of tracks carbonized at (0.21 ± 0.02) W and fluence (3.31 ± 0.32) x 10^3 mJ cm^{-2} at a repetition rate of 0.10 kHz was 56.10 ± 3.10 S.m^{-1} which increased to 146.70 ± 5.10 S.m^{-1} upon overwriting with the laser at (0.50 ± 0.03) W and fluence (7.88 ± 0.47) x 10^3 mJ cm^{-2} at the same repetition rate. The photothermal process of carbonization and graphitization is modelled for the DLW process and the threshold power of both the processes is calculated and validated by Raman spectroscopy. Improved conductivity achieved by detailed understanding of the laser and material parameters involved in this transformation enables process optimization leading to future applications in scalable manufacturing of flexible biosensors and electrochemical energy storage devices.

5.1. Introduction:

In recent years, Direct Laser Writing (DLW) of carbonaceous structures on PI surface has gained interest in the field of graphene-based printed electronics owing to its simple one-step method of inscribing conductive circuits as compared to other printing techniques like ink-jet and screen-printing [1-9]. This process involves an in-situ photothermal conversion of PI to carbonaceous structures using a translated laser beam as the heat source [1]. The current printing techniques involve ink-jet printing of graphene-based conducting inks with conductivity in the order of 10^4 S/m [10] but the resolution of the printed structures are limited by factors such as clogging of nozzles by large suspended particles of Graphene-oxide (GO), flight deviation of ink-drops, coffee ring structures and migration of ink-drops after hitting the surface [11-13]. For laser inscription, the resolution of inscribed structures is controlled by beam size and optical properties of the laser which provides potential to print precise conducting structures at the diffraction limit but provides conductivity in the order of 10^3 S/m [2, 14]. Hence, if the inscription process, material transformation and thus the conductivity of laser-written carbonized structures by DLW can be improved, it could replace the conventional printing used in graphene-based printed electronics because of the scalability and precision of the process.

PI shows excellent thermal stability upto 673 K [15] and has potential applications as a flexible substrate for microelectronics owing to its insulative properties [16], and widespread availability as a high quality, low-cost stable polymer. Laser carbonization of PI was first studied by Schumann et al. in the year 1991 using a 248 nm KrF laser [17] where the conductivity was increased upto 15 times of the virgin PI. The laser irradiation photothermally ruptures the C=O, C-O and C-N bonds in PI leading to the formation of porous and amorphous carbonaceous structures [8] along with gaseous products such as CO, HCN and C_2H_2 [18]. These laser-driven carbonized structures have been applied to energy storage devices, catalysis and sensing [6].

PI to carbon transformation occurs in two steps. Carbonization commences at 673 K (T_{Car}) [15] producing amorphous tetrahedral carbon (ta-C) also known as Diamond-like Carbon [19]. Upon further heating upto 773 K (T_{Gr}), it leads to transformation of the existing sp^3 bonds to sp^2 bonds along with crystallization of the amorphous matrix, which is termed as Graphitization [20], improving its electrical conductivity. A Laser thermal source can be used to induce graphitization in the ta-C by increasing the sp^2 content of the carbon hence increasing the percolation of electrons between the graphitic crystalline domains [20-25]. Hence, an attempt is taken for the first time to heat up the carbonized structures to the T_{Gr} by overwriting the laser inscribed structure with appropriate selection of laser parameters to induce graphitization, improving the conductivity of the tracks.

The main aim of our work is to improve the conductivity of carbonized tracks on PI substrate by laser graphitization using CO_2 laser because of its scalability. We separate the process into the two material transformation processes of carbonization and graphitization (Fig. 5.1) and use modelling to select the optimal laser beam parameters for experimental work. The defect level of the inscribed tracks is measured from the ratio of the intensity of defect and graphitic peaks and the increase in sp^2 content is detected from the blue-shift of the G-peak in the Raman spectra of the tracks [26]. To measure the improved electrical conductivity upon graphitization, electrical contacts to the tracks enable 2-probe conductivity measurement, and resistance is measured from the I-V characterization of the tracks.

The CO_2 laser has a wavelength of 10.60 µm falls in the IR spectrum, which is responsible for excitations by molecular vibrations rather than by electronic excitations. The pulse duration used in our work (30-80 µs) is much greater than the time duration of electronic excitation of PI (34 ps) [27], the transformation process of carbonization and graphitization of PI by CO_2 laser is modelled, by considering it to be a photothermal reaction process. To the best of our knowledge, modelling has been performed only on the carbonization of PI using a continuous wave CO_2 laser [28]. Here, we model both the carbonization and graphitization process with modulated CO_2 laser and provides an insight into optimal control of the process by appropriate selection of laser parameters. This process can be applied to the formation of conducting networks, and porous structures for electrochemical energy storage devices. Hence this work aims to provide insight to improve the conductivity of laser carbonized structures on PI, by appropriate selection of laser parameters such as pulse duration and repetition rate using a modelling approach.

5.2. Experimental and Simulation Method:

5.2.1. Experimental parameters for Direct Laser Writing using CO_2 Laser

A GEM 6O Coherent DEOS CO_2 Laser system equipped with DEI PDG-2510 Digital Pulse Generator was used to write carbonaceous structures on PI. A lens with focal length of 100 mm focused the minimum spot size (400 µm) onto the PI substrate. PI film (Dupont Kapton ® HN) of thickness 127 µm and dimension 15 mm x 10 mm was used for the experiment. The PI sheets were cleaned with ethanol and deionized (DI) water by ultrasonic cleaning for 10 minutes followed by rinsing in DI water and drying. The laser beam was scanned over the PI sheet at power ranging from 0.15-0.65 W (Fluence= $2.36x10^3$ - $10.25x10^3$ mJ/cm^2) by varying pulse duration (τ_p) ranging from 30-80 µs at constant repetition rate (f) of 0.1 kHz and a scan speed of 120 mm/min to obtain carbonized tracks of length 10 mm drawn on the PI surface. The writing patterns were created using Advanced Laser Software and the laser movement was controlled by Unidex 500 program. The laser output power (*P*) was measured with a Thorlabs PM100D laser power meter for each pulse duration. The carbonized track obtained at laser irradiation of 0.21 W power was overwritten with the CO_2 laser with power ranging from 0.21-0.65 W, and corresponding fluence ranging from 3.31 x 10^3 – 10.25 x 10^3 mJ/cm^2 at a scan speed of 120 mm/min at 0.1 kHz. The width of the carbonized tracks was measured using Olympus BX 60M optical microscope (fig 5.11). The pre-carbonized power at 0.21 W, was selected so that the inscribed structure had minimum crystalline graphitic content, and a maximum power of 0.65 W was chosen because, beyond 0.65 W, the carbonized track itself started to peel away from the substrate (fig 5.12).

During laser scanning, there is an overlap of pulses, so firstly, a single laser pulse is investigated, and then the effect of multiple subsequent pulses is considered using the pulse overlapping factor (Υ). The material transformation threshold power for a single pulse was measured by estimated by measuring the threshold for a varying number of pulses. The threshold power decreases as the number of pulses increases. This effect is known as incubation and the coefficient governing the dependence is termed the incubation coefficient (*S*) [29]. Incubation was studied for PI by spot carbonization for a set of a number of pulses (*N*) ranging from 3-7 with laser power ranging from 0.15-0.92 W at 0.1 kHz repetition rate to measure the spot radius, incubation coefficient, and single pulse threshold power. The carbonization diameter of each of the spots was measured using the optical microscope.

5.2.2. Modelling of carbonization and graphitization of PI by CO_2 Laser

The photo-thermal process of PI to carbon transformation was modelled using a time-variant Gaussian equation for laser source and was solved by a commercial finite element analysis (FEA) software package-COMSOL®. During the carbonization, the phase change of polymer to amorphous carbon may alter properties such as specific heat (C_P), thermal conductivity (K), density (ρ), absorption coefficient (α), etc. Hence, photothermal models using a temperature variant C_P and K were used [28]. In our work, single pulse carbonization is modeled, and so α and ρ are assumed to be constant during the process.

Assuming the incident laser beam has a Gaussian spatial beam profile and considering only the absorbed energy taking part in the process, the time-variant heat source density per unit volume at position (x,y) can be written as [30]:

$$Q(x,y) = 2\, F_{eff} \cdot \left[\frac{\alpha(\lambda)}{\sqrt{(\pi/\ln 2)\tau_p}}\right].(1-R_e).\left[exp\left\{-2\left(\frac{x}{\omega_0}\right)^2 - 4\ln 2\left(\frac{t-t_c}{t_P}\right)^2\right\}\right] exp(\alpha(\lambda)y)$$

(5.1)

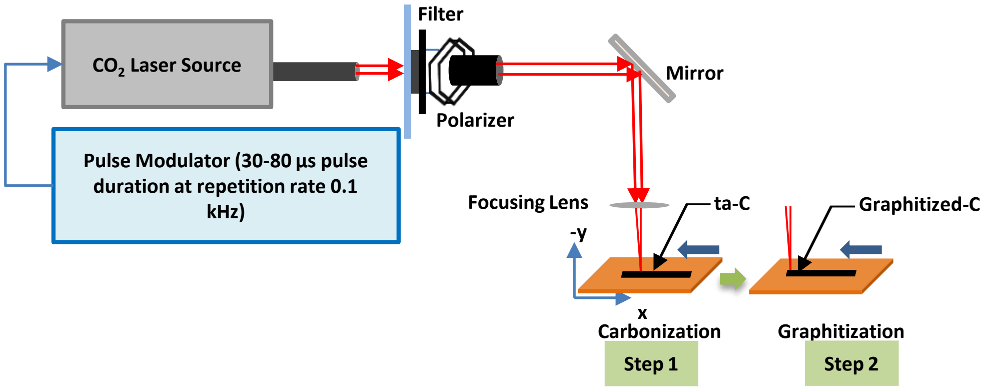

Fig. 5.1. Laser Beam Delivery system used for Step 1- carbonization of PI, followed by Step 2- graphitization of the track.

where t_c is the equilibrium time taken as 10 ns, x is the radial distance from the center of the laser beam and y is the depth measured from the surface of the PI film. For power P, at repetition rate f, the Fluence (F) is given by equation [4]:

$$F = \frac{2P}{f\pi\omega_0^2} \quad (5.2)$$

During a scan in which the laser beam is translated at velocity v, there will be an overlapping of consecutive pulses incident on the material which will cause spatial delivery of packets of heat. Therefore this effect is taken into consideration by the "Overlapping Factor" (γ) which is given by equation [31]:

$$\gamma = \left[1 - \left(\frac{v}{2f\omega_0}\right)\right] \quad (5.3)$$

Owing to the overlapping pulses, F is replaced by the effective fluence F_{eff} which at any instant during a scan is given by the equation:

$$F_{eff} = F(1+\gamma) \quad (5.4)$$

The amount of heat absorbed by the material is governed by its wavelength-dependent absorption coefficient $\alpha(\lambda)$ and reflectivity (R_e) given by [28]:

$$\alpha(\lambda) = \frac{4\pi\kappa}{\lambda}\ ,\ R_e = \left[\frac{(1-n)^2+\kappa^2}{(1+n)^2+\kappa^2}\right] \quad (5.5)$$

where λ is 10.6 µm.

Assuming the laser heat source *Q(x,y)* is responsible for the photothermal conversion of PI, the spatial heat distribution over time is given by the Fourier heat equation [28]:

$$[\rho C_p(T)\left(\frac{\partial T}{\partial t}\right)] - \nabla[K(T)\nabla T] = Q(x,y) \qquad (5.6)$$

Table 5.1. Properties of both PI and ta-C.

Properties	PI	Ta-C
n (refractive index)	1.75 [28]	1.67 [32]
κ (extinction coefficient)	0.03 [28]	0.01 [32]
K(T) (Thermal conductivity)	$0.213 + 3.416 \times 10^{-5}T \quad W/mK, \quad \forall\, 200K < T < 729K$ $-1.314 + 2.13 \times 10^{-3}T \quad W/mK, \quad \forall\, 729K < T < 1500K$ [28]	0.69 W/mK [33]
$C_P(T)$ (Specific Heat)	$1000[\,0.96 + 1.39\left(\frac{T-300}{400}\right) - 0.43\left(\frac{T-300}{400}\right)^2] \quad J/kg-K,$ $\forall 200\mathrm{K} < \mathrm{T} < 1500\mathrm{K}$ [28]	790 J/kg-K [34]

The initial temperature $T(x,y,t=0)=T_{ext}$=293K and the density of PI is 1300 kg/m^3. The radiative losses were taken into consideration.

The photo-thermal reaction model was solved by Finite Element Analysis (FEA) Method using the commercial software package COMSOL® to estimate the time-variant temperature distribution. The length was 400 µm and thickness of the geometric element was 125 µm and beam spot radius was taken to be 201 µm as obtained from D^2 vs ln(P) plot (Fig. 5.2a).

5.2.3. Structural and Electrical Characterization of the carbonized and graphitized tracks

The diameter of the carbonized regions was measured using the Olympus BX60M optical microscope. The PHENOM FEI Scanning Electron Microscope (SEM) measured the depth of the tracks at different powers, using cross-sectional SEM. The defect levels of the carbonized tracks for each of the power and uniformity of defect levels were detected by Raman Spectroscopy using a 532 nm excitation laser with the RENISHAW inTrack Raman Microscope. A Keithley 2450 Source meter integrated with 2-probe resistance measurement setup, was used to measure the IV characteristics of the tracks by applying a potential sweep of 0-20 V, from which the resistance across the two ends of the tracks was calculated. Room temperature curable conductive paste was applied on both ends of the tracks to create suitable contact with the probes.

5.3. Results and Discussion:

5.3.1. Calculation of Incubation coefficient, spot-size radius, and Single Pulse Threshold Power of Carbonization

The carbonized diameter was found to increase with incident laser power (P) and the number of laser pulses, as shown in figure 5.2a. The square of the diameter is given by using equation 7 [4]:

$$D^2 = 2\omega_0^2\,[ln(P) - ln\,(P_{\mathrm{Th}})] \tag{5.7}$$

where P_{Th} is the threshold laser power. The spot size was obtained from the slope and the threshold power of carbonization ($P_{N,Th}$) for each of the corresponding number of pulses (N) was obtained from the x-intercepts of the plot D^2 vs $ln(P)$ as shown in figure 5.2. The values of P_{Th} for each set of the number of pulses is shown in Table 5.2. The average spot size radius (ω_0) was found to be 2.01±0.6 x 10^2 µm. Using equation 5.7 and the value of ω_0, the fluence (F) can be calculated for known power values. The spot size also matches with the measured value for scanning pulses at 120 mm/s (Fig. 5.3).

The incubation coefficient (S) and single pulse threshold fluence ($F_{1,Th}$) were obtained from the slope and y-intercept of the plot $ln(NF_{N,Th})$ vs $ln(N)$ (Fig. 5.2b) using the equation 8 [29]:

$$ln\left(N \cdot F_{N,Th}\right) = ln\left(F_{1,Th}\right) + S \cdot ln(N) \tag{5.8}$$

S was calculated as 0.61 ± 0.04 and $F_{1,Th}$ as (5.12 ± 0.34)x10^3 mJ/cm^2. Using the equation 2, the single pulse threshold power ($P_{1,Th}$) was found to be 0.32 ± 0.002 W.

Table 5.2. Summary of threshold power and fluence for a varying number of pulses (N).

N	**ω_0 (µm)**	**$P_{N,Th}$ (W)**	**$F_{N,Th}$ (mJ.cm^{-2})**

3	192 ± 66	0.21 ± 0.02	(3.28±0.38) x10^3
4	196 ± 55	0.19 ± 0.02	(3.05±0.35) x10^3
5	201 ± 48	0.17 ± 0.01	(2.69±0.18) x10^3
6	208 ± 57	0.17 ± 0.02	(2.62±0.23) x10^3
7	207 ± 58	0.15 ± 0.02	(2.34±0.24) x10^3

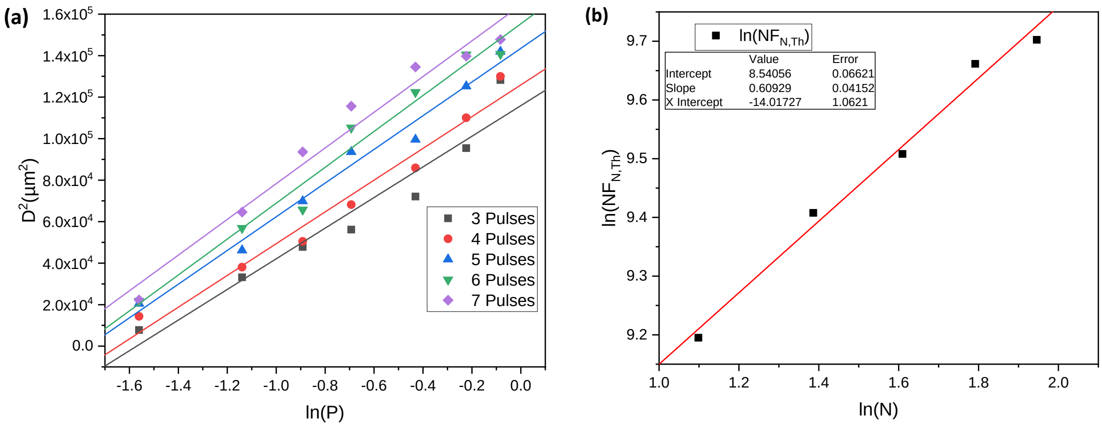

Fig 5.2. (a) D^2 vs *ln(P)* plot for 3-7 pulses, (b) $ln(NF_{N,Th})$ vs *ln(N)* plot.

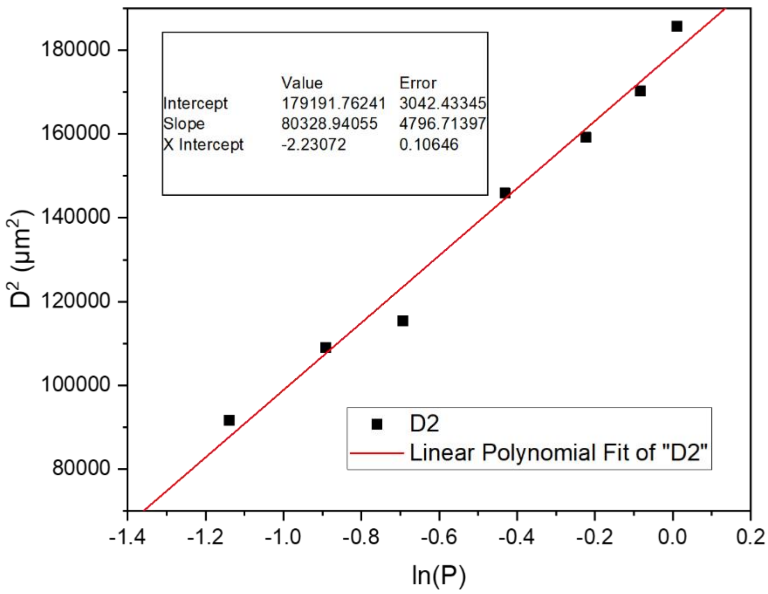

Fig 5.3. D^2 vs *ln(P)* for CO_2 laser scanning at 120 m/min and repetition rate 0.1 kHz.

5.3.2. Calculation of Threshold Power of Graphitization

At first, carbon tracks were written on PI at power (0.21 ± 0.02) W and fluence (3.31 ± 0.32)x10^3 mJ/cm^2, at a scan speed of 120 mm/min and repetition rate 100 Hz. Then, the tracks were overwritten with power ranging from (0.21 ± 0.02) W to (0.65 ± 0.02) W at the same scan speed and repetition rate. The Raman spectra of each of the overwritten tracks were measured. The Raman spectra of the tracks showed three major peaks: a D peak at ~1344 cm^{-1} arising from the defects present within the lattices, G peak at~1576cm^{-1} due to the in-plane vibration mode from E_{2g} phonons of sp^2 hybridized carbon atoms and 2D peak at ~2688 cm^{-1}, originating from the non-disorder induced overtone of D band. For this study, only D and G peaks were considered (Fig. 5.4a) as the ratio of the intensity of D peak (I_D) and (I_G) reveals the defect level within these structures and is given by (I_D/I_G) [35-37] and the position of the G-peak reveals the advent of Graphitization. As the sp^2 content increases, the G-peak shifts to higher wavenumber [26]. G-peak shift was detected at (0.50 ± 0.03) W (Fig. 5.4b), which shows that the threshold Graphitization power to be (0.50 ± 0.03) W and threshold fluence to be (7.88 ± 0.47)x10^3 mJ/cm^2.

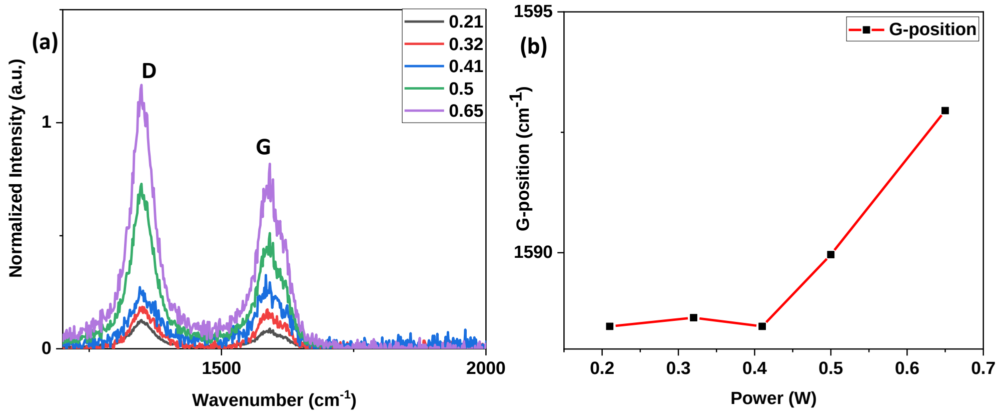

Fig 5.4. (a) Raman spectra of tracks graphitized at 0.21, 0.32, 0.41, 0.5 and 0.65 W, (b) Variation of G-peak position of the Graphitized tracks with increasing power.

5.3.3. Estimation of Temperature for Single-Pulse Threshold Power, Temperature due to Pulse Overlap factor for Carbonization and Temperature at threshold power for Graphitization

The calculated single pulse threshold power, $P_{1,Th}$ = 0.324 W estimated the laser irradiation temperature as 719K (Fig. 4.5a) which is close to T_{Carb} = 673K [15]. Hence, the photo-thermal model can estimate the irradiation temperature for other power values.

The irradiation temperatures estimated for a range of laser powers are given in Table 5.3. Traces of carbonization were observed under the optical microscope at 0.15 W, indicating an irradiation-induced temperature of 685 ± 76K close to the threshold carbonization temperature (Fig. 5.5b). Hence, the irradiation temperature for both single pulse, as well as scanning pulse was successfully calculated from the photo-thermal model. The same model was used to estimate the laser-induced irradiation temperature on the amorphous carbon (Fig. 5.5c). The threshold temperature of graphitization (717 ± 36 K) was estimated as 0.5 W which is close to the threshold graphitization temperature which is 773 K [20]. Hence, the simulation for both carbonization and graphitization is comparable.

The effect of precursor, which in our case is PI for carbonization study and ta-C for graphitization study, on the peak temperature is significant as it varied from 791.59 ± 33.86 K to 1476.84 ± 35.68 K for PI precursor and 484.51 ± 17.09 K to 862.72 ± 25.65 K for ta-C precursor in the power range of 0.21 ± 0.02 W to 0.65 ± 0.02 W respectively (Fig. 5.5d). Hence, this study can also be used for calculation of temporal evolution of temperature for various carbon precursors such as hydrothermally produced carbons (HPC) [38], lignin [39], and cloth, paper and food [40] which can be used to predict the crystallinity and sp^2/sp^3 ratio of the graphitic structures by molecular dynamics[41, 42]. The temperature contours of carbonization and graphittization are shown in Fig. 5.6a and Fig. 5.7a and the temperature evolution along the depth of PI is shown in Fig. 5.6b and Fig. 5.7b.

Table 5.3. Summary of temperatures obtained from simulation for carbonization and graphitization with varying levels of laser power.

τ_p (μs)	v (mm/min)	f (kHz)	γ	P (W)	F (mJ/cm^2)	P_{eff} (W)	$T_{Carbonization}$ (K)	$T_{graphitization}$ (K)
30	120	0.10	0.93	0.15±0.04	(2.37±0.63)x10^3	0.29±0.04	685.08 ±76.42	-
40	120	0.10	0.93	0.21±0.02	(3.31±0.32)x10^3	0.46±0.03	791.59 ±33.86	484.51± 17.09
50	120	0.10	0.93	0.32±0.03	(5.04±0.47)x10^3	0.62±0.05	978.16 ±46.20	587.90± 27.06

60	120	0.10	0.93	0.41±0.04	$(6.46\pm0.63)\text{x}10^{3}$	0.79±0.07	1107.655±59.72	633.28±33.00
70	120	0.10	0.93	0.50±0.03	$(7.88\pm0.47)\text{x}10^{3}$	0.96±0.06	1233.29±45.96	717.15±36
80	120	0.10	0.93	0.65±0.02	$(10.25\pm0.32)\text{x}10^{3}$	1.25±0.05	1476.84±35.68	862.72±25.65

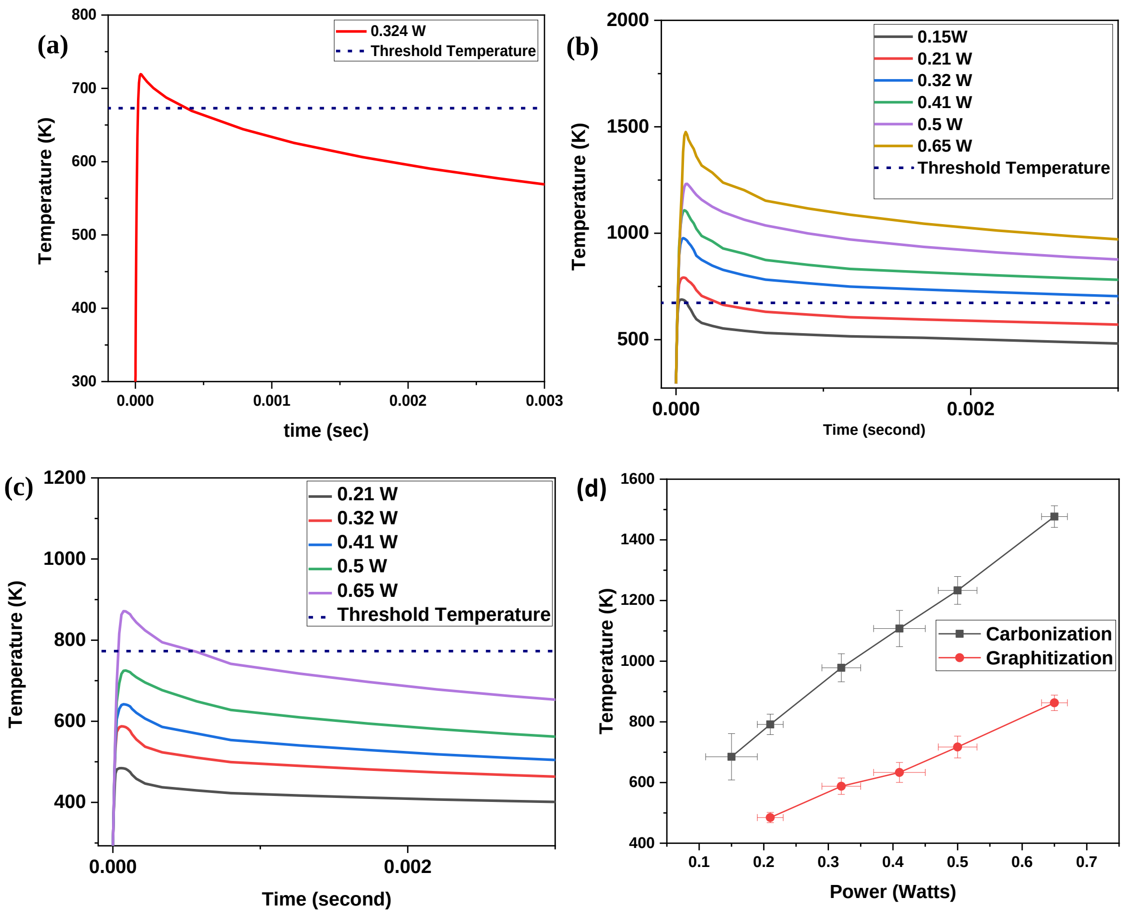

Fig 5.5. Simulation results at (a) single pulse threshold power $P_{1,Th}$= 0.324 W, (b) laser with power 0.15, 0.21, 0.32, 0.41, 0.50 and 0.65 W at scan speed 120 mm/min and repetition rate 0.10 kHz. for carbonization (c) laser with power 0.21, 0.32, 0.41, 0.5 and 0.65 W at scan speed 120 mm/min and repetition rate 0.10 kHz. for graphitization, and (d) Variation of peak temperature with laser power both for carbonization and graphitization as obtained from simulation.

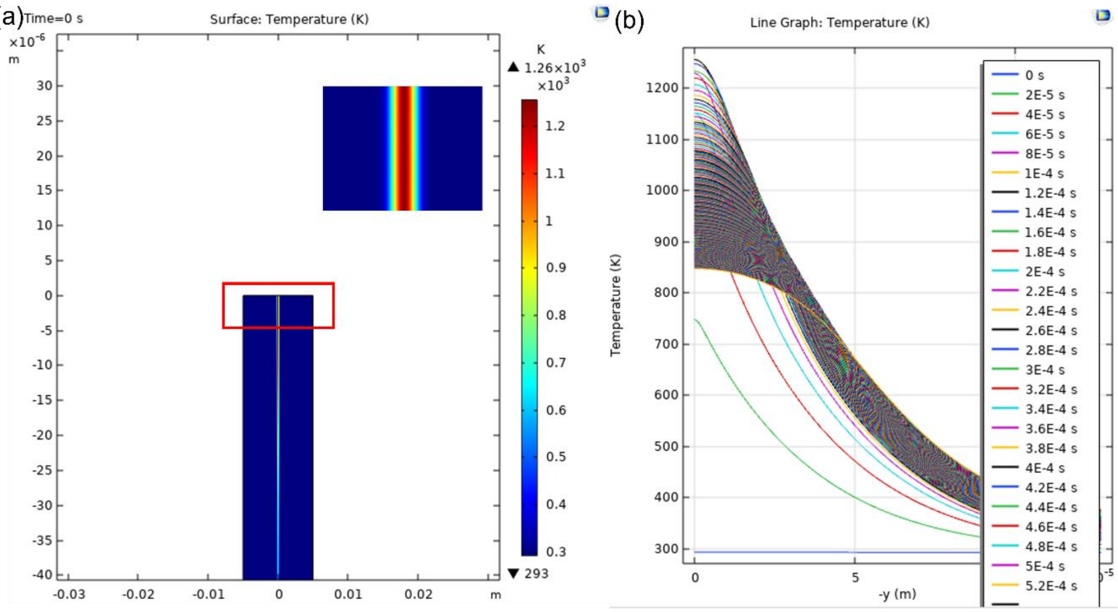

Fig. 5.6. (a) Temperature contour of PI, and (b) Temperature along the cut line 0.5 W.

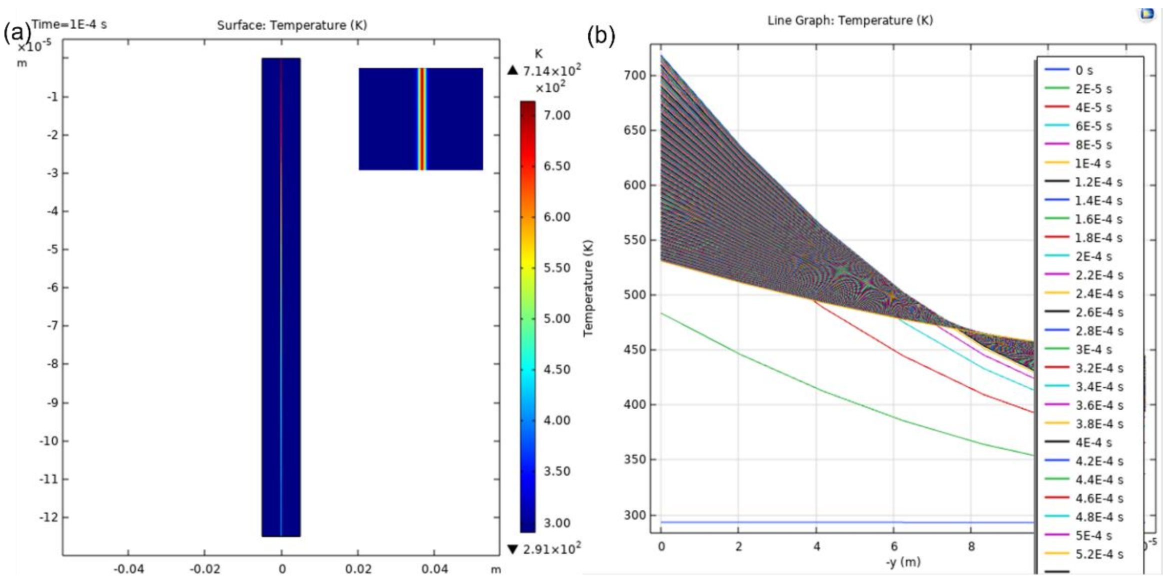

Fig. 5.7. (a) Temperature contour of ta-C, and (b) Temperature along the cut line 0.5 W.

5.3.4. Structural Characterization of the Carbonized tracks

Scanning Electron Microscopy image (fig. 5.8 a) indicated that the CO_2 laser carbonization and graphitization created porous structures, due to the rapid evolution of product gases [4]. Both the width and depth of the tracks increased with increasing power (fig. 5.8 b,c). The width ranged from 280-370 µm upon carbonization at 0.21- 0.65W. When rewriting the laser on the precarbonized tracks, the width increased by 9-30 % and depth increased by 0.02-1.2% with laser power.

The Raman signals associated with carbonization started to be observable from the tracks carbonized at 0.15 W (fig. 5.8 d), at an irradiation temperature at 685.08 K as derived from the simulation and confirms the threshold temperature of carbonization (673K). The I_D/I_G ratio decreased from 2.91 at 0.15 W to 0.99 at 0.65 W because carbonization increases with temperature. The I_D/I_G ratio of the track with a single overwrite of laser decreased from 1.42 at 0.21 W to 0.83 at 0.41 W (fig. 5.9a). Above 0.41 W, the I_D/I_G ratio increased with power due to the oxidation of the ever-present carbonized structures by the high temperature [4]. The I_D/I_G ratio also reveals the average crystallite domain size (L_a) in nm of the graphitic features, calculated from equation [8, 43]:

$$L_a = (2.4 \times 10^{-10}) \times \lambda^4 \times \left(\frac{I_D}{I_G}\right)^{-1} \quad (5.9)$$

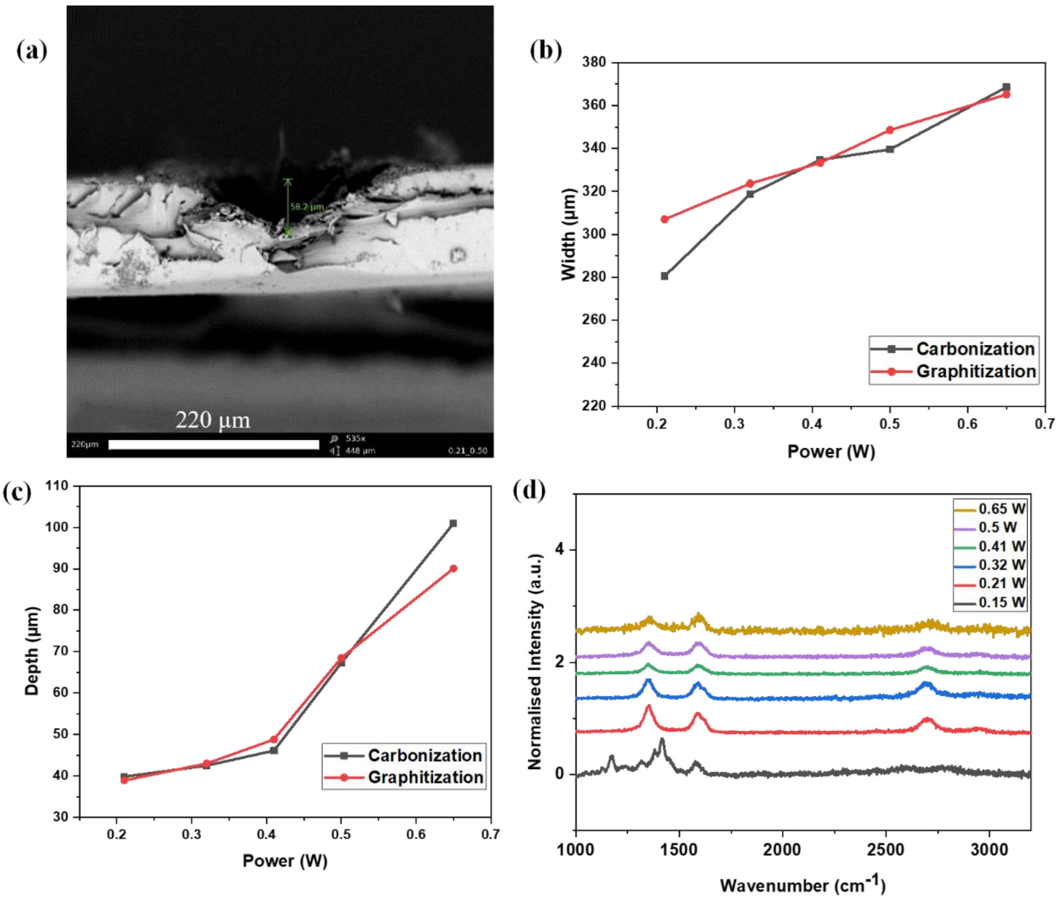

Fig 5.8. Cross-sectional SEM image of (a) graphitized track at 0.5 W on a 0.21 W pre-carbonized track, (b) Varying width of the carbonized and graphitized tracks with power, (c) Varying depth of the carbonized and graphitized tracks with power, (d) Raman spectra of tracks carbonized at 0.15, 0.21, 0.32, 0.41, 0.5 and 0.65 W.

where λ is the wavelength (in nm) of the Raman laser (λ=530 nm). L_a for the carbonized features increased with laser power (Fig. 5.9b) and saturates at ~19 nm beyond 0.20 W. L_a for graphitized features increased to ~23 nm at 0.41 W, and then decreased due to the graphitic features oxidation at higher temperatures [4]. Raman mapping of carbonized track produced at 0.21 W was implemented over a cross-section of 50 x 50 μm^2 (Fig. 5.9c) to measure the uniformity of defect ratio and width of G-band. I_D/I_G ratio ranged from 0.70-1.3 and the G-peak FWHM ranged from 16.3-96.0 cm^{-1}. Raman mapping of graphitized track produced at 0.50 W over a cross-section of 10 x 10 μm^2 showed that the I_D/I_G ratio ranged from 0.7-1.4 and the G-bandwidth ranged from 47.90-70 cm^{-1} (Fig. 5.9d).

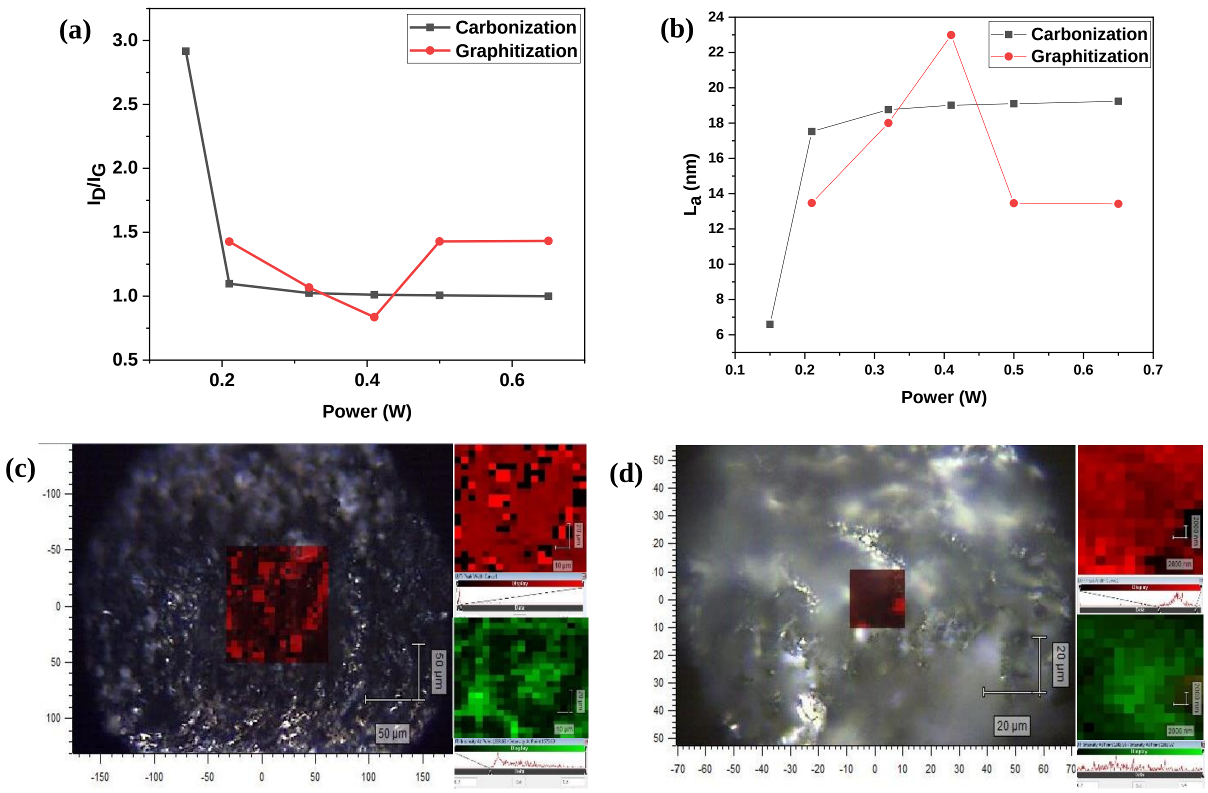

Fig 5.9. (a) Varying I_D/I_G ratio of carbonized and graphitized tracks with laser power, (b) Varying average crystallite domain size as a function of laser power, (c) Raman mapping of carbonized track at 0.21 W, (d) Raman mapping of graphitized track at 0.5 W on a 0.21 W pre-carbonized track.

5.3.5. Electrical Characterization of the carbonized tracks

The IV- plot for each track showed a linear response up to 40 V and resistance was measured from the slope (Fig 5.13a, 5.13b). From the SEM image of the track as in figure 5.8a, dimensions were measured and used to calculate the conductivity of the carbonized tracks, which increased with irradiation due to increasing crystallite size of the graphitic domains. The cross-sectional area (Fig. 5.10) is taken as the area of the segment (*A*) containing LIG under the polyimide surface assuming the LIG is homogenous beneath the surface, using the equation:

$$A = A_1 - [\frac{1}{2}.D.(r-d)] \quad (5.10)$$

where area of the sector, $A_1 = \pi.r.\theta/360$, (5.11)

angle of curvature in degrees, $\theta = 57.29\,.\,2\cos^{-1}\frac{r-d}{r}$, (5.12)

radius of curvature of the arc, $r = \frac{D^2}{8d} + \frac{d}{2}$ (5.13)

where, *d*= carbonization depth and *D*= carbonization width. Conductivity is measured using the equation:

$$\sigma = \frac{1}{R}.L/A \quad (5.14)$$

where *L*= length and *R*= resistance of the LIG track.

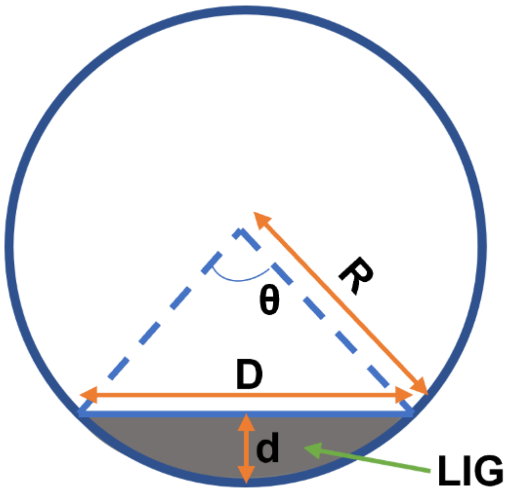

Fig. 5.10. Measurement of cross-sectional area of LIG track.

The tracks carbonized at 0.21 W had a conductivity of 56.14±3.09 $S.m^{-1}$. Upon laser overwriting, the conductivity increased upto 145.1±4.36 $S.m^{-1}$ at 0.50 W (Fig. 5.13c), which can be attributed to the advent of graphitization at this power[44]. Upon further increase in power, the conductivity remained constant explained by the increase in defect level of the graphitic tracks due to ablation of the pre-existing track (Fig. 5.12). The calculation of conductivity is provided in Table 5.4.

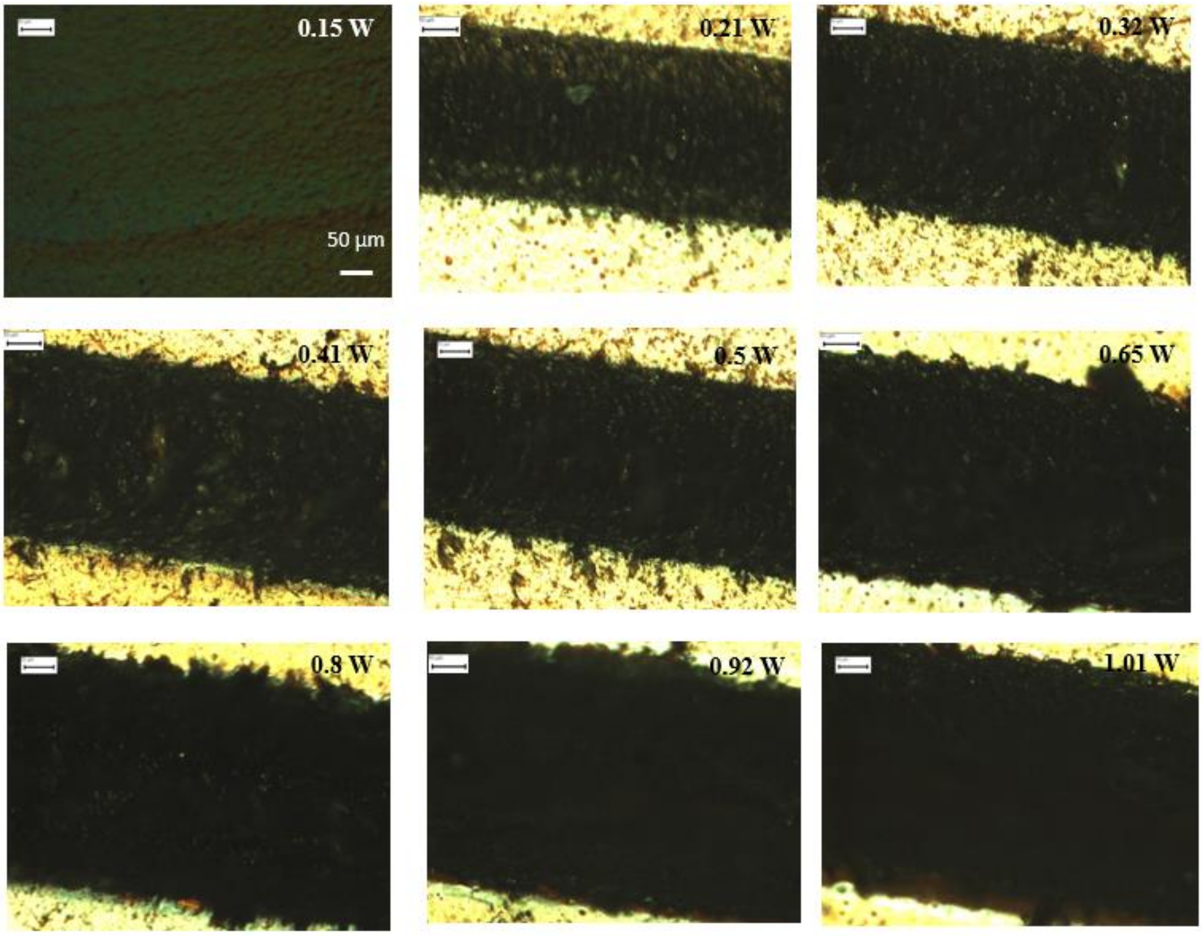

Fig 5.11. Microscopic images of Carbonized vias.

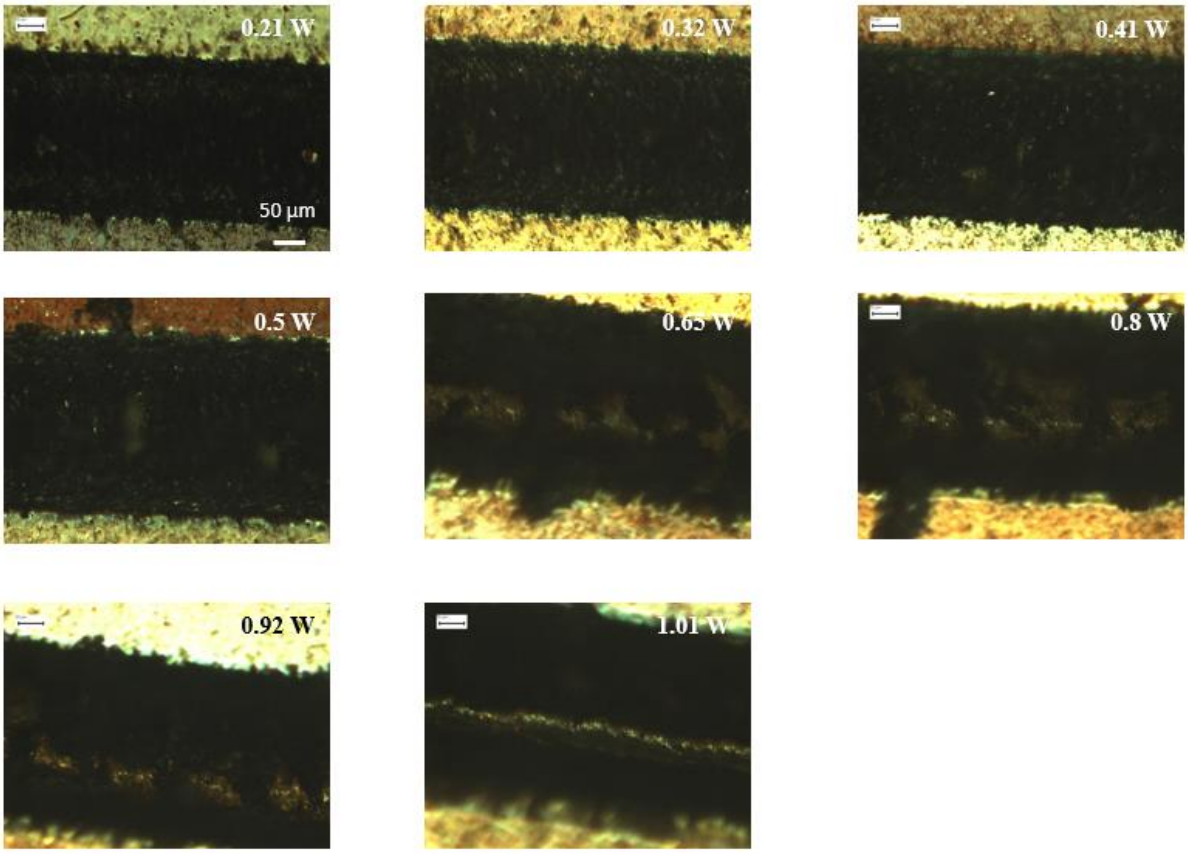

Fig 5.12. Microscopic images of Graphitized vias on pre-carbonized vias at 0.21 W.

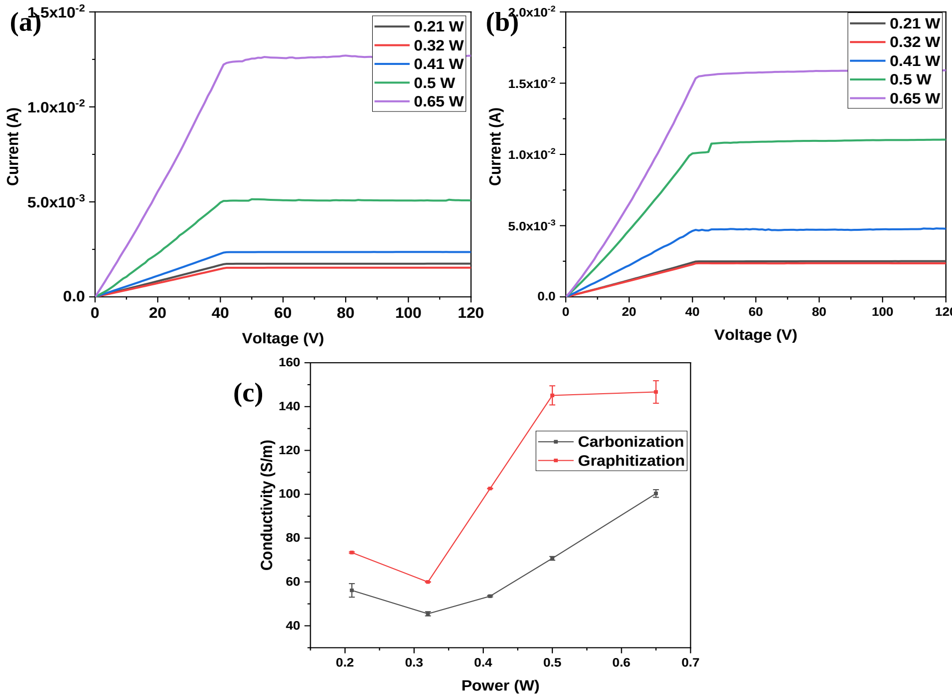

Fig 5.13. (a) I-V plot for carbonized tracks under laser irradiation of power 0.21, 0.32, 0.41, 0.50 and 0.65 W, (b) I-V plot for carbonized tracks under laser irradiation of power 0.21, 0.32,

0.41, 0.5 and 0.65 W on 0.21 pre-carbonized track, (c) Variation of electrical conductivity of the carbonized and graphitized tracks.

Table 5.4. Calculation of conductivity of carbonized and graphitized vias.

Carbonization									
l (mm)	***R (kΩ)***	***ΔR (kΩ)***	***d (μm)***	***Δd (μm)***	***D (μm)***	***ΔD (μm)***	**area (μm²)**	***σ(S/m)***	***Δσ (S/m)***
10.00	23.61	1.30	39.80	0.52	280.47	0.62	7543.75	56.14	3.18
10.00	24.07	0.50	42.50	0.42	318.80	0.72	9132.75	45.49	1.04
10.00	17.95	0.11	46.10	0.32	334.70	0.52	10411.82	53.51	0.50
10.00	8.56	0.10	67.30	0.24	339.70	0.73	16511.15	70.75	0.90
10.00	3.59	0.06	101.00	0.62	368.80	0.85	27770.71	100.34	1.87
Graphitization									
l (mm)	***R (kΩ)***	***ΔR (kΩ)***	***d (μm)***	***Δd (μm)***	***D (μm)***	***ΔD (μm)***	**area (μm²)**	***σ(S/m)***	***Δσ (S/m)***
10.00	16.95	0.08	38.9	0.22	307	0.41	8036.75	73.39	0.33
10.00	17.77	0.03	43	0.27	323.7	0.52	9381.13	59.99	0.11
10.00	8.86	0.01	48.8	0.43	333.3	0.55	10999.56	102.61	0.10
10.00	4.21	0.13	68.5	0.13	348.6	0.67	16375.96	145.11	4.35
10.00	2.97	0.10	90.1	0.38	365.2	0.37	22945.53	146.67	5.13

5.4. Conclusion:

This paper demonstrates a method for improving the electrical conductivity of laser carbonized tracks on PI by Laser graphitization. The laser carbonization of PI was modelled using a simple time-variant Gaussian equation and solved in COMSOL ® software. The idealized model was used to estimate the temperature of laser graphitization of amorphous carbon. The predicted threshold powers of carbonization for scanning pulses were estimated to be 0.15±0.04 W (Fluence= 2.40 ±0.60 x10^3) and graphitization to be 0.50±0.03 W (Fluence= 7.90±0.50 x10^3), at scan speed 120 mm/min and pulse repetition rate 0.10 kHz which were validated from Raman spectra of the corresponding tracks as well. The electrical conductivity increased by a factor of ~2.60 by overwriting the laser at 0.50±0.03 W and fluence 7.90±0.50 x10^3 mJ/cm^2 by maintaining the structural integrity of the substrate. This is due to the graphitization during which the laser increased the conductivity by reducing defect level within the tracks. The conductivity can further be increased but is limited by the thickness of the substrate. Hence, laser graphitization provides a feasible method to improve the conductivity of the laser carbonized structures, and the process is optimized by appropriate selection of laser parameters such as power, repetition rate and scan speed using modelling.

Conflicts of interest:

The authors declare no conflict of interest.

Acknowledgements

Research funding for Ratul Biswas was provided by the College of Science. The laser, simulation and characterization facilities were provided by NCLA, School of Physics, National University of Ireland, Galway. Nazar Farid, Gerard O'Connor acknowledges funding received from a targeted project in SFI Research Centre IPIC 12/RC/2276.

The published journal paper ends here.

5.5. Study with integrated area under the peaks in Raman spectroscopy

Lorrentzian fitting of D, G and 2D peaks were performed for Raman spectra of carbonized tracks (Fig 5.14 a-f) and graphitized tracks (Fig 5.15 a-e) .The integrated area of the Lorrentzian fitted peaks gave a different result as from the peak intensities from the Raman spectra of LIG (Fig 5.16. a) which has been found in other study as well by C. Casiraghi et al [45].

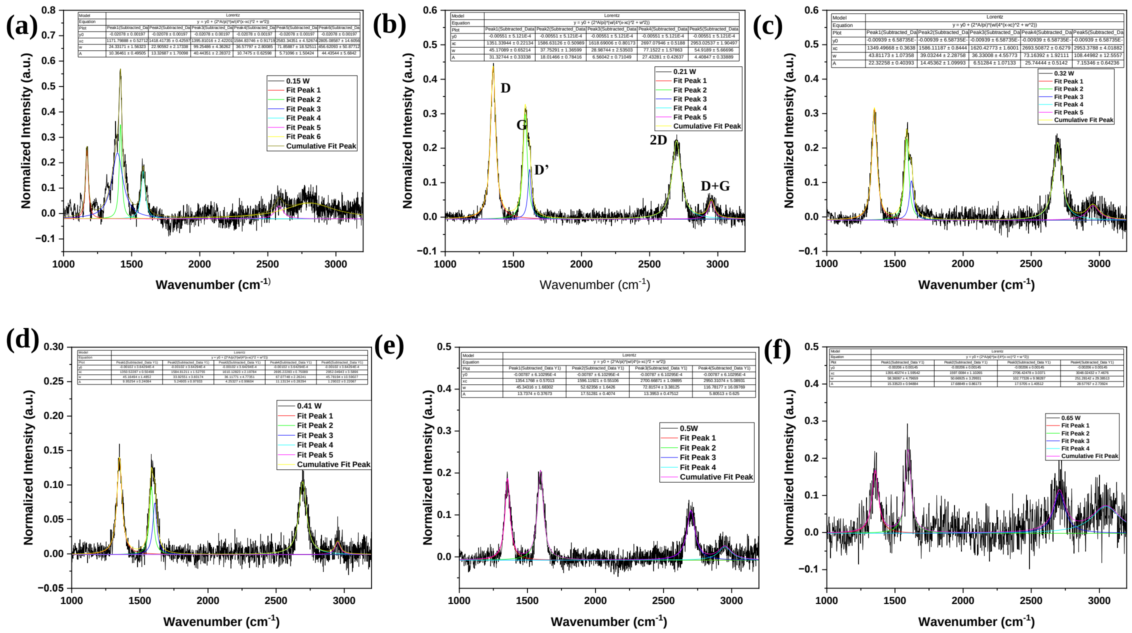

Fig. 5.14. Lorrentzian fitted D, G, D' and 2D peaks in carbonized tracks with laser drawn at (a) 0.15 W, (b) 0.21 W, (c) 0.32 W, (d) 0.41 W, (e) 0.5 W, amd (f) 0.65 W.

The crystallite size of carbonized structures was calculated using the A_D/A_G ratio from the same equation 5.9 and it was found to inrease from 10.88 nm at 0.21 W to 24 nm at 0.5 W followed by a reduction in the size (Fig 5.16. b). The crystallite size of the graphitized structures was calcultaed in the same way and was found to increase from 9.77 nm at 0.21 W to 13.38 nm at 0.32 W followed by decreasign size. The peak position of the G-peak showed a similar trend as Fig. 5.4 b which showed that the graphititzation occurred at 0.5 W (Fig 5.15. f).

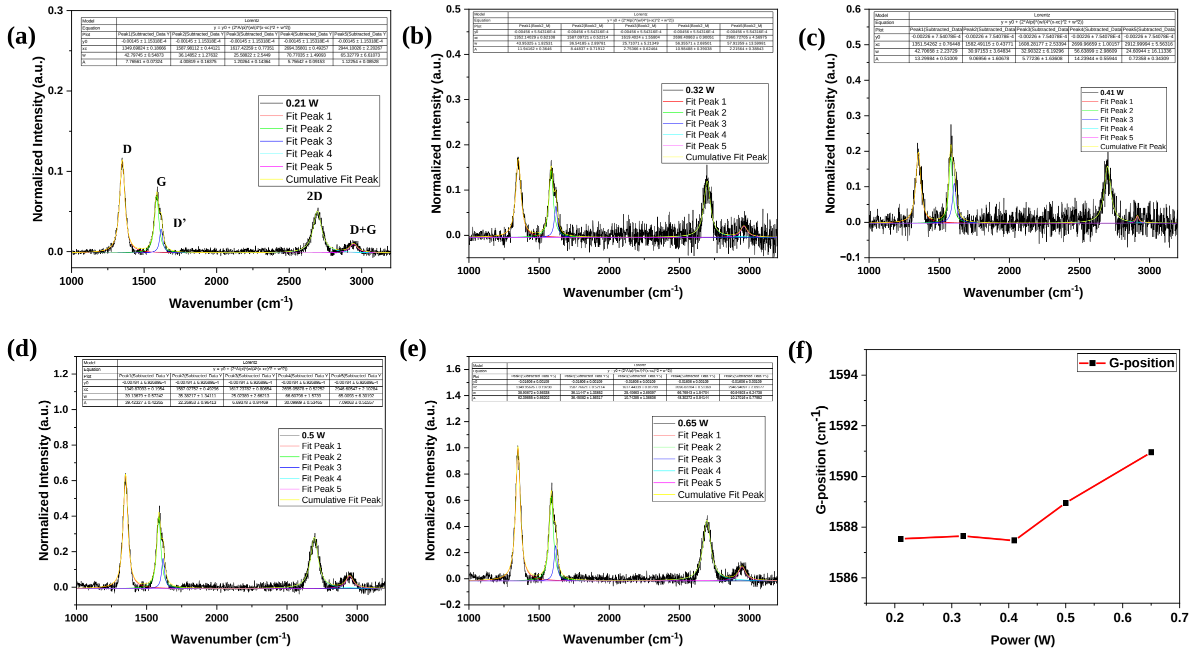

Fig. 5.15. Lorrentzian fitted D, G, D' and 2D peaks in graphitized tracks with laser drawn at (a) 0.21 W, (b) 0.32 W, (c) 0.41 W, (d) 0.5 W, (e) 0.65 W and (f) G-peak position vs power.

Further analysis was done on the deconvolution of the G peak which showed the presence of D' peak at 1621 cm^{-1} the carbonized structures drawn at 0.21-0.41 W. At higher powers, the D' peak was absent which is due to the generation of high defect concentration [45]. The ratio of $A_D/A_{D'}$ reveals the nature of defects present in graphene-based structures [45]. The $A_D/A_{D'}$ ratio decreased upto from ~6 at 0.21 W to ~4 at 0.32W for carbonized structures and then increased to ~5 at 0.41 W (Fig 5.16. c). Higher $A_D/A_{D'}$ ratio is associated with higher sp3 hybridized carbon concentration [45]. The $A_D/A_{D'}$ ratio in graphitized structures showed a sharp fall from ~6 to ~2 at 0.41 W which shows that rewriting the carbonized tracks with CO_2 laser improves the sp2 hybiridization. The $A_D/A_{D'}$ ratio increased again at further powers which could be due to generation of defects at higher laser powers. The fitting of 2D peaks showed that A_{2D}/A_G ratio increased from 1.5 at 0.21 W to 2.1 at 0.41 W and decreased at higher powers (Fig 5.16. d). This shows the number of layers decreased upto 0.41 W and then increased at higher powers.The A_{2D}/A_G ratio of graphititzed tracks increased from 1.4 at 0.21 W to 1.6 at

0.41 W and decreased further at higher powers. This shows that the number of layers in graphitized carbon decreased up to 0.41 W and increased again.

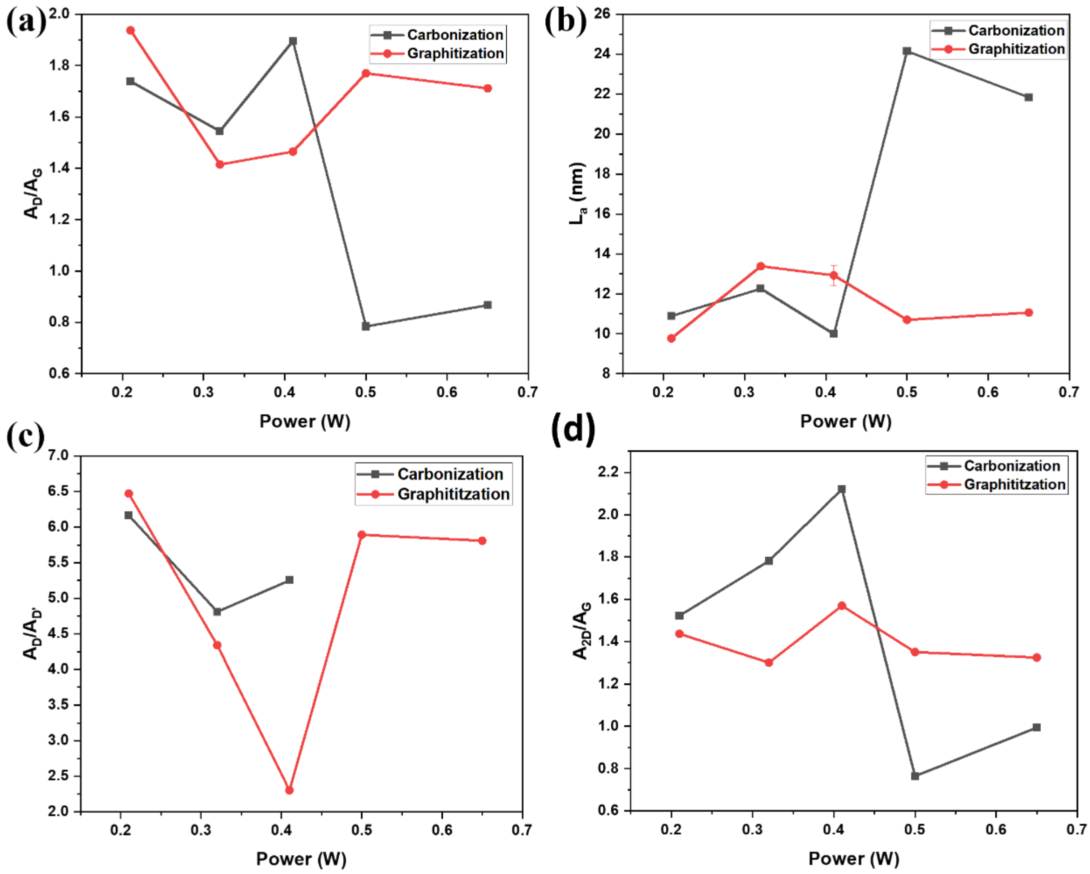

Fig. 5.16. (a) A_D/A_G vs power, (b) L_a vs power, (c) $A_D/A_{D'}$ vs power and (d) A_{2D}/A_G vs power for carbonized and graphtitized tracks.

The Full-width-half-maxima (FWHM) of D, G and 2D peaks were studied from the Lorrentzian fitting. Narrower peaks of D and G (Fig 5.17. a-c) explains the increased crystallinity and narrower peaks of 2D peaks explains the lesser number of layers in it [46, 47]. The FWHM of G peak decreased from 37 cm^{-1} at 0.21 W to 33 cm^{-1} at 0.41 W for carbonized tracks and from 36 cm^{-1} at 0.21 W to 31 cm^{-1} at 0.41 W which showed maximum crystallization occurs for both carbonized and graphitized tracks at 0.41 W. The FWHM of 2D peak decreased at 0.41 W followed by an increase at higher powers for both carbonized and graphitized carbon which showed the number of layers decreased upto 0.41 W and increased at further powers.

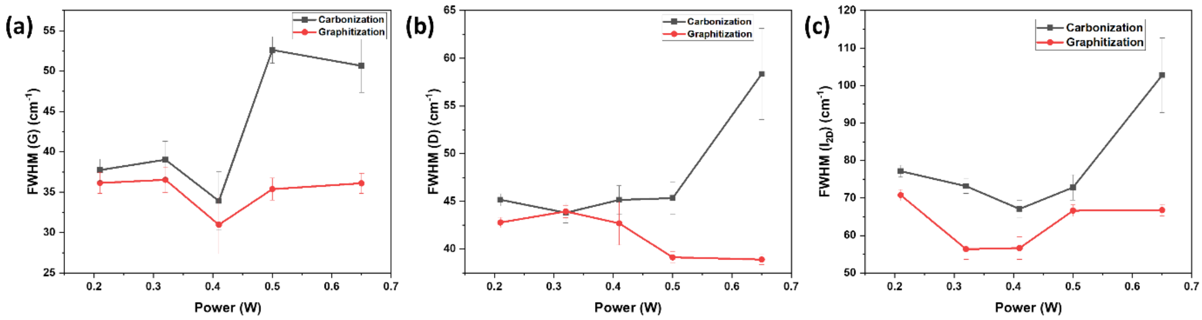

Fig. 5.17. FWHM of (a) G, (b) D and (c) 2D peaks of carbonized and graphitized tracks.

5.6. Summary

The CO_2 laser-Polyimide interaction was modelled in COMSOL and the transformation of PI to sp^2 hybridized carbon was studied. Laser graphitization was done on ta-C and the conductivity improved by ~2.6 times. Hence, the objectives of studying the CO_2 laser-PI interaction and conductivity improvement are met. The models discussed in this chapter can be further used to study the growth kinetics of graphene which will be done in the Chapter 6.

Bibliography

[1] B. Dorin, P. Parkinson, P. Scully, Direct laser write process for 3D conductive carbon circuits in polyimide, Journal of Materials Chemistry C 5(20) (2017) 4923-4930.
[2] S. Luo, P.T. Hoang, T. Liu, Direct laser writing for creating porous graphitic structures and their use for flexible and highly sensitive sensor and sensor arrays, Carbon 96 (2016) 522-531.
[3] J.B. In, Facile fabrication of flexible all solid-state micro-supercapacitor by direct laser writing of porous carbon in polyimide, Carbon v. 83 (2015) pp. 8-151-2015 v.83.
[4] F. Wang, K. Wang, X. Dong, X. Mei, Formation of hierarchical porous graphene films with defects using a nanosecond laser on polyimide sheet, Applied Surface Science (2017) 893-900.
[5] F.J. Romero, A. Salinas-Castillo, A. Rivadeneyra, A. Albrecht, A. Godoy, D.P. Morales, N. Rodriguez, In-Depth Study of Laser Diode Ablation of Kapton Polyimide for Flexible Conductive Substrates, Nanomaterials (Basel) 8(7) (2018) 517.
[6] N. Kurra, Q. Jiang, P. Nayak, H.N. Alshareef, Laser-derived graphene: A three-dimensional printed graphene electrode and its emerging applications, Nano Today 24 (2019) 81-102.
[7] R. Ye, D.K. James, J.M. Tour, Laser-Induced Graphene, Accounts of Chemical Research 51(7) (2018) 1609-1620.
[8] J. Lin, Z. Peng, Y. Liu, F. Ruiz-Zepeda, R. Ye, E.L.G. Samuel, M.J. Yacaman, B.I. Yakobson, J.M. Tour, Laser-induced porous graphene films from commercial polymers, Nature Communications 5 (2014) 5714.
[9] B. Dorin, P. Parkinson, P. Scully, Three-dimensional direct laser written graphitic electrical contacts to randomly distributed components, Applied Physics A 124(4) (2018) 340.
[10] E.B. Secor, P.L. Prabhumirashi, K. Puntambekar, M.L. Geier, M.C. Hersam, Inkjet Printing of High Conductivity, Flexible Graphene Patterns, The Journal of Physical Chemistry Letters 4(8) (2013) 1347-1351.

[11] L. Zhang, H. Liu, Y. Zhao, X. Sun, Y. Wen, Y. Guo, X. Gao, C.-a. Di, G. Yu, Y. Liu, Inkjet Printing High-Resolution, Large-Area Graphene Patterns by Coffee-Ring Lithography, Advanced Materials 24(3) (2012) 436-440.
[12] G. Cummins, M.P.Y. Desmulliez, Inkjet printing of conductive materials: a review, Circuit World 38(4) (2012) 193-213.
[13] J. Alamán, R. Alicante, J.I. Peña, C. Sánchez-Somolinos, Inkjet Printing of Functional Materials for Optical and Photonic Applications, Materials (Basel, Switzerland) 9(11) (2016) 910.
[14] T. Hou, S. Bai, W. Zhou, A. Hu, Laser direct writing of highly conductive circuits on modified polyimide, Journal of Laser Micro Nanoengineering 12(1) (2017) 10.
[15] C.-F. Chen, W.-M. Qin, X.-A. Huang, Characterization and thermal degradation of polyimides derived from ODPA and several alicyclic-containing diamines, Polymer Engineering & Science 48(6) (2008) 1151-1156.
[16] S.D. Senturia, Polyimides in Microelectronics, Polymers for High Technology, American Chemical Society1987, pp. 428-436.
[17] M. Schumann, R. Sauerbrey, M.C. Smayling, Permanent increase of the electrical conductivity of polymers induced by ultraviolet laser radiation, Applied Physics Letters 58(4) (1991) 428-430.
[18] R. Srinivasan, R.R. Hall, W.D. Loehle, W.D. Wilson, D.C. Allbee, Chemical transformations of the polyimide Kapton brought about by ultraviolet laser radiation, Journal of Applied Physics 78(8) (1995) 4881-4887.
[19] M. Fedel, 4 - Blood compatibility of diamond-like carbon (DLC) coatings, in: R. Narayan (Ed.), Diamond-Based Materials for Biomedical Applications, Woodhead Publishing2013, pp. 71-102.
[20] T.V. Kononenko, S.M. Pimenov, V.V. Kononenko, E.V. Zavedeev, V.I. Konov, G. Dumitru, V. Romano, Laser-induced spallation in diamond-like carbon films, Applied Physics A 79(3) (2004) 543-549.
[21] A. Grigonis, A. Medvid, P. Onufrijevs, J. Babonas, A. Rėza, Graphitization of amorphous diamond-like carbon films by laser irradiation, Optical Materials 30(5) (2008) 749-752.
[22] E. Cappelli, C. Scilletta, S. Orlando, V. Valentini, M. Servidori, Laser annealing of amorphous carbon films, Applied Surface Science 255(10) (2009) 5620-5625.
[23] Q. Liu, G. Zhang, H. Zhang, Z. Hou, L. Li, Molecular dynamic simulation on the graphitization of amorphous carbon induced by laser irradiation, 2016 Asia-Pacific Magnetic Recording Conference Digest (APMRC), 2016, pp. 1-2.
[24] T. Roch, A. Lasagni, E. Beyer, Nanosecond UV laser graphitization and delamination of thin tetrahedral amorphous carbon films with different sp3/sp2 content, Thin Solid Films 519(11) (2011) 3756-3761.
[25] J. Narayan, A. Bhaumik, Research Update: Direct conversion of amorphous carbon into diamond at ambient pressures and temperatures in air, APL Materials 3(10) (2015) 100702.
[26] M. He, C. Yeo, Evaluation of Thermal Degradation of DLC Film Using a Novel Raman Spectroscopy Technique, Coatings 8(4) (2018) 143.
[27] S. Küper, J. Brannon, K. Brannon, Threshold behavior in polyimide photoablation: Single-shot rate measurements and surface-temperature modeling, Applied Physics A 56(1) (1993) 43-50.
[28] X. Ruan, R. Wang, J. Luo, Y. Yao, T. Liu, Experimental and modeling study of CO2 laser writing induced polyimide carbonization process, Materials & Design 160 (2018) 1168-1177.
[29] F. Di Niso, C. Gaudiuso, T. Sibillano, F.P. Mezzapesa, A. Ancona, P.M. Lugarà, Influence of the Repetition Rate and Pulse Duration on the Incubation Effect in Multiple-Shots Ultrafast Laser Ablation of Steel, Physics Procedia 41 (2013) 698-707.

[30] L. Jiang, H.-L. Tsai, Improved Two-Temperature Model and Its Application in Ultrashort Laser Heating of Metal Films, Journal of Heat Transfer 127(10) (2005) 1167-1173.
[31] S. Prakash, S. Kumar, CO2Laser Microchanneling Process: Effects of Compound Parameters and Pulse Overlapping, IOP Conference Series: Materials Science and Engineering 149 (2016) 012018.
[32] R.I. Wu, D ; McCormick, A ; Rai, A ; Pronko, P ; Woollam, J ; De, B ; Ianno, N, Diamondlike Carbon Coatings for Optical Systems
U.S. ARMY MATERIALS TECHNOLOGY LABORATORY (1989) 119.
[33] M. Shamsa, W.L. Liu, A.A. Balandin, C. Casiraghi, W.I. Milne, A.C. Ferrari, Thermal conductivity of diamond-like carbon films, Applied Physics Letters 89(16) (2006) 161921.
[34] M. Hakovirta, J.E. Vuorinen, X.M. He, M. Nastasi, R.B. Schwarz, Heat capacity of hydrogenated diamond-like carbon films, Applied Physics Letters 77(15) (2000) 2340-2342.
[35] A.C. Ferrari, D.M. Basko, Raman spectroscopy as a versatile tool for studying the properties of graphene, Nature Nanotechnology 8 (2013) 235.
[36] N.R. Arutyunyan, M.S. Komlenok, E.V. Zavedeev, S.M. Pimenov, Raman Spectroscopy of Amorphous Carbon Films Modified by Single-Pulse Irradiation of Nanosecond and Femtosecond Lasers, physica status solidi (b) 255(1) (2018) 1700225.
[37] C. Ferrante, A. Virga, L. Benfatto, M. Martinati, D. De Fazio, U. Sassi, C. Fasolato, A.K. Ott, P. Postorino, D. Yoon, G. Cerullo, F. Mauri, A.C. Ferrari, T. Scopigno, Raman spectroscopy of graphene under ultrafast laser excitation, Nature Communications 9(1) (2018) 308.
[38] W. Zhang, Y. Lei, Q. Jiang, F. Ming, P.M.F.J. Costa, H.N. Alshareef, 3D Laser Scribed Graphene Derived from Carbon Nanospheres: An Ultrahigh-Power Electrode for Supercapacitors, Small Methods 3(5) (2019) 1900005.
[39] S. Wang, Y. Yu, S. Luo, X. Cheng, G. Feng, Y. Zhang, Z. Wu, G. Compagnini, J. Pooran, A. Hu, All-solid-state supercapacitors from natural lignin-based composite film by laser direct writing, Applied Physics Letters 115(8) (2019) 083904.
[40] Y. Chyan, R. Ye, Y. Li, S.P. Singh, C.J. Arnusch, J.M. Tour, Laser-Induced Graphene by Multiple Lasing: Toward Electronics on Cloth, Paper, and Food, ACS Nano 12(3) (2018) 2176-2183.
[41] D.X. Luong, K.V. Bets, W.A. Algozeeb, M.G. Stanford, C. Kittrell, W. Chen, R.V. Salvatierra, M. Ren, E.A. McHugh, P.A. Advincula, Z. Wang, M. Bhatt, H. Guo, V. Mancevski, R. Shahsavari, B.I. Yakobson, J.M. Tour, Gram-scale bottom-up flash graphene synthesis, Nature 577(7792) (2020) 647-651.
[42] Y. Dong, S.C. Rismiller, J. Lin, Molecular dynamic simulation of layered graphene clusters formation from polyimides under extreme conditions, Carbon 104 (2016) 47-55.
[43] L.G. Cançado, K. Takai, T. Enoki, M. Endo, Y.A. Kim, H. Mizusaki, A. Jorio, L.N. Coelho, R. Magalhães-Paniago, M.A. Pimenta, General equation for the determination of the crystallite size La of nanographite by Raman spectroscopy, Applied Physics Letters 88(16) (2006) 163106.
[44] S. Lee, S. Jeon, Laser-Induced Graphitization of Cellulose Nanofiber Substrates under Ambient Conditions, ACS Sustainable Chemistry & Engineering 7(2) (2019) 2270-2275.
[45] A. Eckmann, A. Felten, A. Mishchenko, L. Britnell, R. Krupke, K.S. Novoselov, C. Casiraghi, Probing the Nature of Defects in Graphene by Raman Spectroscopy, Nano Letters 12(8) (2012) 3925-3930.
[46] A. Sharif, N. Farid, A. Collins, A. Jilani, G.M. O'Connor, Extensive reduction of graphene oxide on thin polymer substrates by ultrafast laser for robust flexible sensor applications, Applied Surface Science 613 (2023) 156067.

[47] S. Karamat, S. Sonuşen, Ü. Çelik, Y. Uysallı, E. Özgönül, A. Oral, Synthesis of few layer single crystal graphene grains on platinum by chemical vapour deposition, Progress in Natural Science: Materials International 25(4) (2015) 291-299.

6. Chapter 6: Graphene growth kinetics in laser carbonization

In this chapter, the growth of graphene on PI surface in the laser carbonization process is investigated for the first time. The kinetics for other processes such as CVD, epitaxy were previously studied but not for for the laser carbonization process. In the first paper, published in Materials Letters, Elsevier, 2022, the growth kinetics are studied using the Arrhenius model and the activation energy of graphene growth in this process is calculated. In the second paper, submitted in Materials Letters, 2023, the planar growth of graphene on PI is optimized using a cold Argon plasma treatment of PI where such a treatment increases the wettability of the PI surface which improves the step-flow growth of graphene nuclei on PI. Both papers together contribute to understanding the kinetics of growth of graphene on PI and the controlling factors of the growth which falls within the scope of this project. Ratul Biswas conducted the experiments with CO_2 laser and plasma pen and characterized the LIG using Raman spectroscopy in NCLA, UoG and wrote the paper. SEM was performed at the Centre of Microscopy and Imaging, UoG. R. K. Vijayaraghavan and Patrick McNally assisted with the X-Ray diffraction study of the LIG done in the Dublin City University. Peter McGlynn assisted with the plasma-pen experiments. The contribution of Ratul Kumar Biswas in this chapter is 80%, Peter McGlynn is 10%, R. K. Vijayaraghavan is 5%, and Patrick McNally is 5%. Patricia Scully supervised and helped in the overall conceptualization of the project and Gerard O’Connor co-supervised and provided access to the lasers and characterization tools at the NCLA. The supplementary information of the papers are included in this chapter within the context.

6.1. Graphene Growth Kinetics for CO_2 Laser Carbonization of Polyimide

Ratul Kumar Biswas[a], Rajani K. Vijayaraghavan[b], Patrick McNally[b], Gerard M. O'Connor[*a], Patricia Scully[*a]

[a]*NCLA, National University of Ireland, Galway, Ireland.*

[b]*School of Electronic Engineering, Dublin City University.*

Mater. Lett., 15 January 2022, **307**, 131097

Abstract: The study of growth kinetics of graphene on Polyimide upon carbon-dioxide (CO_2) laser irradiation enables optimisation of crystal size for maximum electrical conductivity. We report the first study on growth kinetics of graphene produced by laser carbonization of polyimide using the Arrhenius equation. The peak irradiation temperature (T_{irr}) for each laser fluence was calculated from the photothermal model, solved by Finite Element Analysis in COMSOL software. Studies of the Raman spectra of the laser induced graphene revealed that the crystallite size increases with decreasing scan-speed at constant laser fluence. The barrier activation energy for graphene growth was found to be 0.20±0.03 eV.

Keywords

Laser carbonization; graphene; crystal growth; Arrhenius kinetic

6.1.1. Introduction:

Laser carbonization is a promising method for large scale patterning of graphene on Polyimide (PI), for manufacturing which involves photothermal conversion of PI to graphene, called Laser Induced Graphene (LIG), by irradiation of Carbon-di-oxide (CO_2) laser [1-4]. LIG has been used in flexible sensor devices such as urea, glucose sensors, and energy storage applications such as supercapacitors [3, 4]. However, LIG is mostly limited to nanoflakes having edge-defects [5] inhibiting its intrinsic electrical conductivity and limiting its application in flexible electronics. Each laser pulse at a constant fluence, should thermalize PI with controlled kinetics, and graphene growth from PI follows the Arrhenius classic kinetic equation as a function of temperature and time [6]. Since both irradiation temperature and time are governed by the laser fluence and scan-speed, the Arrhenius kinetic parameters such as growth barrier activation energy and pre-exponential coefficient can also be calculated for this process to control LIG crystallite size. Kinetic parameters for graphene growth have been calculated previously, for other thermally activated processes such as Chemical Vapour Deposition, where the barrier energy for growth on copper calculated from the Arrhenius plot is 2.6±0.5 eV [7]. A Molecular Dynamics study of laser carbonization has shown that the formation of crystalline graphene clusters from PI occurs without a catalyst at very low activation temperature (>2400 K or 0.207 eV), due to generation of high pressure (~3 GPa) [8, 9]. Here, we have estimated the peak laser irradiation temperature (T_{irr}) from photothermal model using the Finite Element Method in COMSOL software, laser irradiation time (t_{irr}) from scan-speed [10], and the average crystallite size (L_a) from the defect ratio in the Raman spectra of LIG [11] produced at varying scan-speed under constant laser fluences. Such parameters will enable the appropriate scan-speed to be derived for varying laser fluence to obtain maximum crystallite size of graphene.

6.1.2. Experimental Methods:

Laser carbonization was performed with GEM 6O Coherent DEOS CO_2 laser system of wavelength (λ) 10.6 µm, integrated with a DEI PDG-2510 Digital Pulse Generator. 127 µm PI film (Dupont Kapton^R HN) with dimension 25 mm x 10 mm was cleaned with ethanol and de-ionized (DI) water in an ultrasonic apparatus and rinsed for 10 minutes followed by drying. The laser was focused with a lens of focal length 100 mm onto the film.

Single laser pulse carbonization was carried out to measure the spot-radius (ϖ_0) of laser and threshold power (P_{Th}) for carbonization. Single pulse carbonization was performed at a power (P) range of 0.550-1.115 W by varying pulse duration (t_p) from 70-120 µs at constant repetition rate (f) 100 Hz. The output power was measured using a Thorlabs PM100D power meter integrated with a S322C thermal sensor.

Linear tracks of carbonized structures of length 10mm were drawn on PI surface at scan-speeds (v) of 350, 450, 550, 650, and 750 mm/min individually at power (P) 0.55, 0.65, 0.77, 0.89, 0.99 and 1.12 W, and corresponding fluences (F) $6.07x10^3$ mJ/cm^2, $7.19x10^3$ mJ/cm^2, $8.56x10^3$ mJ/cm^2, $9.85x10^3$ mJ/cm^2, $1.09x10^4$ mJ/cm^2, and $1.23x10^4$ mJ/cm^2 respectively at repetition rate (f) 100 Hz. The length and scan-speed were defined by Advanced Laser Software and Unidex 500 program.

6.1.3. Structural Characterization of carbonized tracks:

The diameter of single pulse carbonized features and LIG linear tracks were measured using a Olympus BX60M optical microscope by averaging along two perpendicular axes. The average crystallite size was calculated from Raman spectroscopy of LIG taken over 5 points through the central positions of each track measured by RENISHAW inVia Raman Spectrometer using 532 nm excitation laser.

6.1.4. Modelling of laser irradiation temperature (T_{irr}):

T_{irr} was estimated using a Finite Element Analysis (FEA) software package-COMSOL^R for a time-variant Gaussian equation for laser source at position (x,y) written as [12]:

$$Q(x,y) = 2F \cdot \left[\frac{\alpha(\lambda)}{\sqrt{(\pi/ln\,2)\tau_p}}\right].(1-R_e).[exp\left\{-2\left(\frac{x}{\omega_0}\right)^2 - 4\,ln\,2\left(\frac{t-t_c}{t_P}\right)^2\right\}]\,exp(\alpha(\lambda)y) \quad (6.1)$$

Where, absorption coefficient (*α(λ)*) and reflectivity (R_e) are given by [12]:

$$\alpha(\lambda) = \frac{4\pi\kappa}{\lambda}\ ,\ R_e = \left[\frac{(1-n)^2+\kappa^2}{(1+n)^2+\kappa^2}\right] \quad (6.2)$$

Where n and κ are refractive index and extinction coefficient of Polyimide, respectively shown in table 6.1, and reference time, $t_c=2t_p$. Single pulse fluence (*F*) given by [13]:

$$F = \frac{2P}{f\pi\omega_0^2} \quad (6.3)$$

Table 6.1. Summary of optical and thermal properties of Polyimide.

Material	*n*	*κ*	*K(T)* (W/cm.K)	$C_P(T)$ (J/g.K)
PI	1.75 [14]	0.03[14]	$1.55.10^{-3}.\left(\frac{T}{300}\right)^{0.28}$ [15]	$2.55 - 1.59.\exp\left[\frac{300-T}{460}\right]$ [15

The temporal temperature distribution was measured from the Fourier heat equation [14]:

$$\rho C_p(T)\left(\frac{\partial T}{\partial t}\right)[-\nabla[K(T)\nabla T] = Q(x,y) \quad (6.4)$$

Where, ρ, $C_p(T)$, and $k(T)$ are density, specific heat, and thermal conductivity of PI respectively, shown in Table 6.1. T_{irr} at each fluence was calculated from simulation and t_{irr} is given by [10]:

$$t_{irr} = \frac{2\omega_0}{v} \quad (6.5)$$

6.1.5. Results and Discussion:

6.1.5.1. Calculation of spot-size, threshold laser fluence, and irradiation temperature:

Single pulses of CO_2 laser created carbonized spots with diameter increasing with laser power (Fig. 6.1 a-f). The relation between ω_0 and P is given by equation [13]:

$$D^2 = 2\omega_0^2[\ln(P) - \ln(P_{Th})] \quad (6.6)$$

Where P_{Th} is threshold laser power for single pulse. ω_0 and P_{Th} were calculated from the slope and *x*-intercept of plot D^2 vs *ln(P)* (Fig. 6.1g) and were found to be 240.167 μm and 0.489 W respectively.

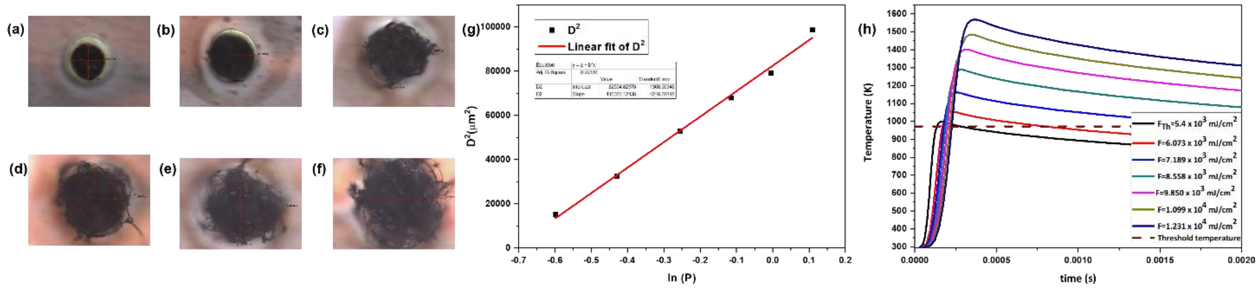

Fig. 6.1. (a-f) Carbonized spots on PI with single pulse CO_2 laser for power 0.55-1.12 W, (g) D^2 vs ln(P) of LIG. (h) Temporal evolution of temperature at laser fluence of $6.07 x 10^3$-$1.23 x 10^4$ mJ/cm^2.

The single pulse threshold fluence (F_{Th}) was calculated using equation (3) and evaluated as 5.4 x 10^3 mJ/cm^2.

The peak threshold temperature of carbonization (T_{Th}) by laser irradiation at fluence F_{Th} was estimated by solving equations 1 and 4 in COMSOL, and was determined as 997.83 K (724.83^{0}C), which is close to threshold carbonization temperature of 700^{0}C obtained from other studies [16]. Hence, this model was used to find the peak T_{irr} at laser spot for different fluences (Fig. 6.1h) and was used to study the growth of LIG over a given irradiation time, t_{irr}.

6.1.5.2. Surface morphology of LIG:

According to cross-sectional SEM (Hitachi S-2600) analysis, the carbonization depth increased with increasing power and decreased with increasing scan speed at constant power (Fig. 6.2). Fiber growth was observed at higher powers and higher scan speeds.

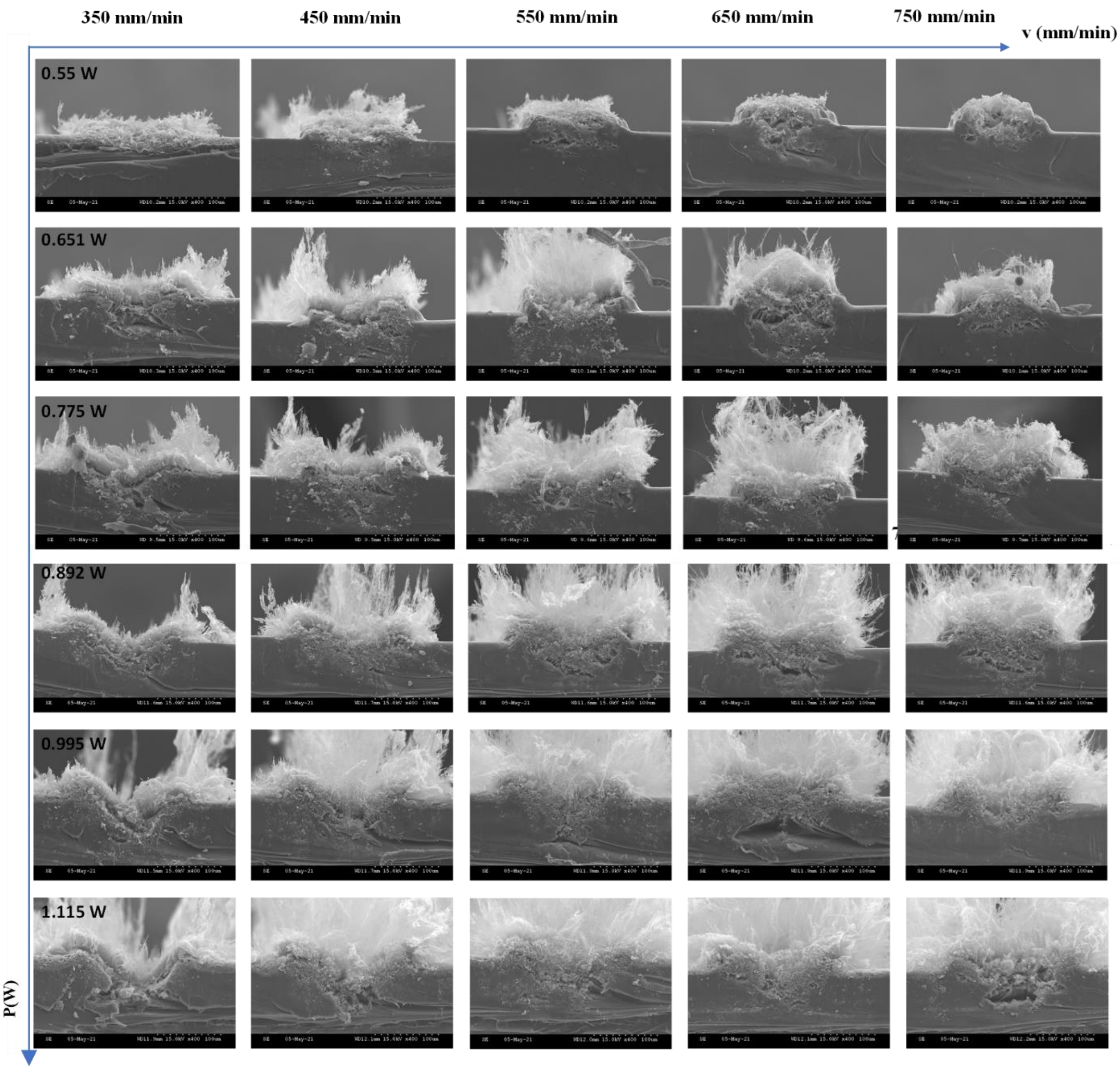

Fig. 6.2. Cross-sectional SEM images of carbonized tracks at P=0.55W, 0.651W, 0.775W, 0.892 W, 0.995 W, and 1.115 W at scan speeds 350-750 mm/min.

6.1.5.3. Calculation of Arrhenius kinetic parameters from crystallite size at different laser fluence and scan-speed:

Like every graphene-based material, three major peaks D, G, and 2D, situated at ~1344 cm^{-1}, ~1576 cm^{-1}, and ~2688 cm^{-1} respectively, were found in LIG for all fluences and scan-speed studied (Fig. 6.3). The D-peak is associated with breathing mode of phonons of A_{1g} symmetry and shows defect content in graphene. The G-peak is associated with in-plane vibrations of E_{2g} phonons and 2D-peak arises from overtone of D-band. The average graphene crystallite size (L_a)

is calculated from the ratio of intensity of D and G peaks, termed as I_D/I_G ratio from equation [11]:

$$L_a = (2.4 \times 10^{-10}) \times \lambda^4 \times (\frac{I_D}{I_G})^{-1} \quad (6.7)$$

I_D/I_G was found to increase with increasing scan-speed (fig. 6.4a). The crystallite growth of Graphene from PI follows Arrhenius equation, given by [6]:

$$\frac{dL}{dt} = k_0 \exp\left(-\frac{E_A}{R.T_{irr}}\right) \quad (6.8)$$

Where, E_A= Activation energy, k_0= pre-exponential growth constant, and R= universal gas constant= 8.314 $J.K^{-1}.mol^{-1}$.

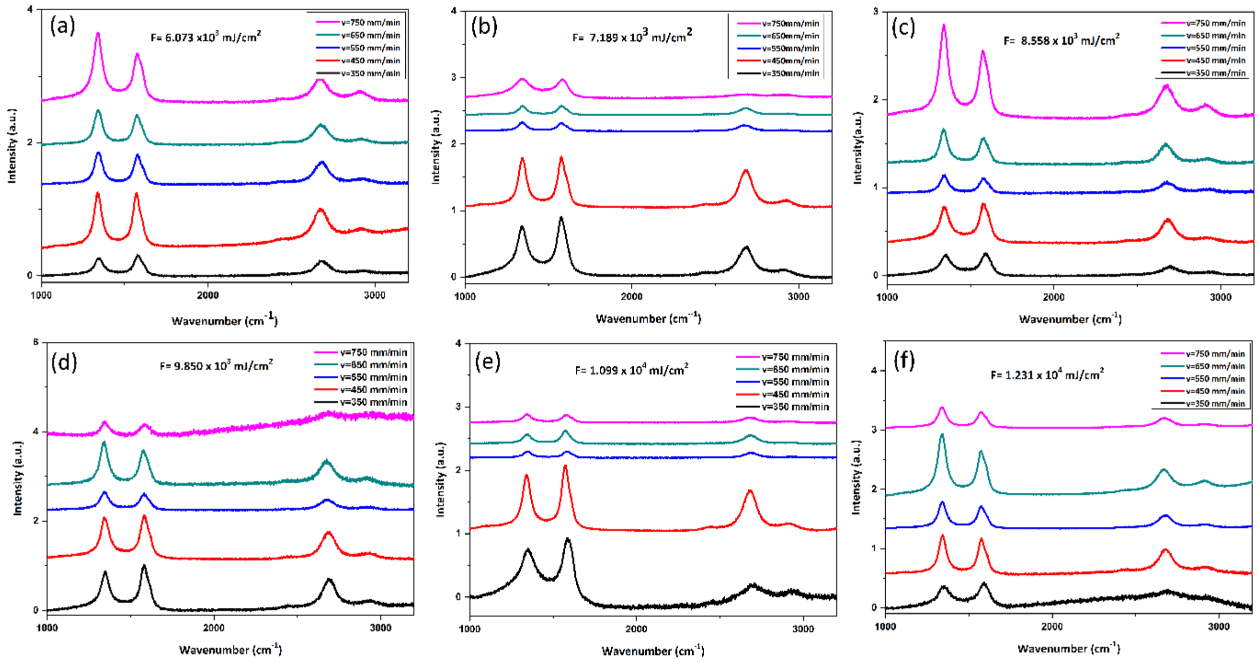

Fig. 6.3. Raman spectroscopy of LIG written at scan-speed 350-750 mm/min at laser fluence (a) $6.07x10^3$ mJ/cm^2, (b) $7.19x10^3$ mJ/cm^2, (c) $8.56x10^3$ mJ/cm^2, (d) $9.85x10^3$ mJ/cm^2, (e) $1.09x10^4$ mJ/cm^2, and (f) $1.23x10^4$ mJ/cm^2.

Integrating equation 8 on both sides:

$$\int_{L_0}^{L_a} dL = k \int_0^{t_{irr}} dt$$

$$L_a = L_0 + k.t_{irr} \quad (6.9)$$

Where L_0= nuclei size formed during the initial stage of carbonization before reaching the peak temperature T_{irr}, and

$$k = k_0 \exp\left(-\frac{E_A}{R.T_{irr}}\right)$$

$$\ln k = \ln(k_0) - \frac{E_A}{R.T_{irr}} \tag{6.10}$$

For each scan-speed, t_{irr} was calculated from eq. 6.5, and L_a was plotted against t_{irr} for each fluence studied (Fig. 6.4b) from which the slope and y-intercepts give the value of k and L_0 respectively. The obtained values of k were plotted as $ln(k)$ vs $1/T$ (Fig. 6.4d), from which the slope and y-intercept give the value of activation temperature (T_A) and k_0 as 2.35 ± 0.30 x 10^3 K and 437 ± 17 nm/s respectively. The barrier activation energy for growth E_A ($=k_BT_A$) was found to be 0.20±0.03 eV, where k_B is the Boltzmann constant and 19.54 ± 2.49 x 10^3 J/mol for ($E_A= RT_A$). Molecular dynamics studies have shown that the PI lattice needs to thermalize to ~2.40 x 10^3 K for graphene ring formation [8].

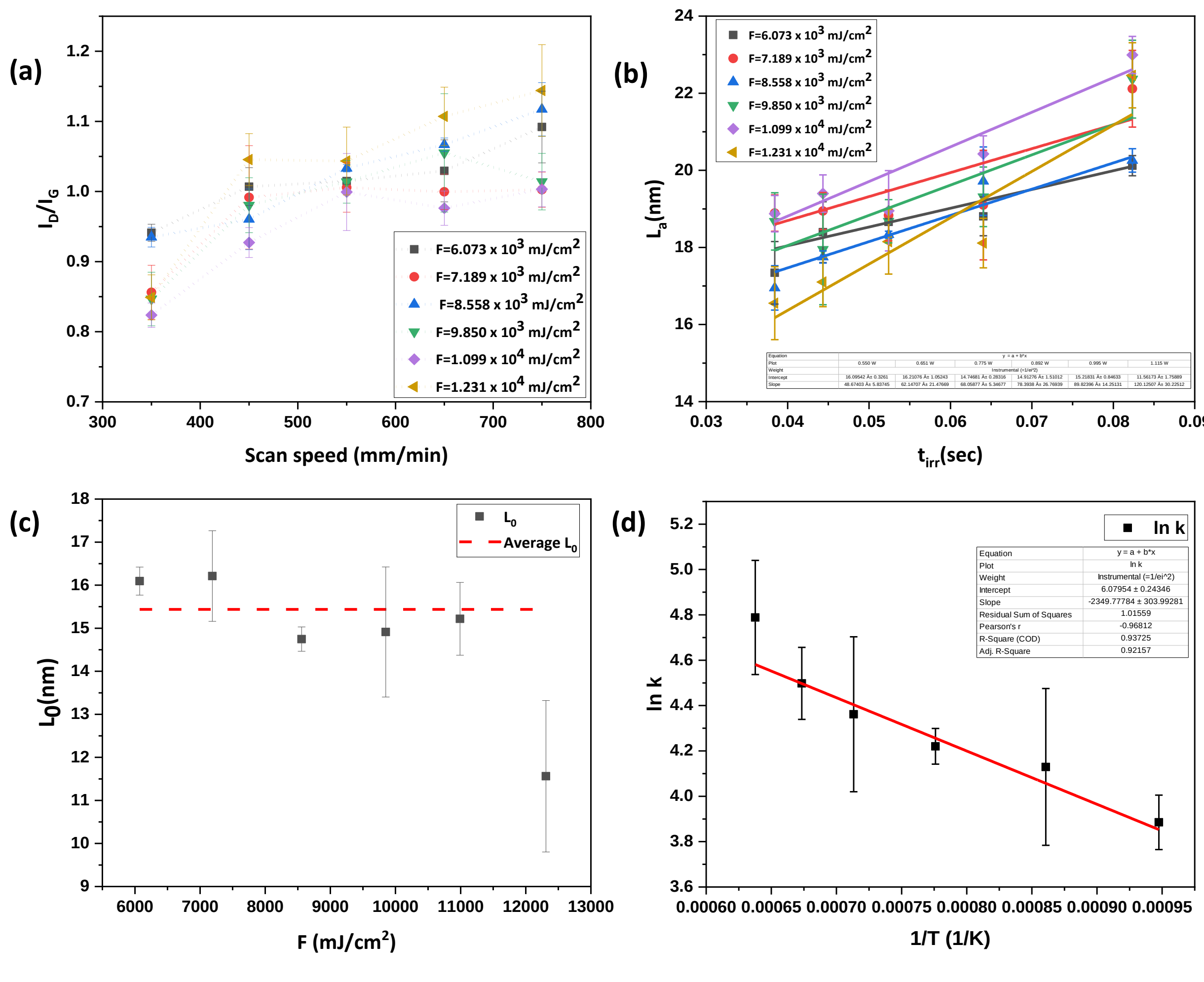

Fig. 6.4. (a) I_D/I_G vs laser scan-speed, (b) Crystallite size vs irradiation time at individual fluence 6.07x10^3-1.23x10^4 mJ/cm^2, (c) Nuclei size vs laser fluence, and (d) $ln(k)$ vs $1/T$.

Hence, the calculation of activation energy is satisfactory. The average nuclei size within fluence range 6.07 x 10^3 -1.09 x 10^4 mJ/cm^2 was found to be 15.44±2.07 nm (Fig 6.4c). The nuclei size decreased to 11.56±1.76 nm at fluence= 1.23 x 10^4 mJ/cm^2, due to keyhole defect formations increasing with fluence, similar to that studied from melt-pool dynamics for various other materials [17]. This reveals that the laser scan at lower fluence (F_{Th}<F<1.09 x 10^4 mJ/cm^2) is preferred to obtain larger graphene nuclei.

Raman mapping of LIG track written at 0.892 W and scan speed 650 mm/min was performed along the length (Fig. 6.5 a) and width (Fig. 6.5 b) of the LIG track to find the consistency of the I_D/I_G values. The I_D/I_G value varied from 0.9-1.1 along the central line of the length, showing better consistency within throughout the central position of the tracks. In addition, the Raman spectra from five points along the length was studied and the I_D/I_G ratio was measured from it (Fig. 6.5 d, e) which showed an average value of 1.02.

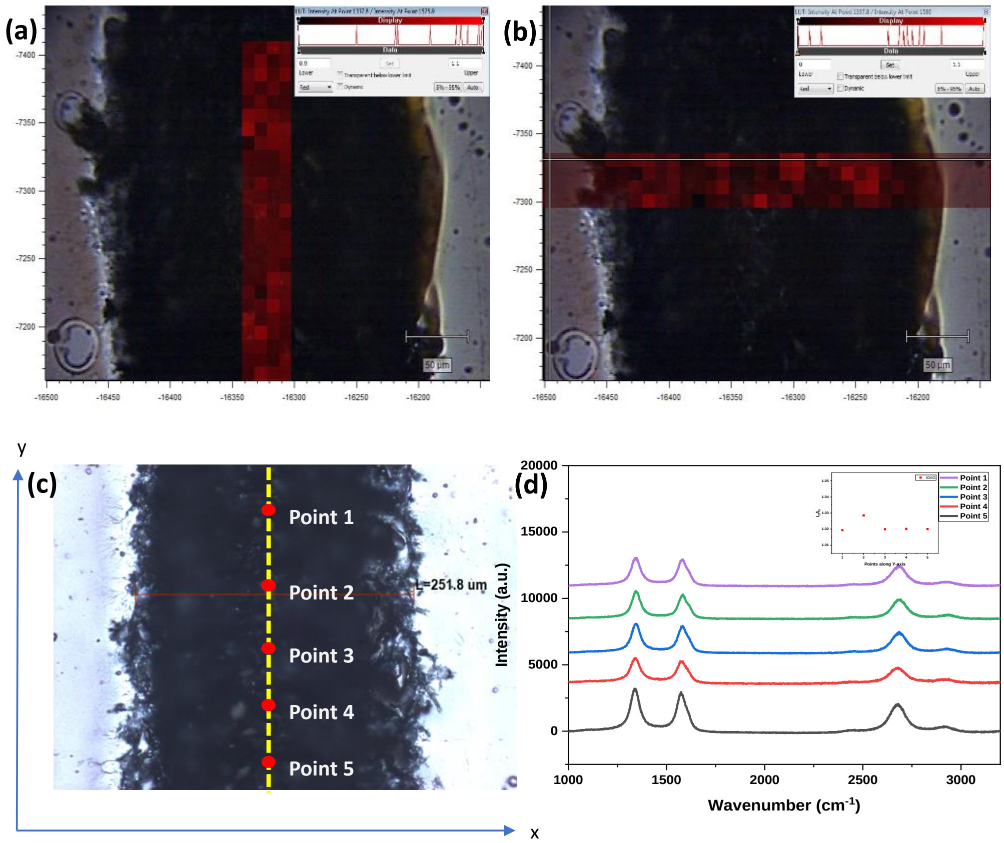

Fig. 6.5. Raman mapping of LIG across (a) length, and (b) width of the track, (c) LIG track written at 0.892 W, 650 mm/min, (d) Raman spectra taken at 5 points along Y-axis with inset of I_D/I_G values at 5 points.

6.1.5.4. Optical microscopy and Electrical characterization of LIG at different laser fluence and scan-speed:

The carbonization width and depth reduced with increasing scan speed. As reported from Raman spectra of graphene, the crystallite size decreases with increasing scan speed, due to which, the electrical conductivity of LIG decreased with increasing scan speed at constant laser power (Fig. 6.8). IV measurments of LIG are shown in Fig. 6.7. Calculation of conductivity and crystallite size are shown in table 6.2 and 6.3 respectively. Necking of carbonized tracks was observed due to varying pulse overlap at varying scan speeds. The dimensions of the necks are plotted in the Appendix Fig. SS17.

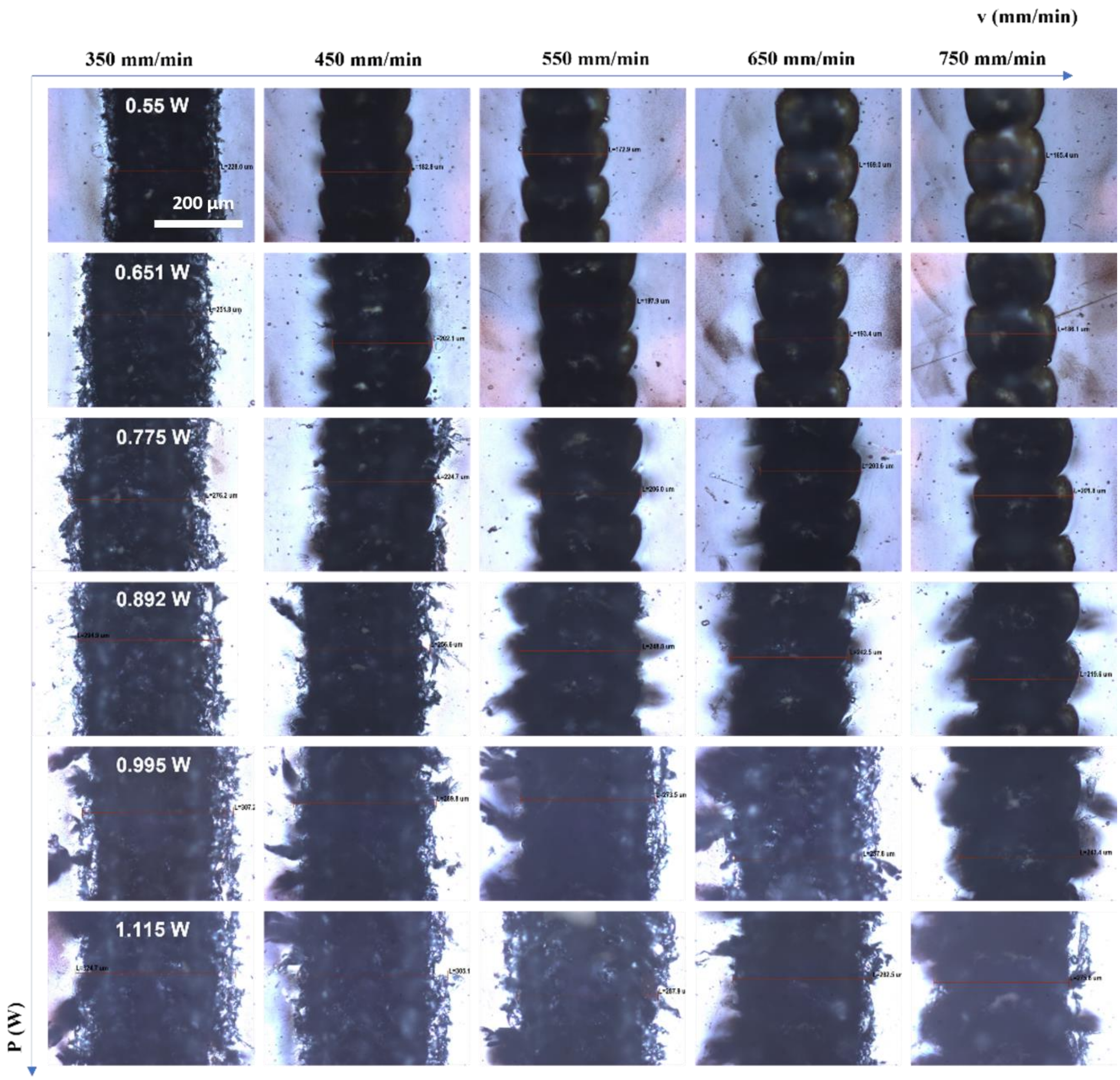

Fig. 6.6. Optical microscopy images of carbonized tracks at P=0.55W, 0.651W, 0.775W, 0.892 W, 0.995 W, and 1.115 W at scan speeds 350-750 mm/min.

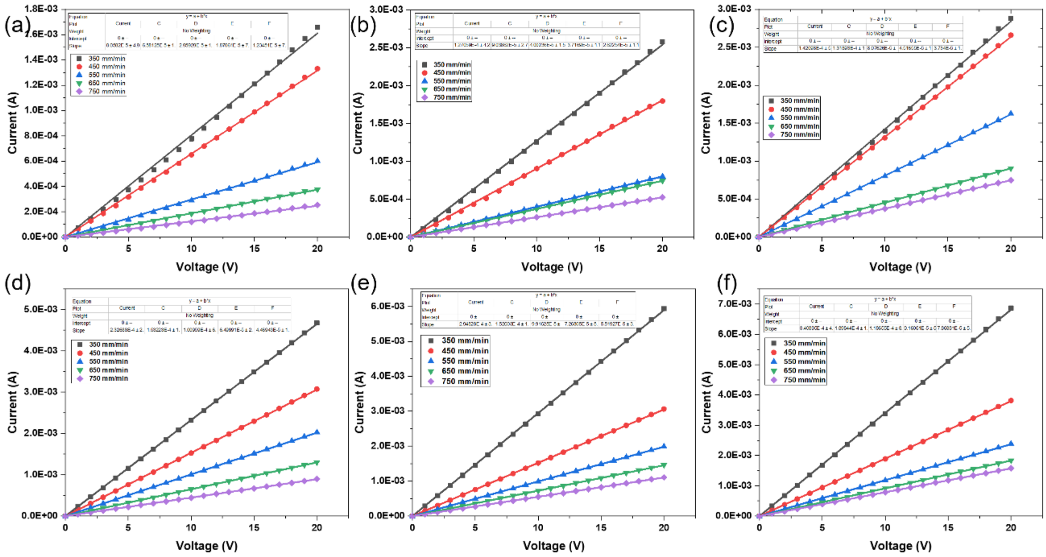

Fig. 6.7. IV measurement of LIG written at scan-speed 350-750 mm/min at laser power (a) 0.55 W, (b) 0.651 W, (c) 0.775 W, (d) 0.892 W, (e) 0.995 W, and (f) 1.115 W.

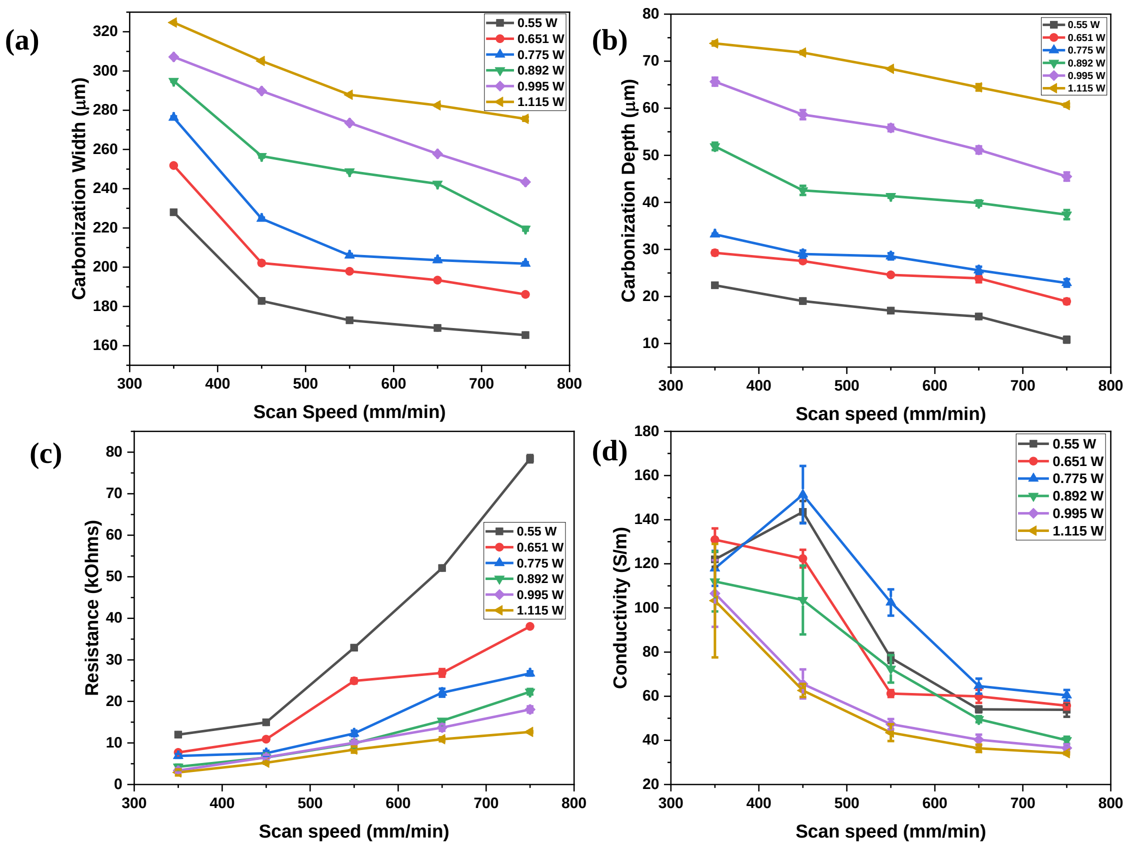

Fig. 6.8. (a) Carbonized width vs scan speed, (b) carbonized depth vs scan speed, (c) Resistance vs scan speed, and (d) Conductivity vs scan speed of LIG at P= 0.55 W, 0.651 w, 0.775 W, 0.892W, 0.995 W, 1.115 W.

Table 6.2. Calculation of uncertainty in conductivity.

P	0.55 W								
***v* (mm/min)**	***R* (kΩ)**	***ΔR* (kΩ)**	***d* (μm)**	***Δd* (μm)**	***D* (μm)**	***ΔD* (μm)**	**area (μm²)**	***σ(S/m)***	***Δσ* (S/m)**
350.00	12.01	0.23	22.39	0.45	228.00	0.62	3411.07	122.01	3.37
450.00	14.96	0.31	19.03	0.51	182.80	0.72	2328.32	143.52	4.93
550.00	32.94	0.53	16.98	0.41	172.90	0.52	1962.34	77.36	2.27
650.00	52.10	0.51	15.74	0.36	169.00	0.73	1775.11	54.06	1.35
750.00	78.42	0.87	10.82	0.62	165.40	0.85	1183.76	53.86	3.17
P	0.651 W								
***v* (mm/min)**	***R* (kΩ)**	***ΔR* (kΩ)**	***d* (μm)**	***Δd* (μm)**	***D* (μm)**	***ΔD* (μm)**	**area (μm²)**	***σ(S/m)***	***Δσ* (S/m)**
350.00	7.72	0.27	29.28	0.52	251.80	0.17	4948.88	130.90	5.14
450.00	10.88	0.32	27.54	0.40	202.10	0.98	3754.70	122.35	4.00
550.00	24.95	0.61	24.60	0.15	197.90	0.36	3273.62	61.22	1.55
650.00	26.86	0.92	23.87	0.85	193.40	0.42	3104.64	59.95	2.97
750.00	38.05	0.36	18.95	0.55	186.10	0.85	2358.80	55.71	1.71
P	0.775 W								
***v* (mm/min)**	***R* (kΩ)**	***ΔR* (kΩ)**	***d* (μm)**	***Δd* (μm)**	***D* (μm)**	***ΔD* (μm)**	**area (μm²)**	***σ(S/m)***	***Δσ* (S/m)**
350.00	6.88	0.46	33.20	0.15	276.20	0.65	6160.87	117.94	7.92
450.00	7.53	0.62	29.02	0.76	224.70	0.56	4390.26	227.32	19.52
550.00	12.30	0.65	28.53	0.65	206.00	0.76	3966.48	102.48	5.95
650.00	22.10	0.97	25.57	0.76	203.60	0.89	3503.10	64.59	3.42
750.00	26.73	0.52	22.87	0.79	201.80	0.69	3095.66	60.42	2.40
P	0.892 W								
***v* (mm/min)**	***R* (kΩ)**	***ΔR* (kΩ)**	***d* (μm)**	***Δd* (μm)**	***D* (μm)**	***ΔD* (μm)**	**area (μm²)**	***σ(S/m)***	***Δσ* (S/m)**
350.00	4.28	0.51	51.91	0.78	294.90	0.34	10434.33	111.99	13.56
450.00	6.50	0.97	42.54	0.96	256.60	0.69	7420.53	103.60	15.60
550.00	9.88	0.85	41.34	0.35	248.80	0.47	6991.67	72.41	6.23
650.00	15.35	0.36	39.86	0.56	242.50	0.36	6568.32	49.58	1.37
750.00	22.33	0.65	37.39	0.97	219.60	0.96	5588.06	40.07	1.58
P	0.995 W								
***v* (mm/min)**	***R* (kΩ)**	***ΔR* (kΩ)**	***d* (μm)**	***Δd* (μm)**	***D* (μm)**	***ΔD* (μm)**	**area (μm²)**	***σ(S/m)***	***Δσ* (S/m)**
350.00	3.37	0.48	65.66	0.85	307.20	0.32	13907.13	106.56	15.10

450.00	6.53	0.65	58.65	0.97	289.80	0.34	11676.46	65.57	6.58
550.00	10.06	0.47	55.82	0.69	273.50	0.24	10494.76	47.36	2.30
650.00	13.71	0.76	51.15	0.75	257.80	0.41	9048.39	40.30	2.31
750.00	18.08	0.75	45.49	0.86	243.40	0.65	7571.71	36.53	1.66
P	1.115 W								
***v* (mm/min)**	***R* (kΩ)**	***ΔR* (kΩ)**	***d* (μm)**	***Δd* (μm)**	***D* (μm)**	***ΔD* (μm)**	**area (μm²)**	***σ(S/m)***	***Δσ* (S/m)**
350.00	2.92	0.73	73.77	0.43	324.70	0.15	16590.83	103.32	25.72
450.00	5.25	0.25	71.84	0.32	305.10	0.23	15223.07	62.61	2.94
550.00	8.40	0.74	68.38	0.15	287.90	0.16	13682.77	43.51	3.81
650.00	10.89	0.48	64.45	0.68	282.50	0.32	12614.04	36.41	1.64
750.00	12.66	0.17	60.67	0.32	275.60	0.98	11554.15	34.19	0.49

Table 6.3. Calculation of uncertainty in crystallite-size.

P= 0.55 W	***v* (mm/min)**	***tirr* (s)**	***ID/IG***	***ΔID/IG***	***La* (nm)**	***ΔLa* (nm)**
	350.00	0.08	0.94	0.01	20.12	0.26
	450.00	0.06	1.01	0.03	18.81	0.50
	550.00	0.05	1.02	0.01	18.66	0.08
	650.00	0.04	1.03	0.04	18.39	0.79
	750.00	0.04	1.09	0.05	17.34	0.81
P= 0.651 W	***v* (mm/min)**	***tirr* (s)**	***ID/IG***	***ΔID/IG***	***La* (nm)**	***ΔLa* (nm)**
	350.00	0.08	0.86	0.04	22.12	1.00
	450.00	0.06	0.99	0.07	19.10	1.42
	550.00	0.05	1.01	0.04	18.83	0.66
	650.00	0.04	1.00	0.03	18.94	0.48
	750.00	0.04	1.00	0.03	18.89	0.47
P= 0.775 W	***v* (mm/min)**	***tirr* (s)**	***ID/IG***	***ΔID/IG***	***La* (nm)**	***ΔLa* (nm)**
	350.00	0.08	0.94	0.01	20.26	0.30
	450.00	0.06	0.96	0.04	19.72	0.89
	550.00	0.05	1.03	0.01	18.33	0.09
	650.00	0.04	1.07	0.01	17.75	0.16
	750.00	0.04	1.12	0.04	16.95	0.58
P= 0.892 W	***v* (mm/min)**	***tirr* (s)**	***ID/IG***	***ΔID/IG***	***La* (nm)**	***ΔLa* (nm)**
	350.00	0.08	0.84	0.04	22.37	1.01
	450.00	0.06	0.98	0.04	19.31	0.77

	550.00	0.05	1.02	0.03	18.68	0.56
	650.00	0.04	1.06	0.08	17.95	1.44
	750.00	0.04	1.01	0.04	18.67	0.74
P= 0.995 W	***v (mm/min)***	***tirr (s)***	***ID/IG***	***ΔID/IG***	***La (nm)***	***ΔLa (nm)***
	350.00	0.08	0.82	0.02	22.99	0.48
	450.00	0.06	0.93	0.02	20.42	0.47
	550.00	0.05	1.00	0.05	18.95	1.04
	650.00	0.04	0.98	0.02	19.40	0.48
	750.00	0.04	1.00	0.03	18.87	0.47
P= 1.115 W	***v (mm/min)***	***tirr (s)***	***ID/IG***	***ΔID/IG***	***La (nm)***	***ΔLa (nm)***
	350.00	0.08	0.85	0.03	22.31	0.85
	450.00	0.06	1.05	0.04	18.11	0.64
	550.00	0.05	1.04	0.05	18.15	0.84
	650.00	0.04	1.11	0.04	17.10	0.64
	750.00	0.04	1.14	0.07	16.55	0.95

6.1.6. Conclusion:

This article describes the first study of growth kinetics of graphene from laser carbonization of polyimide using Arrhenius equation. The peak temperature for each laser fluence was calculated using a photothermal model implemented by Finite Element Analysis and irradiation time was controlled by varying scan-speed. The peak activation energy for graphene crystal growth was found to be 0.20±0.03 eV and peak activation temperature was found to be $2.35 \pm 0.30 \times 10^3$ K which is close to the minimum lattice temperature (~2.40×10^3 K) required for ring opening in polyimide, confirmed by molecular dynamics studies. The pre-exponential rate constant was calculated as 436.83±0.04 nm/s. The average nuclei size was found to be 15.44±2.07 nm. Such values reveal that the ideal condition for obtaining larger LIG crystallites, is to scan the laser at low fluence ($F_{Th}<F<1.09 \times 10^4$ mJ/cm^2) and low scan-speed for larger nuclei formation and higher growth rate. Writing structures at higher fluence ($F>1.23 \times 10^4$ mJ/cm^2) leads to keyhole-induced defects. This study will facilitate application of the laser carbonization process to produce continuous defect-free graphene on Polyimide, which can be used for flexible electronics applications.

The published journal paper ends here.

After studying the growth kinetics, the method of improving the growth will be discussed in the next section.

6.2. Plasma Enhanced Planar Crystal Growth of Laser Induced Graphene

Ratul Kumar Biswas[a], Peter McGlynn, Gerard M. O'Connor[a], Patricia Scully[a]
[a]*NCLA, Univerisity of Galway, Ireland.*
Mater. Lett., 15 July 2023, **343**, 134362

Abstract:

The effect of wettability of Polyimide (PI) surface on crystallite size and electrical conductivity of Laser Induced Graphene (LIG) was studied for the first time. The wettability of PI was adjusted by varying the scan speed of a localised Argon cold plasma pen on the PI surface. The effect of this exposure was obtained by contact angle (θ) measurement using two solvents such as water and Ethylene Glycol (EG). The maximum improvement of conductivity of 49.68 % occurred at lower CO_2 laser power (0.65 W, 0.77 W) on PI pre-treated at a lower plasma scan speed (200 mm/min). Raman spectra of LIG showed that such improvement occurred due to an increased crystallite size by 21 %. Such a study shows that increased wettability of PI surface assists in the planar growth of LIG crystallite.

Keywords
Laser carbonization; graphene; crystal growth; plasma

6.2.1. Introduction:

Laser carbonization of Polyimide is a method of creating conducting tracks of graphene by scanning an Infra-Red laser on Polyimide and is used in flexible electronics[11, 18-20]. Such a method allows free-form fabrication of conducting circuits on Polyimide without any need for liquid chemicals or intermediate stages compared to ink-jet printing and physical vapour deposition techniques. However, LIG has poor electrical conductivity compared to other methods. The reason behind such low conductivity lies in high defect density, lower crystallite size and three-dimensional growth rather than planar growth of graphene [18]. For better conductivity, planar crystalline growth is desired since the end-end voltage source across the LIG tracks are confined to a single plane. Such 3D growth is due to the amorphous nature of Kapton HN.

Epitaxial large films of graphene is produced when the underlying substrate is crystalline with minimum lattice mismatch [21]. Amorphous substrates will have no control over the orientation of crystal growth and will result in the growth of random orientations resulting in 3D growth. The growth of thin films can be categorized into three main modes [21, 22]: Fran-van-Der-Merwe mode, Volmer-Weber mode, and Stranski-Krastanov mode. Frank-van-Der-Merwe mode is the preferable mode of growth since it forms layer-by-layer (LBL) growth of crystalline thin films. This growth occurs when there is maximum wettability of the substrate ($\theta \approx 0$) and the interfacial surface energy between surface and vapour (γ_{sv}) is greater than or equal to the sum of the interfacial energies between film and surface (γ_{fs}), and film and vapour (γ_{fv})[21], i.e., $\gamma_{sv} \geq \gamma_{fs} + \gamma_{fv}$. This makes the nucleation energy of a new layer on the surface larger than the activation energy on top of the existing layer which forms the LBL epitaxial growth of multiple layers[23]. Stranski-Kranstanov mode leads to island formation on the previous layers and Volmer-Weber mode leads to island formation from the surface itself. The wettability of Polyimide can be increased using an Argon (Ar) plasma treatment since it increases the stretching of C=0 bond in PI resulting into negatively charged oxygen bonds dangling near the surface making the surface polar[24]. Here, we study the effect of scanning speed of of a spatially confined Ar plasma on the wettability of PI using water and Ethylene Glycol (EG) and the resistance of LIG is measured upon scanning CO_2 laser on the plasma treated PI. The crystallite size (L_a) of LIG on untreated PI and plasma-treated PI is measured from the defect ratio in the Raman spectra of graphene. Such a study provides a pathway to improve crystallinity of LIG and will facilitate the laser carbonization process to compete with the existing methods of thin-film deposition of graphene.

6.2.2. Experimental procedure:

The cold plasma scan was performed using a neoplas kINPen MED plasma tool with Ar Gasfluss at 5 slm with an effective diameter of 1 mm on 127 µm PI film (Dupont Kapton HN) with dimensions of 20 mm x 20 mm at varying scan speeds between 200-1000 mm/min with a hatch spacing of 0.25 mm. The PI film was pre-cleansed with ethanol and de-ionized (DI) water and dried. The tip of the plasma tool was set at a height 2 mm. The process schematic is shown in Fig. 6.9.

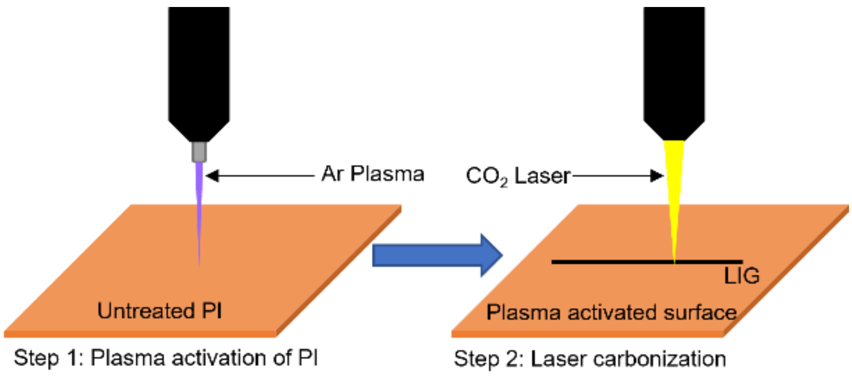

Fig. 6.9. Graphical abstract of laser carbonization of plasma-activated Polyimide.

Laser carbonization on untreated PI and plasma-treated PI was performed with the GEM 6O Coherent DEOS CO_2 laser system of wavelength 10.6 µm, spot-size 240.17 µm, integrated with a DEI PDG-2510 Digital Pulse Generator. Linear tracks of carbonized structures of length 5 mm were drawn on PI surface at scan-speed 450 mm/min at power (P) 0.65 ±0.02W, 0.77±0.01 W, 0.89±0.02 W, 0.99±0.04 W and 1.12±0.03 W, at repetition rate (f) 100 Hz. The length and scan-speed were defined by Advanced Laser Software and Unidex 500 program.

The surface roughness of the untreated and plasma-treated PI was measured using the Zygo profilometer. Contact angle measurement was performed using two solvents, water and EG on PI and the angle was calculated by measuring the radius of curvature and base-length of a solvent drop of volume 1 µl using an Olympus BX60M optical microscope. The morphology of the LIG was studied using a cross-sectional Scanning Electron Microscopy using Hitachi S-2600 SEM. The average crystallite size of LIG drawn on untreated and plasma treated PI was calculated from the defect ratio (I_D/I_G) obtained from Raman spectroscopy measured by RENISHAW inVia Raman Spectrometer using λ=514 nm excitation laser. The resistance of the LIG tracks was measured from the IV characteristics of the tracks by applying a potential sweep of 0-20 V using a Keithley 2450 Source meter integrated with 2-probe resistance measurement setup.

6.2.3. Results and discussion:

The effect of plasma-pen scan speed on crystallite size and conductivity of laser-indued graphene drawn on untreated and plasma-treated polyimide was studied. The plasma treatment improved the wettability of polyimide surface and the contact angle reduced with increasing plasma-pen scan speed. The planar crystal growth is enhanced by improved surface wettability. Christen et al. studied the step flow growth dynamics in LBL growth method [25] and found that LBL growth depends on the ratio (D_s/F_s) where D_s is diffusivity of newly formed species and F_s is deposition flux of the species on the substrate. Increasing exposure of plasma at lower scan speed increases the wettability of PI by surface activation which increases diffusivity for newly formed graphene crystallites, which will tend to attach to the substrate.

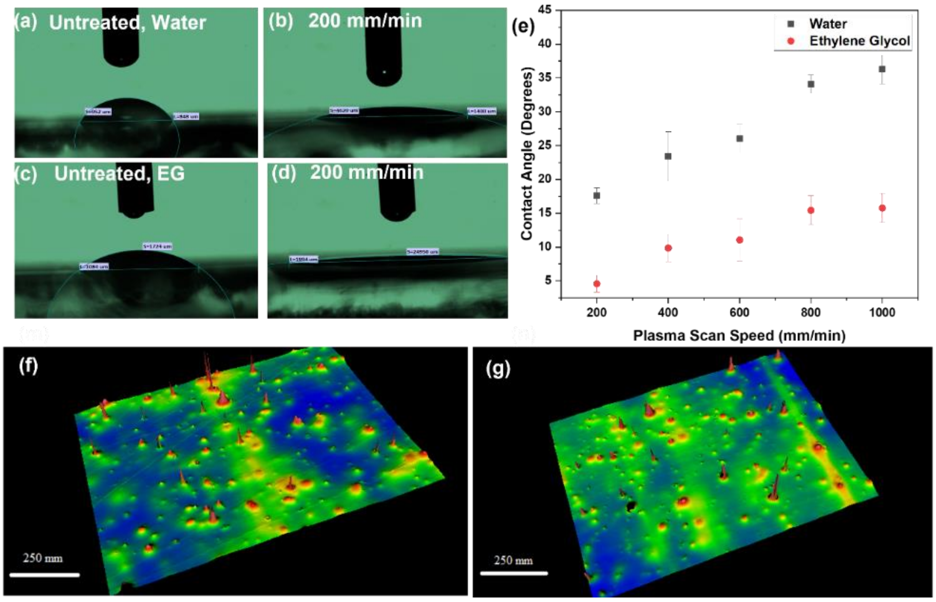

Fig. 6.10. (a, b) Contact angle measurement of water droplets on untreated PI and plasma treated PI at scan-speed 200 mm/min), (c, d) Contact angle measurement of EG on untreated PI and plasma treated PI at scan-speed 200 mm/min, (e) Contact angle vs Plasma scan-speed, (f) Surface roughness measurement of untreated PI, (g) of plasma treated PI at 200 mm/min.

At low laser powers, flux of graphene nuclei generated on PI is small, and hence D/F is maximum; this assists LBL growth of graphene. The contact angle of both water and EG was found to increase proportionally with scan speed due to decreased plasma exposure at faster scan speeds (Fig 6.10 a-d). Contact angle was measured using the equation: $\theta = 90 \pm \cos^{-1} b/d$, where b= base-length and d= diameter of curvature of solvent drop. Contact angle of water reduced from $62.97^0 \pm 3.41^0$ to $17.60^0 \pm 1.16^0$ and the contact angle of EG reduced from $38.96^0 \pm 3.41^0$ to $4.58^0 \pm 1.26^0$ upon scanning plasma at 200 mm/min which indicates an increased wettability of PI surface upon plasma treatment (Fig. 6.10e) [26]. The contact angle measurement of deionized water and Ethylene Glycol on untreated and plasma-treated PI at scan speed 400-1000 mm/min are shown in Fig. 6.20.

The surface profile measurement showed that the roughness remained unchanged before and after plasma treatment (Fig. 6.10 f,g) which indicates that wettability increased due to surface activation due to the plasma treatment. It was previously reported by Huyesin et al. that the Ar plasma-treated PI showed stronger absorption of infrared light by bending and stretching vibrations of C=O and C-O-C bonds than the untreated PI as found from the FTIR study [24]. The IV measurements and resistance values are shown in Fig. 6.11 and 6.12 respectively.

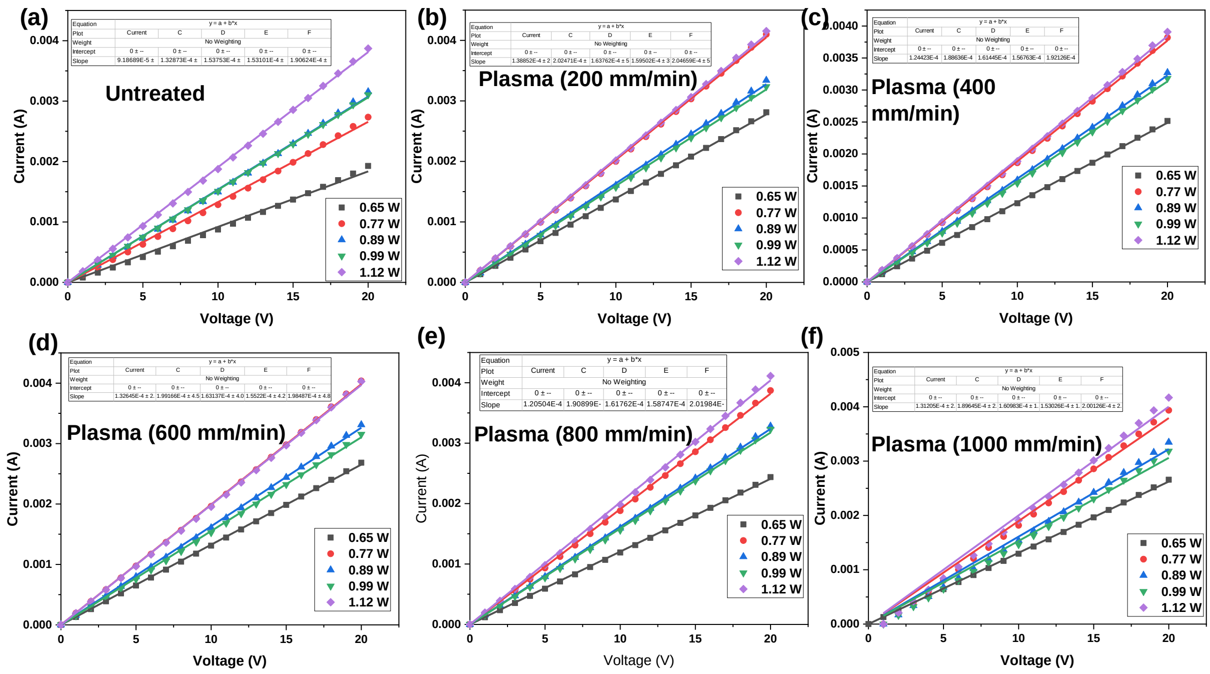

Fig. 6.11. IV measurements of LIG drawn at 0.65-1.12 W on untreated PI and plasma treated PI at scan speed 200-1000 mm/min.

The average crystallite size of LIG was measured from equation 6.11 [11]:

$$L_a = (2.4 \times 10^{-10}) \times \lambda^4 \times \left(\frac{I_D}{I_G}\right)^{-1} \qquad 6.11$$

where I_D and I_G are D peak intensity and G peak intensity at 1344 cm^{-1} and 1576 cm^{-1} respectively (Fig. 6.15 b,c). The crystallite size increased from 18.94 to 20.23 nm (6.86 %) for laser power of 0.65 W and 19.31 to 23.38 nm (21.07 %) for 0.77 W upon scanning the plasma at 200 mm/min (Fig. 6.15 d). Hence, maximum improvement in crystallite size and conductivity occurred for lower laser powers and lower plasma scan speeds, whereas they remained almost same for increased laser powers and higher plasma scan speeds. Raman spectra of LIG on plasma treated PI at scan speed 400-1000 mm/min is shown in Fig. 6.20.

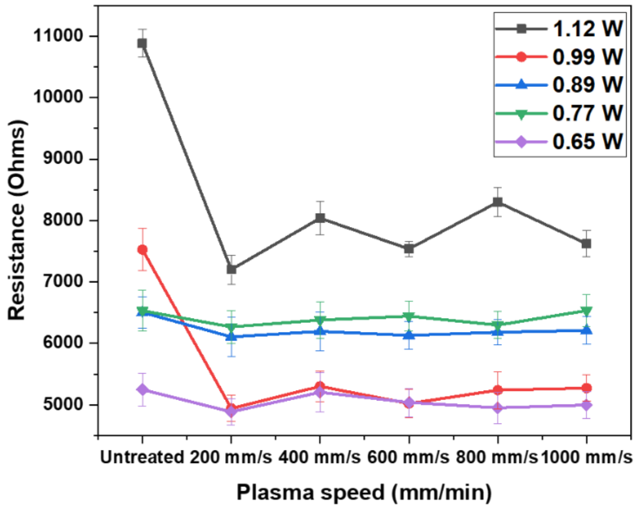

Fig. 6.12. (a) Resistance vs laser power of LIG drawn at 0.65-1.12 W on untreated PI and plasma treated PI at scan speed 200-1000 mm/min.

Cross-sectional SEM of LIG showed that there was no variation in carbonization depth and morphology of LIG upon plasma treatment in the micro-scale (Fig. 6.13).

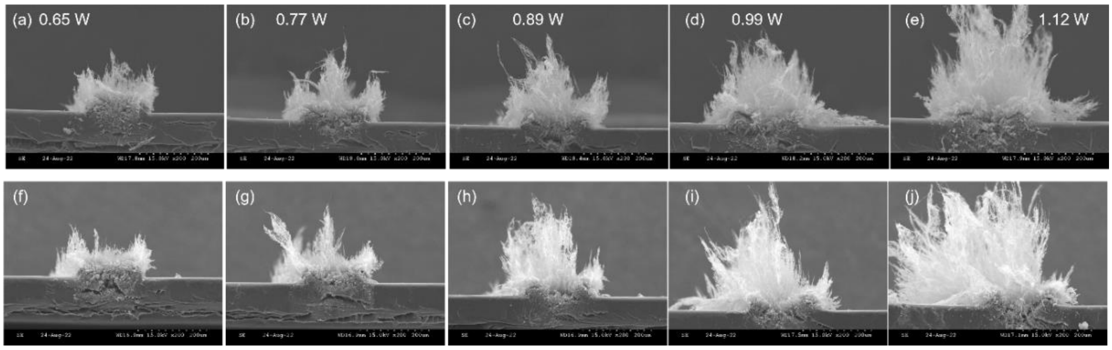

Fig. 6.13. Cross-sectional SEM images of LIG drawn at 0.65-1.12 W at 450 mm/min, f=100 Hz on (a-e) untreated PI, and on (f-j) plasma treated PI at plasma scan speed 200 mm/min.

The conductivity increased with increased crystallite size of LIG due to plasma treatment. The largest improvement of electrical conductivity occurred at lower laser powers (0.65 W and 0.77 W) when plasma was scanned at 200 mm/min, while for higher laser powers, there was no significant improvement (Fig. 6.14d). Conductivity of LIG drawn at 0.65 W on plasma treated PI changed from 122.35 ±4.05 S/m to 184.91 ±15.37 S/m. The dimensions of carbonized tracks remained same before and after plasma treatment on PI which shows that cold plasma treatment does not affect the thermal and optical properties of PI (Fig 6.14f).

For both untreated and plasma-treated PI, the I_{2D}/I_G ratio increased which shows that number of graphene layers decreased with increasing laser power (Fig. 6.14e) [27]. At laser powers below 0.9 W, number of graphene layers on plasma-treated PI was greater than that on untreated PI. At laser powers above 0.9 W, number of layers formed on plasma-treated PI was less than those on untreated PI. This means that at low laser powers with plasma treatment, more layered and larger graphene crystallites were formed and at higher laser power and plasma-treated PI, reduced layered and smaller graphene crystallites were formed which explains that Frank der Merwe assisted LBL growth is favoured at low laser power on plasma treated PI. The calculation of crystallite size and conductivity is shown in table 6.4 and 6.5 respectively.

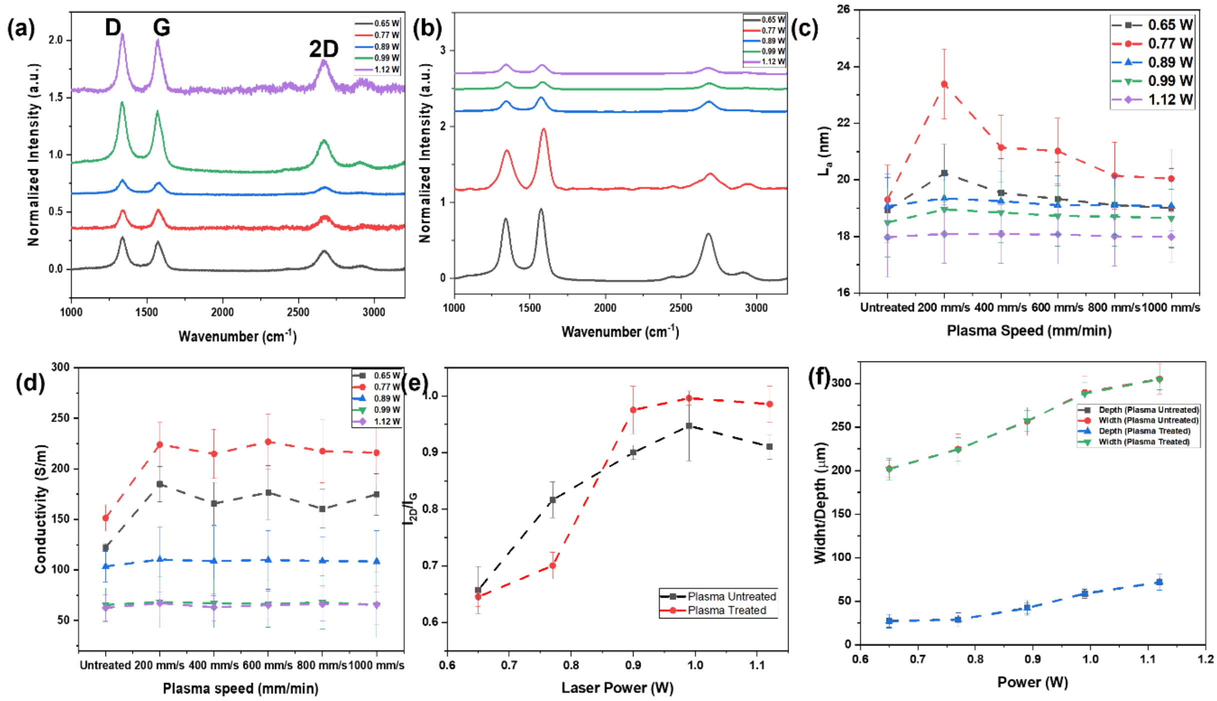

Fig. 6.14. (a) Raman spectra of LIG on untreated PI, and (b) on plasma treated PI at scan speed 200 mm/min, (c) L_a vs plasma scan-speed, and (d) Conductivity vs plasma scan-speed on untreated PI and plasma treated PI at 200-1000 mm/min, (e) I_{2D}/I_G vs laser power, and (f) width and depth of LIG on untreated and plasma-treated PI at 200 mm/min.

Table 6.4. Calculations of uncertainty in conductivity.

Untreated									
P (W)	***R (kΩ)***	***ΔR (kΩ)***	***d (μm)***	***Δd (μm)***	***D (μm)***	***ΔD (μm)***	**area (μm²)**	***σ(S/m)***	***Δσ (S/m)***
0.65	10.88	0.22	27.54	7.41	202.10	10.14	3754.70	122.35	33.59

0.77	7.53	0.35	29.02	8.22	224.70	17.26	4390.26	151.33	44.93
0.89	6.50	0.25	42.54	8.31	256.60	15.98	7420.53	103.60	21.62
0.99	6.53	0.34	58.65	5.22	289.80	18.72	11676.46	65.56	7.96
1.12	5.25	0.27	71.84	9.13	305.10	17.32	15223.07	62.61	9.28
Plasma- treated 200 mm/min									
P (W)	***R (kΩ)***	***ΔR (kΩ)***	***d (μm)***	***Δd (μm)***	***D (μm)***	***ΔD (μm)***	**area (μm^2)**	***σ(S/m)***	***Δσ (S/m)***
0.65	7.20	0.24	27.14	8.13	201.90	12.15	3694.82	187.90	57.71
0.77	5.08	0.22	29.11	7.32	224.50	13.27	4401.44	223.44	58.45
0.89	6.11	0.32	42.14	6.29	257.10	12.16	7361.32	111.23	18.33
0.99	6.27	0.27	59.01	7.15	288.50	12.33	11704.60	68.14	9.22
1.12	4.89	0.22	72.03	9.27	304.90	12.16	15257.00	67.07	9.51
Plasma-treated 400 mm/min									
P (W)	***R (kΩ)***	***ΔR (kΩ)***	***d (μm)***	***Δd (μm)***	***D (μm)***	***ΔD (μm)***	**area (μm^2)**	***σ(S/m)***	***Δσ (S/m)***
0.65	8.04	0.27	27.14	8.13	201.90	12.15	3694.82	117.94	36.23
0.77	5.30	0.25	29.11	7.32	224.50	13.27	4401.44	227.32	59.66
0.89	6.19	0.32	42.14	6.29	257.10	12.16	7361.32	102.48	16.86
0.99	6.38	0.30	59.01	7.15	288.50	12.33	11704.60	64.59	8.84
1.12	5.20	0.32	72.03	9.27	304.90	12.16	15257.00	60.42	8.96
Plasma- treated 600 mm/min									
P (W)	***R (kΩ)***	***ΔR (kΩ)***	***d (μm)***	***Δd (μm)***	***D (μm)***	***ΔD (μm)***	**area (μm^2)**	***σ(S/m)***	***Δσ (S/m)***
0.65	7.54	0.13	27.14	8.13	201.90	12.15	3694.82	111.99	34.25
0.77	5.02	0.24	29.11	7.32	224.50	13.27	4401.44	103.60	27.18
0.89	6.13	0.23	42.14	6.29	257.10	12.16	7361.32	72.41	11.64
0.99	6.44	0.24	59.01	7.15	288.50	12.33	11704.60	49.58	6.63
1.12	5.04	0.23	72.03	9.27	304.90	12.16	15257.00	40.07	5.70
Plasma- treated 800 mm/min									
P (W)	***R (kΩ)***	***ΔR (kΩ)***	***d (μm)***	***Δd (μm)***	***D (μm)***	***ΔD (μm)***	**area (μm^2)**	***σ(S/m)***	***Δσ (S/m)***
0.65	8.30	0.24	27.14	8.13	201.90	12.15	3694.82	106.56	32.68
0.77	5.24	0.30	29.11	7.32	224.50	13.27	4401.44	65.57	17.34
0.89	6.18	0.21	42.14	6.29	257.10	12.16	7361.32	47.36	7.59
0.99	6.30	0.22	59.01	7.15	288.50	12.33	11704.60	40.30	5.36
1.12	4.95	0.26	72.03	9.27	304.90	12.16	15257.00	36.53	5.27
Plasma- treated 1000 mm/min									
P (W)	***R (kΩ)***	***ΔR (kΩ)***	***d (μm)***	***Δd (μm)***	***D (μm)***	***ΔD (μm)***	**area (μm^2)**	***σ(S/m)***	***Δσ (S/m)***
0.65	7.62	0.21	27.14	8.13	201.90	12.15	3694.82	103.32	31.68

0.77	5.27	0.22	29.11	7.32	224.50	13.27	4401.44	62.61	16.36
0.89	6.21	0.23	42.14	6.29	257.10	12.16	7361.32	43.51	7.00
0.99	6.54	0.26	59.01	7.15	288.50	12.33	11704.60	36.41	4.90
1.12	5.00	0.22	72.03	9.27	304.90	12.16	15257.00	34.19	4.84

Table 6.5. Table for uncertainty calculation of crystallite-size.

0.65 W				
Plasma Scan speed (mm/min)	***ID/IG***	***Δ (ID/IG)***	***La***	***ΔLa***
Untreated	1.00	0.06	18.94	1.14
200.00	0.94	0.05	20.23	1.01
400.00	0.97	0.06	19.54	1.20
600.00	0.98	0.07	19.33	1.30
800.00	0.99	0.05	19.11	1.05
1000.00	1.00	0.07	19.01	1.40
0.77 W				
Plasma Scan speed (mm/min)	***ID/IG***	***Δ (ID/IG)***	***La***	***ΔLa***
Untreated	0.98	0.06	19.30	1.22
200.00	0.81	0.04	23.39	1.23
400.00	0.90	0.05	21.15	1.14
600.00	0.90	0.05	21.02	1.17
800.00	0.94	0.06	20.15	1.18
1000.00	0.95	0.05	20.04	1.04
0.89 W				
Plasma Scan speed (mm/min)	***ID/IG***	***Δ (ID/IG)***	***La***	***ΔLa***
Untreated	0.99	0.06	19.07	1.14
200.00	0.98	0.05	19.35	1.01
400.00	0.98	0.05	19.25	1.05
600.00	0.99	0.05	19.11	1.04
800.00	0.99	0.05	19.10	1.03
1000.00	0.99	0.05	19.08	0.89
0.99 W				
Plasma Scan speed (mm/min)	***ID/IG***	***Δ (ID/IG)***	***La***	***ΔLa***
Untreated	1.02	0.07	18.50	1.21
200.00	1.00	0.05	18.95	1.03

400.00	1.01	0.06	18.85	1.06
600.00	1.01	0.06	18.73	1.07
800.00	1.01	0.06	18.70	1.05
1000.00	1.02	0.06	18.65	1.03
1.12 W				
Plasma Scan speed (mm/min)	***ID/IG***	***Δ (ID/IG)***	***La***	***ΔLa***
Untreated	1.05	0.08	17.97	1.42
200.00	1.05	0.06	18.09	1.04
400.00	1.05	0.06	18.09	1.04
600.00	1.05	0.06	18.07	1.03
800.00	1.05	0.06	18.00	1.05
1000.00	1.05	0.05	17.99	0.89

6.2.4. Test of uniformity of conductivity and crystallite size of LIG:

The uniformity of electrical conductivity of 30 mm LIG track prepared at 0.65 W and 0.75 W for both untreated and plasma treated at 200 mm/s were measured by measuring the resistance at intervals of 10 mm, 20 mm, and 30 mm by placing the electrical probes at contacts prepared using Bare conductive paste as shown in Fig. 6.15. The resistance of untreated LIG at 0.65W was found to be 21.78 kΩ, 45.30 kΩ and 65.30 kΩ at intervals of 10 mm, 20 mm and 30 mm which showed that the resistance increased proportionally with length of the track.

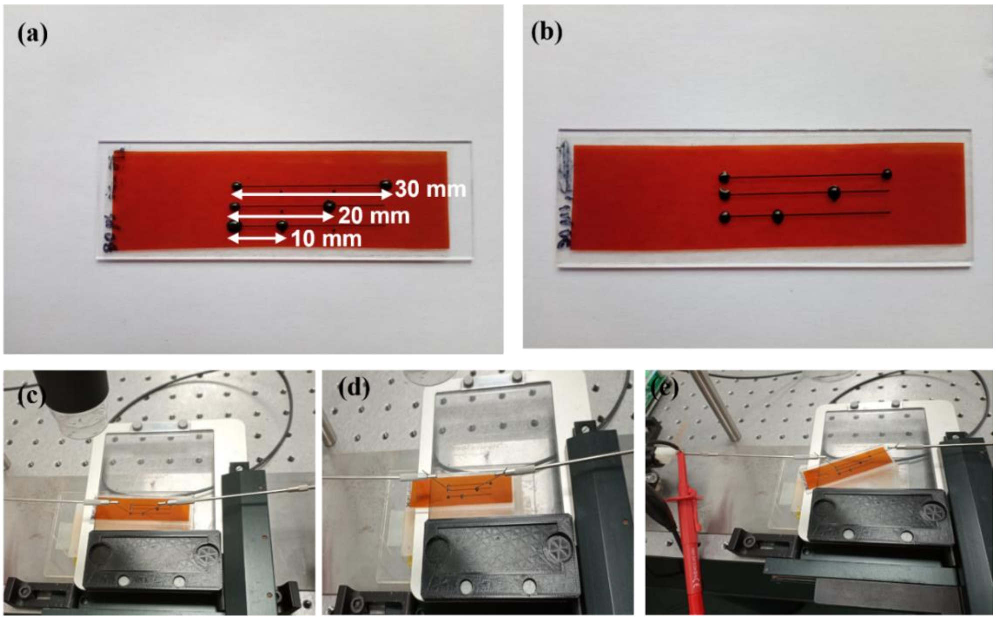

Fig. 6.15. Conductive ink-based contacts at distances 10 mm, 20 mm and 30 mm on LIG drawn at 9a) 0.65 W, (b) 0.77 W, (c, d, e) IV-measurement probes placed at the contacts for resistance measurement.

The regression plots of conductivity measured across 3 points are summarized in Table 6.6.

Table 6.6. Slope and R-Square values of regression plots of conductivity along the LIG track.

LIG	Slope	R-square
0.65 W, untreated	-0.012	0.0051
0.65 W, plasma-treated	-0.0056	0.0015
0.77 W, untreated	-0.015	0.62
0.77 W, plasma-treated	-0.021	0.065

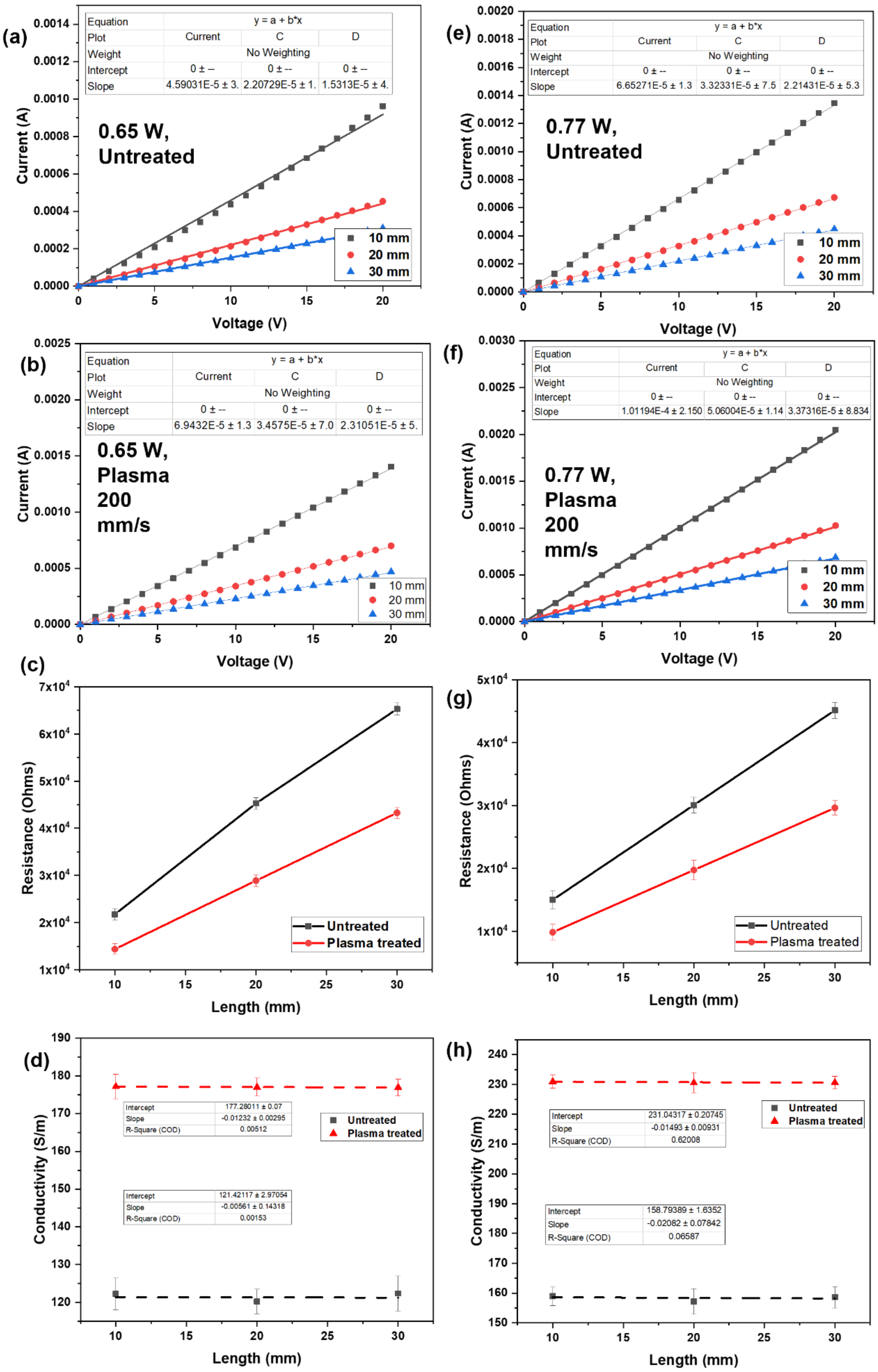

Fig. 6.16. IV of LIG drawn at 0.65 W on (a) untreated PI, and (b) plasma treated PI, (c) Resistance vs length of LIG track drawn at 0.65 W, (d) Conductivity measured at 3 points 10 mm, 20 mm, 30 mm drawn at 0.65 W; IV of LIG drawn at (e) 0.77 W on untreated PI, and (f) plasma treated PI, (g) Resistance vs length of LIG track drawn at 0.65 W, (h) Conductivity

measured at 3 points 10 mm, 20 mm, 30 mm drawn at 0.65 W, the conductivity was found to be consistent throughout the track.

Such low values of slopes and R-square in Fig. 6.16 d,h explain the consistency of conductivity of LIG throughout the track and shows that there is regression pattern in the conductivity values. For both 0.65 W and 0.77 W, the conductivity improved significantly by ~51% after the plasma treatment.

The mapping data over an area of 290 x 15 μm^2 on LIG drawn at 0.65 W and 0.77 W for both untreated and plasma treated PI is shown in Fig. 6.17 and Fig. 6.18 and showed uniform distribution of I_D/I_G ratio over the mapped region. From the Raman mapping, the I_D/I_G ratio was found to be in the range 1.66-1.22 on untreated PI and 0.96-0.98 on plasma treated PI for 0.65 W laser power. For 0.77 W laser power, the I_D/I_G ratio was found to be in the range 1.02-1.05 on untreated PI and 0.806-0.818 on plasma treated PI. For 0.65 W and 0.77 W, the crystallite-size improved by ~7% and ~21% respectively after the plasma treatment.

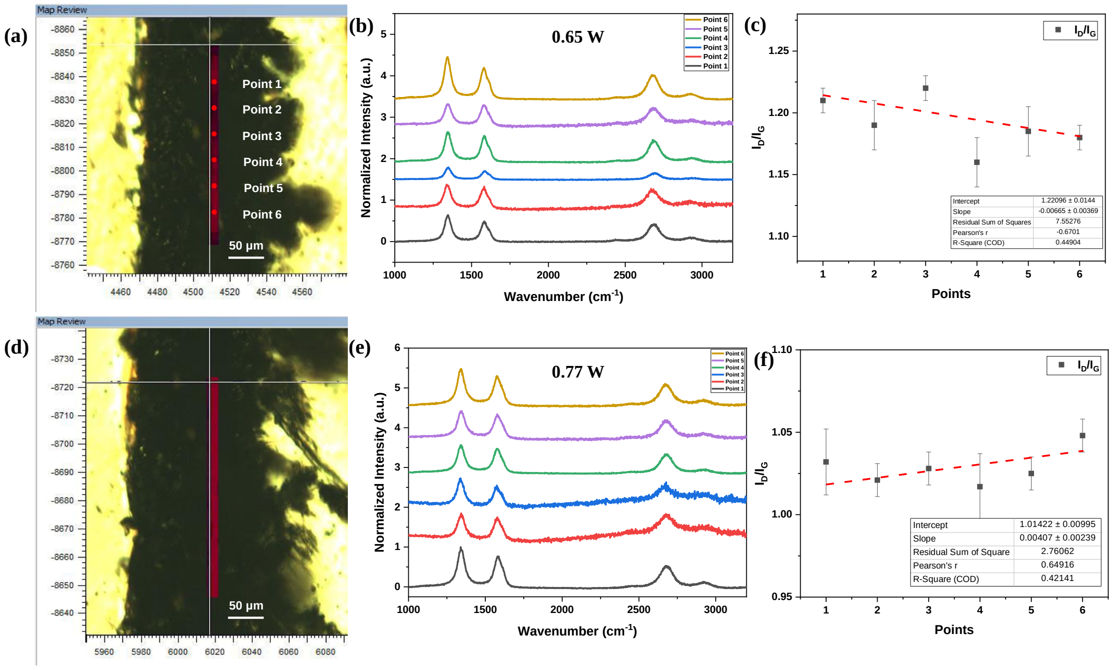

Fig. 6.17. Raman mapping of LIG at laser power 0.65 W, 0.77 W on untreated PI.

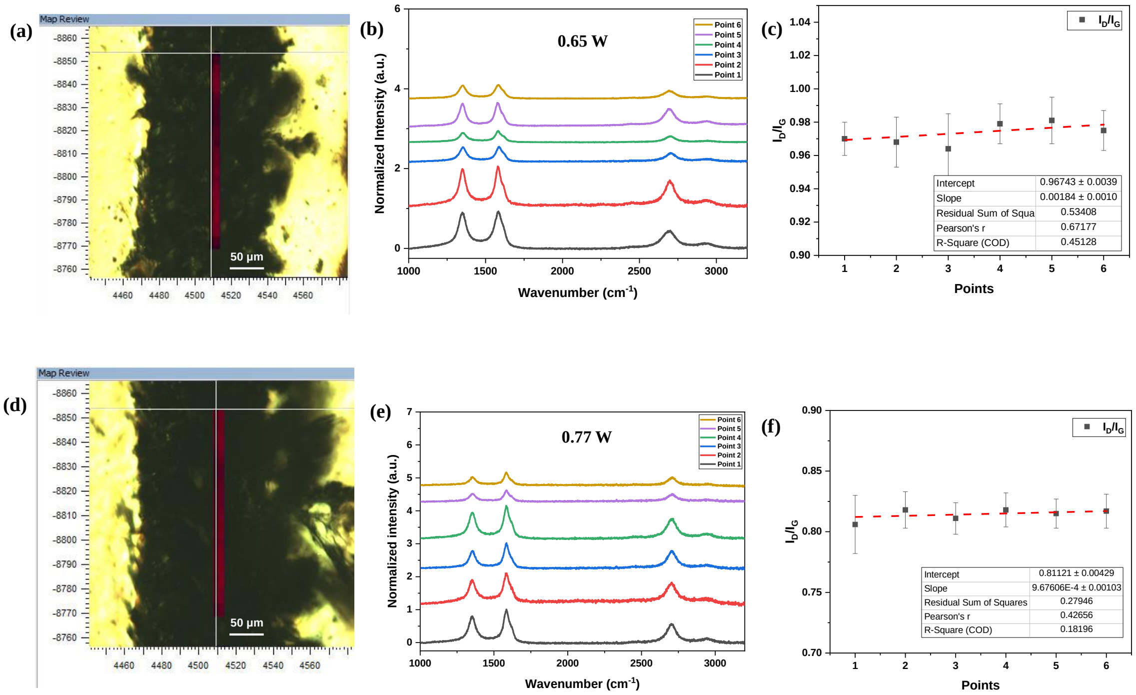

Fig. 6.18. Raman mapping of LIG at laser power 0.65 W, 0.77 W on plasma-treated PI at scan speed 200 mm/min.

The regression plots of I_D/I_G ratio measured across 6 points are summarized in Table 6.7.

Table 6.7. Slope and R-Square values of regression plots of I_D/I_G ratio along the LIG track.

LIG	Slope	R-square
0.65 W, untreated	-0.0066	0.45
0.65 W, plasma-treated	-0.0041	0.65
0.77 W, untreated	0.0018	0.45
0.77 W, plasma-treated	0.00097	0.18

Such low values of slopes and R-square explain the consistency of I_D/I_G ratio of LIG throughout the track and shows that there is regression pattern in the I_D/I_G ratio values.

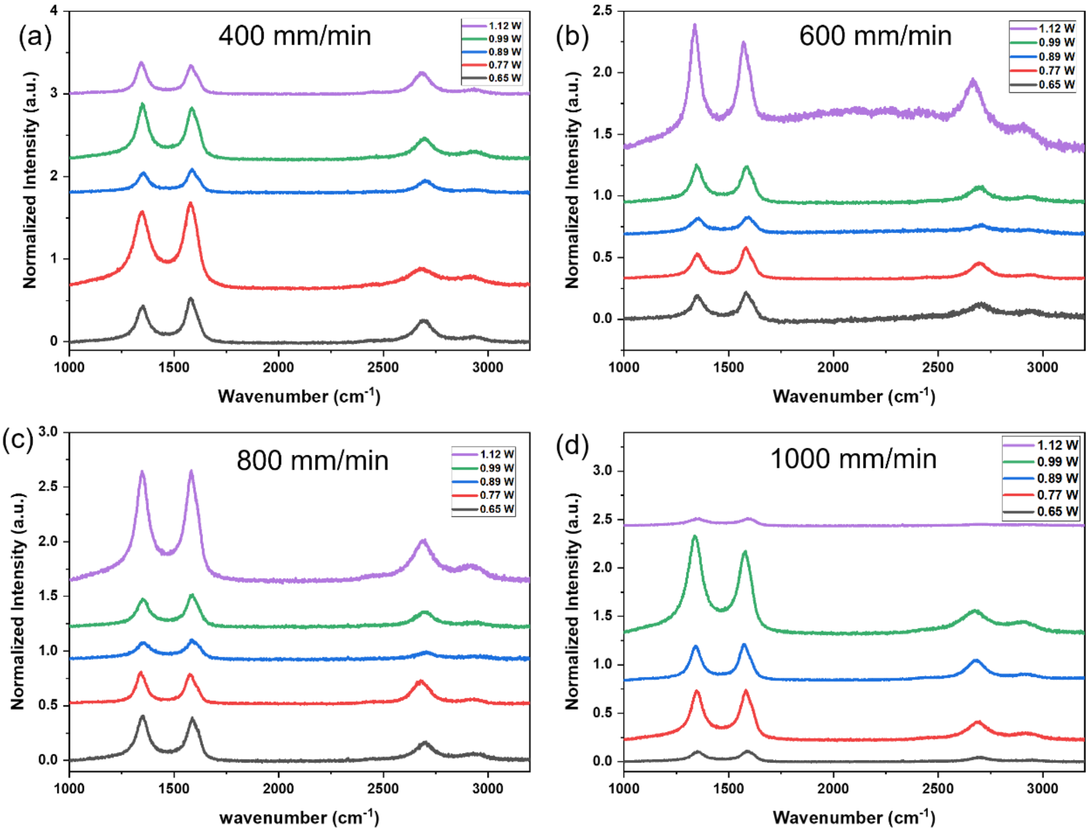

Fig. 6.19. Raman spectra of LIG on plasma-treated PI at scan speed (a) 400 mm/min, (b) 600 mm/min, (c) 800 mm/min, (d) 1000 mm/min.

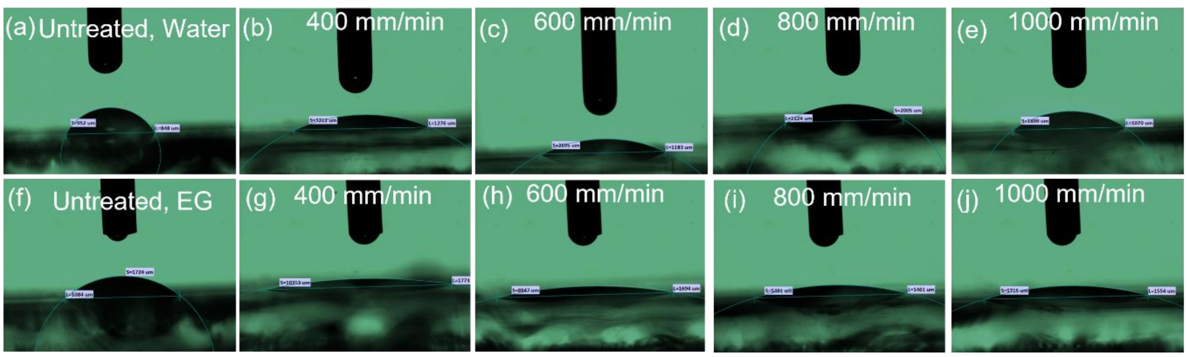

Fig. 6.20. Contact angle measurement of (a-f) deionized water and (g-l) Ethylene Glycol on untreated and plasma-treated PI at scan speed 400-1000 mm/min.

6.2.5. Conclusion:

The effect of surface wettability of PI on the electrical conductivity and crystallite size of LIG was studied. Surface wettability was improved by scanning plasma at a low scan speed of 200 mm/min and a significant increase in crystallite size of ~21% and conductivity of ~51% was demonstrated for LIG prepared at low laser powers (0.65 W, 0.77 W). This shows that increasing wettability of PI by surface scanning plasma favours the LBL growth of graphene which increases the crystallite size of LIG, hence improving its conductivity.

The published journal paper ends here.

6.3. Summary

In this chapter, the growth kinetics of graphene on PI in the laser carbonization process was studied and the growth was improved using the cold-plasma treatment of the PI. The growth kinetics was studied using the Arrhenius kinetic model, and the activation energy and the pre-exponential rate constant were calculated as 0.20±0.03 eV and 436.83±0.04 nm/s respectively. The growth was further improved by the Argon plasma treatment which increased the crystallite size by ~21% and conductivity by ~51%. This chapter meets the objectives of the study of growth and conductivity improvement of LIG. After discussing the CO_2 laser-PI interaction and growth kinetics in Chapters 5 and 6, the femtosecond laser-PI interaction will be studied in Chapter 7 and a comparative analysis between the two LIG will be done.

Bibliography

[1] W. Zhang, Y. Lei, Q. Jiang, F. Ming, P.M.F.J. Costa, H.N. Alshareef, 3D Laser Scribed Graphene Derived from Carbon Nanospheres: An Ultrahigh-Power Electrode for Supercapacitors, Small Methods 3(5) (2019) 1900005.

[2] J.B. In, B. Hsia, J.-H. Yoo, S. Hyun, C. Carraro, R. Maboudian, C.P. Grigoropoulos, Facile fabrication of flexible all solid-state micro-supercapacitor by direct laser writing of porous carbon in polyimide, Carbon 83 (2015) 144-151.

[3] R. Rahimi, M. Ochoa, W. Yu, B. Ziaie, Highly Stretchable and Sensitive Unidirectional Strain Sensor via Laser Carbonization, ACS Applied Materials & Interfaces 7(8) (2015) 4463-4470.

[4] R. Ye, D.K. James, J.M. Tour, Laser-Induced Graphene: From Discovery to Translation, Advanced Materials 31(1) (2019) 1803621.

[5] E.R. Mamleyev, N. Nordin, S. Heissler, K. Länge, N. MacKinnon, S. Sharma, Flexible Carbon-based Urea Sensor by Laser Induced Carbonisation of Polyimide, 2018 International Flexible Electronics Technology Conference (IFETC), 2018, pp. 1-6.

[6] J.A. Newell, D.D. Edie, E.L. Fuller Jr, Kinetics of carbonization and graphitization of PBO fiber, Journal of Applied Polymer Science 60(6) (1996) 825-832.

[7] H. Kim, C. Mattevi, M.R. Calvo, J.C. Oberg, L. Artiglia, S. Agnoli, C.F. Hirjibehedin, M. Chhowalla, E. Saiz, Activation Energy Paths for Graphene Nucleation and Growth on Cu, ACS Nano 6(4) (2012) 3614-3623.

[8] Y. Dong, S.C. Rismiller, J. Lin, Molecular dynamic simulation of layered graphene clusters formation from polyimides under extreme conditions, Carbon 104 (2016) 47-55.

[9] D.S. Firaha, M. Döntgen, B. Berkels, K. Leonhard, Pressure-Dependent Rate Constant Predictions Utilizing the Inverse Laplace Transform: A Victim of Deficient Input Data, ACS Omega 3(7) (2018) 8212-8219.

[10] S. Faas, U. Bielke, R. Weber, T. Graf, Prediction of the surface structures resulting from heat accumulation during processing with picosecond laser pulses at the average power of 420 W, Applied Physics A 124(9) (2018) 612.

[11] J. Lin, Z. Peng, Y. Liu, F. Ruiz-Zepeda, R. Ye, E.L.G. Samuel, M.J. Yacaman, B.I. Yakobson, J.M. Tour, Laser-induced porous graphene films from commercial polymers, Nature Communications 5(1) (2014) 5714.

[12] L. Jiang, H.-L. Tsai, Improved Two-Temperature Model and Its Application in Ultrashort Laser Heating of Metal Films, Journal of Heat Transfer 127(10) (2005) 1167-1173.

[13] F. Wang, K. Wang, X. Dong, X. Mei, Z. Zhai, B. Zheng, J. Lv, W. Duan, W. Wang, Formation of hierarchical porous graphene films with defects using a nanosecond laser on polyimide sheet, Applied Surface Science 419 (2017) 893-900.

[14] X. Ruan, R. Wang, J. Luo, Y. Yao, T. Liu, Experimental and modeling study of CO2 laser writing induced polyimide carbonization process, Materials & Design 160 (2018) 1168-1177.

[15] N. Bityurin, B.S. Luk'yanchuk, M.H. Hong, T.C. Chong, Models for Laser Ablation of Polymers, Chemical Reviews 103(2) (2003) 519-552.

[16] M. Inagaki, S. Harada, T. Sato, T. Nakajima, Y. Horino, K. Morita, Carbonization of polyimide film "Kapton", Carbon 27(2) (1989) 253-257.

[17] F. Lu, X. Li, Z. Li, X. Tang, H. Cui, Formation and influence mechanism of keyhole-induced porosity in deep-penetration laser welding based on 3D transient modeling, International Journal of Heat and Mass Transfer 90 (2015) 1143-1152.

[18] R. Ye, D.K. James, J.M. Tour, Laser-Induced Graphene, Accounts of Chemical Research 51(7) (2018) 1609-1620.

[19] Y. Chyan, R. Ye, Y. Li, S.P. Singh, C.J. Arnusch, J.M. Tour, Laser-Induced Graphene by Multiple Lasing: Toward Electronics on Cloth, Paper, and Food, ACS Nano 12(3) (2018) 2176-2183.
[20] D.X. Luong, K. Yang, J. Yoon, S.P. Singh, T. Wang, C.J. Arnusch, J.M. Tour, Laser-Induced Graphene Composites as Multifunctional Surfaces, ACS Nano 13(2) (2019) 2579-2586.
[21] I.V. Markov, Crystal Growth for Beginners, WORLD SCIENTIFIC2003.
[22] C.L. Andrea, K. Miroslav, Theory and simulation of crystal growth, Journal of Physics: Condensed Matter **9**(2) (1997) 299.
[23] H. Wang, Z. Yao, G.S. Jung, Q. Song, M. Hempel, T. Palacios, G. Chen, M.J. Buehler, A. Aspuru-Guzik, J. Kong, Frank-van der Merwe growth in bilayer graphene, Matter 4(10) (2021) 3339-3353.
[24] H. Kizil, M.O. Pehlivaner, L. Trabzon, Surface Plasma Characterization of Polyimide Films for Flexible Electronics, Advanced Materials Research 970 (2014) 132-135.
[25] H.M. Christen, G. Eres, Recent advances in pulsed-laser deposition of complex oxides, Journal of Physics: Condensed Matter 20(26) (2008) 264005.
[26] K. Zhang, X. Guo, C. Wang, F. Liu, L. Sun, Effect of plasma-assisted laser pretreatment of hard coatings surface on the physical and chemical bonding between PVD soft and hard coatings and its resulting properties, Applied Surface Science 509 (2020) 145342.
[27] Y. Bleu, F. Bourquard, A.-S. Loir, V. Barnier, F. Garrelie, C. Donnet, Raman study of the substrate influence on graphene synthesis using a solid carbon source via rapid thermal annealing, Journal of Raman Spectroscopy 50(11) (2019) 1630-1641.

7. Chapter 7: Femtosecond laser carbonization and ablation of Polyimide

In this chapter, the interaction of femtosecond laser with PI for graphene formation will be modelled for the first time and the dual application of the femtosecond laser for two operating conditions: ablation and carbonization are shown. Carbonization is claimed to occur due to heat accumulation which leads to photothermal conversion of PI to LIG. Ablation is claimed to occur due to multiphoton absorption which leads to photochemical etching of PI creating ablated tracks. Both these phenomena are utilized to prepare a Kirigami-inspired strain sensor which shows enhanced sensitivity upon bending and twisting of knee-joints. The heat accumulation process is modelled in Python with code provided in the Appendix A. The structural mechanical study of the sensor is performed using COMSOL which showed the enhanced stress accumulation occurring in the Kirigami sensor as compared to the planar sensor which explains the improved response of the Kirigami sensor. In the scope of the project, it represents theoretical understanding of the interaction of femtosecond laser with PI for both carbonization and ablation and how the LIG can be used for sensor applications.

Ratul Biswas performed the laser experiments, sensor designing, sensor DAQ, Raman spectroscopy and IV measurements of LIG at NCLA, UoG and wrote the paper. SEM was performed at the Centre of Microscopy and Imaging, UoG. Nazar Farid assisted this chapter with the laser setup. Bharat Bhushan Bhatt and Dipti Gupta studied the mechanical characterization of the sensor for Gauge Factor measurement and elastic to plastic transition of the sensor at IIT, Bombay. The work has been published in the Journal of Physics D: Applied Physics, Institute of Physics. The contribution of Ratul Kumar Biswas in this chapter is 80%, Nazar Farid is 10%, Bharat Bhushan Bhatt is 5%, and Dipti Gupta is 5%. Patricia Scully supervised and helped in the overall conceptualization of the project and Gerard O'Connor co-supervised and provided access to the lasers and characterization tools at the NCLA. The supplementary information of this paper is included in this chapter within the context.

Femtosecond laser ablation and carbonization for Kirigami-Inspired strain sensor

*Ratul Kumar Biswas[1], Nazar Farid[1], Bharat Bhushan Bhatt[2], Dipti Gupta[2], Gerard M. O'Connor[*1], Patricia Scully[*1]*

[1]School of Physics, NCLA, University of Galway, Ireland.

[2]Indian Institute of Technology, Bombay, Maharashtra, India.

J. Phys. D: App. Phys., 2023, **56**, 085101

Abstract

Microfabrication of Polyimide (PI) with femtosecond laser of wavelength 1030 nm is studied in two process conditions. Firstly, the low power-low scan speed regime is investigated for laser carbonization producing piezoresistive Laser Induced Graphene (LIG). The heat accumulation model is modelled to find the temporal evolution of temperature at the laser focus for a single laser scan. Secondly, the high power-high scan speed regime is studied for laser ablation where clean ablation was observed due to multiphoton absorption. To demonstrate the application of this process, a 2-Dimensional (2D) LIG based strain sensor is drawn on a Kapton PI sheet using laser carbonization and transformed into a 3-Dimensional conformal sensor by cutting into a Kirigami design using laser ablation. The strain in the sensor is calculated from Finite Element Analysis (FEA) and the Gauge Factor (GF) is 88.58±0.16. This laser process enables the transformation of any 2D PI sheet into a 3D conformal sensor using femtosecond laser, which is useful for wearable sensors and health-monitoring applications. The fabricated sensor is demonstrated used on a knee-joint to monitor real-time tracking of bending and twisting knee movements.

7.1. Introduction

Femtosecond-pulsed laser processing is widely used for laser microfabrication of optically transparent polymers because of its high precision and controllable thermal effects [1]. A femtosecond laser beam interacts differently with polymers when compared with lasers with higher pulse durations, due to non-linear absorption arising from high pulse intensity (~10^{12} W/cm^2). Since its pulse duration (t_p) is shorter than the electron-lattice relaxation time, the ablation process in the laser-affected zone happens faster than the transfer of energy to its surrounding regions, enabling more precise microfabrication, when compared to picosecond and longer pulse-duration counterpart processes [2]. Femtosecond Infra-Red (IR) laser processing of Polyimide (PI) gives rise to many interesting properties because of its optical transparency at 1030 nm and its ability for both surface and sub-surface precise microfabrication [3, 4]. PI has a bandgap of 3.1 eV [5] causing it to absorb at 400nm wavelength, at which single-photon absorption occurs causing electronic excitation from Higher Occupied Molecular Orbital (HOMO) to Lower Occupied Molecular Orbital (LUMO) creating photochemical scission of the ring structures in the PI molecule causing the clean ablation [6, 7]. Photochemical ablation can also be achieved by a multi-photon absorption process (MPP) with femtosecond IR lasers at high intensity, in which the ablation threshold (F_{Th}) decreases with decreasing pulse duration ($F_{Th} \propto t_p^{1/2}$) [8]. In addition, due to having a pulse duration less than the electron-lattice coupling time of PI (~34 ps) [9], the energy does not thermalize into the lattice, enabling a clean ablation process.

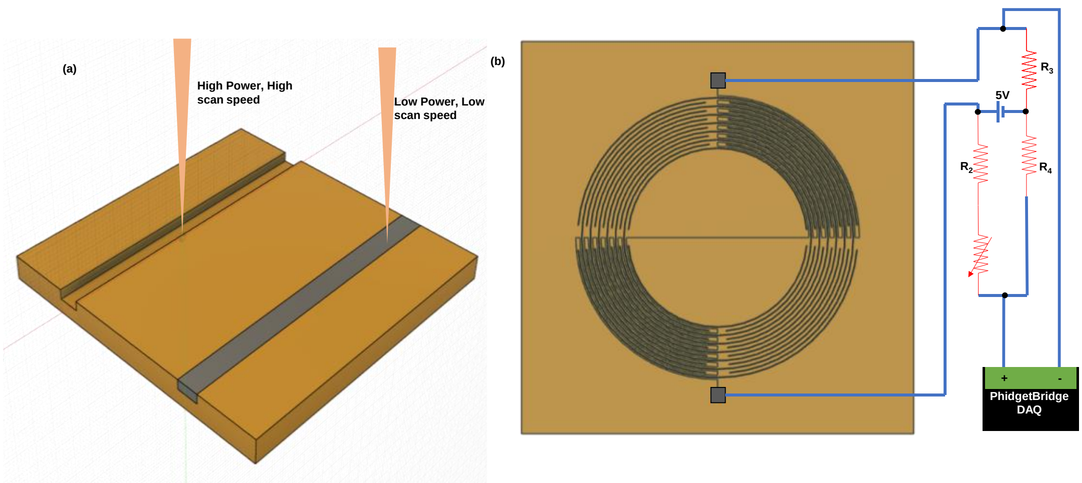

Fig. 7.1. (a) Process conditions of femtosecond laser printing, (b) Kirigami sensor connected to Wheatstone Bridge and PhidgetBridge DAQ, R_2, R_3 and R_4 used in this application are of 1 MΩ each and potentiometer was used in series with R_2 to balance the bridge.

When thermally heated, PI forms graphene by a process called carbonization, which exhibits excellent piezoresistive properties and is often used in strain-sensor applications [10-15]. Such a thermal process can be achieved by the heat accumulation process using femtosecond lasers where the residual fraction of heat from each of the laser pulses is accumulated over the laser spot, causing vibrational excitation, which results in photothermal conversion of PI to LIG [16-18]. So, if the laser is scanned at a fluence below the ablation threshold and at a low speed and high repetition rate, it will allow heat accumulation to occur due to the number of pulses per spot, generating sufficient heat at the laser focus to thermalize PI creating graphene without any ablation. Both photochemical ablation and photothermal carbonization have a wide range of applications. Ablation is applied to surface modification for Very Large-Scale Integration (VLSI) applications [19, 20] and carbonization enables creation of conducting circuits for flexible sensor applications (Figure 7.1a) [13]. Hence, a study on laser parameters to achieve selective ablation and carbonization is required.

Kirigami is a Japanese art form involving cutting ("Kiri") of papers ("-gami") or any 2-dimensional surface to convert them into 3-dimensional objects, which have various applications in soft-robotics, solar tracking, health-monitoring and wearable sensors [21-28]. Kirigami design enables functional sensor structures to be printed on a 2D planar surface, with cuts to enable the sensor structures to conform to a 3D topological surface. Such design enables the engineering of increased elasticity into composites while adding stress-concentrating points at which to place strain sensors, enabling targeted and unique sensor applications [27]. Such a designing strategy can be applied to a PI film to overcome its stiffness and allow conformal fitting on human body-joints such as knee, ankle, shoulder, etc. for health-monitoring applications [24]. Ultraviolet (UV) lasers are mostly used for ablation [9] and carbonization [29] of PI, while CO_2 lasers are used for carbonization of PI only [30, 31], but both types of laser lack precision in micro-structuring because of longer pulse durations. Femtosecond IR laser allows us to apply both the photochemical and photothermal processes from a single laser with higher precision [32] to create a Kirigami design from PI and LIG sensors by laser writing or printing.

In this paper, a rotationally symmetric concentric circular Kirigami cut pattern is designed for Polyimide to leverage the photochemical ablation effect of femtosecond laser exposure to cut the design boundaries. The LIG sensor is printed within the inner boundaries of the design (Figure 6.1b) utilizing the photothermal carbonization effect of IR laser. The Kirigami structure allows the 2D printed sensor structure to morph into a 3D conformal sensor structure. Out-of-plane displacement is modelled using FEA analysis which accurately predicts the displacement of the Kirigami-designed sensor structure upon loading of various weights at the central point of the sensor structure. This model is used to calculate the average strain of the sensor upon loading of 100-700 mg by calculating the von-Mises stress around the notches and edges of the sensor. The sensor is designed for knee-joint monitoring applications detecting the bending and twisting of knees. A comparative study of ablation and carbonization provides a set of values of threshold fluence and incubation coefficient for both processes. Carbonization of PI using femtosecond laser has been reported in other literatures but the process of carbonization using such a laser needs to be studied [33, 34]. Such a process of carbonization of PI was modelled for the first time in this paper using the heat accumulation model in Python, enabling estimation of the process parameters to reach the threshold carbonization temperature of 700^0C [35] to initiate the carbonization process. Such a process enables scalable innovative pathways for femtosecond laser microfabrication applications [2].

7.2. Experimental Methods

7.2.1.Laser System:

A femtosecond laser (Amplitude Systems S-PULSE HP) with wavelength centered at 1030 nm and generating pulses of width 550 fs at a repetition rate 200 kHz, was used for this experiment. The laser was linearly polarized in TEM00 (Lowest Order Transverse) mode and had a Gaussian distributed intensity profile. The laser beam was focused on the Kapton HN PI film of thickness 127 µm using a beam scanner (Hurryscan, Scanlabs) with a telecentric lens (f = 100 mm, NA= 0.014) achieving a maximum scan speed (v) of 2000 mms^{-1}. The laser power was controlled by using a combination of half-wave plates and a polarized beam-splitter to attenuate the intensity. The power was measured by an adjustable power-meter placed in the beam-path before the focusing lens. The PI film target was placed on an adjustable motor-controlled stage (Aerotech 3200 XYZ) controlled by ViewMMI software, and the locus of the laser scan on this target, was prepared in Dynamic Machine Control (DMC) interface.

7.2.2.Laser Carbonization and Ablation of Polyimide:

Polyimide film (Dupont Kapton ® HN) sheet of thickness 125 µm was cut into dimension of 60 mm x 60 mm, washed with isopropyl alcohol, rinsed, dried, and fixed on the Aerotech stage assisted with a vacuum pump to keep the PI sheet in place, ensuring the focused laser position remained constant throughout the laser scan. Both carbonization and ablation were carried out at a focal point with spot-radius (ω_0) 22.66 µm (Figure 6.2, 6.3). A linear pattern of 5 mm was designed in the DMC interface for both experiments and the PI sample was monitored by a CCD. The femtosecond laser was scanned at two process conditions (PC): (PC1) Low Power-Low scan speed to study carbonization, and (PC2) High Power-High scan speed to study ablation. For PC1, power was varied between 0.242-0.281 W and scan speed was varied between 2-3 mm/s at individual power with an interval of 0.25 mm/s at a repetition rate (f) 200 kHz. For PC2, power was varied from 1.726-2.512 W at a scan speed of 200-300 mm/s with an interval of 25 mm/s for each power at repetition rate 200 kHz. A parameter space was developed to find the desired process parameters for carbonization and ablation alone (Figure 6.12). The Kirigami cut pattern was designed and cut using the laser ablation process and the sensor pattern was designed and printed using the laser carbonization process.

7.2.3.Laser Scan Feature Measurements and Characterizations:

The widths (D) of the carbonized and ablated features were measured using an Olympus BX60M optical microscope. For carbonized features, the presence of graphene was detected by Raman Spectroscopy using a 532 nm excitation laser with a RENISHAW inVia Raman Microscope. The depth of the carbonized and ablated tracks was measured using a cross-sectional Hitachi S-2600 Scanning Electron Microscope (SEM). The diameter of single pulse ablated craters was measured by the SEM and the depths were calculated using an optical surface profilometer (Zygo OMP-0360C).

7.2.4.Laser Printing of Kirigami Inspired Sensor:

The Kirigami sensor with external diameter of 51 mm, with a radial spacing of 3 mm between each concentric circle and angular spacing of 5^0, was designed in Autodesk Fusion 360 (Figure 6.1) and imported into DMC software to create the process recipe. The sensor element was drawn within the inner boundaries of the design which helps the 2-D sensor element to stretch conformally in 3D. The sensor element was printed with a single pass of a laser at a power 0.242±0.001 W, scan speed 2 mm/s, repetition rate 200 kHz, utilizing the photothermal process to create Laser Induced Graphene (LIG). Then the sensor was covered by 51mm x 50mm 3M clear scotch tape of thickness 54 µm to prevent delamination of LIG from PI. The boundaries were printed on the scotch tape coating the PI, with 100 passes at power 2.524 W, scan speed 300 mm/s, repetition rate 200 kHz, thus utilizing the photochemical process to create pure ablation of the PI along with the scotch-tape. Silver pads were created at both ends of the LIG track with commercial silver conductive paint (RS Pro), and steel wires (D = 1 mm) were pasted on them followed by encapsulation with epoxy resin. Sensor Data Acquisition (DAQ) was performed by connecting the sensor to one of the arms of a balanced Wheatstone Bridge and connecting the bridge output to the PhidgetBridge Wheatstone Bridge Sensor Interface with a voltage supply of 5V powered by USB (Figure 7.1b). A gain of 128 x was selected for monitoring the changes in the output.

7.2.5.Electromechanical Characterization of the Sensor:

The electromechanical characterization of a single LIG track of length 30 mm drawn at 0.242 ± 0.001 W, 2 mm/s and repetition rate 200 kHz, printed on ASTM D638 Dog-Bone PI was performed using a motorized force tester system (MARK-10 ESM303) to measure the Elastic modulus (*E*), elastic to plastic deformation strain point, and the Gauge Factor (*GF*) of the single-track sensor element. Tensile stress was applied to the Dog-Bone and resistance was measured along with the strain using a source meter unit (Keysight B2900A) at the same sampling rate.

7.3. Results and Discussion

7.3.1.Calculation of spot-size and ablation threshold:

The spot radius of the Gaussian laser beam is calculated from the equation 7.1:

$$\omega_0 \approx \frac{\lambda}{\pi\,\theta} \tag{7.1}$$

$NA \approx sin\theta = 0.014, \lambda = 1030$ nm [36] which gives us the theoretical value of spot radius to be 23.41 µm. Single pulse study was performed at power (*P*) range 0.8-3.0 W by scanning the laser at 4000 mm/s at a repetition rate of 200 kHz. The diameters (*D*) of the spots were measured by optical microscopy. The spot size (ω_0) was calculated from the slope of Equation 1. ω_0 was found to be 22.66 µm from the slope (Figure 7.2) which is close to the theoretical value. No carbonaceous structures were found from single spots.

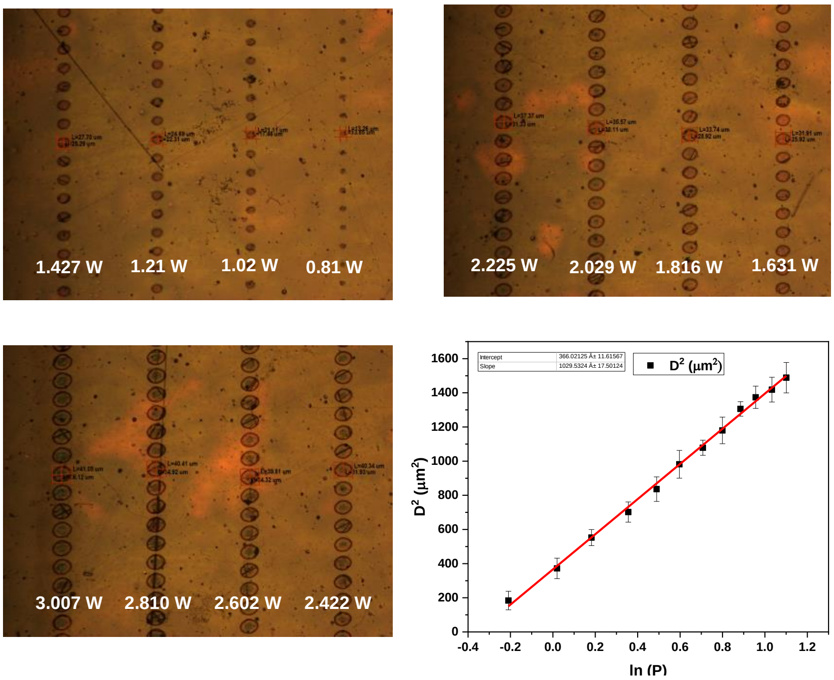

Fig. 7.2. Spot-size measurement from ablated spots on PI.

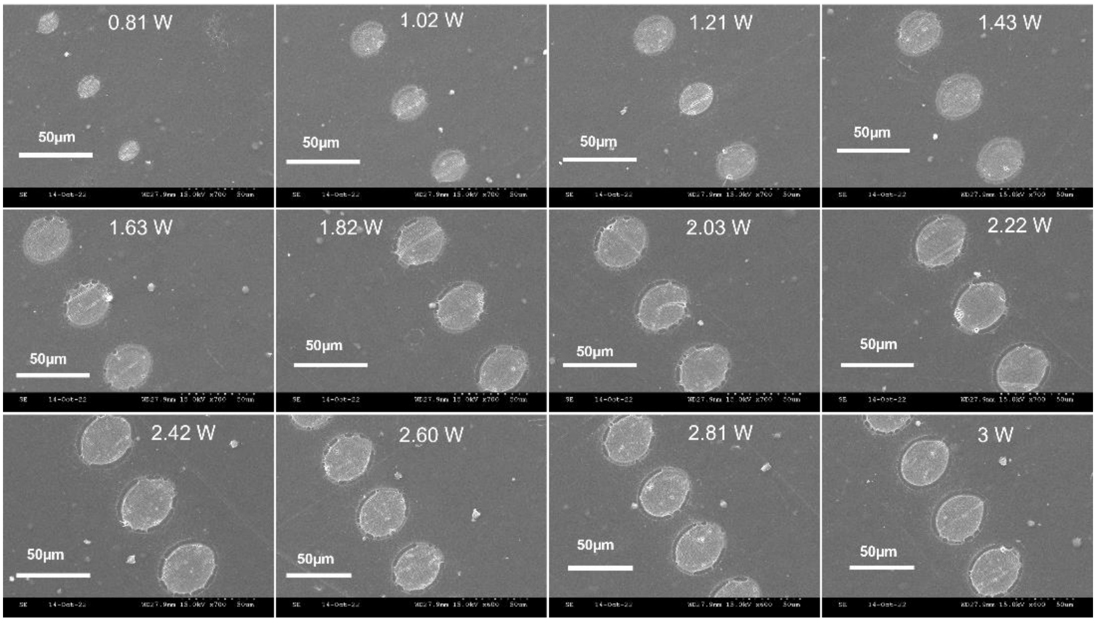

Fig. 7.3. SEM images of laser ablated spots on PI.

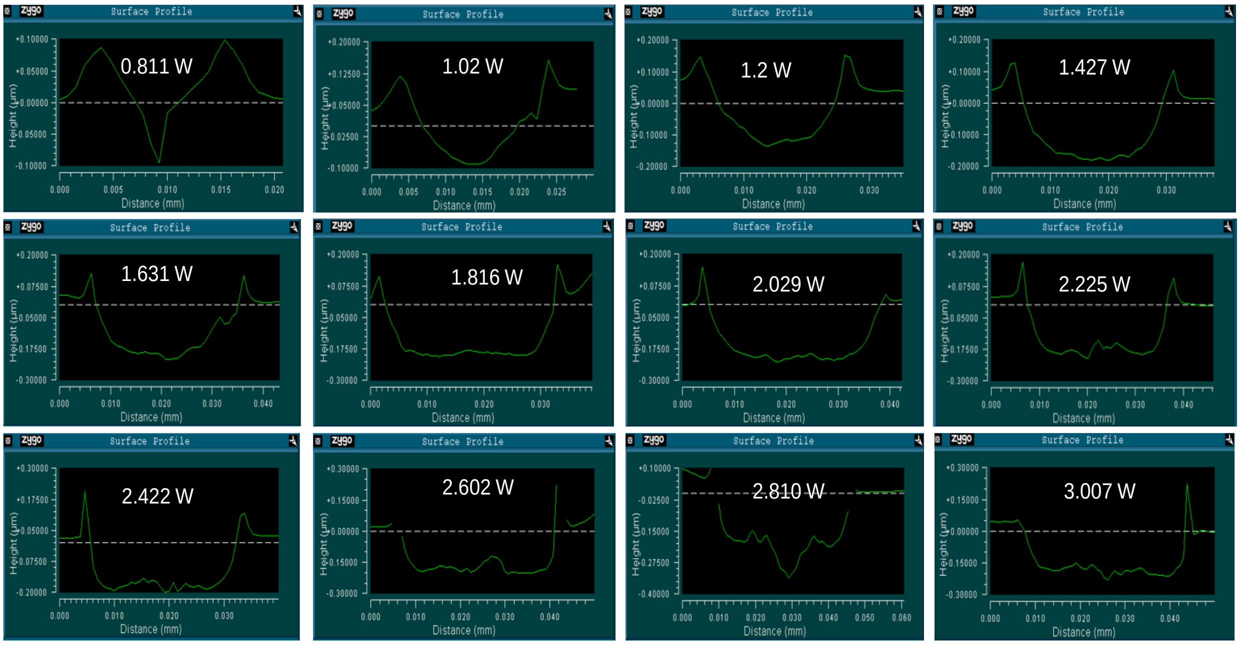

Fig. 7.4. Ablated depth by single laser pulses of power 0.8-3 W measured by Zygo profilometer. Detailed results in the Appendix B.

Single pulse ablation threshold ($P_{1,Th}$) was calculated from the ablated depths (d) measured by Zygo profilometer using the x-intercept of the plot d vs ln(P) from Equation 7.2.

$$d = \frac{1}{\alpha_{eff}}(\ln\frac{F}{F_{Th}}) \quad (7.2)$$

where α_{eff}= effective absorption coefficient at a fixed scan speed, F_{Th}= Threshold fluence of ablation. $P_{1,Th}$ was found to be 0.29 W.

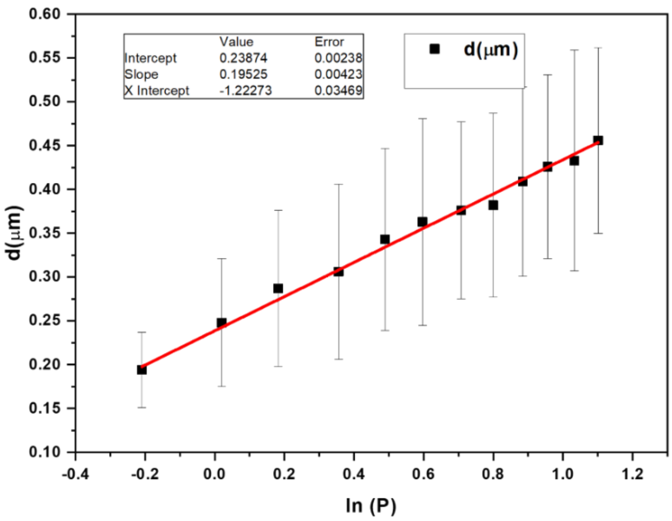

Fig. 7.5. Single pulse ablation threshold power measured from ablated spots on PI.

7.3.2.Laser Carbonization of PI:

For laser powers ranging from 0.242-0.281 W, carbonization occurred only at low scan speeds (2-3 mm/s) as fluence lower than the single pulse ablation threshold (0.29 W, 182.98 mJ/cm^2, Figure 7.6, 7.14) does not have sufficient photon flux to cause photochemical ablation [37]. Spallation of LIG was observed above 0.29 W (Figure 7.13) due to ablation. The low scan speed enabled heat accumulation from pulses per spot [38, 39] to be sufficient to create the photothermal conversion of PI to LIG. The threshold fluence of carbonization at each scan speed ($F_{N,Th}$) was calculated from the x-intercept of the plot D^2 vs ln(F) at individual scan speed and the single pulse threshold fluence ($F_{1,Th}$). The incubation coefficient (S) of carbonization was calculated from the y-intercept and slope of the plot ln($N.F_{N,Th}$) vs ln(N) respectively (Figure 7.10a,b) from Equation 7.3 and Equation 7.4 [31, 38] :

$$D^2 = 2\omega_0^2[\ln(F) - \ln(F_{N,Th})] \tag{7.3}$$

$$\ln(N.F_{N,Th}) = \ln(F_{1,Th}) + S.\ln(N) \tag{7.4}$$

where, Equation 7.4 is derived from $F_{N,Th} = (F_{1,Th}).N^{S-1}$, number of laser pulses per spot $N = 2\omega_0 f/v$. S and $F_{1,Th}$ for carbonization were calculated to be 0.21±0.03 and (5.6±1.5) x 10^4 mJ/cm^2 respectively. Such a low value of incubation coefficient indicates that heat accumulation plays an important role at low scan speed [39]. The higher value of $F_{1,Th}$ indicates that it will never be possible to carbonize the material with a single laser pulse since it exceeds the single pulse threshold fluence for ablation, and ablation will predominate over carbonization at such high fluence. The threshold fluence values are summarized in Table 7.1.

Cross-sectional SEM images (Figure 7.11a-e) showed that the morphology of LIG is not fibrous, compared with LIG obtained from CO_2 lasers found in other studies. This indicates that the crystallite growth is more planar in the axis vertical to PI substrate [40]. The carbonization depth increased with increasing fluence and decreasing scan speed (Figure 7.11f) due to increasing heat accumulation. The Raman spectra showed three distinct peaks D, G and 2D at ~1344 cm^{-1}, ~1576 cm^{-1}, and ~2688 cm^{-1} respectively (Figure 7.7a-e) associated with the breathing mode of phonons having A_{1g} symmetry, in-plane vibrations of E_{2g} phonons, and overtone of D band respectively [30]. The average crystallite size (L_a) was measured from the ratio of the intensity of D and G peak (I_D/I_G) and increased with scan speed, indicating that the planar growth is favoured at higher scan speed [30] (Figure 7.7f). The electrical conductivity also increased with scan speed, due to increasing crystallite size, L_a (Figure 7.9b). The conductivity of LIG is summarized in Table 7.2.

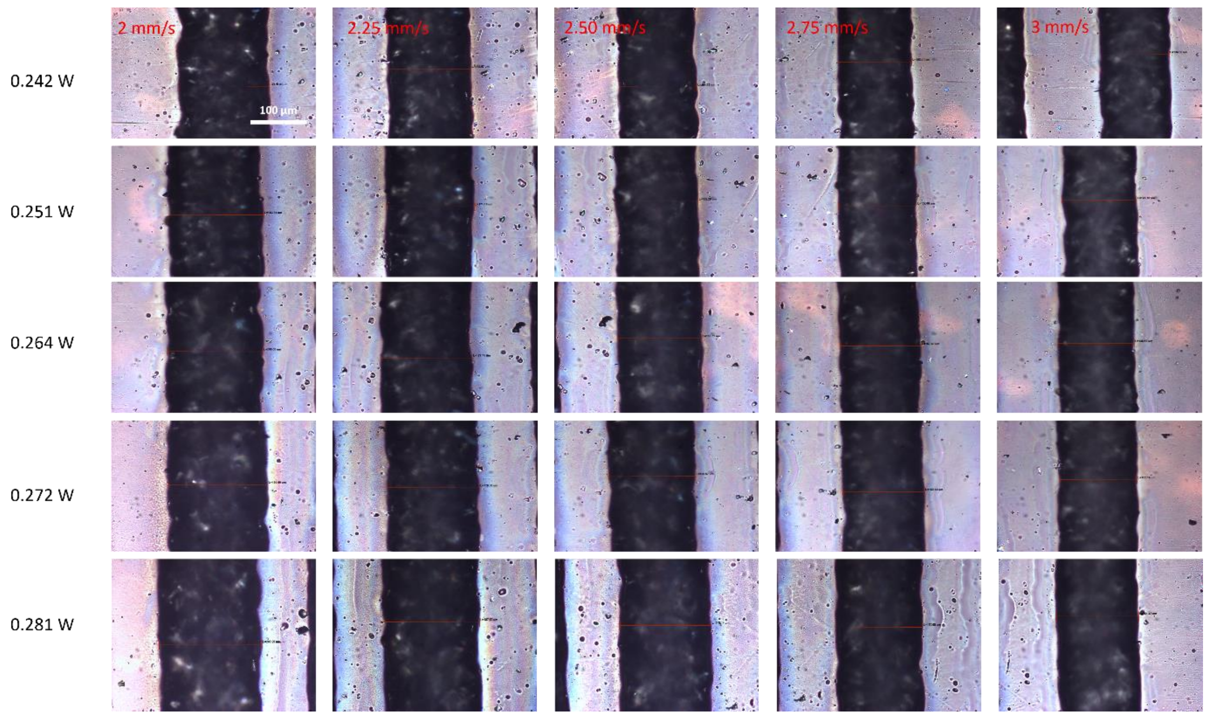

Fig. 7.6. Optical microscope images of LIG drawn at laser power 0.242-0.281 W at 2-3 mm/s at 200 kHz.

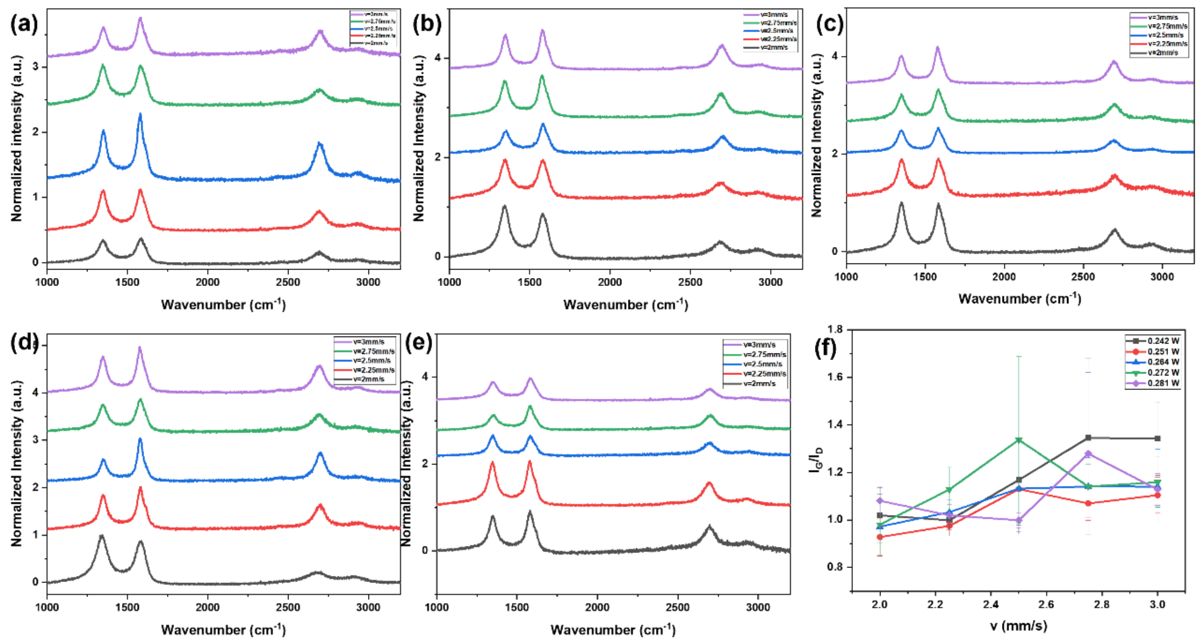

Fig. 7.7. (a-e) Raman Spectra of LIG drawn at laser power 0.242-0.281 W at 2-3 mm/s at 200 kHz, (f) Defect ratio (I_D/I_G) of the LIG.

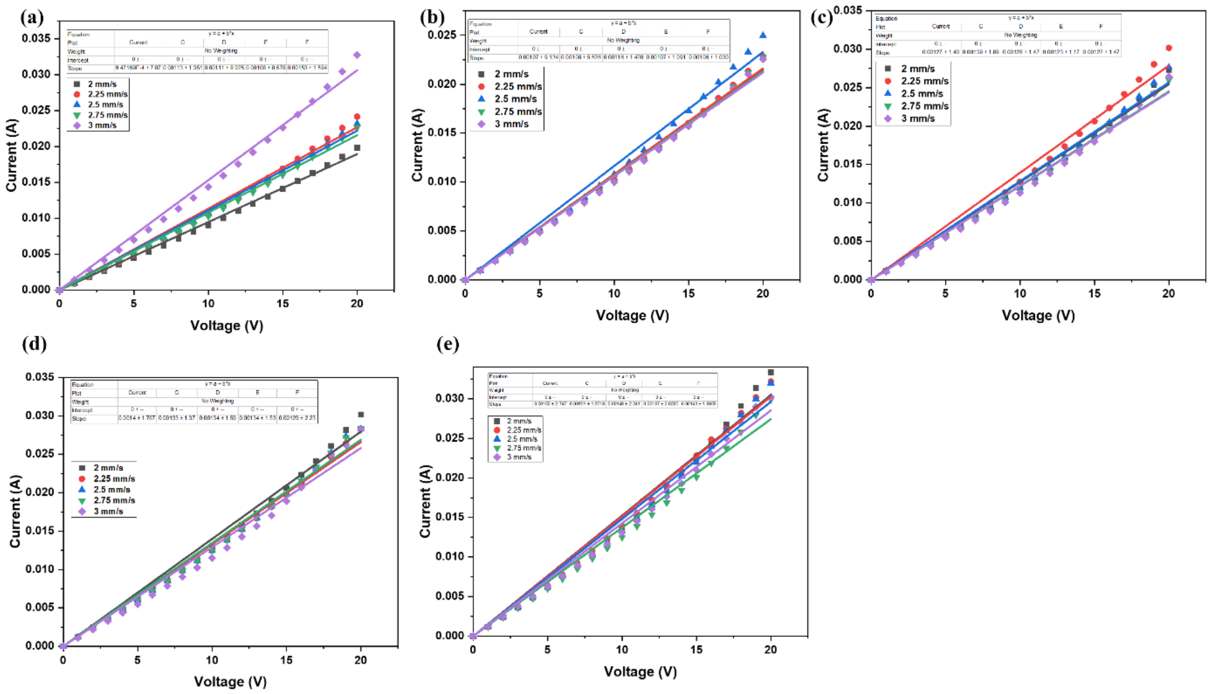

Fig. 7.8. (a-e) IV measurement of LIG drawn at laser power 0.242-0.281 W at 2-3 mm/s at 200 kHz.

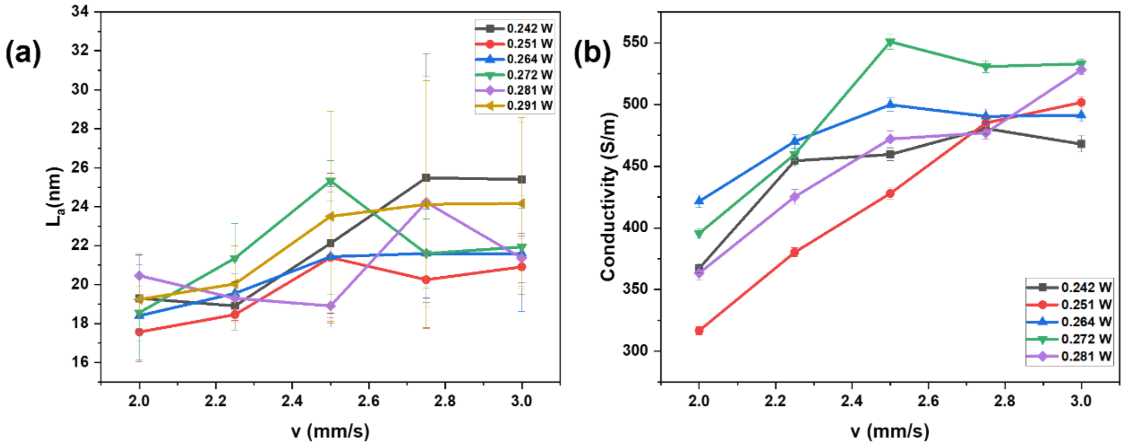

Fig. 7.9. (a) L_a of LIG vs v, (b) electrical conductivity vs v for laser power 0.242-0.281 W.

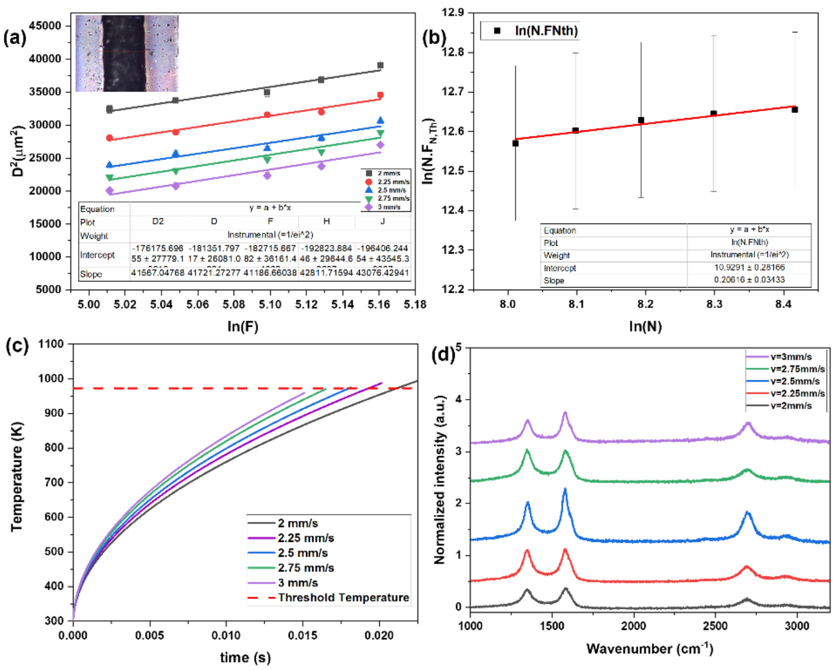

Fig. 7.10. (a) D^2 vs ln F, (b) Calculation of incubation coefficient in the photothermal regime from ln(N. $F_{N,Th}$) vs ln(N), (c) T vs t from heat accumulation model at threshold fluences for scan speed 2-3 mm/s, (d) Raman spectra of LIG drawn at 0.242 W at 2-3 mm/s.

Table 7.1. Calculation of uncertainties in threshold fluences.

v (mm/s)	*N*	**lnN**	***FN,Th***	***Δ FN,Th***	**ln(N. FN,Th)**	**Δln (N.FN,Th)**
2.00	4520.00	8.42	69.29	13.61	12.65	0.20
2.25	4017.78	8.30	77.23	15.18	12.65	0.20
2.50	3616.00	8.19	84.46	16.59	12.63	0.20
2.75	3287.27	8.10	90.38	17.79	12.60	0.20
3.00	3013.33	8.01	95.53	18.75	12.57	0.20

Table 7.2. Calculation of uncertainties in conductivity.

0.242 W									
v (mm/s)	***R (Ω)***	***ΔR(Ω)***	***D (μm)***	***ΔD (μm)***	***D (μm)***	***Δd (μm)***	**Area (μm2)**	***σ (S/m)***	***Δσ (S/m)***
2.00	1109.09	10.43	180.10	2.12	44.39	1.55	12277.47	367.19	4.00
2.25	948.15	8.13	167.57	3.32	41.22	0.85	11608.88	454.26	4.44
2.50	944.60	9.54	154.72	2.64	39.45	0.75	11521.35	459.43	5.09
2.75	976.23	8.65	148.71	3.26	37.23	0.54	10658.08	480.55	5.29

3.00	697.93	7.85	141.86	2.33	34.17	0.62	9186.59	467.90	6.52
0.251 W									
v (mm/s)	***R (Ω)***	***ΔR(Ω)***	***D (μm)***	***ΔD (μm)***	***D (μm)***	***Δd (μm)***	**Area (μm2)**	***σ (S/m)***	***Δσ (S/m)***
2.00	984.10	9.41	183.71	1.03	45.52	1.45	16045.98	316.64	3.29
2.25	979.27	8.46	170.14	3.27	43.24	0.86	13428.98	380.21	3.68
2.50	925.16	8.16	160.29	2.15	40.62	0.97	12630.62	427.89	4.30
2.75	1002.22	8.47	152.00	2.19	38.88	0.44	10286.81	484.98	5.12
3.00	1004.10	7.12	144.15	2.14	35.63	0.62	9042.61	550.68	4.78
0.264 W									
v (mm/s)	***R (Ω)***	***ΔR(Ω)***	***D (μm)***	***ΔD (μm)***	***D (μm)***	***Δd (μm)***	**Area (μm2)**	***σ (S/m)***	***Δσ (S/m)***
2.00	843.53	9.45	187.00	1.20	48.09	1.12	14064.38	421.45	5.04
2.25	782.60	9.15	177.71	1.44	45.47	0.74	13591.99	470.05	5.88
2.50	837.28	8.15	162.71	1.19	42.27	0.66	11949.97	499.73	5.43
2.75	867.60	9.45	157.43	1.35	40.45	0.87	11752.26	490.38	5.95
3.00	885.94	8.45	149.57	1.75	37.26	0.56	11486.64	491.33	5.16
0.272 W									
v (mm/s)	***R (Ω)***	***ΔR(Ω)***	***D (μm)***	***ΔD (μm)***	***D (μm)***	***Δd (μm)***	**Area (μm2)**	***σ (S/m)***	***Δσ (S/m)***
2.00	776.47	7.15	192.00	1.25	50.05	1.06	16282.92	395.47	3.88
2.25	803.87	8.56	178.86	1.32	47.02	0.94	13534.64	459.55	5.20
2.50	805.40	7.61	167.57	2.36	45.70	0.74	11270.82	550.81	5.91
2.75	802.57	6.45	161.14	2.16	42.50	0.61	11738.68	530.72	4.85
3.00	871.73	5.17	154.14	2.17	39.27	0.67	10763.72	532.87	3.81
0.281 W									
v (mm/s)	***R (Ω)***	***ΔR(Ω)***	***D (μm)***	***ΔD (μm)***	***D (μm)***	***Δd (μm)***	**Area (μm2)**	***σ (S/m)***	***Δσ (S/m)***
2.00	740.26	10.52	197.75	2.16	51.04	1.05	18598.07	363.18	5.32
2.25	718.77	9.46	186.01	2.20	48.30	1.01	16361.42	425.17	5.82
2.50	752.68	9.64	175.14	2.15	46.04	0.22	14071.92	472.07	6.32
2.75	802.49	8.16	170.00	1.16	44.64	0.62	13062.26	476.99	5.21
3.00	767.04	5.15	164.43	3.14	41.65	0.62	12343.87	528.08	4.04

7.3.3.Modelling of Heat Accumulation:

The temporal evolution of temperature using femtosecond laser has been previously modelled in many literatures[18, 41-43]. But most of them have been reported for other materials such as steel, Polymethylacrylate (PMMA). Here we have modelled the thermal accumulation for carbonization of PI using a 2D heat accumulation model [18]. Heat accumulation occurs when a certain fraction of fluence of a single laser pulse, called the residual heat coefficient ($\eta_{Heat}(v)$) is converted into thermal energy before the heat is dissipated. Thus, energy from the consecutive pulses is incident on the material and accumulates, causing increased temperature. Thermal effects are visible when the temperature accumulated at the laser-spot reaches the threshold temperature which is 973 K for carbonization of PI [35]. To model such effects, it is necessary to calculate the value of $\eta_{Heat}(v)$ as a function of scan speed (v). The rise in temperature for a given power and scan speed is calculated from Equation 7.5 [16] and the minimum temperature required for thermal effect by heat accumulation caused by subsequent pulses (HAP) for 1D heat flow is calculated from Equation 7.6 [17].

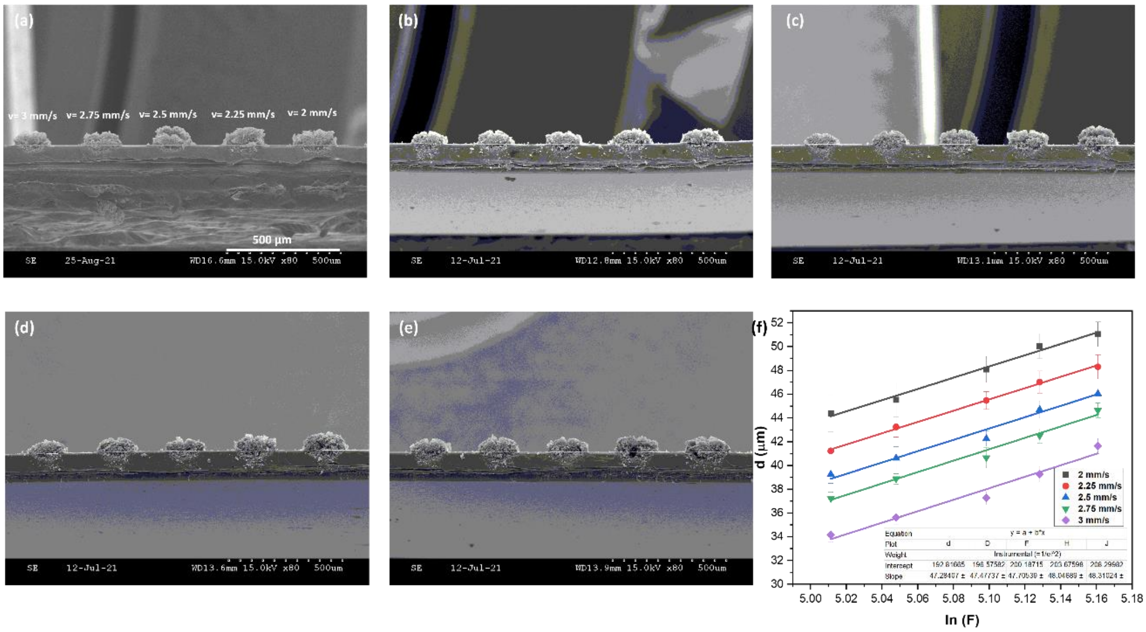

Fig. 7.11. (a-e) Cross-sectional SEM images of femtosecond LIG at 0.242W, 0.251 W, 0.264 W, 0.272 W and 0.281 W respectively at 2-3 mm/s at 200 kHz, (f) d vs ln F.

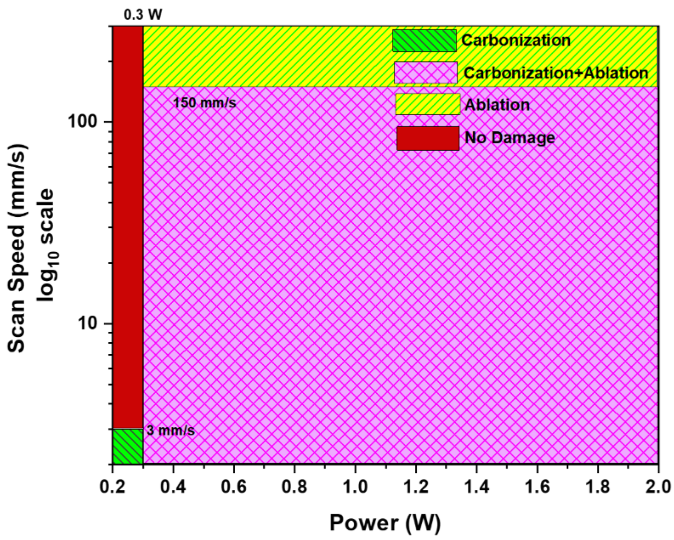

Fig 7.12. Parameter Space of 1030 nm fs laser microfabrication on Polyimide.

Hence $\eta_{Heat}(v)$ is calculated by equating Equation 7.5 and Equation 7.6:

$$P_{Th} = \frac{\pi\, v\, \omega_0\, \rho\, \Delta T C_p}{4 \eta_{abs} \alpha \gamma} \tag{7.5}$$

Also, $$P_{Th} = \frac{C_{Mat}\, \Delta T\, A \sqrt{f}}{\sigma\ (2\sqrt{N} + C_1)}, \tag{7.6}$$

where for 1-dimensional heat flow, $$C_{Mat} = \frac{\rho C_p (4\pi D_T)^{1/2}}{\eta_{Heat}(v)\, \eta_{abs}} \tag{7.7}$$

Using Equations 7.5, 7.6 and 7.7:

$$\frac{\pi\, v\, \omega_0\, \rho\, \Delta T C_p}{4 \eta_{abs}\, \alpha\, \gamma} = \frac{C_{Mat}\, \Delta T\ A \sqrt{f}}{\sigma\ (2\sqrt{N} + C_1)}$$

$$\frac{\pi\, v\, \omega_0\, \rho\, \Delta T C_p}{4 \eta_{abs}\, \alpha\, \gamma} = \frac{\frac{\rho C_p (4\pi D_T)^{1/2}}{\eta_{Heat}(v).\, \eta_{abs}}\ \Delta T\ \pi\, \omega_0^2 \sqrt{f}}{\sigma\ (2\sqrt{N} + C_1)}$$

$$\eta_{Heat}(v) = \frac{4\, A\, \alpha\, \gamma\ \ \omega_0 (4\pi D_T f)^{1/2}}{v\ \ \sigma\ (2\sqrt{N} + C_1)} \tag{7.8}$$

The accumulated temperature over a spot is given by[18]:

$$\Delta T = \frac{8\, \eta_{abs}\, \eta_{Heat}(v) E_p \sqrt{f}}{\pi d_s^2} . \frac{1}{\rho C_p \sqrt{4\pi D_T}} .(2\sqrt{ft} - 1.46) \tag{7.9}$$

Where, peak laser energy, $E_p = \frac{2P}{\pi f.\varpi_0^2}$, d_s= $2\varpi_0$, and t= duration of processing. The parameters are explained in Table 4.5.

F_{Th} for each scan speed was calculated from Figure 7.10a, and then used to calculate the temporal evolution of temperature at the laser spot on PI using Equation 7.9. Each of the threshold fluences gave the peak spot temperature around 900 K, which is the threshold temperature of carbonization of PI, validating the model (Figure 7.10c). Hence such a model can be used to find the peak spot temperature for a set of scan speed and fluence values.

At low scan speed, power above the photochemical threshold power (0.29 W) creates spallation of the LIG structures due to ablation and at higher power and intermediate scan speed (50-150 mm/s), carbonized residues were found alongside the ablated tracks. Such a process window is not desired in any applications, neither in graphene-based sensor printing nor in ablation. Hence, a scan speed of 2-3 mm/s was chosen for low power scan to allow heat accumulation for photothermal carbonization, and a scan speed of 200-300 mm/s was chosen for high power scan for photothermal clean ablation.

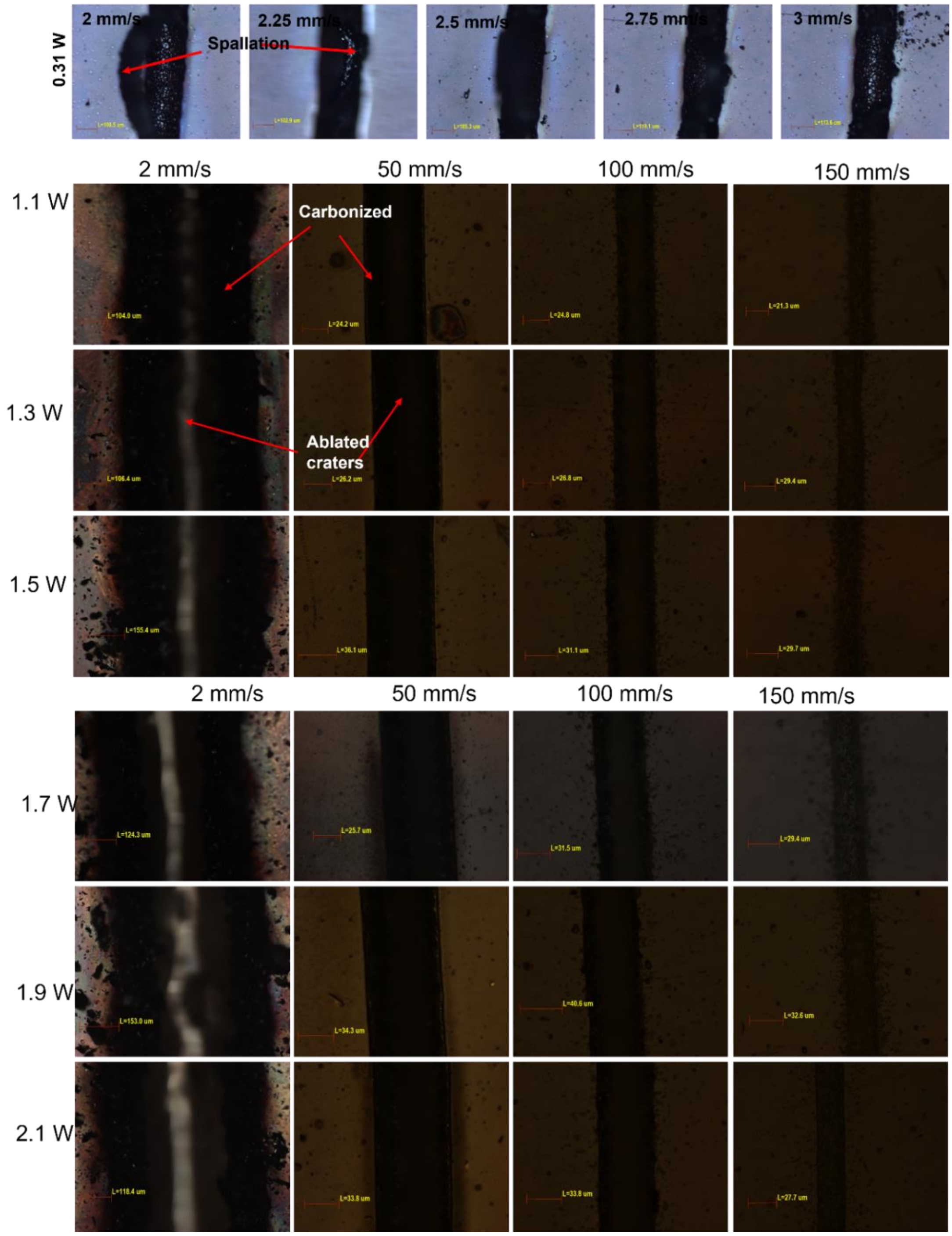

Fig. 7.13. Optical microscope images of fs laser drawn patterns on PI at power 0.31 W at *v*=2-3 mm/s and 1.1-2.1 W at *v*= 2-150 mm/s at *f*=200 kHz. The patterns show that spallation of LIG occurs at power above ablation threshold (0.29 W) at low scan speed and carbonization occurs along with the ablation at high power-low scan speed.

7.3.4.Laser Ablation of PI:

In the high-power regime, clean ablation occurred due to the photochemical process (Figure 7.16a-e), caused by the high photon flux leading to multiphoton absorption, but the high scan speed did not allow any heat accumulation. S and $F_{1,Th}$ for ablation were calculated to be 0.66±0.08 and (1.89±0.56) x 10^3 mJ/cm^2 respectively from equations 7.3 and 7.4 (Figure 7.15a,b). The ablation depths were calculated from the cross-sectional SEM which showed clean ablation without any residual debris. The depth decreased with increasing scan speed at individual fluences (Figure 7.16f). The effective absorption coefficient at each scan speed can be calculated using the equation 7.2 [44]. The incubation coefficients and single pulse threshold fluences are summarized in Table 7.3. The higher value of S for ablation as compared to carbonization, explains the minimal thermal effect at higher powers. The slope of α_{eff} vs v (Figure 7.17) indicates that the effective absorption coefficient increases with scan speed, which explains the saturable absorber property of Polyimide [45, 46].

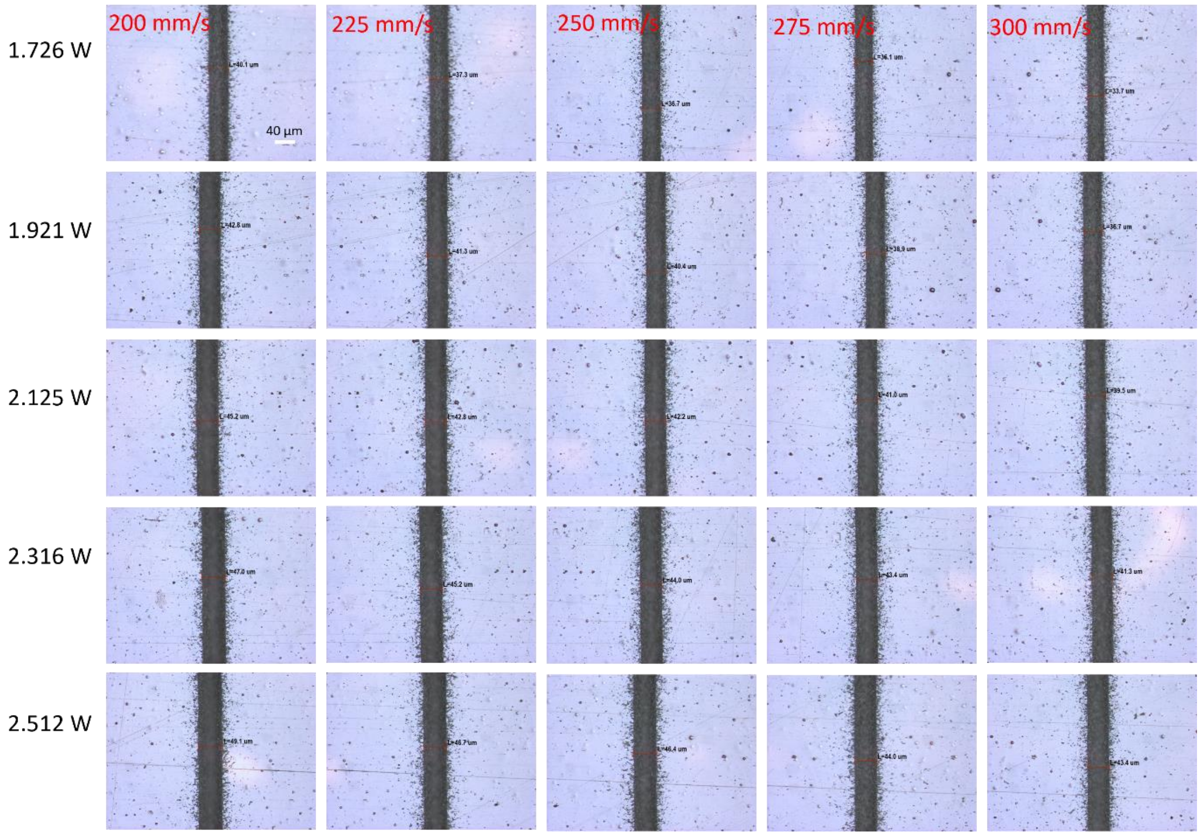

Fig. 7.14. Optical microscope images of ablated track drawn at laser power 1.726-2.512 W at 200-300 mm/s at 200 kHz.

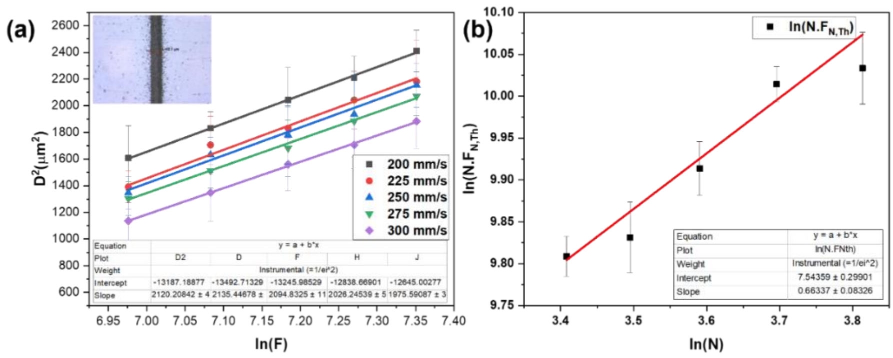

Fig. 7.15. (a) D^2 vs ln F, (b) Calculation of incubation coefficient in the photochemical regime from ln(N. $F_{N,Th}$) vs ln(N).

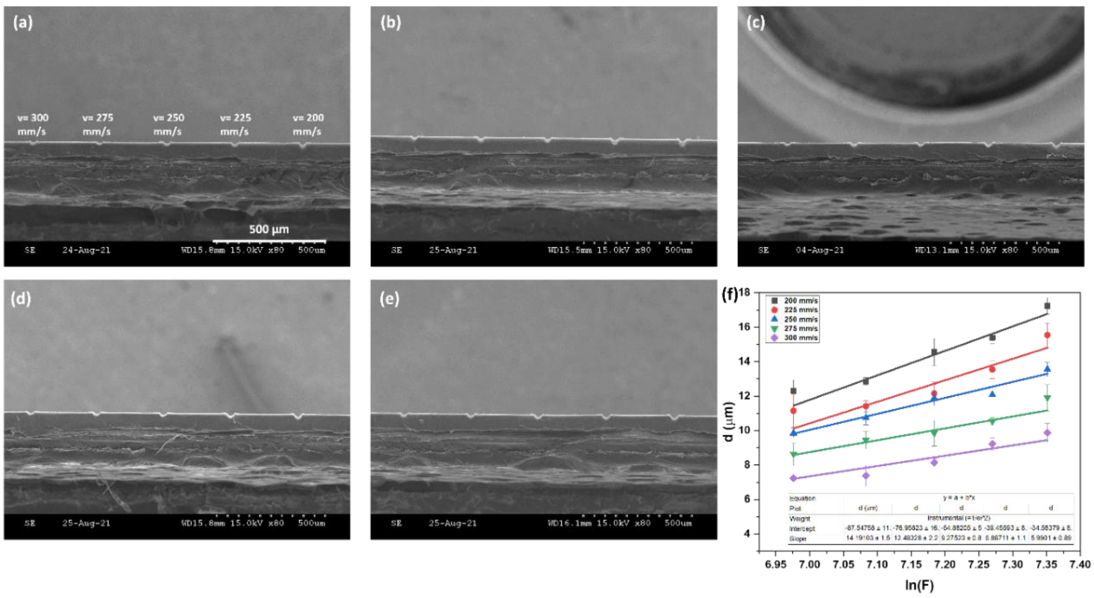

Fig. 7.16. (a-e) Cross-sectional SEM images of ablated tracks at 1.726W, 1.921W, 2.125W, 2.316W,2.512W-2.512 W at 200-300 mm/s at 200 kHz, (b) d vs ln F.

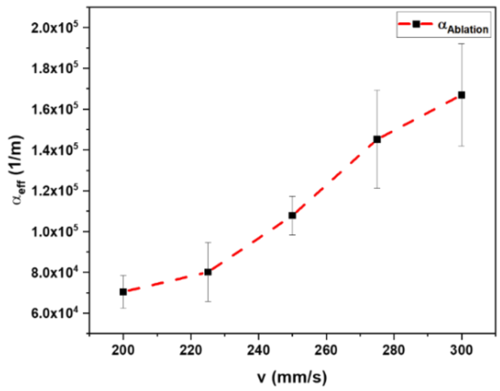

Fig. 7.17. The saturation effect is observed from the effective absorption coefficient (α_{eff}) measured from slopes in Figure. 3f.

Table 7.3. Summary of Laser carbonization and ablation.

Process	Power range (W)	Repetition Rate (kHz)	Scan speed (mm/s)	Incubation coefficient (S)	Single pulse threshold Fluence (mJ/cm^2)
Carbonization	0.242-0.281	200	2-3	0.21±0.03	(5.6±1.5) x 10^4
Ablation	1.726-2.512	200	200-300	0.66±0.08	(1.89±0.56) x 10^3

7.3.5.Kirigami designed sensor characterization:

A Kirigami designed sensor was created using the femtosecond laser (Figure 7.18a). From the electromechanical characterization of the LIG printed PI (Figure 6.18b), Elastic Modulus (*E)* was found to increase non-linearly with strain, which is acceptable since PI is a hyper-elastic polymer [47, 48]. The elastic-plastic transition occurs at around 1% strain (Figure 6.18c) as reported previously [49]. The resistance of the LIG track increased with applied tensile strain (ε) due to increased separation between the graphene crystallites and the *GF* was measured in the elastic region from the equation 7.10:

$$GF = {}^{\Delta R/R}/_{\in} \tag{7.10}$$

GF was found to be 96.97±3.17 (Figure 7.18d). The resistance of the Kirigami sensor was measured to be 1.04 MΩ (Figure 7.20) using IV characterisation. The change in the output voltage from the sensor connected with the PhidgetBridge DAQ system was measured by loading 0-700 mg at the center of the sensor at amplification of 128x (Figure 7.21b,c) and the off-plane displacement was measured by a travelling microscope placed in the plane of the sensor (Figure 7.21a). Finite Element Analysis (FEA) was performed using the Kirigami design in COMSOL to model the displacement along the z-axis upon loading of weights at the center of the innermost concentric circle (Figure 7.21d).

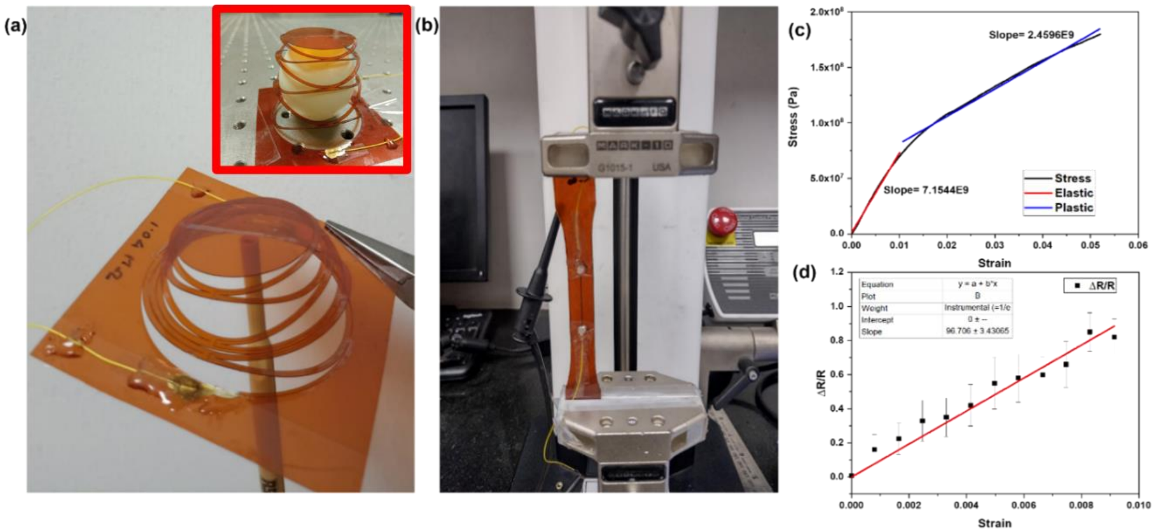

Fig. 7.18. (a) Kirigami designed Sensor, (b) ASTM D638 Dog-Bone Structure of PI for *GF* measurement, (c) Tensile Stress measurement of Polyimide by UTM, (d) *ΔR/R* vs Strain for Gauge Factor measurement of 30 mm LIG track made by femtosecond laser (0.242 W, 2 mm/s, 200 kHz).

A parametric scan of load mass was performed over 0-700 mg to find the displacement as a function of load which generated a displacement of 5.41-21.38 mm close to the experimentally calculated displacement (Figure 7.21e). Hence, this model was used to calculate the von Mises Stress distribution across the sensor as a function of loading (Figure 7.21a). Further loading above 700 mg caused strain more than 1% which is beyond the elastic limit and was not used for GF calculation (Figure 7.24). The FEA results showed that maximum stress of the order 10^7 N/m^2 occurred around the notches of the Kirigami design (Figure 7.21d) as compared to 10^5 N/m^2 in the planar structure (Figure 7.23) which are mostly responsible for the strain-sensitive response of the sensor. The average strain of the sensor for each loading was calculated using the model, and then used to measure the *GF* by plotting the relative change in the voltage (*ΔV/V*) vs strain (Figure 7.21c). *GF* was evaluated as 88.58±1.11 which is close to that calculated for a single LIG sensor element (96.97±3.17).

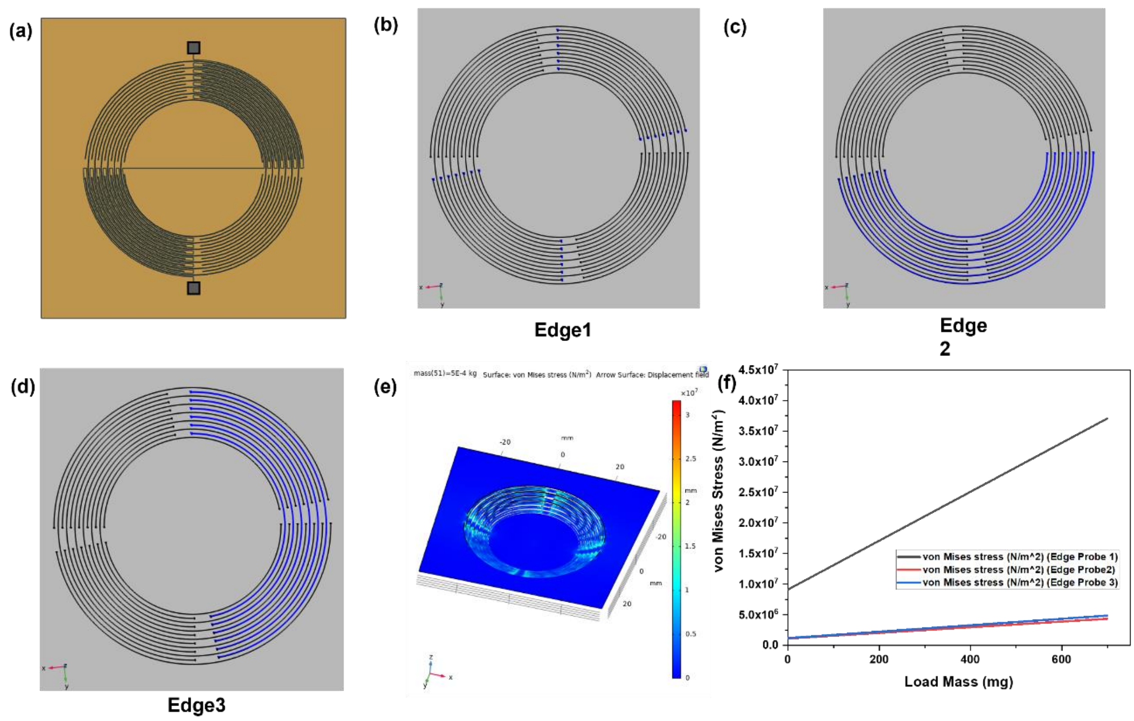

Fig. 7.19. (a) Sensor designed on Fusion 360, (b) Edge probe at the notches, (c,d) Edge probe at the boundaries, (e) von Mises Stress distribution under 500 mg load, (f) von Mises Stress at edge probe 1, 2, 3 for a parametric scan of load 0-700 mg.

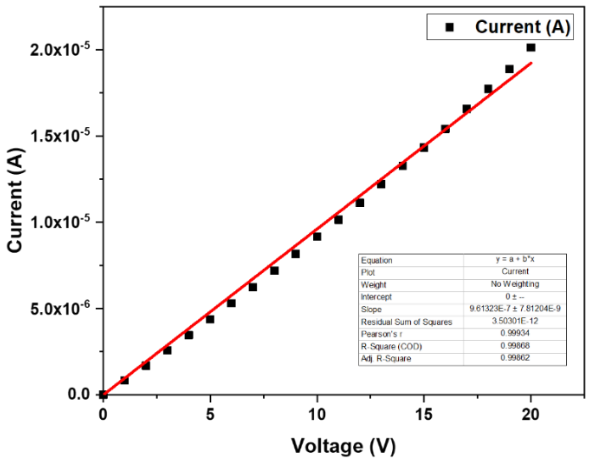

Fig. 7.20. I-V measurement of the Kirigami sensor.

The sensor response to bending (X-Z plane) and twisting (X-Y plane) actions of the knee-joint was monitored by placing the sensor on the right knee under a knee-cap (Figure 7.21a) along with a Phidget gyroscope to measure the change in angle upon bending and twisting of the knee. The sensor measured the relative change in voltage for bending and twisting of the knee joint, over 16 repetitions which showed an average change of 10.7%±1.4 % in relative voltage (*dV/V*) upon an average knee-bending angle of $68.24^0 \pm 2.21^0$ (Figure 7.21g) and an average change of 2.23%±0.74% upon an average knee-twist angle of $10.06^0 \pm 2.37^0$ (Figure 7.21h). The sensor showed good reproducibility with a standard deviation of 0.603 in GF (Figure 7.22). Such motion monitoring is useful for various applications such as Gait analysis, knee-joint health monitoring, and motion tracking [50].

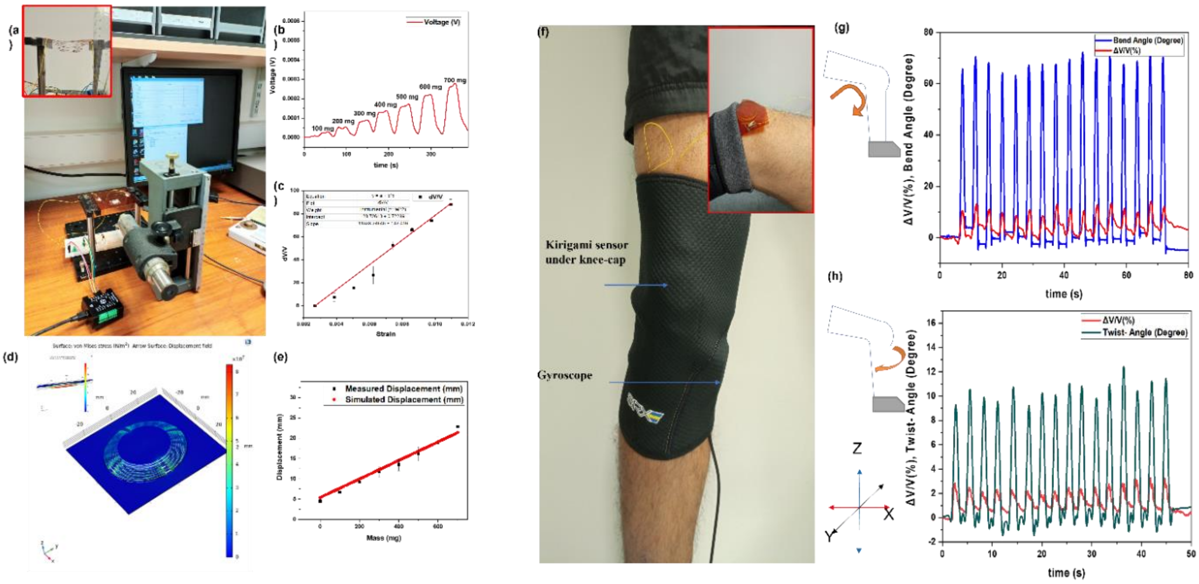

Fig. 7.21. (a) Displacement measurement setup upon loading of weight bars (Inset: Deformation of the Kirigami Sensor upon loading of 500 mg, (b) Change in PhidgetBridge voltage upon loading of 100-700 mg, (c) *GF* measurement from *ΔV/V* vs strain, (d) Stress Distribution in the Kirigami sensor under a load of 500 mg modelled in COMSOL (Inset: Stress Accumulation around the notches), (e) Out-of-plane displacement vs load mass from simulation and experiment, (f) Femtosecond laser printed Kirigami inspired strain sensor used under knee-cap along with gyroscope (Inset: Conformal fitting of the sensor on knee-joint under Knee-Cap), (g) Relative change in output voltage from PhidgetBridge DAQ system upon bending along X-Z plane, and (h) twisting of the knee along X-Y plane for 16 times.

7.3.5.1. Repeatability and reproducibility test of the Kirigami sensor:

GF was calculated Knee bending test was performed for 16 cycles using the 3 sensors fabricated using the same laser parameters using the Phidget DAQ system at 128x amplification and the result is summarised in the table 7.4.

Table 7.4. Summary of sensor reproducibility test.

Kirigami Sensors	***GF* (Fig 6.22 d-f)**	**Angular change upon bending**	**Percentage change in voltage upon bending (Fig. 6.22 g-i)**
Sensor 1	88.58±1.11	$68.24^{0}\pm2.21^{0}$	10.72%±1.42 %
Sensor 2	87.65±3.91	$68.38^{0}\pm2.34^{0}$	9.58%±1.4%
Sensor3	87.45±5.28	$68.66^{0}\pm2.15^{0}$	9.63%±1.02%

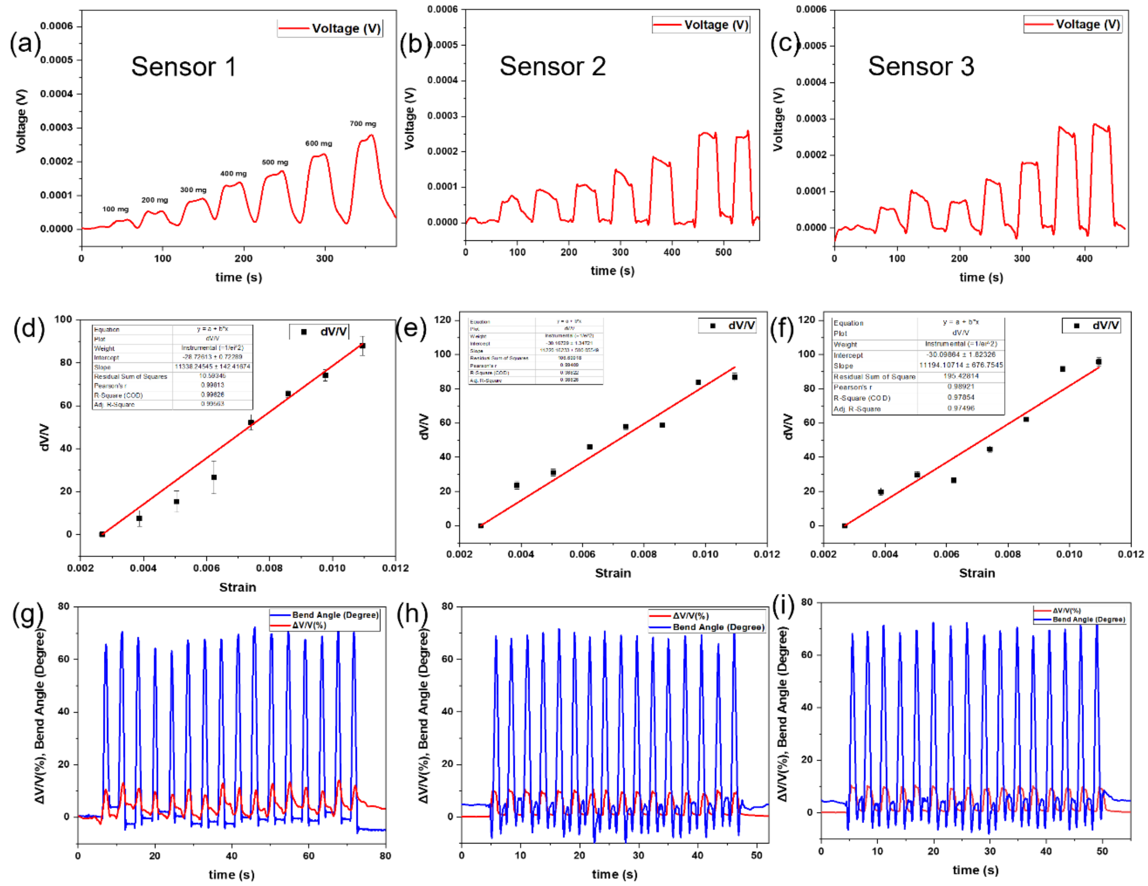

Fig. 7.22. (a-c) Voltage output from Phidget Sensor DAQ system at amplification 128x using 3 sensors fabricated using the same laser parameters (Carbonization at *P*=0.242 W at *v*=2mm/s, *f*=200 kHz, Ablation at *P*=2.524 W at *v*=300mm/s, *f*=200 kHz), (d-f) Calculation of *GF* from *ΔV/V* vs strain for the three sensors respectively, (g-i) Percentage change in *ΔV/V* vs time for bending of knee-joint for 16 cycles.

7.3.5.2. Comparative analysis of the Kirigami sensor vs Planar sensor:

Sensitivity of the sensor is measured in terms of Gauge Factor (GF) which is the relative change in output voltage ($\Delta V/V$) with respect to strain (ε) and was found to be almost close to the value of GF of a single LIG track (Fig. 7.18d). Hence, we believe that the sensitivity of the LIG stays the same. But the Kirigami cuts allow the stress accumulation upon placing minimal loads (upto 100 mg) which causes enough strain to be measured by the sensor. Similar weights (100-700 mg) were placed on the planar sensor to measure the changes in output voltage, but no change was found because of low stress generated upon loading. Measurable changes in output voltage were found upon loading of 1 g on the planar sensor. FEM simulation was performed for a planar sensor of same dimension as the Kirigami sensor to find the stress distribution throughout the sensor and the maximum stress upon placing 500 mg at the centre of the planar

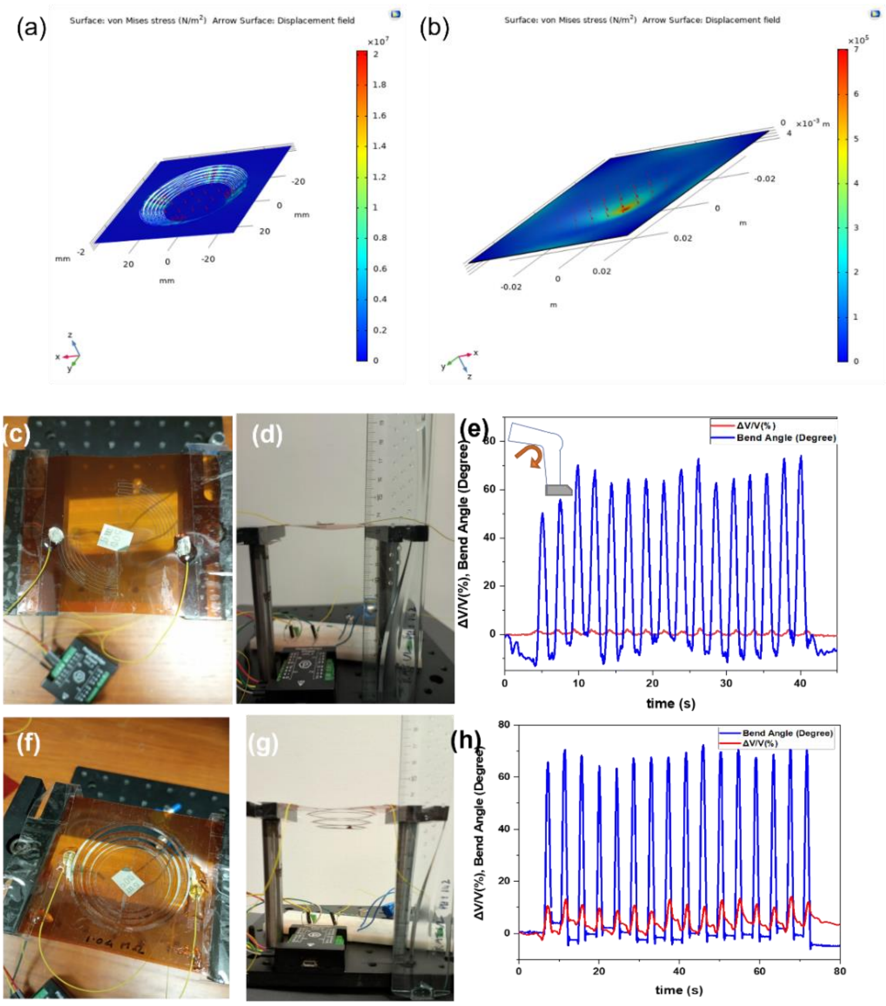

Fig. 7.23. Stress distribution upon 500 mg placed at centre of (a) Kirigami sensor and (b) Planar sensor, (c) Top-view of 500 mg placed at centre of planar sensor, (d) Side-view shows no change in displacement upon loading of 500 mg at the centre of the planar sensor and no change in Phidget signal was observed, and (e) Relative change in voltage of 3.0 %±0.7 % from the planar sensor upon bending of knee, (f) Top-view of 500 mg placed at centre of Kirigami sensor, (g) Side-view shows change in displacement upon loading of 500 mg at the centre of the Kirigami sensor and no change in Phidget signal was observed, and (h) Relative change in voltage of 10.7 %±1.4 % from the Kirigami sensor upon bending of knee.

sensor was found to be 6.74×10^5 N/m^2 as compared to 2.11×10^7 N/m^2 in Kirigami sensor (Figure. 7.23 a,b) which describes how Kirigami cut patterns can lead to stress concentrating regions for a same value of external stimuli. Also, the Kirigami cuts allow the stress to be concentrated around the cut patterns rather than distributing across the whole surface as in the planar sensor which allows us to print the sensors at the point of interest. The planar sensor was also placed over the knee joint to measure the changes in output voltage with bending of knees and was found to change by around 3.0 %±0.7 % as compared to 10.7 %±1.4 % in Kirigami sensor (Figure. 7.23e, h). All of these explain that the Kirigami sensor has better sensitivity towards same value of external stimuli as compared to the planar ones.

7.3.5.3. Plastic regime of the sensor:

The working of sensor was investigated in the plastic regime (Figure. 7.24), and from COMSOL we found that upon loading of 800 mg, the strain was 0.012 which is above the elastic strain limit of PI (0.01) and in this plastic range, the relative change in voltage ($\Delta V/V$) deviates from linearity. Therefore, the sensor does not work in the plastic deformation range.

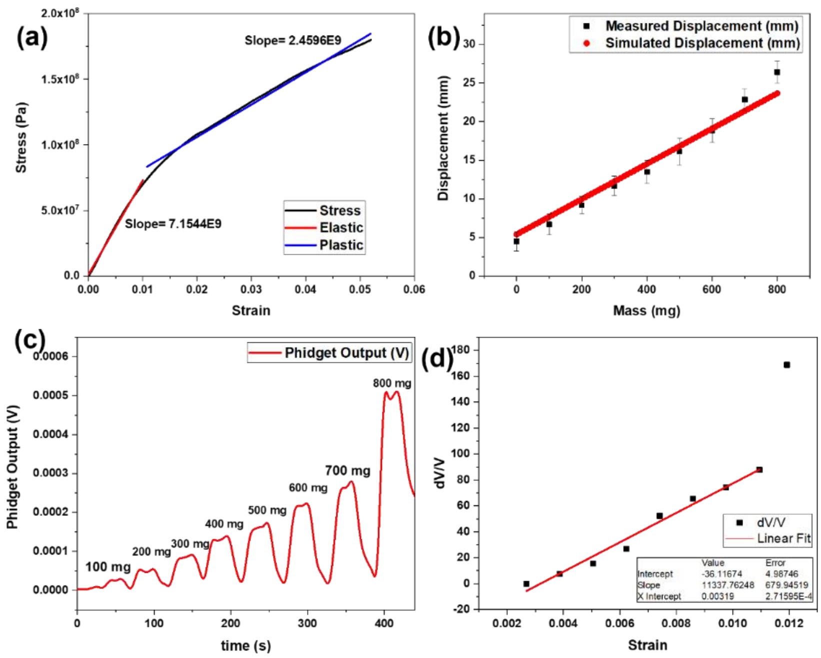

Fig. 7.24. (a) Stress vs Strain curve of ASTM D638 Dog-Bone Structured PI measured by UTM, (b) Measured and simulated displacement vs mass on the Kirigami sensor, (c) Phidget voltage output for varying load-mass, (d) Relative change in voltage vs strain shows that the dV/V is non-linear at 800 mg.

7.4. Conclusion

The interaction of Polyimide (PI) with femtosecond laser of wavelength 1030 nm, pulse duration 550 fs, and repetition rate 200 kHz was studied for two process conditions: PC1- Low Power-Low Scan Speed (0.242-0.281 W at 2-3 mm/s), and PC2- High Power-High Scan Speed (1.726-2.512 W at 200-300 mm/s). In PC1, carbonization only was observed without any traces of ablation. The single pulse ablation threshold and incubation coefficient for Case 1 were (5.6±1.5) x 10^4 mJ/cm^2 and 0.21±0.03, respectively. In PC2, ablation only was observed without any traces of carbonization. High fluence causes high photon flux, enabling photochemical ablation of polyimide. The single pulse ablation threshold and incubation coefficient for Case 2 were (1.89±0.56) x 10^3 mJ/cm^2 and 0.66±0.08, respectively. This result indicates that the single pulse carbonization threshold is higher than the single pulse ablation threshold, and thus carbonization cannot be achieved by a single pulse but by the accumulation of laser pulses per spot with a lower fluence for each pulse, which can only be achieved by scanning at low speed at a higher repetition rate. The heat accumulation model was modelled in Python, to determine the temporal evolution of temperature per spot upon scanning the femtosecond laser at various scan speeds over a range of individual powers. The model satisfied the carbonization thresholds at various scan speeds. These parameters provide insight into the selection of laser parameters for a range of microfabrication applications using femtosecond laser processing.

The Kirigami inspired strain sensor was fabricated using the parameters for such defined process conditions. PC1 was utilized to print piezoresistive LIG and PC2 was utilized to transform the 2D oriented sensor into a 3D conformal sensor, by ablating the boundaries of the Kirigami design. FEA analysis was performed using the sensor design, to obtain the von Mises stress distribution across the sensor, and the average strain was calculated for different loadings. Stress concentration points were located at the notches of the Kirigami design, which optimised the sensitivity of the strain-sensor. The change in output voltage from the PhidgetBridge DAQ was measured for individual loading, and thus the *GF* was calculated to be 88.58±0.16. The sensor fitted conformally on the knee-joint and provided distinct responses for individual bending and twisting of the knee-joint, which are useful for human health monitoring, Gait analysis and motion tracking applications. Hence, the work presented here, demonstrates an application of high precision carbonization and ablation using femtosecond IR laser in Kirigami-inspired sensor fabrication and opens scalable pathways for other microfabrication applications.

The published journal paper ends here.

7.5. Comparative study of femtosecond laser carbonization and CO_2 laser carbonization

(a) The morphology of LIG studied from the cross-sectional SEM in Fig. 6.2 and Fig. 7.11 shows that the CO_2 laser produces fibrous structures at higher powers as compared to femtosecond laser. This shows better control of planar crystal growth of LIG with femtosecond laser over CO_2 laser due to the higher *D/F* ratio for femtosecond laser because of its lower average fluence (1.25 x 10^2 mJ/cm^2) as compared to CO_2 laser (7.25 x 10^3 mJ/cm^2).

(b) The electrical conductivity of LIG was found to be decreasing with increasing scan speed for CO_2 laser (Fig. 6.8 d), whereas it was found to be increasing with increasing scan speed for femtosecond laser (Fig. 7.9 b). This shows that femtosecond laser allows to break the trade-off of conductivity and scalability for highly crystalline graphene.

(c) The incubation coefficient (S) for carbonization was found to be 0.61 for CO_2 laser and 0.21 for femtosecond laser. Such lower value of S shows that carbonization by femtosecond laser is due to heat accumulation from multiple pulses at the laser spot as compared to the CO_2 laser where single pulse of laser can carbonize PI.

(d) Gauge Factor of LIG from femtosecond laser was found to be ~88 (Fig. 7.18d) as compared to ~22 (Fig. 7.25) from CO_2 laser. Hence, femtosecond laser can be used to print more sensitive LIG based strain sensors. Also, the versatility of femtosecond laser for clean ablation helps to create Kirigami cuts which adds more sensitivity and conformity to the sensor over uneven surfaces.

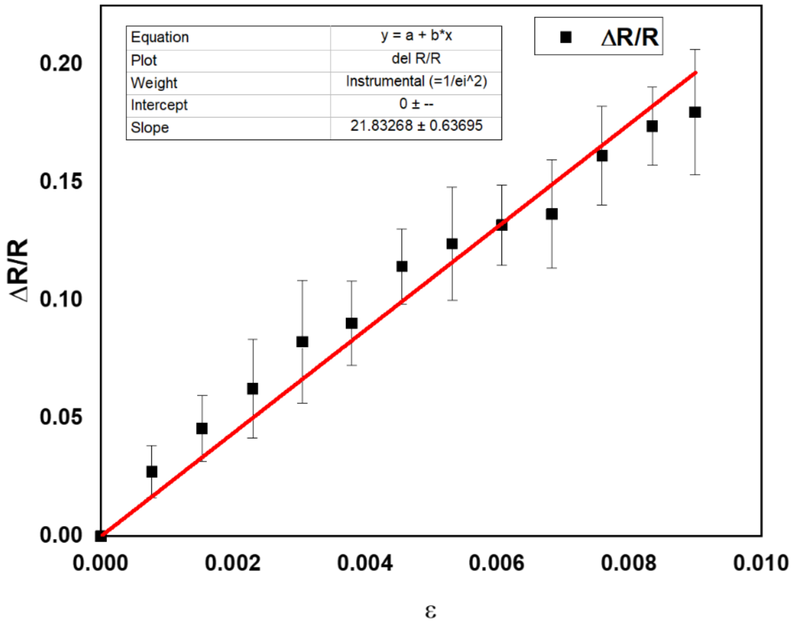

Fig. 7.25. Gauge Factor measurement of LIG using CO_2 laser at 0.65 W, 2 mm/s, 100 Hz.

7.6. Summary

In this chapter, the interaction of femtosecond laser with PI was studied in two process conditions: PC1- low power-low scan speed and PC2- high power-high scan speed. PC1 was used for photothermal carbonization and PC2 was used for photochemical ablation. Carbonization process was modelled using heat accumulation model and was found to satisfy the threshold powers at varying scan speeds. The morphology was found to be less fibrous compared to the LIG obtained from CO_2 laser carbonization. The sensitivity of LIG obtained from the femtosecond laser was improved by Kirigami cutting of the PI substrate using PC2 and the sensor showed ~3 times better sensitivity to knee-bending and twisting. This chapter meets the objective of studying the femtosecond laser-PI interaction and improving the sensor performance of LIG obtained from femtosecond laser carbonization of PI.

Bibliography

[1] S. Butkus, E. Gaižauskas, D. Paipulas, Ž. Viburys, D. Kaškelyė, M. Barkauskas, A. Alesenkov, V. Sirutkaitis, Rapid microfabrication of transparent materials using filamented femtosecond laser pulses, Applied Physics A 114(1) (2014) 81-90.
[2] S.M. Eaton, C. De Marco, R. Martinez-Vazquez, R. Ramponi, S. Turri, G. Cerullo, R. Osellame, Femtosecond laser microstructuring for polymeric lab-on-chips, Journal of Biophotonics 5(8-9) (2012) 687-702.
[3] Y. Wang, Y. Abe, Y. Matsuura, M. Miyagi, H. Uyama, Refractive indices and extinction coefficients of polymers for the mid-infrared region, Appl. Opt. 37(30) (1998) 7091-7095.
[4] B. Dorin, P. Parkinson, P. Scully, Direct laser write process for 3D conductive carbon circuits in polyimide, Journal of Materials Chemistry C 5(20) (2017) 4923-4930.
[5] M.-S. Jung, T.-W. Lee, J. Hyeon-Lee, B. Hee Sohn, I.-S. Jung, Synthesis and characterizations of a polyimide containing a triphenylamine derivative as an interlayer in polymer light-emitting diode, Polymer 47(8) (2006) 2670-2676.
[6] S. Mao, C.P. Grigoropoulos, Laser processing of organic materials, in: C.P. Grigoropoulos (Ed.), Transport in Laser Microfabrication: Fundamentals and Applications, Cambridge University Press, Cambridge, 2009, pp. 265-281.
[7] L.V. Zhigilei, P.B.S. Kodali, B.J. Garrison, Molecular Dynamics Model for Laser Ablation and Desorption of Organic Solids, The Journal of Physical Chemistry B 101(11) (1997) 2028-2037.
[8] E.G. Gamaly, A.V. Rode, B. Luther-Davies, V.T. Tikhonchuk, Ablation of solids by femtosecond lasers: Ablation mechanism and ablation thresholds for metals and dielectrics, Physics of Plasmas 9(3) (2002) 949-957.
[9] H. Schmidt, J. Ihlemann, B. Wolff-Rottke, K. Luther, J. Troe, Ultraviolet laser ablation of polymers: spot size, pulse duration, and plume attenuation effects explained, Journal of Applied Physics 83(10) (1998) 5458-5468.
[10] R. Rahimi, M. Ochoa, W. Yu, B. Ziaie, Highly Stretchable and Sensitive Unidirectional Strain Sensor via Laser Carbonization, ACS Applied Materials & Interfaces 7(8) (2015) 4463-4470.
[11] D. Birchfield, X. Jackson, T. Pasternak, A. Hanson, M. Atashbar, Strain Sensor Fabrication by Means of Laser Carbonization, 2019 IEEE International Conference on Flexible and Printable Sensors and Systems (FLEPS), 2019, pp. 1-3.
[12] R. Ye, D.K. James, J.M. Tour, Laser-Induced Graphene, Accounts of Chemical Research 51(7) (2018) 1609-1620.
[13] Y. Chyan, R. Ye, Y. Li, S.P. Singh, C.J. Arnusch, J.M. Tour, Laser-Induced Graphene by Multiple Lasing: Toward Electronics on Cloth, Paper, and Food, ACS Nano 12(3) (2018) 2176-2183.
[14] W. Liu, Y. Huang, Y. Peng, M. Walczak, D. Wang, Q. Chen, Z. Liu, L. Li, Stable Wearable Strain Sensors on Textiles by Direct Laser Writing of Graphene, ACS Applied Nano Materials 3(1) (2020) 283-293.
[15] D.X. Luong, K. Yang, J. Yoon, S.P. Singh, T. Wang, C.J. Arnusch, J.M. Tour, Laser-Induced Graphene Composites as Multifunctional Surfaces, ACS Nano 13(2) (2019) 2579-2586.

[16] R.P. BerndKeller, Wei-Nien Su, Peter Eyerer, Temperature Dependent Optical Properties of Polymers as a Basis for Laser Process Modeling, International Solid Freeform Fabrication Symposium, University of Texas Libraries (1998).
[17] R. Weber, T. Graf, C. Freitag, A. Feuer, T. Kononenko, V.I. Konov, Processing constraints resulting from heat accumulation during pulsed and repetitive laser materials processing, Opt. Express 25(4) (2017) 3966-3979.
[18] S. Faas, U. Bielke, R. Weber, T. Graf, Prediction of the surface structures resulting from heat accumulation during processing with picosecond laser pulses at the average power of 420 W, Applied Physics A 124(9) (2018) 612.
[19] C.S. David, P.D. Scott, R. Mordechai, H.C.S. Jan, Laser-induced metal deposition and laser cutting techniques for fixing IC design errors, Proc.SPIE, 1991.
[20] A.S. Holmes, S.M. Saidam, Sacrificial layer process with laser-driven release for batch assembly operations, Journal of Microelectromechanical Systems 7(4) (1998) 416-422.
[21] A. Brooks, S. Chakravarty, M. Ali, V. Yadavalli, Kirigami-Inspired Biodesign for Applications in Healthcare, Advanced Materials 34 (2022) 2109550.
[22] S. Chen, J. Chen, X. Zhang, Z.-Y. Li, J. Li, Kirigami/origami: unfolding the new regime of advanced 3D microfabrication/nanofabrication with "folding", Light: Science & Applications 9(1) (2020) 75.
[23] E.E. Evke, C. Huang, Y.-W. Wu, M. Arwashan, B. Lee, S.R. Forrest, M. Shtein, Kirigami-Based Compliant Mechanism for Multiaxis Optical Tracking and Energy-Harvesting Applications, Advanced Engineering Materials 23(4) (2021) 2001079.
[24] E.E. Evke, D. Meli, M. Shtein, Developable Rotationally Symmetric Kirigami-Based Structures as Sensor Platforms, Advanced Materials Technologies 4(12) (2019) 1900563.
[25] L. Gamble, A. Lamoureux, M. Shtein, Multifunctional composite kirigami skins for aerodynamic control, Applied Physics Letters 117(25) (2020) 254105.
[26] A. Lamoureux, K. Lee, M. Shlian, S.R. Forrest, M. Shtein, Dynamic kirigami structures for integrated solar tracking, Nature Communications 6(1) (2015) 8092.
[27] T.C. Shyu, P.F. Damasceno, P.M. Dodd, A. Lamoureux, L. Xu, M. Shlian, M. Shtein, S.C. Glotzer, N.A. Kotov, A kirigami approach to engineering elasticity in nanocomposites through patterned defects, Nature Materials 14(8) (2015) 785-789.
[28] H. Zhang, J. Paik, Kirigami Design and Modeling for Strong, Lightweight Metamaterials, Advanced Functional Materials 32(21) (2022) 2107401.
[29] F. Raimondi, S. Abolhassani, R. Brütsch, F. Geiger, T. Lippert, J. Wambach, J. Wei, A. Wokaun, Quantification of polyimide carbonization after laser ablation, Journal of Applied Physics 88(6) (2000) 3659-3666.
[30] J. Lin, Z. Peng, Y. Liu, F. Ruiz-Zepeda, R. Ye, E.L.G. Samuel, M.J. Yacaman, B.I. Yakobson, J.M. Tour, Laser-induced porous graphene films from commercial polymers, Nature Communications 5(1) (2014) 5714.
[31] F. Wang, K. Wang, X. Dong, X. Mei, Z. Zhai, B. Zheng, J. Lv, W. Duan, W. Wang, Formation of hierarchical porous graphene films with defects using a nanosecond laser on polyimide sheet, Applied Surface Science 419 (2017) 893-900.
[32] S.A. Ashforth, R.N. Oosterbeek, O.L.C. Bodley, C. Mohr, C. Aguergaray, M.C. Simpson, Femtosecond lasers for high-precision orthopedic surgery, Lasers in Medical Science **35**(6) (2020) 1263-1270.
[33] S. Wang, Y. Yu, R. Li, G. Feng, Z. Wu, G. Compagnini, A. Gulino, Z. Feng, A. Hu, High-performance stacked in-plane supercapacitors and supercapacitor array fabricated by femtosecond laser 3D direct writing on polyimide sheets, Electrochimica Acta 241 (2017) 153-161.
[34] Y. Yu, S. Bai, S. Wang, A. Hu, Ultra-Short Pulsed Laser Manufacturing and Surface Processing of Microdevices, Engineering 4(6) (2018) 779-786.

[35] M. Inagaki, S. Harada, T. Sato, T. Nakajima, Y. Horino, K. Morita, Carbonization of polyimide film “Kapton”, Carbon 27(2) (1989) 253-257.
[36] P. Zorabedian, 8 - Tunable External-Cavity Semiconductor Lasers, in: F.J. Duarte (Ed.), Tunable Lasers Handbook, Academic Press, San Diego, 1995, pp. 349-442.
[37] W. Husinsky, G. Grabner, I. Baumgartner, F. Skorpik, S. Mitterer, T. Temmel, Mechanisms of Laser Ablation of Biological Tissue, in: G. Betz, P. Varga (Eds.) Desorption Induced by Electronic Transitions DIET IV, Springer Berlin Heidelberg, Berlin, Heidelberg, 1990, pp. 362-367.
[38] F. Di Niso, C. Gaudiuso, T. Sibillano, F.P. Mezzapesa, A. Ancona, P.M. Lugarà, Influence of the Repetition Rate and Pulse Duration on the Incubation Effect in Multiple-Shots Ultrafast Laser Ablation of Steel, Physics Procedia 41 (2013) 698-707.
[39] F. Di Niso, C. Gaudiuso, T. Sibillano, F.P. Mezzapesa, A. Ancona, P.M. Lugarà, Role of heat accumulation on the incubation effect in multi-shot laser ablation of stainless steel at high repetition rates, Opt. Express 22(10) (2014) 12200-12210.
[40] M. Abdulhafez, G.N. Tomaraei, M. Bedewy, Fluence-Dependent Morphological Transitions in Laser-Induced Graphene Electrodes on Polyimide Substrates for Flexible Devices, ACS Applied Nano Materials 4(3) (2021) 2973-2986.
[41] C. Zheng, A. Hu, K.D. Kihm, Q. Ma, R. Li, T. Chen, W.W. Duley, Femtosecond Laser Fabrication of Cavity Microball Lens (CMBL) inside a PMMA Substrate for Super-Wide Angle Imaging, Small 11(25) (2015) 3007-3016.
[42] J. Finger, M. Reininghaus, Effect of pulse to pulse interactions on ultra-short pulse laser drilling of steel with repetition rates up to 10 MHz, Opt. Express 22(15) (2014) 18790-18799.
[43] R. Weber, T. Graf, P. Berger, V. Onuseit, M. Wiedenmann, C. Freitag, A. Feuer, Heat accumulation during pulsed laser materials processing, Opt. Express 22(9) (2014) 11312-11324.
[44] K. Venkatakrishnan, B. Tan, B.K.A. Ngoi, Femtosecond pulsed laser ablation of thin gold film, Optics & Laser Technology 34(3) (2002) 199-202.
[45] H. Zhang, D. van Oosten, D.M. Krol, J.I. Dijkhuis, Saturation effects in femtosecond laser ablation of silicon-on-insulator, Applied Physics Letters 99(23) (2011) 231108.
[46] M.C. Chuang, A.C. Tam, On the saturation effect in the picosecond near ultraviolet laser ablation of polyimide, Journal of Applied Physics 65(7) (1989) 2591-2595.
[47] J. Bergström, 5 - Elasticity/Hyperelasticity, in: J. Bergström (Ed.), Mechanics of Solid Polymers, William Andrew Publishing2015, pp. 209-307.
[48] P.K. Valavala, T.C. Clancy, G.M. Odegard, T.S. Gates, Nonlinear multiscale modeling of polymer materials, International Journal of Solids and Structures 44(3) (2007) 1161-1179.
[49] D.Y.W. Yu, F. Spaepen, The yield strength of thin copper films on Kapton, Journal of Applied Physics 95(6) (2004) 2991-2997.
[50] E. Papi, Y.N. Bo, A.H. McGregor, A flexible wearable sensor for knee flexion assessment during gait, Gait Posture 62 (2018) 480-483.

8. Chapter 8: Summary

8.1. Review of papers

a. Paper 1- *J. Mater. Chem. C,* 2020, 8, 4493-4501:

In this paper, the photothermal process due to the interaction of CO_2 laser with Polyimide and ta-C was modelled in COMSOL and the threshold power for carbonization and graphitization was estimated and experimentally validated. Conversion of sp^3-sp^2 hybridized ta-C to sp2 hybridized graphene was studied using Raman spectroscopy. The electrical conductivity was found to be improved by ~2.6 times upon laser graphitization.

Objectives met: This paper meets the objective of the study of the transformation of PI to sp^2 hybridized carbon in the laser carbonization process. This is the first published work that entails the graphitization process using CO_2 laser and meets the objective of improving the electrical conductivity of LIG and answers the research question whether the electrical conductivity of LIG can be increased.

While there has been a considerable amount of research paper on laser carbonization, this paper provides insight into the laser graphitization process for the first time. This paper has received 12 citations in papers and chapters in books. The impact of this paper is on the research group of M. Terakawa et al. who distinguished between the carbonization and graphitization processes and to evaluate the morphological transition occurring during these processes [1, 2].

b. Paper 2- *Mater. Lett.,* 2022, 307, 131097:

Based on the photothermal models in the first paper, the growth kinetics of LIG on PI was studied for the first time using Arrhenius model in this paper, and the activation temperature for LIG formation from PI was found to be $2.35 \pm 0.30 \times 10^3$ K which is close to the value 2.4×10^3 K estimated from molecular dynamics.

Objectives met: This paper meets the objective of studying the growth kinetics of LIG.

This paper has received 3 citations in papers and the impact of this paper is on the research group of D. Diao et al. who worked on wear-resistant LIG films [3].

c. Paper 3- *Mater. Lett.*, 2023, 343, 134362:

In this paper, the planar growth of LIG was enhanced by increasing the wettability of PI surface by the Argon cold plasma treatment. The effect of plasma treatment on wettability was studied by varying the scan speed of plasma-pen on PI and the wettability was found to be maximum at lower scan speed, 200 mm/min. The planar crystallite size of LIG drawn on such plasma-treated PI improved by 21% which improved the conductivity by 49.68%.

Objectives met: This paper meets the objective of improving the crystal size to optimize the electrical conductivity. This paper provides an understanding of the surface properties of PI on LIG and can be used for further improvement of the conductivity of LIG.

d. Paper 4- *J. Phys. D: App. Phys.*, 2023, 56, 085101

In this paper, the interaction of femtosecond IR laser with PI was studied for both carbonization and ablation and the incubation coefficient and threshold values were calculated. The incubation coefficient for carbonization was calculated as 0.21 as compared to 0.66 for ablation which shows the effect of heat accumulation in the carbonization process using this laser. The heat accumulation model was modelled in Python and the threshold power for carbonization at scan speed of 2-3 mm/s was estimated and experimentally validated.

Objectives met: This paper meets the objective of studying the interaction of femtosecond laser with PI and comparing it with the interaction of CO_2 laser with PI. The carbonization process and ablation process were used to print a Kirigami-inspired strain sensor which showed 10.7 % ± 1.4 % change in output voltage for knee movements as compared to 3.0 %±0.7 % in planar sensors. The gauge factor of a single linear LIG track from femtosecond laser and CO_2 laser were calculated to be 88.58±0.16 and 21.67±0.05 respectively. Hence, this paper shows how femtosecond laser can increase the sensitivity of strain sensors by cutting Kirigami patterns in them which meets the objective of improving the sensitivity of LIG and its application in strain sensors.

This paper provides the interaction of femtosecond laser with Polyimide for the first time and can be used for scalable manufacturing of Kirigami-inspired strain sensors.

8.2. Conclusions

a) CO_2 laser-Polyimide interaction was modelled in COMSOL using the Photothermal model. Laser graphitization method was applied to improve the conductivity by ~2.6 times and was modelled in COMSOL. The threshold values of laser fluence for both carbonization and graphitization were experimentally calculated and validated using COMSOL. Average crystallite size of LIG was measured indirectly from the defect ratio (I_D/I_G) using Raman Spectroscopy of LIG.

b) Growth kinetics of PI to LIG transformation was studied using Arrhenius kinetics and the activation energy and pre-exponential coefficient were calculated from the Arrhenius (ln k vs 1/T) fitting. The activation energy was found to be close to the theoretical value calculated from Molecular Dynamics. Cross-sectional SEM images showed that 3D fibrous growth is enhanced at higher powers and higher scan speed, while planar and compact structures are formed at low-power and low scan speed. Conductivity of LIG decreases with increasing scan speed for a fixed laser fluence due to the smaller crystallite size of LIG formed due to rapid cooling at faster laser scan speed.

c) Plasma treatment of PI surface was performed to increase the wettability of PI. The effect of wettability on the planar crystallite size and electrical conductivity was studied. Plasma scan at low scan speed (≤200 mm/s) showed improvement of crystallite size by ~21% and conductivity by ~ 51% of LIG drawn at lower powers which showed that surface wettability enhances the Layer-By-Layer growth mode of graphene on PI but fails to maintain such growth when the wettability is not high enough to limit the out-of-plane growth of graphene at higher fluences.

d) Femtosecond IR laser-Polyimide interaction was modelled in Python for laser carbonization and was postulated to be happening due to heat accumulation unlike CO_2 laser where a single pulse of the laser was able to carbonize PI. A single pulse of femtosecond laser creates clean ablation without any traces of carbonization at higher power. Carbonization occurred due to photothermal interaction and ablation occurred due to photochemical interaction. Femtosecond laser at high fluence and high scan-speed created multiphoton ionization of PI creating a photochemical ablation. Whereas, at low fluence and low scan-speed, heat accumulation occurred from multiple pulses within a laser spot without causing any ablation creating a continuous track of LIG. This process window was utilized to develop a Kirigami-inspired strain sensor where a photothermally converted LIG strain sensor drawn in 2D can be conformed into 3D shapes by cutting Kirigami designs using photochemical ablation using the same femtosecond laser. Such a sensor showed sensitivity improved by ~3 times compared to planar sensors upon bending of knee joint.

e) Morphological differences were found in femtosecond laser induced graphene from that obtained from CO_2 laser. Non-fibrous and porous LIG was found for femtosecond laser due to lower interaction time between the laser and PI for all laser fluence and scan speeds. Also the lower average fluence of femtosecond laser assists in layer-by-layer growth improved the planar crystal growth of graphene. The electrical conductivity of LIG obtained from femtosecond laser increased with increasing scan speed at fixed laser fluence due to increasing crystallite size as compared to the CO_2 laser. Hence, femtosecond laser helps to improve the scalability of higher conductive graphene as compared to the other graphene manufacturing methods.

8.3. Future Work

This research thesis has the potential of recycling waste composites into value-added composites. Some trial experiments have been performed on Geopoly-based composites supplied by e4 composites (UK) (Appendix D) and have successfully tested to produce LIG upon laser irradiation and have shown strain-sensitive properties.

The heat accumulation model has been proven to estimate irradiation temperatures occurring from a femtosecond laser scan and can be used to estimate temperatures for ultrafast laser having higher repetition rate (~80 MHz). This model was used in the SFI Frontiers for the Future 20/FFP-P/8627, 2020 and was successfully awarded with a value of €476970.00 for 48 months.

The morphological difference between the LIG obtained from CO_2 laser and femtosecond laser shows that the Layer-By-Layer growth is more favoured for femtosecond laser due to higher D_s/F_s ratio, i.e., with higher repetition rate, the F can be decreased which would further increase the D_s/F_s ratio. Hence, it is hypothesized that larger crystallites of LIG can be obtained at higher repetition rates.

The innovative method of restructuring of 2D surfaces into 3D Kirigami designed surfaces can be utilized to transform 2D shapes into any 3D shapes using the inverse problem solving software and can be used to implant sensors on complex geometries such body-organs.

The femtosecond laser due to its multiphoton absorption property with PI has demonstrated the production of LIG inside the PI by the P.Scully research group in 2017 [4] and can be used to prepare completely encapsulated sensor matrix and can replace the already existing optical-fiber based sensor matrix [5]. Such sensors can be used to prepare rollable and portable GAIT analysis devices and functional medical devices such as sensorized stents.

Publications and Conferences

1. "Plasma Enhanced Planar Crystal Growth of Laser Induced Graphene"- *Mater. Lett.*, 2023, **343**, 134362, R. Biswas, P. McGlynn, G. O'Connor, P. Scully.
2. "Femtosecond Infra-Red Laser Carbonization and Ablation of Polyimide for Fabrication of Kirigami Inspired Strain Sensor"- *J. Phys. D: Appl. Phys.*, 2023, **56**, 085101, R. Biswas, G. O'Connor, P. Scully.
3. "Graphene Growth Kinetics of CO_2 Laser Carbonization of Polyimide"- *Mater. Lett.*, 2022, **307**, 131097, R. Biswas, R. Vijayaraghavan, P. McNally, G. O'Connor, P. Scully, NUIG.
4. "Improved Conductivity of Carbonized Polyimide by CO_2 Laser Graphitization"- *J. Mater. Chem. C*, 2020,**8**, 4493-4501, R. Biswas, N. Farid, G. O'Connor, P. Scully, NUIG.
5. Conference Oral presentation on the topic "Experimental and Modelling of Two-step Laser Graphitization of Polyimide for Improved Conductivity" in IONS Ireland, 2021.
6. Conference poster presentation in ISSC'23, 2021, IOP, UK.
7. Conference poster presentation in Photonics Ireland, 2021, Ireland.

Appendix

A. Python code for Heat Accumulation Modelling

```
import numpy as np
import matplotlib.pyplot as plt
import math as math
import pandas as pd


wo= 22.66*10**-6            #Spot radius
d=2*wo                      #Spot Diameter in m
f=200*10**3                 #Pulse Repetition Rate in Hz
```

```
P=0.2                              #Power in Watts
F=2*P/(f*3.14*(wo)**2)         #Laser Fluence in J/m^2
Ep0= F*3.14*wo**2              #Laser Intensity in J
v= 3/1000                      #Scan Speed in m/s
rho= 1.42*1000                 #Density in kg/m^3
Cp= 1.09*1000                  #Specific Heat in J/kg.K
K= 0.12                        #Thermal Conductivity in W/m.K
sigma=2                        #Dimensionality
ri=1.6                         #Refractive Index
OF=1-(v/(f*d))                 #Overlapping Factor
C1= -1.46
C3=2.61
extinc=10**-4
wavelength= 1030*10**-9
alpha= 4*3.14*extinc/wavelength                        #Absorption Coeff
dmat= 125*10**-6                                   #thickness in m
R=(((1-ri)**2)+extinc**2)/(((1+ri)**2)+extinc**2)      #Refelctivity
nabs=1-np.exp(-alpha*dmat)
SPA= d/(v/f)                                   #Spots per Area
N=d/(v/f)                                      #Pulses per spot
Overlap= 100*(1-(v/(2*wo*f)))



T0= 300                        #Initial Temperature
tirr=d/v                       #Irradiation time
tpp=1/f                        #pulse-pulse delay

t0=0
ep1=[]
tm=[]
T=[]

#Threshold Condition
```

```
S=0.20616                       #Incubation Coefficient
F1th=np.exp(10.929)*10          #Single pulse Carbonization threshold
FNth= F1th*N**(S-1)             #Multipulse carbonization threshold

#nheat(v):

nheat= 4*alpha*OF*math.sqrt(4*3.14*k*f)*wo/(v*sigma*((2*math.sqrt(N))+C1))

#Temperature:

def func(t):
    Thap=
T0+((8*nabs*nheat*Ep0*math.sqrt(f)/(3.14*d**2))*(1/(rho*Cp*math.sqrt(4*3.14*k)))*(2*
math.sqrt(f*t)-1.46))
    return(Thap)

t0=0
tm=[]

#Heat Accumulation

for i in np.arange(0, N, 1):
    for t in np.arange(t0, (i+1)*tpp, 10**-6):
        Tsp= func(t)
        #Tsp1= func(t)-(np.heaviside(t-tp)*func(t-tp))
        T.append(Tsp)
        t0=(i+1)*tpp
        tm.append(t)

plt.plot(tm,T)
plt.xlabel("time (sec)")
plt.ylabel("T(K)")
plt.show()
```

print('Power (W)=',P,'fluence (mJ/cm2)=',F/10,'Threshold Fluence (mJ/cm2)=',FNth/10,'repetition rate (Hz)=',f, 'Scan speed (mm/s)=',v*1000,'Number of pulses per spot=',N,'Absorption Quota =', nabs,'Heat Accumulation Parameter (nheat)=',nheat, 'Total Residual heat coeff (nheat) =',nheat,'Peak spot Temperature (K)=',Tsp, 'Pulse overlap=',Overlap)

B. Surface Profilometry results of femtosecond laser ablated craters

The data from the Zygo OMP-0306C optical profilometer is summarized here.

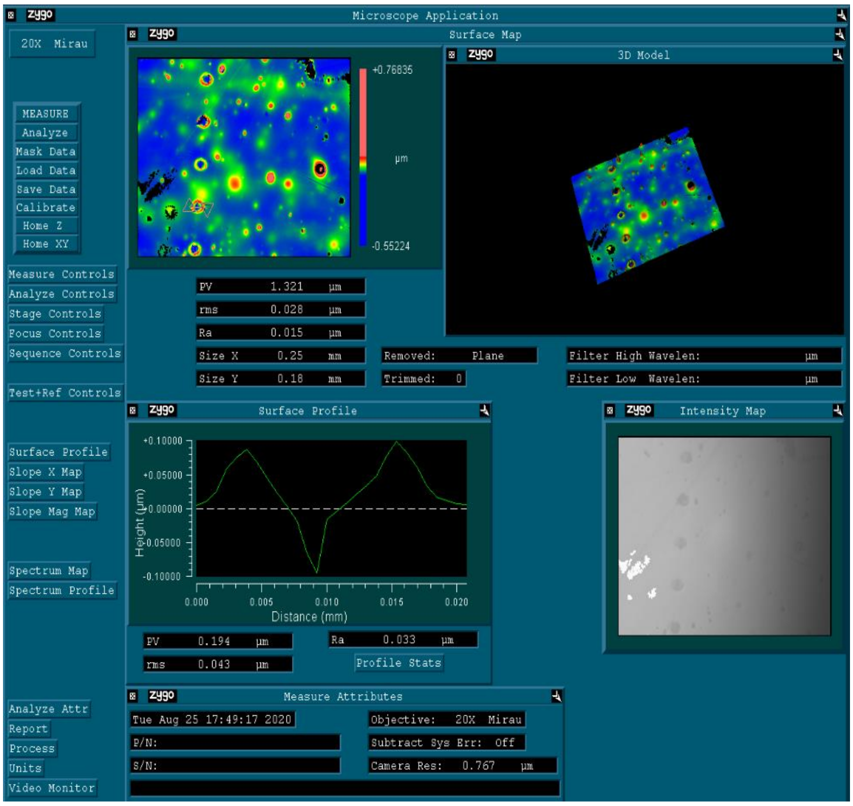

Fig. SS 1. Surface profile of ablated crater at laser power 0.811 W.

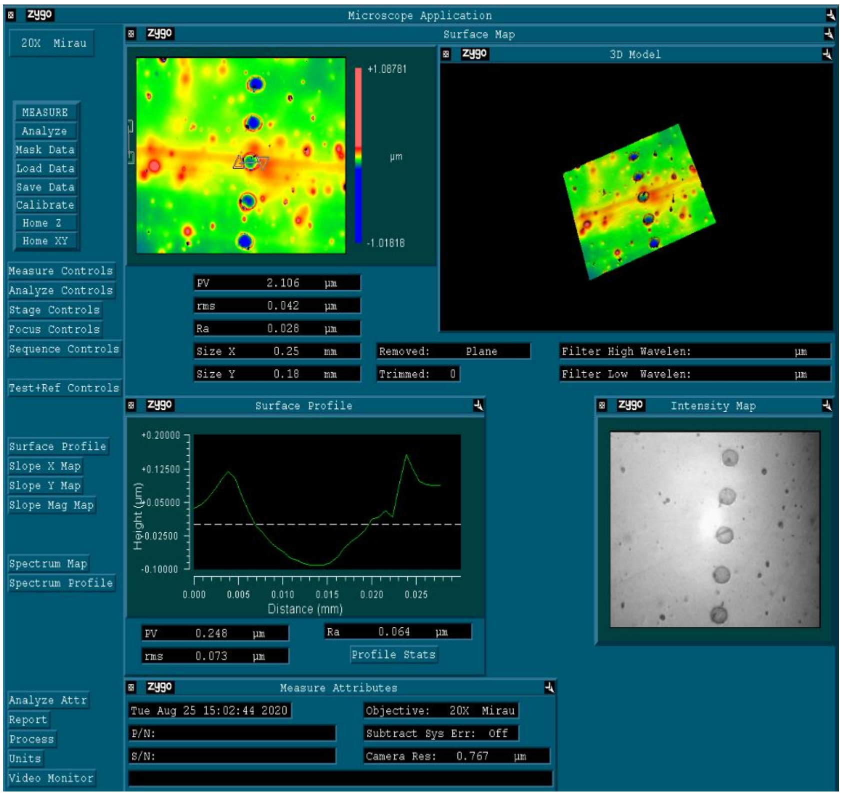

Fig. SS 2. Surface profile of ablated crater at laser power 1.02 W.

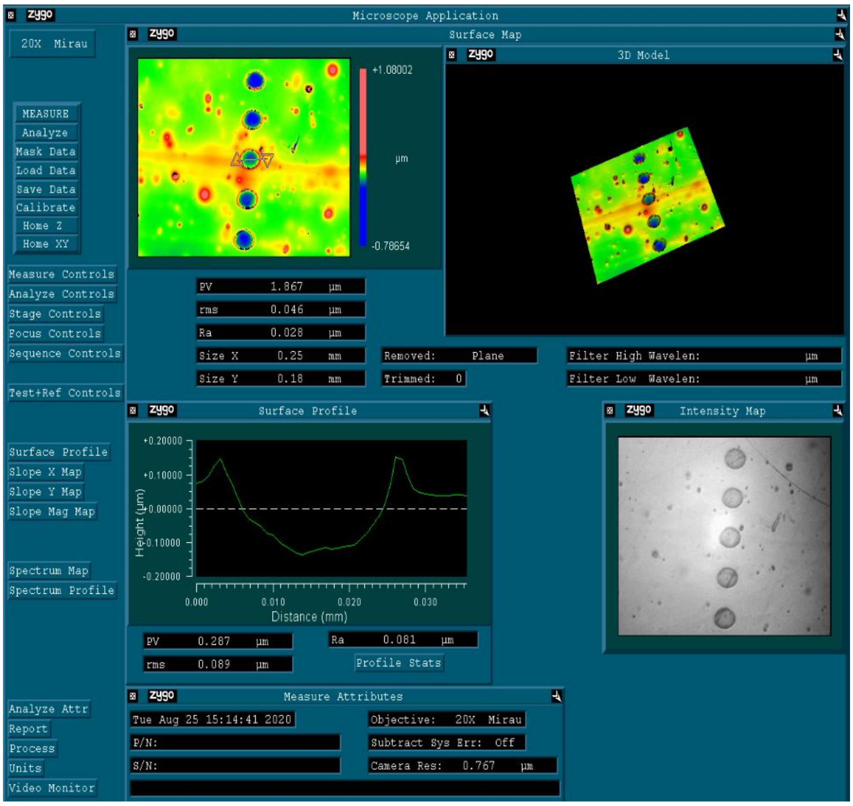

Fig. SS 3. Surface profile of ablated crater at laser power 1.20 W.

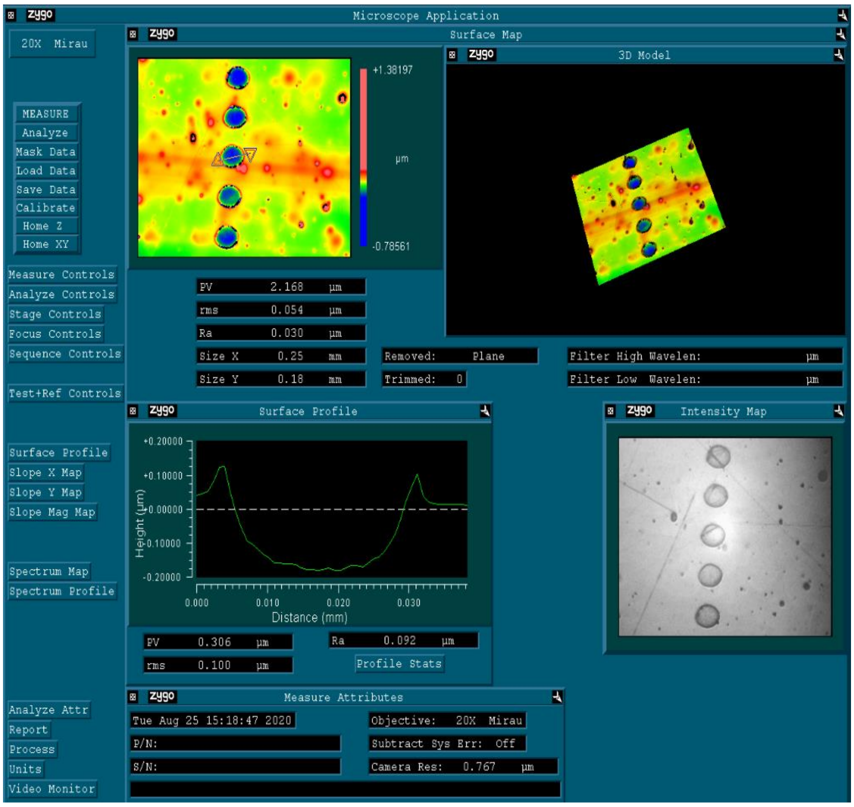

Fig. SS 4. Surface profile of ablated crater at laser power 1.43 W.

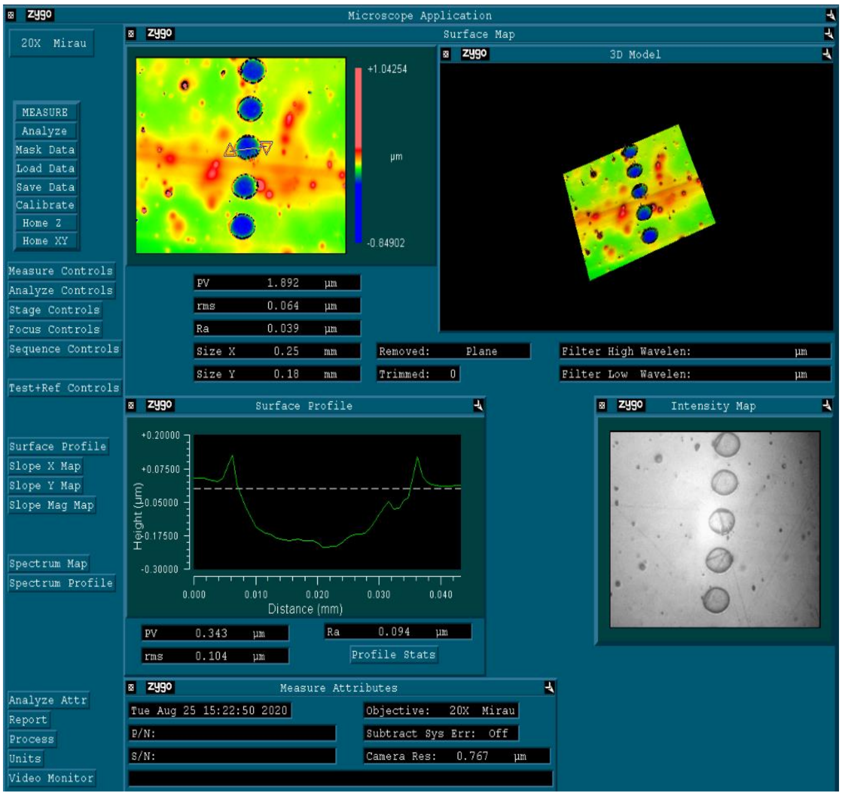

Fig. SS 5. Surface profile of ablated crater at laser power 1.63 W.

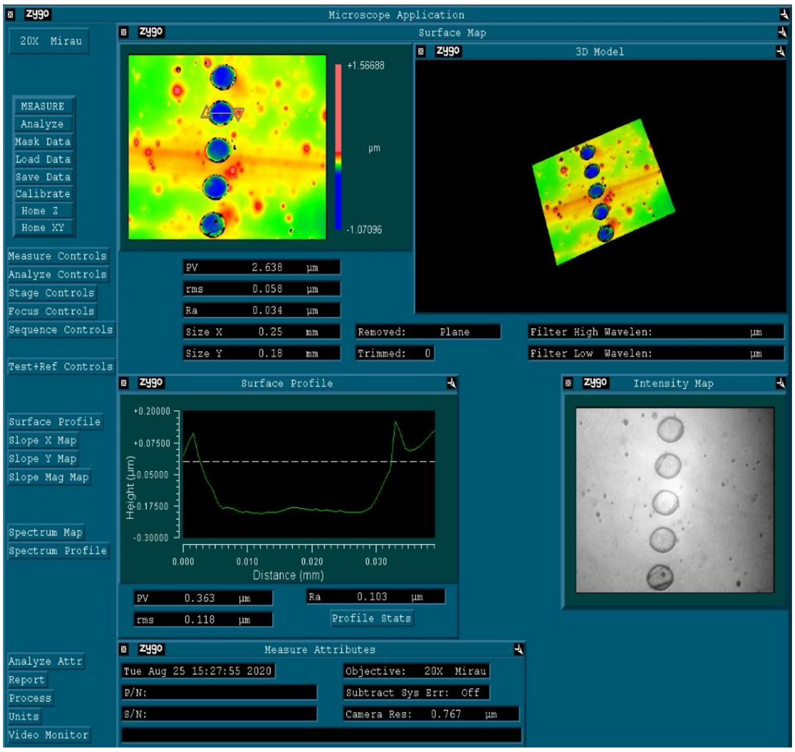

Fig. SS 6. Surface profile of ablated crater at laser power 1.82 W.

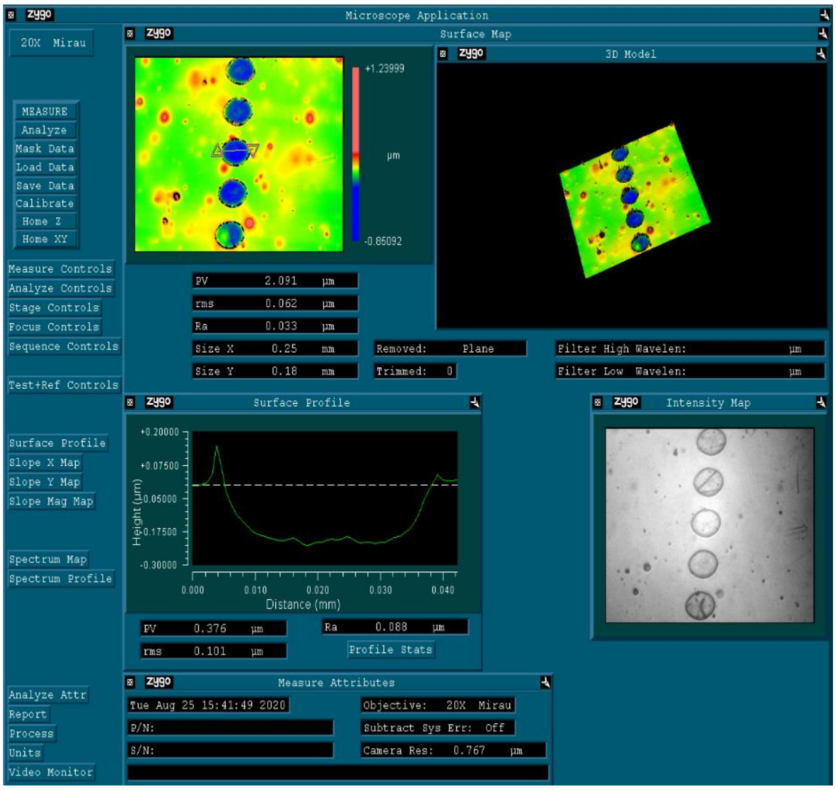

Fig. SS 7. Surface profile of ablated crater at laser power 2.03 W.

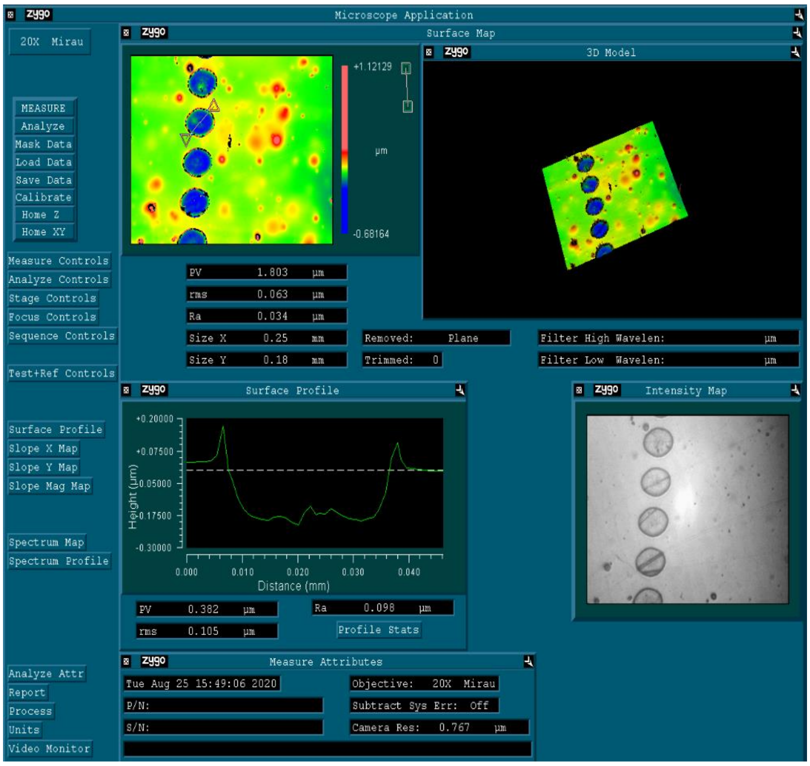

Fig. SS 8. Surface profile of ablated crater at laser power 2.23 W.

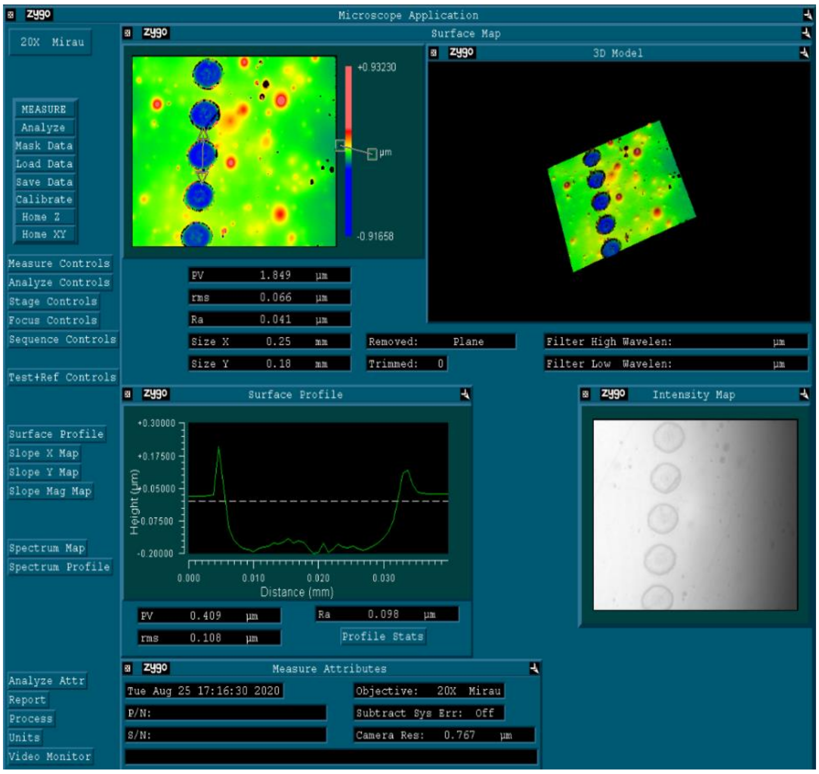

Fig. SS 9. Surface profile of ablated crater at laser power 2.42 W.

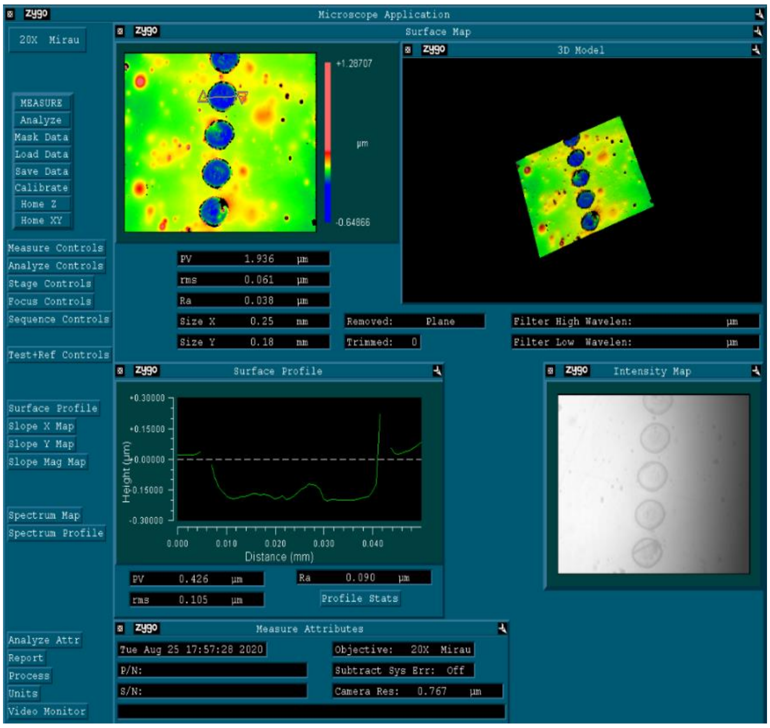

Fig. SS 10. Surface profile of ablated crater at laser power 2.60 W.

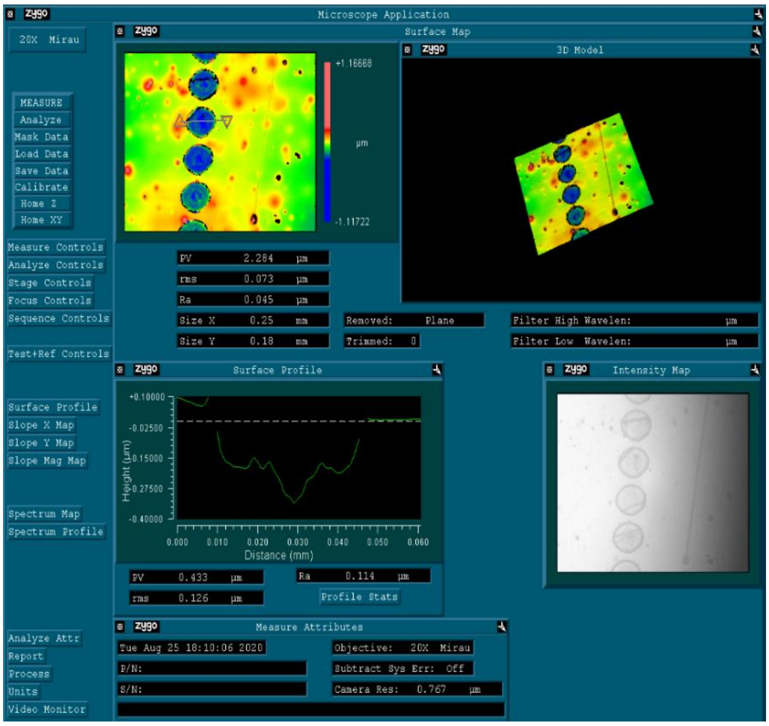

Fig. SS 11. Surface profile of ablated crater at laser power 2.81 W.

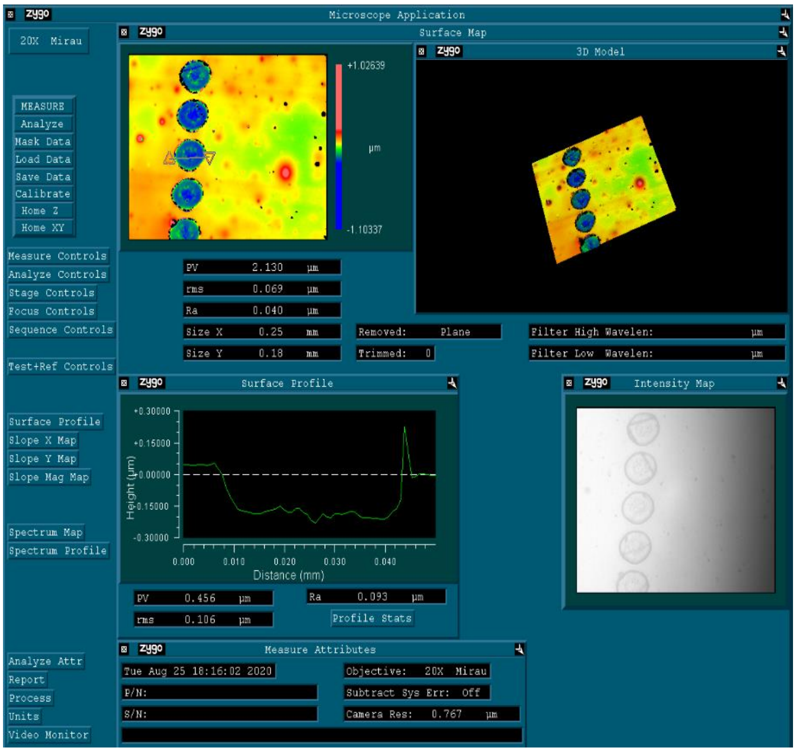

Fig. SS 12. Surface profile of ablated crater at laser power 3.01 W.

C. X-Ray Diffraction study of LIG

XRD study failed to separate peaks of LIG on PI from the peaks of unaltered PI and hence the crystallite size could not be made from such a study.

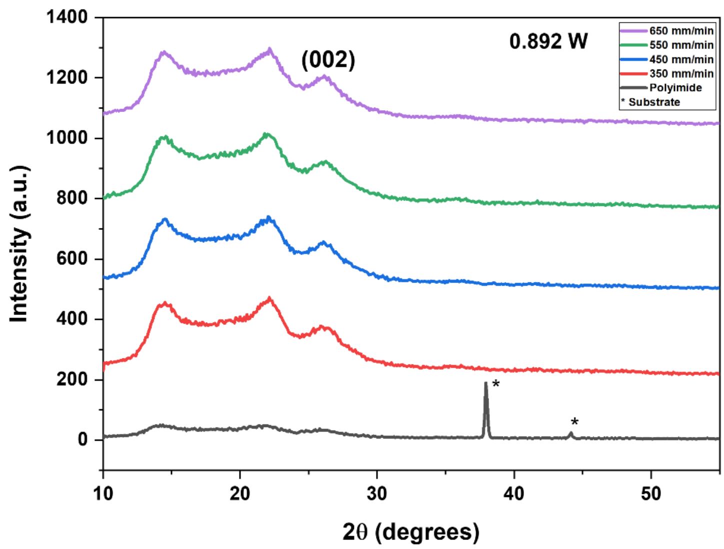

Fig. SS 13. XRD spectra of PI and LIG on PI at CO_2 laser power 0.892 W at scan speeds 350-850 mm/min.

D. **Laser carbonization of Geopoly-based industrial wastes**

(a) (b) (c) (d)

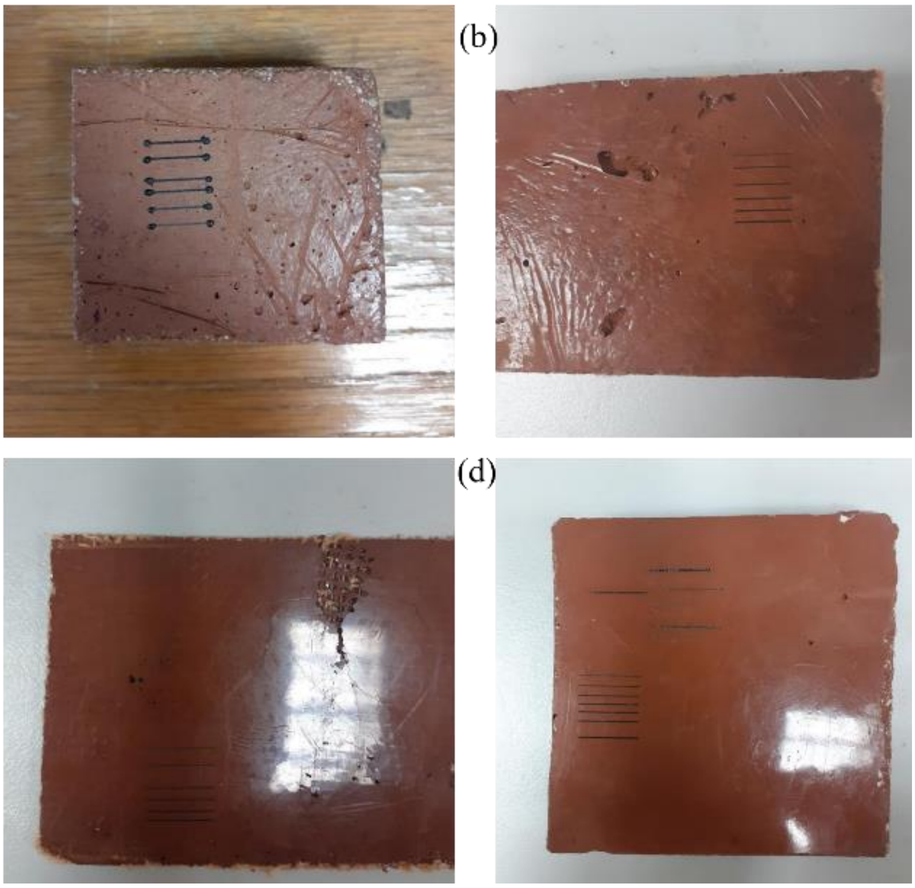

Fig. SS14 LIG drawn on (a) Cellulose filled Geopoly, (b) Mixed cellulose long fiber filled Geopoly, (c) Hemp FIber filled Geopoly, (d) ABS on Geopoly, at laser powers 0.45-0.95 W, *f*=100 Hz, *v*=100 mm/min.

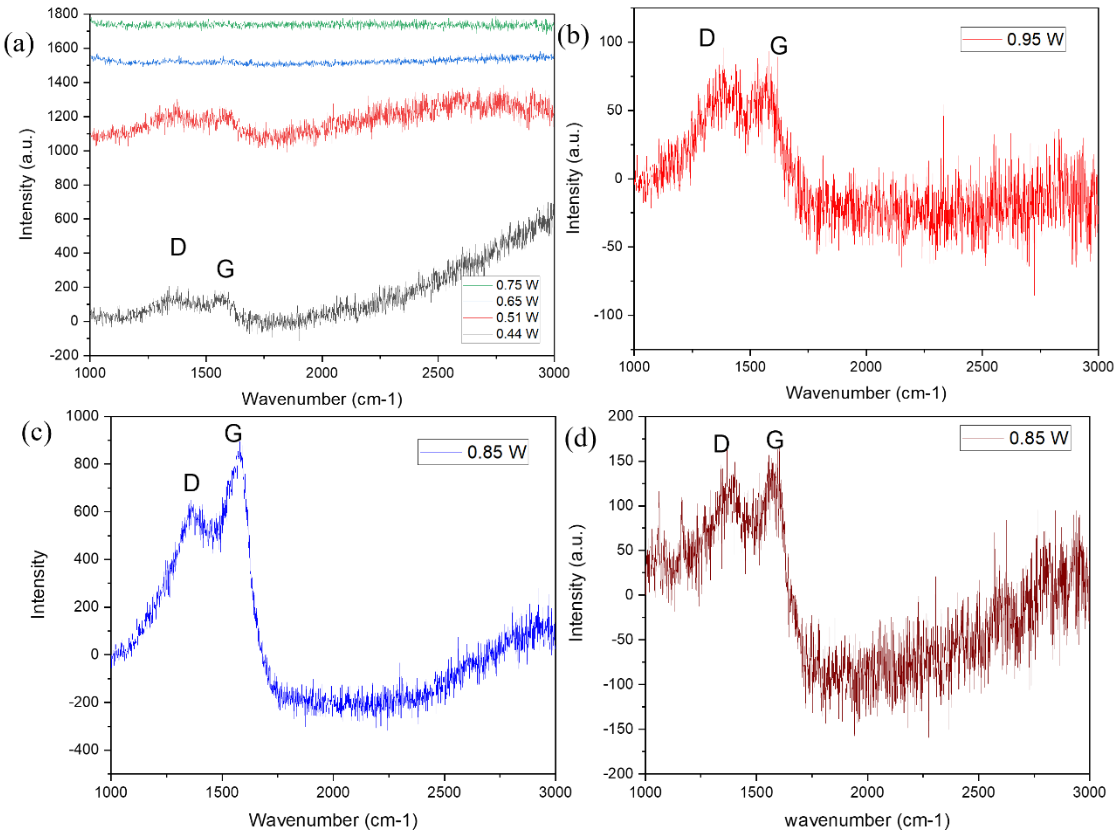

Fig. SS15 Raman spectra of LIG drawn on (a) Cellulose filled Geopoly, (b) Mixed cellulose long fiber filled Geopoly, (c) Hemp Fiber filled Geopoly, (d) ABS on Geopoly. The presence of D and G peaks prove that the laser drawn structures are LIG.

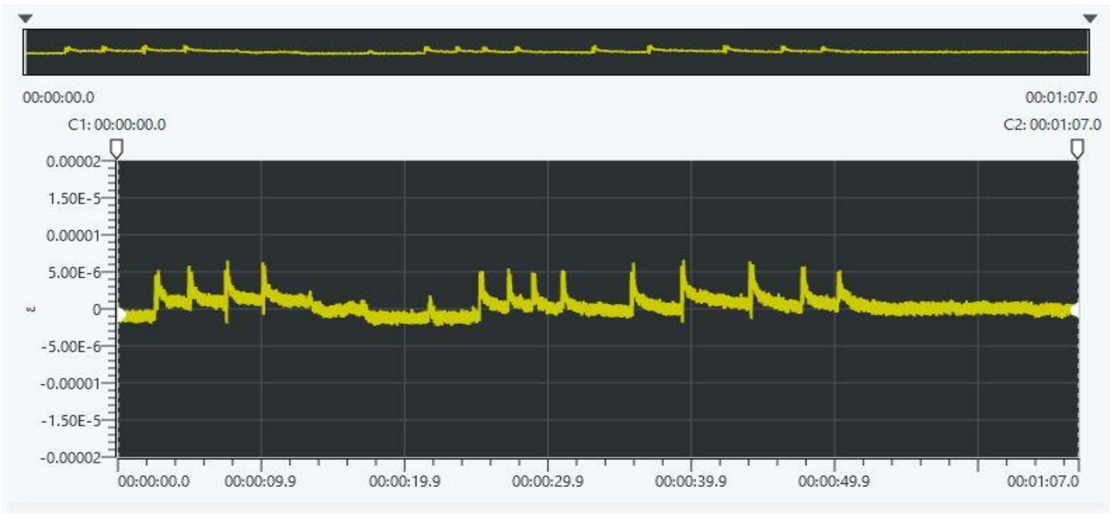

Fig. SS16 LIG obtained from Geopoly-based composites sensing repetitive stresses.

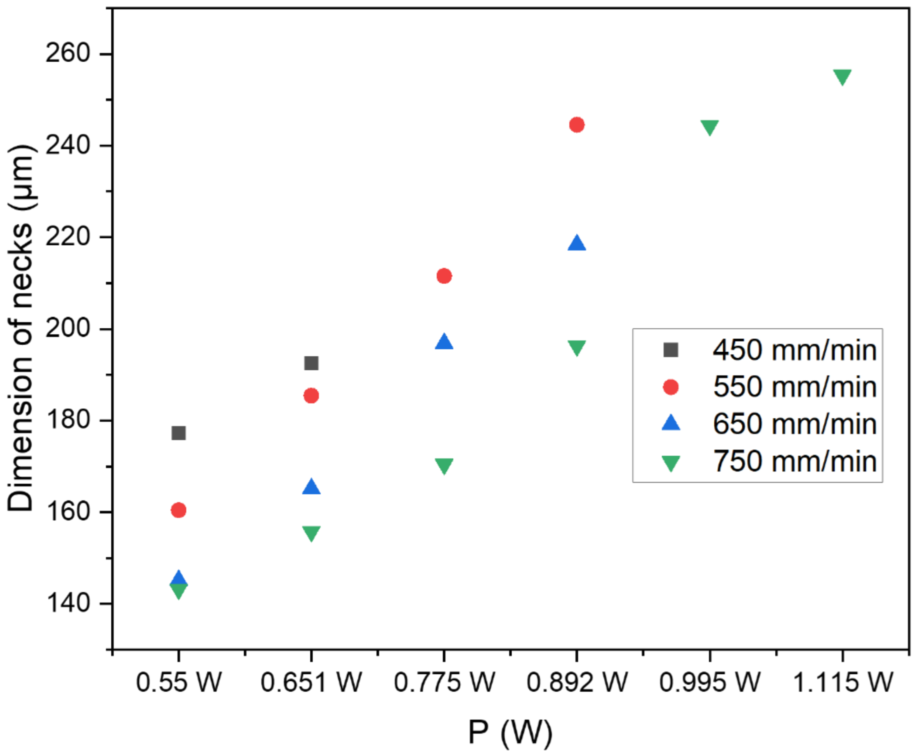

Fig. SS17 Dimension of necks of carbonized tracks due to varying pulse overlap at varying scan speeds.

Bibliography

[1] M. Abdulhafez, G.N. Tomaraei, M. Bedewy, Fluence-Dependent Morphological Transitions in Laser-Induced Graphene Electrodes on Polyimide Substrates for Flexible Devices, ACS Applied Nano Materials **4**(3) (2021) 2973-2986.

[2] M. Terakawa, Laser-Induced Carbonization and Graphitization, in: K. Sugioka (Ed.), Handbook of Laser Micro- and Nano-Engineering, Springer International Publishing, Cham, 2021, pp. 857-878.

[3] Z. Huang, P. Xue, C. Chen, D. Diao, Rapid fabrication of ultra-wear-resistant graphene nanocrystallite film by direct laser writing, Applied Surface Science 604 (2022) 154658.

[4] B. Dorin, P. Parkinson, P. Scully, Direct laser write process for 3D conductive carbon circuits in polyimide, Journal of Materials Chemistry C 5(20) (2017) 4923-4930.

[5] P. Scully, K. Ozanyan, Smart mats using embedded polymer optical fibres to classify human motion characteristics, Physica Medica 84 (2021) 304.